Dissertation ETH Nr. 15659

NEW ELECTROACTIVE MATERIALS FOR LITHIUM-ION RECHARGEABLE BATTERIES

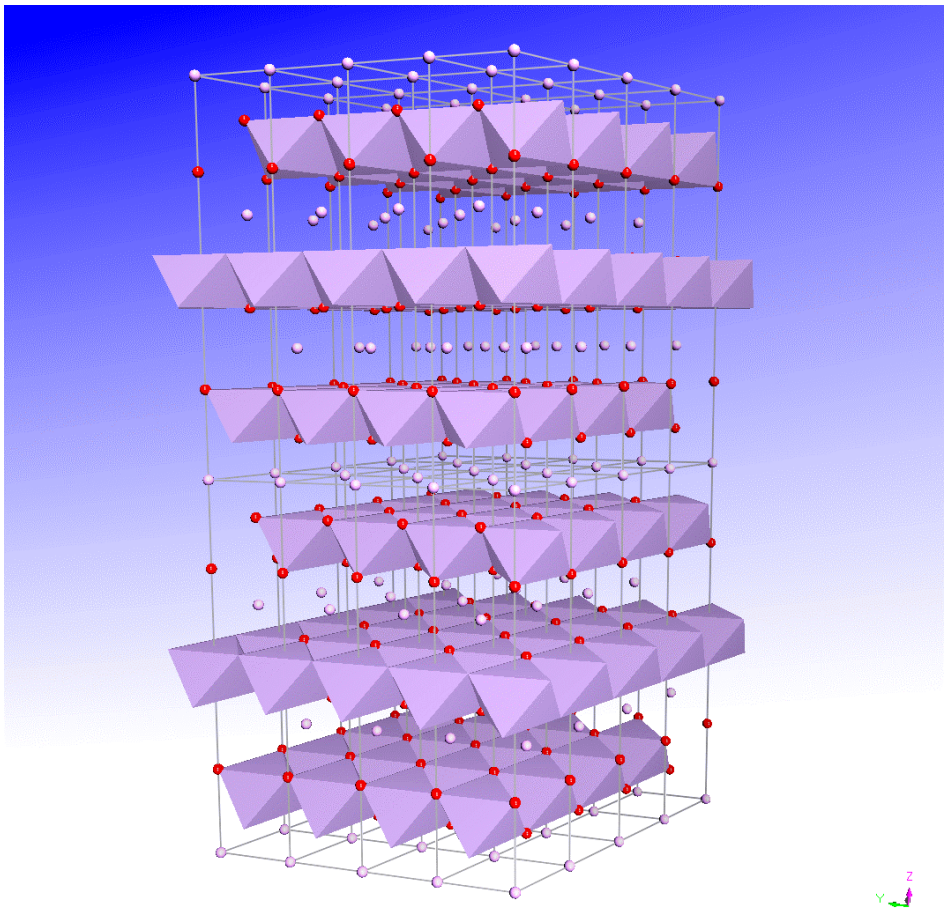

Andrea Piotto Piotto

Zürich, 2004

Dissertation ETH Nr. 15659

NEW ELECTROACTIVE MATERIALS FOR LITHIUM-ION RECHARGEABLE BATTERIES

A dissertation submitted to the
SWISS FEDERAL INSTITUTE OF TECHNOLOGY ZÜRICH

For the degree of
PHILOSOPHICAL DOCTOR OF NATURAL SCIENCES

Presented by
ANDREA PIOTTO PIOTTO
Dottore in chimica presso
L'Università "La Sapienza" di Roma
25/5/1988

Accepted on the recommendation of
Prof. Dr. Reinhard Nesper, examiner
Prof. Dr. Alexander Wokaun, co-examiner
PD Dr. Petr Novák, co-examiner

Zürich, 2004

Ai miei figlioletti, Luca e Silvia

Symbols and abbreviations

Name	Symbol	Unit
Activity coefficient	a_i	[-]
Avogadro's number	N	[mol^{-1}]
Boltzmann constant	k	[J/K]
Charge capacity	Q	[Ah]
Curie constant	C	[K]
Current density	j	[A/cm^2]
Electric current	I	[A]
Electrode area	A	[cm^2]
Faraday constant	F	[C/mol]
Gas constant	R	[J/(mol K)]
Gibbs free energy	ΔG	[J/mol]
Magnetic field	H	[G]
Magnetic moment	M, μ	[emu]
Mass	m, m_i	[kg]
Molar magnetic susceptibility	χ_{mol}	[cm^3/mol]
Molar weight	M_r	[g/mol]
Number of electrons exchanged	z	[-]
Potential	U	[V]
Power density	P_V	[W/l]
Practical charge density of the active material	Q_V	[Ah/l]
Practical energy density of the active material	W_V	[Wh/l]
Practical specific charge of the active material	q	[Ah/kg]
Practical specific energy of the active material	w	[Wh/kg]
Specific current	i_w	[A/kg]
Specific electrical conductivity	κ_0	[S/cm]
Specific power	p	[W/kg]
Standard Gibbs free energy	ΔG^0	[J/mol]
Standard potential	E^0	[V]
Stoichiometric coefficient	n_i	[-]
Temperature	T	[K]
Theoretical cell voltage	ΔE^0, U^0	[V]
Theoretical charge density	$Q_{V,th}$	[Ah/l]
Theoretical energy density	$W_{V,th}$	[Wh/l]
Theoretical specific charge	q_{th}	[Ah/kg]
Theoretical specific energy	w_{th}	[Wh/kg]
Volume	V, V_i	[l]
Weiss constant	Θ	[K]

Abbreviation	Name
DEC	Diethyl carbonate
DEMS	Differential electrochemical mass spectrometry
DMC	Dimethyl carbonate
DTA	Differential thermal analysis
EC	Ethylene carbonate
EMC	Ethyl methyl carbonate
GIC	Graphite intercalation compound
LP30	$LiPF_6$ 1M in EC:DMC = 1:1 weight
PC	Propylene carbonate
PTFE	Polytetrafluoroethylene
PVDF	Polyvinylidenfluoride
SEI	Solid electrolyte interface
SHE	Standard hydrogen electrode
XRD	X-ray diffraction

Table of contents

Chapter 1. Abstract 15

Chapter 2. Riepilogo 17

Chapter 3. Introduction 21

Chapter 4. Basic concepts 25

4.1 Electrochemical cells 26
4.2 Batteries 27
4.3 Cathode and anode 28
4.4 Characterization of electrochemical cells 30
4.4.1 Cell voltage 30
4.4.2 Current density 30
4.4.3 Charge capacity 30
4.4.4 Theoretical specific charge and theoretical charge density 31
4.4.5 Practical specific charge and practical charge density 31
4.4.6 Theoretical specific energy and theoretical energy density 31
4.4.7 Practical specific energy and practical energy density 32
4.4.8 Specific power and power density 32

Chapter 5. Lithium-ion reversible batteries 35

5.1 Introduction 35
5.2 Materials for rechargeable lithium-ion batteries 37
5.2.1 Electrolyte 37
5.2.2 Negative electrodes 39
5.2.3 Positive electrodes 42
5.3 Classification of insertion compounds 43

5.4 Principle of Li-ion cells 45
5.5 Advantages of Li-ion batteries 46

Chapter 6. Solid state syntheses and characterization 49

6.1 Oxide syntheses 49
6.1.1 Nomenclature for complex oxide systems 49
6.1.2 Wet synthesis procedure 50
6.1.3 Dry synthesis procedure 52
6.1.4 Thermal treatment 53
6.2 X-ray powder diffraction (XRD) characterization 54
6.2.1 In-situ XRD cell 54

Chapter 7. Electrochemical characterization 57

7.1 Instrumentation 57
7.2 The cell 58
7.3 Electrode preparation 58
7.3.1 The working electrode 58
7.3.2 The reference electrode 60
7.3.3 The counter electrode 61
7.3.4 The electrolyte 61
7.4 Cyclic voltammetry 62
7.5 Galvanostatic measurements 64
7.6 Differential specific charge plot 65
7.7 Coulometric titration 65

Chapter 8. Experimental data analysis 67

8.1 The program Comparis 67
8.2 XRD powder pattern data analyses 68
8.2.1 Raw pattern fitting 68
8.2.2 Cell parameter calculation 69

8.2.3 Deviation calculations 71
8.3 Specific charge vs. cycles: an empirical description 72

Chapter 9. Electroactive Manganese-based materials 77

9.1 Manganese dioxide 77
9.2 $LiMn_2O_4$ spinel 79
9.3 $LiMnO_2$ 81

Chapter 10. Characterization and doping of $LiMn_{0.5}Ni_{0.4}Al_{0.1}O_2$ .. 83

10.1 Introduction 83
10.2 $LiMn_{0.5}Ni_{0.4}Al_{0.1}O_2$ doped with Sodium 84
10.3 Boron – Aluminum replacement in $LiMn_{0.5}Ni_{0.4}Al_{0.1}O_2$ 87
10.4 $LiMn_{0.5}Ni_{0.4}Al_{0.1}O_2$: treatment with graphite oxide 90
10.4.1 Synthesis procedure 90
10.4.2 Electrochemical characterization 91
10.5 Conclusions 93

Chapter 11. Investigation on $LiMn_aNi_bAl_cO_2$ compounds 95

11.1 $LiMn_{0.5}Ni_{0.4}Al_{0.1}O_2$ crystal superstructure 95
11.1.1 Superstructure models 96
11.2 $LiMn_{0.5}Ni_{0.4}Al_{0.1}O_2$: changing composition to fit superstructure requirements 97
11.3 Syntheses 97
11.4 XRD characterization 98
11.5 Electrochemical characterization 104
11.6 Conclusions 111

Chapter 12. Investigations on $LiMn_aCo_bNi_cAl_dO_2$ compounds .. 113

12.1 Synthesis 113
12.2 XRD characterization 115

12.3 Electrochemical characterization 119
12.3.1 LiMnNiCoAl.283.566.141.010-950°C 124
12.3.2 LiMnNiCoAl.335.495.160.010-950°C 126
12.3.3 LiMnNiAl.500.400.100-950°C 128
12.4 Conclusions 130

Chapter 13. Further investigations on $LiMn_{0.283}Ni_{0.566}Co_{0.141}Al_{0.01}O_2$ and $LiMn_{0.335}Ni_{0.495}Co_{0.160}Al_{0.01}O_2$. 131

13.1 Cycling in different galvanostatic conditions. 131
13.2 Syntheses at different temperatures 134
13.3 Irreversible capacity at the first cycle 140
13.3.1 Experimental 140
13.3.2 Conclusions 142
13.4 Coulometric titration of LiMnNiCoAl.283.566.141.010-950°C 143
13.5 How lithium intercalation affects the structure 144
13.5.1 Discussion of the results 146
13.6 How cycling affects the structure 148
13.7 Syntheses of non-Al doped compounds 150
13.8 Conclusions 155

Chapter 14. Specific charge vs. cell parameter 157

14.1 Experimental 157
14.2 Results 158
14.3 Conclusions 158

Chapter 15. Characterization of other oxides 165

15.1 $H_2V_3O_8$ nano fibers 165
15.1.1 Conclusions 169
15.2 Titanium dioxide 170
15.2.1 TiO_2 anatase 170

15.2.2 Zirconia coated Titanium dioxide 182

Chapter 16. Conclusions 185

References **..... 189**

Acknowledgements **..... 191**

Curriculum vitae **..... 192**

Chapter 1.

Abstract

Rechargeable batteries are becoming more and more important in our life, and get increasingly present in our civilization. They supply energy to many battery-powered appliances and open new fields of everyday application (Pocket PCs, mobile phones, household appliances etc.), not to mention the electrically powered car application, which is still an attractive area. In this evolving field, Li-ion technology seems to be superior to other technologies, because of its high performances, in terms of specific charge and in terms of work temperature range.

Schematically a Li-ion accumulator is composed of:

- Anode (negative pole): constituted by special kind of graphite
- Non-aqueous electrolyte
- Cathode (positive pole): constituted by compounds (mainly oxides) which allow the reversible insertion of Li^+ within their crystal structure.

The term "Li-ion" derives from the fact that inside the system lithium is present only as ionic specie, metallic lithium is absent.

In Li-ion technology, $LiCoO_2$ is the most extensively used cathodic material with a specific charge of about 140Ah/kg. Despite this interesting performance, its cobalt content causes problems of costs and environmental pollution.

The actual research is thus devoted to eliminate, or at least to reduce, these problems. The research of this thesis was exclusively oriented to the synthesis and characterization of cathodic materials. The starting point was the previous

work of a mixed Mn-Ni based oxide, $LiMn_{0.5}Ni_{0.4}Al_{0.1}O_2$, from which performances analogues to $LiCoO_2$ have been obtained.

Several products have been synthesized and characterized with electrochemical (cyclovoltammetry, chronopotentiometry) and structural (X-ray diffraction, scansion electron microscopy and transmission electron microscopy) techniques.

All products obtained belong to the crystallographic space group $R\bar{3}m$ (n.166), they have 2D layered structure (see Figure 25).

Two of the new products synthesized, $LiMn_{0.283}Ni_{0.566}Co_{0.141}Al_{0.01}O_2$ and $LiMn_{0.335}Ni_{0.495}Co_{0.160}Al_{0.01}O_2$ respectively, furnished 170Ah/kg and 160Ah/kg. This made them good candidates for a $LiCoO_2$ replacement in Li-ion batteries, because the materials are cheaper, better performers and have less environmental impact. In both products a small amount of aluminum is present (1%), because this is supposed to stabilize the structure and reduce the distortion due to the Jahn-Teller effect (which acts mainly on Mn and Ni).

A new empirical description, following the specific charge vs. cycles, has been proposed and applied to all products synthesized in this work. According to this description, a correlation between cell parameter and electrochemical performances is visible: smaller cell parameters ***a*** and ***c*** favour the electrochemical performances.

Several other products as TiO_2-(anatase) based materials were also tested; they performed very high specific charges, which is mainly due to the low Li^+ insertion potential (~1.8 Volts compared to 3.7 Volts of Mn-based oxides), and it furnished a specific energy of approximately the half, in comparison to the best Mn-based oxides.

Noticeable were the performances of $H_2V_3O_8$ nanofibers, which show a specific energy of 10-15% higher than the best Mn-based products, with a current rate 13 times higher. Unfortunately, these amazing performances last only for 50-60 cycles, after that, the product undergoes quick fading, which does not make them competitive to Mn-oxides.

Chapter 2.

Riepilogo

Con l'avvento della civiltà dell'informazione, e coll'incessante crescita nella domanda di dispositivi elettronici portatili, quali notebook, palmari, telefonini ecc., il mercato degli accumulatori ha avuto una fortissima espansione.
Inoltre le crescenti prestazioni di tali dispositivi, vanno di pari passo con la richiesta di nuovi tipi di accumulatori più capaci e leggeri.
Ed è in questa corsa che gli accumulatori Li-ion sembrano per il momento prevalere nettamente su altre tecnologie, in virtù sia delle loro prestazioni in termini di capacità specifica che in termini intervallo di temperatura di funzionamento.
Schematicamente, un accumulatore Li-ion è costituito da:

- Anodo (polo negativo): costituito da particolari tipi di grafite.
- Elettrolita non acquoso.
- Catodo (polo positivo): costituito da particolari composti (generalmente ossidi) che consento l'inserzione reversibile del Li^+ all'interno della loro struttura.

Il termine Li-ion deriva dal fatto che all'interno del sistema non è mai presente litio metallico ma solo litio ione.
Lo stato dell'arte attuale vede prevalere $LiCoO_2$ come materiale catodico con capacità specifica di 140Ah/kg. Nonostante le sue interessanti prestazioni, quest'ossido presenta problemi di costi e inquinamento ambientale entrambe dovuti al cobalto. L'attuale ricerca è orientata quindi sia ad eliminare od almeno ridurre la percentuale di cobalto e ad incrementarne le prestazioni.

In questa tesi l'attenzione verrà esclusivamente focalizzata alla sintesi e caratterizzazione di materiali catodici. Essa prese spunto da un precedente lavoro in cui, con un ossido misto manganese-nichel $LiMn_{0.5}Ni_{0.4}Al_{0.1}O_2$, prestazioni analoghe al $LiCoO_2$ erano state ottenute.

Diversi prodotti sono stati sintetizzati e caratterizzati con tecniche elettrochimiche (ciclovoltammetria, cronopotenziometria) e strutturali (diffrazione di raggi-X, microscopia a scansione e a trasmissione elettronica).

Tutti i prodotti ottenuti appartenevano allo stesso gruppo cristallografico $R\bar{3}m$ (n.166). Avevano quindi tutti la stessa struttura stratiforme di cui un esempio è mostrato in Figure 25. Allo scopo di meglio classificare i prodotti, è stato proposto un nuovo modello per descrivere l'andamento della capacità specifica durante la ciclazione. Seguendo questo modello è stato possibile correlare tra loro grandezze quali la capacità specifica con i parametri di cella, ne è scaturito un l'interessante risultato che le prestazioni elettrochimiche dei composti sono tanto più buone quanto più piccoli risultano i parametri reticolari ***a*** e ***c***.

Da questo studio sono risultati due nuovi composti, $LiMn_{0.283}Ni_{0.566}Co_{0.141}Al_{0.01}O_2$ and $LiMn_{0.335}Ni_{0.495}Co_{0.160}Al_{0.01}O_2$ che fornirono rispettivamente 170Ah/kg e 160Ah/kg, che quindi sono seriamente candidati alla sostituzione dell' $LiCoO_2$ in quanto più prestanti, più economici e aventi minore impatto ambientale.

In entrambe i prodotti, seppur in percentuale molto limitata (1%) è stato mantenuto l'alluminio, in quanto non essendo elettroattivo contribuisce alla stabilizzazione della struttura, limitandone la distorsione dovuta all'effetto Jahn-Teller che agisce principalmente sul nichel e sul manganese distorcendone la sfera di coordinazione destabilizzandone quindi la struttura.

Sono stati inoltre testati e caratterizzati numerosi altri prodotti a base di TiO_2 anatasio. I quali hanno fornito eccellenti prestationi in termini di capacità specifica, ma principalmente a causa del loro basso potenziale di inserzione del

Li^+ (~1.8Volts rispetto ai 3.7Volts degli altri ossidi) hanno fornito una energia specifica di circa la metà rispetto ai migliori prodotti.

Notevole invece è stata la prestazione di un composto a base di Vanadio $H_2V_3O_8$ in forma di nanofibre, che ha dato valori di energia specifica 10-15% superiori ai migliori ossidi basati sul manganese, con una corrente specifica circa 13 volte più alta. Purtroppo queste sorprendenti prestazione durano solo per una sessantina di cicli, dopodiché la veloce perdita di carica specifica del materiale lo rende praticamente inutilizzabile ai nostri scopi.

Chapter 3.

Introduction

Nowadays we are all battery consumers. Batteries are everywhere, but hidden inside a large variety of articles ranging from tiny electronics via toys, medical implants to cars and even houses. But not all batteries are alike. Some of them are used until they are discharged and then discarded (hopefully recycled) because they cannot be recharged (not rechargeable batteries). Both conventional and alkaline batteries belong to this class. Rechargeable batteries are a better solution, but many requirements arise. They should last a long time and be ready anytime after recharge. Two main types of rechargeable batteries dominate the market right now: Lead-acid and Nickel-Cadmium batteries.

Lead acid batteries have been used in cars for many decades because of their high current peak. The capability they provide is mainly used for starting, lighting and ignition. Although they can be used for automotive, they are far from being competitive with the internal combustion engine in terms of power density.

In absence of better technologies, nickel-cadmium batteries (NiCd) were adopted for small applications, such as portable phones and computers. But any user of these batteries is waiting for necessary technical improvements: they run out of

charge too quickly, even when not in use and they may have a "memory effect" that causes loss of capacity.

Yet, in addition to these problems, there are also indirect problems for the environment, due to the high toxicity of certain elements used, especially lead and cadmium.

There are many reasons to believe in the “promises” of lithium batteries. First of all, lithium is the lightest metal and this results in a high specific charge. Furthermore, it has the lowest reduction potential, which allows for a high potential and thus is correlated to a high specific energy.

The first attempts of making Li-batteries were highly unsuccessful due to safety reasons. This was due to frequent explosions arising from the formation of dendrites of Li metal on charging which lead to short cuts of the cells. Further research solved this problem in a satisfactory way due to the introduction of the new lithium-ion technology. In these systems, the negative electrode is not made of pure lithium metal, but of materials such as graphite or other carbons, which are able to intercalate the lithium ions and prevent dendrite formation.

In recent years, the rechargeable battery market further expanded with the large demands for electronic equipment, such as mobile phones and pocket PCs. Miniaturization of various electronic equipments rapidly advances. Despite of ongoing miniaturization, the electric power consumption in portable devices tends to increase continuously. For these reasons, new products for lithium-ion batteries have been investigated and developed.

Lithium–ion batteries actually represent the “leading edge” in small rechargeable batteries, due to their high specific energy operating at about 4 volts.

The Li-ion technology is based on the use of suitable intercalation compounds for the electrodes, which host Li^+ ions in both cathode and anode, respectively [1]. In general, a lithium transition metal oxide is employed in the cathode and a

[1] Intercalation reactions refer to a guest specie (ion or molecule) insertion into a solid host lattice without any rearrangement of its framework. The host lattice can change in terms of cell parameter, but not in terms of space group.

carbonaceous material for the anode. Most of these lithium-ion batteries use the lithium carbon/lithium cobalt oxide pair, separated by a liquid ionic conductor. Due to elevated toxicity and high cost of cobalt, the present work focuses on the synthesis and the electrochemical characterization of new, cobalt-poor and cobalt-free, layered electroactive compounds with a high cycling stability.

Based on previous work in our group the target compounds were of the general formula $Li_xMn_aNi_bCo_cAl_dO_2$ (with $a+b+c+d=1$) crystallizing with a layered structure (α-$NaFeO_2$ structure type, space group $R\bar{3}m$, no. 166).

As 3d-transition metals are the target redox centers for the cathodes because of their high redox potentials and their relatively low weight, they are a general focus of present battery research. In this work, many other transition metal oxides have been checked for possible electrochemical application but only two other ones which show attractive properties were subject of more extended investigations, namely $H_2V_3O_8$ and TiO_2 in the anatase modification.

Chapter 4.

Basic concepts

The main purpose of modern electrochemistry is to study ion behavior in different microscopic environments. The fundamental knowledge to be obtained should have important impact on applications in several fields, such as batteries, fuel cells, catalysis, corrosion and biological membranes.

Experimental conditions in general are not at the thermodynamic equilibrium, nevertheless, the knowledge of equilibrium electrochemistry is a fundamental base for studying also non-equilibrium processes.

Thermodynamics is directly applicable to electrochemical processes at equilibrium, but keeping in mind the character of the electric charge complication with respect to simple models have to be taken into account because: 1.) electrostatic interaction between ions even at large distances influence the specific ion properties; 2.) ions are sensitive to changes of the electric potentials arising from local environmental situations, which means that their chemical activity does change with the slightest change of coordination. Wherever more phases are present (for example: a metallic electrode immersed in an electrolytic solution), each of them may influence the chemical potential of the other and vice versa. This observation is the core of electrochemistry [**1**].

4.1 Electrochemical cells

An electrochemical or voltaic cell consists of two electrodes immersed in an electrolyte solution. The electrodes are electronic conductors and the electrolyte solution is an ionic conductor. At the interface between electronic and ionic conductors, a passage of electrical charge is connected to a chemical reaction, a so-called *redox reaction*.

An explanatory example is the system [**2**]:

$$Pt, H_2|HCl|AgCl, Ag$$

which means a platinum/hydrogen electrode interacts with a silver/silverchloride electrode via an HCl ionic conductor. The simplicity of such a cell is the presence of one electrolyte (HCl), which unifies the solution potential Φ(S) for both electrodes. This particular cell is so called "*without liquid contact"*, and its treatment is rather simplified. Both electrode interfaces have a specified standard electrode potential, E^0, which can be calculated from the thermodynamic data of the reaction. For equilibrium conditions we find:

$$E^0 = \frac{-\Delta G^o}{z \cdot F} \qquad [V] \qquad \textit{(eq. 1)}$$

with: ΔG^0: Standard Gibbs free energy z: number of electrons exchanged
F: Faraday constant E^0: standard electrode potential.

In this work, the following cells without liquid contact have been used:

anodic side ($^{(-)}$Me, Li)|LP30 electrolyte|cathodic side ($Me^{(+)}$)

Because it is impossible to measure individual electrode potentials in an absolute sense, electrode potentials are determined with reference to another electrode, which may be set as a standard or normal. The normal electrode used for this purpose is the standard hydrogen electrode (SHE) (T = 25 °C, p = 1 bar, all active species at unity activity). For non-standard conditions we use the Nernst equation to calculate the potential of the half-reactions at equilibrium:

(eq. 2) $$E = E^0 - \frac{R \cdot T}{z \cdot F} \sum \ln a_i^{\nu_i}$$ [V] (Nernst equation)

with: R: gas constant *T: absolute temperature*

ν_i: stoichiometric coefficient *a_i: activity*

The cell voltage of an electrochemical cell is calculated from the electrode potentials (reduction potentials) of the half-reactions. The overall *theoretical cell voltage*, ΔE^0 or U^0, is obtained by subtracting the negative electrode potential, $E^{0,(-)}$, from the positive electrode potential, $E^{0,(+)}$:

(eq. 3) $$U^0 = \Delta E^0 = E^{0,(+)} - E^{0,(-)}$$ [V]

4.2 Batteries

Batteries can be divided into several groups:

- **Primary batteries:** Primary batteries means ‘primary’ source of electricity, which delivers energy right from the start. Daniel’s cell for example can furnish energy after a fresh cell is assembled, commercial alkaline cells are primary batteries.
- **Secondary batteries**: Secondary batteries means ‘secondary’ source of electricity. Unlike the primary battery, a freshly fabricated cell cannot deliver electricity until the cell is charged. Lead acid cells are a typical example of secondary batteries, because they need to be charged before use.
- **Not rechargeable**: Not rechargeable batteries cannot be charged, therefore they must necessarily be ‘primary batteries’.
- **Rechargeable batteries**: Rechargeable batteries are designed to be recharged, they can be ‘primary’ or ‘secondary’. Two important criteria must be considered to evaluate these batteries: the number of possible recharge cycles and their specific charge.

- **Mechanically rechargeable batteries:** In this kind of batteries the charging process consists of renewing one of the electrodes of the cell once it is consumed during discharge (e.g. the zinc electrode in zinc-air cells).

4.3 Cathode and anode

The terms *cathode* and *anode* are defined as follows:

- ***Cathode*** is an electrode, which undergoes a reduction reaction at its interface. That means, the electrode transfers the electrons to the species present at the interface.
- ***Anode*** is an electrode with an oxidation reaction at its interface. And thus "takes" the electrons from species present at the interface.

In our particular case, we have cell assemblages as follows:

$^{(-)}$Me, Li|LP30 electrolyte|Cathodic material, Me$^{(+)}$

The reactions at the positive electrode are:

$$y \cdot Li^{+}_{solution} + Li_x(HOST) \xrightarrow{+y \cdot e^-} Li_{x+y}(HOST) \quad \text{reduction}$$

and

$$Li_{x+y}(HOST) \xrightarrow{-y \cdot e^-} Li_x(HOST) + y \cdot Li^{+}_{solution} \quad \text{oxidation}$$

Since we are considering a positive electrode (highest potential), only the reduction process can take place spontaneously (eg: when discharging the cell), that is why we are referring to the transition metal oxides investigated herein as "*cathodic materials*". The oxidation process takes place only if it is forced by external (during charging).

Values of potentials for various half-cell reactions are referred in [**3**]. Theoretical cell voltages can be calculated if two half-cell reactions are known. Some important standard potential values in battery technology are shown in Figure 1.

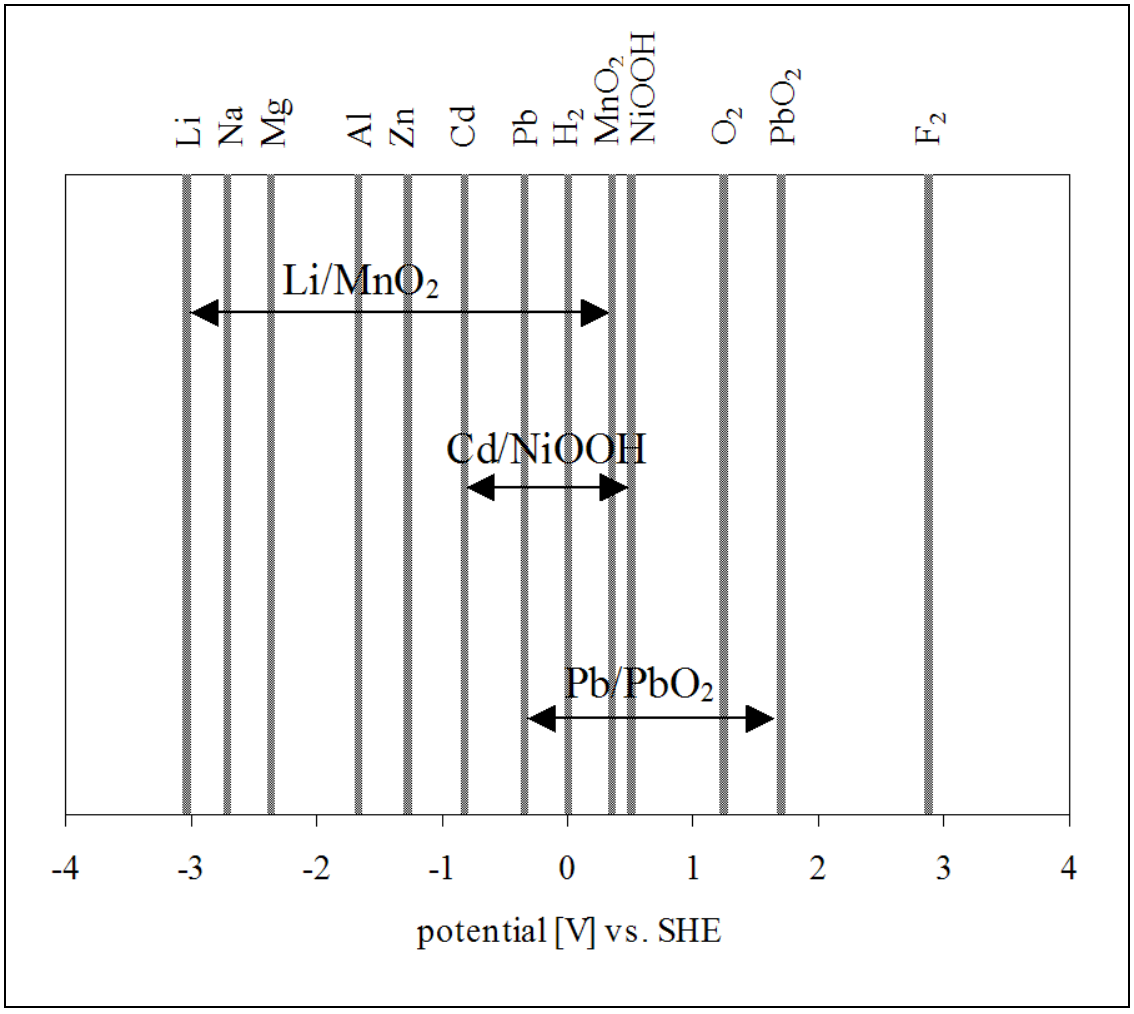

Figure 1: Some selected standard electrode potentials.

A high cell voltage is obtained by combining two electrode systems with very different potentials from each other.

The Nernst equation (eq. 2) is valid at equilibrium conditions. If this situation is disturbed for example by application of an external potential which causes current drain, the voltage between the electrodes will begin to fall from its equilibrium value. This process is called *polarization* or *overvoltage*. Overvoltage is a responsible value for the losses appearing as a result of the current flow.

4.4 Characterization of electrochemical cells

There are several criteria to evaluate the performance of electrochemical power sources. A distinction must be made between the theoretical values and the practical values. Theoretical values are calculated from the thermodynamics of the electrochemical cell reaction. Practical values are related to the total mass of the complete battery, including the mass of the electrolyte, the separators, the current collectors, the terminals and the cell housing [4]. In this work the specific charge always refers to the weight of the active component only. A list of the definitions for the measured parameters is given below:

4.4.1 Cell voltage

The cell voltage can be calculated from the Gibbs free energy of the corresponding chemical reaction:

$$U^0 = \Delta E^0 = \frac{-\Delta G^0}{z \cdot F} \quad [\mathrm{V}] \qquad \textit{(eq. 4)}$$

4.4.2 Current density

The current density j is calculated by dividing the total current I flowing through an electrode by the electrode area A. The normal case is that the geometrical area is used:

$$j(t) = \frac{I(t)}{A} \qquad \textit{(eq. 5)}$$

4.4.3 Charge capacity

The charge capacity Q is the total amount of charge obtainable from a cell:

$$Q = \int_{t_1}^{t_2} I(t) \cdot dt \quad [\mathrm{Ah}] \qquad \textit{(eq. 6)}$$

4.4.4 Theoretical specific charge and theoretical charge density

The theoretical specific charge q_{th} is the amount of charge per kg of reactants m_i, and it can be calculated from the stoichiometry of the overall cell reaction:

$$q_{th} = \frac{z \cdot F}{\sum_i m_i} \quad \text{[Ah/kg]} \qquad \textit{(eq. 7)}$$

The charge divided by the volume of reactants V_i leads to the theoretical charge density $Q_{V,th}$:

$$Q_{V,th} = \frac{z \cdot F}{\sum_i V_i} \quad \text{[Ah/l]} \qquad \textit{(eq. 8)}$$

4.4.5 Practical specific charge and practical charge density

The practical specific charge q, or the practical charge density Q_V, is the total charge obtainable from a practical cell, divided by the total mass or the volume of the cell, respectively:

$$q = \frac{1}{m} \int_{t_1}^{t_2} I(t) \cdot dt \qquad \text{[Ah/kg]} \qquad \textit{(eq. 9)}$$

$$Q_V = \frac{1}{V} \int_{t_1}^{t_2} I(t) \cdot dt \qquad \text{[Ah/l]} \qquad \textit{(eq. 10)}$$

Another quantity often used is the so-called *irreversible specific charge*. It is defined as the difference between the specific charge spent on charging and the one obtained on discharging a cell. To obtain a normalized value this difference is then divided by the specific charge spent on charging.

4.4.6 Theoretical specific energy and theoretical energy density

The theoretical specific energy w_{th}, or the theoretical energy density $W_{V,th}$, can be calculated from the Gibbs energy change of the electrochemical cell reaction,

divided by the sum of the stoichiometric masses of the reactants or by their volumes, respectively:

$$w_{th} = \frac{z \cdot F \cdot \Delta E^0}{\sum_i m_i} \qquad \text{[Wh/kg]} \qquad \textit{(eq. 11)}$$

$$W_{V.th} = \frac{z \cdot F \cdot \Delta E^0}{\sum_i V_i} \qquad \text{[Wh/l]} \qquad \textit{(eq. 12)}$$

4.4.7 Practical specific energy and practical energy density

The practical specific energy w, or the practical energy density W_V, is the total electrical energy obtainable from a practical cell divided by the mass or the volume of the cell, respectively:

$$w = \frac{1}{m} \int_{t_1}^{t_2} I(t) \cdot U(t) \cdot dt \qquad \text{[Wh/kg]} \qquad \textit{(eq. 13)}$$

$$W_V = \frac{1}{V} \int_{t_1}^{t_2} I(t) \cdot U(t) \cdot dt \qquad \text{[Wh/l]} \qquad \textit{(eq. 14)}$$

4.4.8 Specific power and power density

The specific power p is the capability to deliver power per mass. The specific power of a cell depends on the discharge current and decreases during discharge. The power density P_V is the power divided by the volume of the cell. Again, one distinguishes between theoretical and practical values:

$$p = \frac{I \cdot U}{\sum_i m_i} \qquad \text{[W/kg]} \qquad \textit{(eq. 15)}$$

$$P_V = \frac{I \cdot U}{\sum_i V_i} \qquad \text{[W/l]} \qquad \textit{(eq. 16)}$$

In battery technology the term *c-rate* (C/Δt) is often used. C means a nominal or, sometimes, a theoretical charge capacity of a cell or battery in [Ah]. Therefore, C/2, for example, means a current theoretically allowing a full discharge in two hours.

Chapter 5.

Lithium-ion reversible batteries

5.1 Introduction

In the past, the first lithium batteries were assembled with metallic lithium as negative electrode (anode) [**5**], because it is the most effective Li source and because its unique characteristic to have the lowest E^0 = -3.04 V vs. SHE, q_{th} = 3860 Ah/kg. The firsts commercial Li rechargeable batteries were commercialized by Exxon and later, by Moli Energy [**6**]. Unfortunately, fires and even explosions took place due to the assembly technique. The main problem was the high thermodynamic instability of lithium in non-aqueous electrolytes, which are immediately reduced at the interface to the electrode.

Although the decomposed electrolyte immediately passivates the lithium surface, forming a Li permeable film ("solid electrolyte interface", SEI), two more problems arise during cycling:

1. Lithium deposition over the anode is obstacled by SEI already formed. Starting with an irregular deposition, it is immediately degenerated into dendritic formation [**7**]. This phenomenon is favoured by a high electric field gradient over an irregular deposit.

2. These dendritic formations often tend to be electrically isolated from the anodic substrate, reducing further the anodic lithium available for the cycling.

In Figure 2, dendrite formation and isolating mechanism of lithium portions are schematically shown.

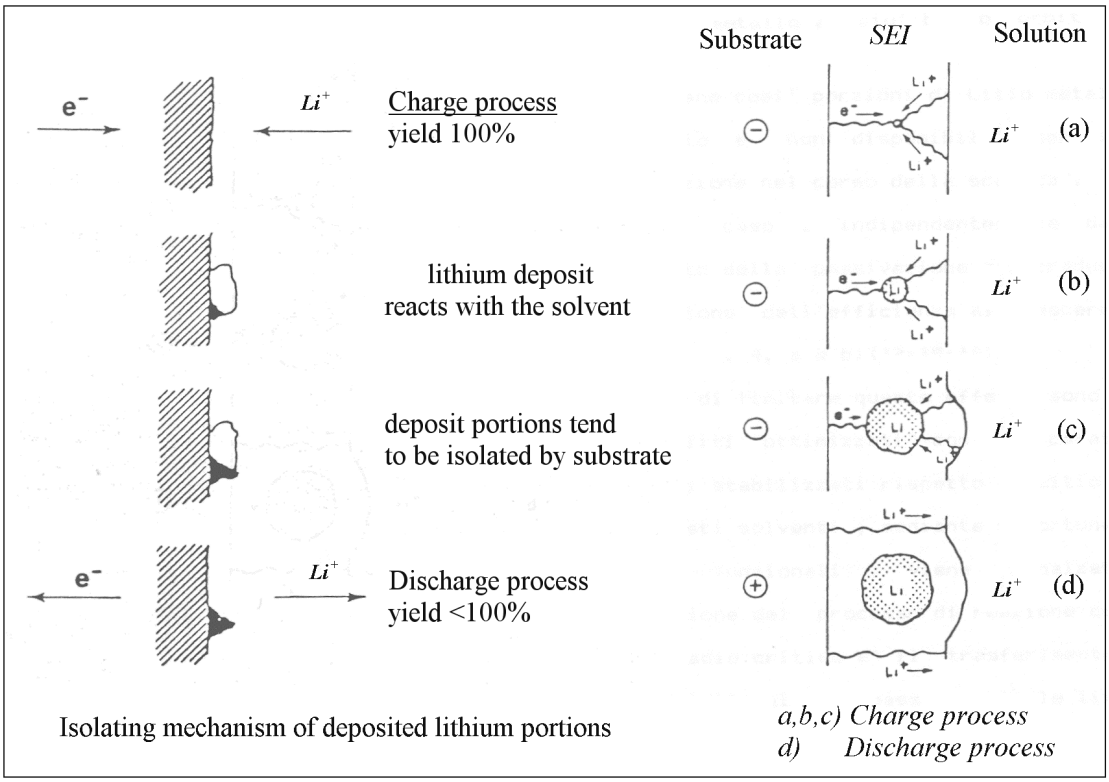

Figure 2: Dendrite formation (left side) and isolating mechanism of deposit lithium portions (right side).

The growing of dendrites becomes a problem when they perforate the separator placed between anode and cathode, shortcutting the cell, and all stored energy of the cell is instanteneously transformed into heat. Explosions and fires are possible, due to the low melting point (ca. 180°C) and the high reactivity of lithium and the low thermal stability of the whole system [**8**,**9**].

These problems can be avoided partially, by increasing the distance between anode and cathode, using a fivefold excess of lithium to compensate its reaction with the electrolyte and a loss of lithium by the entrapped phenomenon. Nevertheless, it is clear that elemental lithium can not be used further for the battery. Sony proposed a new system in 1991, with carbon as

anode material. This replacement, although with different specific charge than that of lithium (ca. 10 times less), was nevertheless more reliable and safer. This new generation of lithium rechargeable batteries were called *"Lithium-ion batteries"*, to emphasize that no metallic lithium was contained. Of course the anodic specific charge of these new systems was dramatically reduced at about 10% of the Li-metal specific charge, but this fact opened a new research field. The field of the anodic materials.

The main aim of the rechargeable lithium battery research program at the Paul Scherrer Institute (PSI) and at the Swiss Federal Institute of Technology (ETHZ) is to develop batteries with high energy density, high power density, long life cycles and good charge retention. These high performances must be delivered in a safe and reliable way. In this context the choice of the cell components however, is a compromise in order to achieve best results.

5.2 Materials for rechargeable lithium-ion batteries

5.2.1 Electrolyte

In this work, the term *electrolyte* refers to the solution composed by the solvent and the lithium salt. The choice of the electrolyte and the solvent for lithium-ion batteries can be critical. The use of high potential cathode materials (more than 4 V vs. Li^+/Li) requires a high stability of the electrolyte, as well as the solvent in a wide potential range. Some characteristics that *electrolytes* have to fulfill are listed below [**8, 10**]

- a wide electrochemical voltage window, ideally from 0 to 5 V vs. Li^+/Li;
- thermodynamically stable or at least kinetically stable in the voltage range considered;
- a good ionic conductivity (>1 mS/cm) so as to minimise the internal resistance (to achieve this, the viscosity should be small);
- a good thermal stability (up to 90 °C);
- good compatibility with other components of the cell;

- low costs, reliable safety, and small environmental impact.

The classes of electrolytes used in lithium-ion batteries are:

- **Liquid organic electrolytes** consisting of pure, or mixtures of aprotic organic solvents with a lithium salt dissolved in it. In particular, organic carbonates such as propylene carbonate (PC), ethylene carbonate (EC), dimethyl carbonate (DMC) and diethyl carbonate (DEC) were in the centre of interest [**10**].
- **Liquid inorganic electrolytes.** Are mainly SO_2-based. Their very high ionic conductivity contributes to a low ohm dispersion [**11**], unfortunately they also show hazardous and safety problems.
- **Polymer electrolytes.** Are a valid alternative to liquid electrolytes. Lithium ions are incorporated into a polymer matrix. The polymer is solid and flexible, so that the design and the assembling of the battery are kept simplified. The main disadvantage is that polymer electrolytes have lower ionic conductivity compared to liquid electrolytes. A typical example of the polymer is polyethylene oxide (PEO) [**12**].
- **Polymer gel electrolytes.** Liquid carbonate-based electrolytes (in which the solvent is: propylene carbonate, ethylene carbonate, dimethyl carbonate) are ionic conductors for most lithium batteries currently sold for portable electronics. These electrolytes can operate between -20 and +60 °C and provide good conductivity of the order of 1 mS/cm at ambient temperatures. However, they do not offer better conditions in terms of safety or assembly facility. Dry polymers, although safer due to the absence of liquid, have conductivity levels much too low for the use at ambient temperatures. At the other hand, polymer gel films were developed with the aim of increased safety. They have greater volume energy densities and greater flexibility of shape with reduced manufacturing costs. These advantages are due to the fact, that the polymer gel ensures cohesion between positive and negative electrode films and therefore allow the conventional rigid metal container to be

replaced by a flexible and waterproof packaging. A polymer matrix, ensuring mechanical stability, composes these electrolytic membranes in which the liquid electrolyte is kept. The liquid fraction varies between 50 and 70%, so the ionic conductivity is close to that of the liquid while maintaining a good mechanical stability for films of several tens of microns thickness.

The lithium salt also has to fulfill certain criteria, such as low price, high performance and reliable safety. As far as the performance is concerned, the most important factors are conductivity, thermal as well as electrochemical stability, and cycling efficiency.

The most frequently used lithium salts are: $LiClO_4$, $LiPF_6$, and $LiN(SO_2CF_3)_2$. Of course each of these salts has its own advantages and disadvantages [**10**].

The electrolyte used in this work was 1M $LiPF_6$ dissolved in EC:DMC=1:1 (in weight) .

5.2.2 Negative electrodes

Nowadays, carbon-based materials are the most used negative electrodes employed in Li-ion batteries, because of their good cyclability and reliability, as well as their environmental amicability. But also other materials have been investigated. In Table 1 some possible materials for negative electrodes are listed.

Table 1: Negative electrode materials [8].

Material	Potential range vs. Li^+/Li [V]	Theoretical specific charge [Ah/kg]
Li (metallic)	0	3860
LiAl	ca. 0.3	790
LiC_6	0.0-0.5	372
$LiWO_2$	0.3-1.4	120
$LiMoO_2$	0.8-1.4	199
$LiTiS_2$	1.5-2.7	226
TiO_2	1.5-2.2	200 (practical capacity)[1]

The compounds of negative electrodes are divided in the two categories of *carbon* and *non-carbon based materials*.

- **Non-carbon based materials**

The unsuccessful use of pure lithium, suggested the introduction of alloys with different metals like Sn, Pb, Bi, Sb, and As. With these alloys, the activity of lithium is smaller than in pure lithium, and it contributes to the decrease of the reactivity of lithium towards the electrolyte. Alloys also turned out to reduce the problem of dendrite formation. Among the more investigated alloy components are Sn, Si Bi, Pb, and Al [**13**,**14**,**15**,**16**]. Corresponding Li-compounds belong to the class of intermetallic compounds with low free energy formation and small potential variation over a wide composition range. Problems of lithium alloy electrodes arise from the huge difference in volume between the lithium-rich and the lithium-poor materials. Mechanical stress and cracks are therefore a result during cycling. In the case of LiAl a volume change of about 97% was observed [**17**] and even more in the case of Sb alloys. Other possible candidates for negative electrodes are transition metal compounds with layered structures. Lithium ions can intercalate and deintercalate the structures during charge and discharge. An important feature to be fulfilled is that their electrochemical potential must be comparable with

[1] See section 15.2.

that of lithium metal or of lithiated carbon in order to achieve a high cell voltage.

- **Carbon-based materials**

Carbon-based materials became the most attractive and investigated materials eligible as anode in Li-ion batteries.

This "success" was mainly due to:

- low cost;
- high safety for people and environment;
- the Li insertion potential, which is very close to the one for metallic lithium;
- good cycling stability because of high mechanical electrode stability (compared to alloys);
- the specific charge which is higher compared to transition metal oxides or sulphides (see Table 1).

Lithium insertion in carbons, whenever not degenerating towards exfoliation, proceeds reversibly (without changes in the structure) and is often referred to as intercalation. Lithium ions intercalate into the carbon during charging and are subsequently released during discharge. This process can be described as follows:

(eq. 17) $$Li_xC_n \leftrightarrow x \cdot Li^+ + x \cdot e^- + C_n$$

From many types of carbonaceous material two families can be distinguished:

- Graphitic carbons;
- Non-graphitic carbons.

In graphitic carbons a maximum amount of lithium corresponding to x=1 in Li_xC_6 can be reached, giving rise to a theoretical specific charge value of 372 Ah/kg, according to equation (eq. 17). In practice, more than the theoretical amount of charge, corresponding to LiC_6, is consumed during the first charging process. This extra amount of charge is irreversibly used for the electrolyte reduction with consequent formation of a *Solid electrolyte interface* (SEI).

Once the film is formed, further electrolyte reduction is kinetically suppressed and the electrode can be cycled reversibly. In other terms, SEI is necessary to protect the Li_xC_n interface from further reduction, prolonging the lifetime of the cell.

In any case, the irreversible specific charge has to be kept to a low value, since the only lithium source is the positive electrode. Therefore, the electrolyte composition plays a fundamental rule, because SEI formation depends strongly on the electrolyte composition (solvent and lithium salt dissolved in it).

Nitrogen and boron-doped carbons [**18**, **19**] have also been used as anodic material, but their specific capacities undergo quick fading during cycling.

5.2.3 Positive electrodes

Manganese oxide has been used for many decades as positive electrode in 1.5 Volt alkaline cells (eg: Leclanché type). At the beginning of the 1980s, it was incorporated in the first 3V lithium cells and is still used until today, mainly in calculators, cameras and many other general-purpose applications. The relative abundance of manganese, its consequent low cost and its low toxic level in comparison with other compounds currently used in the manufacture of lithium storage batteries (cobalt, nickel, vanadium, etc.), makes it an excellent choice for this market. But these days, this is not the only possible choice.

There is a wide range of materials that can be used for positive electrodes. The best ones are those, with no or little structural modification during cycling. Typical insertion or intercalation compounds are therefore preferred candidates. In these materials, removal and subsequent insertion of lithium ions in the host lattice proceeds topotactically (without change in the structure). The reaction at the positive electrode can be described as follows:

(eq. 18) $$Li_x(HOST) \leftrightarrow Li_{x-y}(HOST) + y \cdot Li^+ + y \cdot e^-$$

(HOST): insertion cathode.

Several factors can affect the insertion performances of a cathodic compound, and they must be considered carefully:

- High free energy of reaction with lithium;
- Wide range of x (amount of insertion);
- Small structural changes on reactions;
- High insertion reversibility;
- High diffusivity of lithium in the HOST;
- Good electronic conductivity;
- Non-solubility in electrolyte;
- Availability or facility of synthesis.

Possible candidates are transition metal oxides, sulphides and selenides. In Table 2 selected materials for the positive electrode and their characteristics are listed.

Table 2: Positive electrode materials and some of their characteristics [20**].**

Material	Average potential vs. lithium [V]	Reversible range, Δx	Specific charge [Ah/kg] (charge density [Ah/l])	Specific power [Wh/kg] (power density [Wh/l])
Li_xTiS_2	2.1	1.0	239 (782)	502 (1642)
Li_xMoS_2	1.7	0.8	134 (678)	228 (1152)
$Li_xV_2O_5$	2.8	1.0	147 (495)	412 (1386)
$Li_xV_6O_{13}$	2.3	3.6	188 (734)	432 (1688)
Li_xMnO_2	3.0	0.5	154 (775)	462 (2325)
Li_xNbSe_3	1.9	3.0	244 (2121)	464 (4030)
Li_xCoO_2	3.7	0.5	137 (706)	507 (2612)
Li_xNiO_2	3.5	0.7	192 (919)	672 (3216)
$Li_xMn_2O_4$	3.8	1.0	148 (634)	562 (2409)

5.3 Classification of insertion compounds

The insertion compounds can be subdivided into three categories depending on their intrinsical structure, see Figure 3.

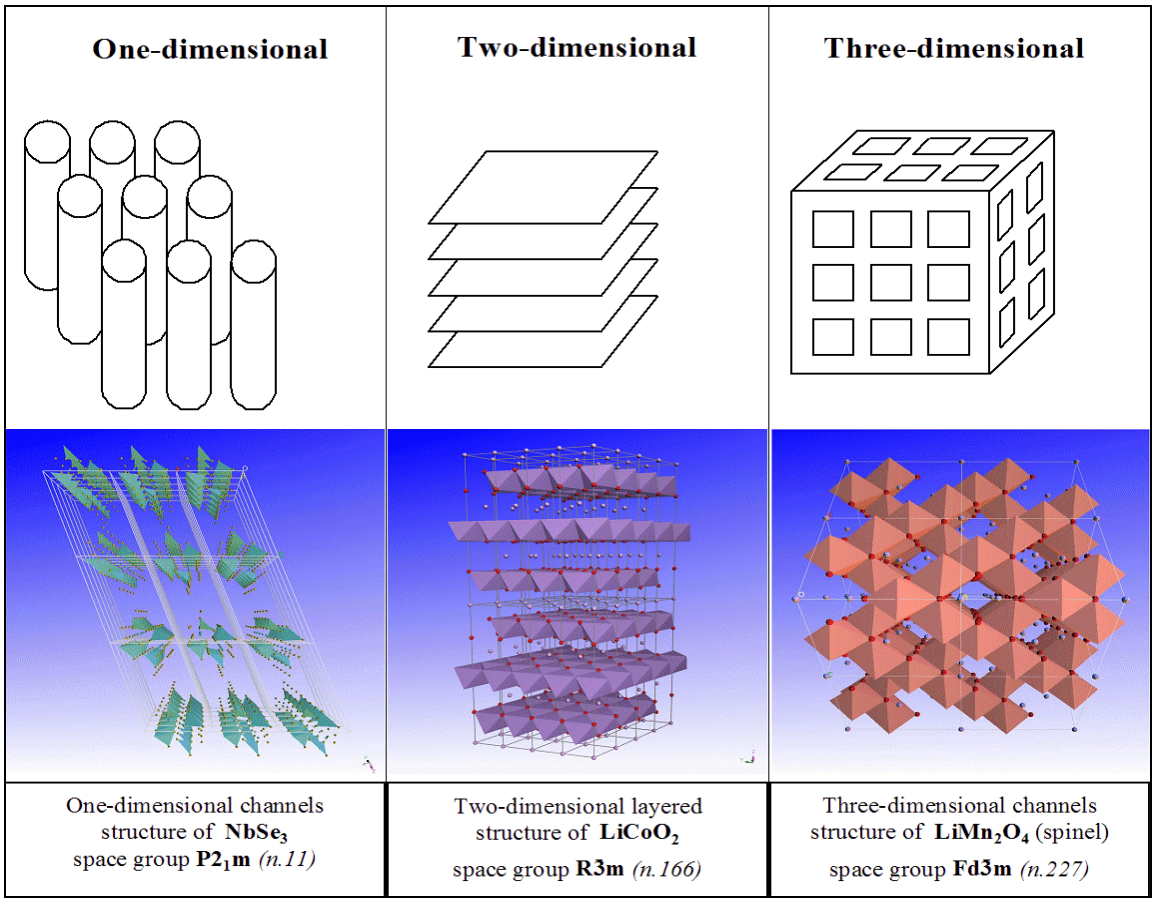

Figure 3: Classification of insertion compounds for the positive electrode.

- ***One-dimensional chain hosts***

In this kind of hosts, lithium can diffuse and migrate through the channels in one directions, but cannot cross it. Examples of this rare series of compounds are $NbSe_3$, TiS_3, and MoO_3.

- ***Two-dimensional layered hosts***

In this kind of hosts, lithium can diffuse and migrate through the single layer in two-dimensions but cannot cross it. Many of these layered compounds are made of close-packed anions (X) with transition metals (M) in octahedral or trigonal prismatic sites. In these systems, the guest ions can intercalate between the X-M-X sandwiches. The two most important compounds of this family for

Li-ion batteries are $LiNiO_2$ [**21**,**22**] and $LiCoO_2$ [**23**,**24**], as well as graphite for the negative electrode.

- ***Three-dimensional channels hosts***

In these systems the guest ions are inserted into a three-dimensional network, consisting of cross-linked channels. Examples of compounds of this class are some zeolites and spinels (e.g. $LiMn_2O_4$) with a cubic framework. In the latter, the sites available, both for the transition metal and guests, are either octahedrally or tetrahedrally coordinated by oxygen.

5.4 Principle of Li-ion cells

The term *"Li-ion cell"* derives from the fact, that no metallic lithium is present. Typically, a Li-ion cell (Figure 4) is composed of two insertion compounds. The lithium ions move back and forth between the positive and negative electrode. The electrochemical process is the uptake of lithium ions at the negative electrode during charge and their release during discharge. Thus, the net current-forming reaction is reduced to a continuous pumping of lithium ions between the two host materials. A strength of this system is, contrary to lead acid batteries, that no electrolyte is consumed, such that only a very small amount of electrolyte is needed. A more compact cell construction is therefore possible.

Lithium-ion cells consist of a lithium-rich compound as positive electrode and a lithium-sink compound as negative electrode. The cell is activated by charging, which means that Li^+ ions are assembled in the sink. Due to the fact that the latter can mainly not be manufactured in the lithium-loaded state due to moisture and air sensitivity. Positive electrodes, not containing lithium after their synthesis have to be chemically lithiated before using.

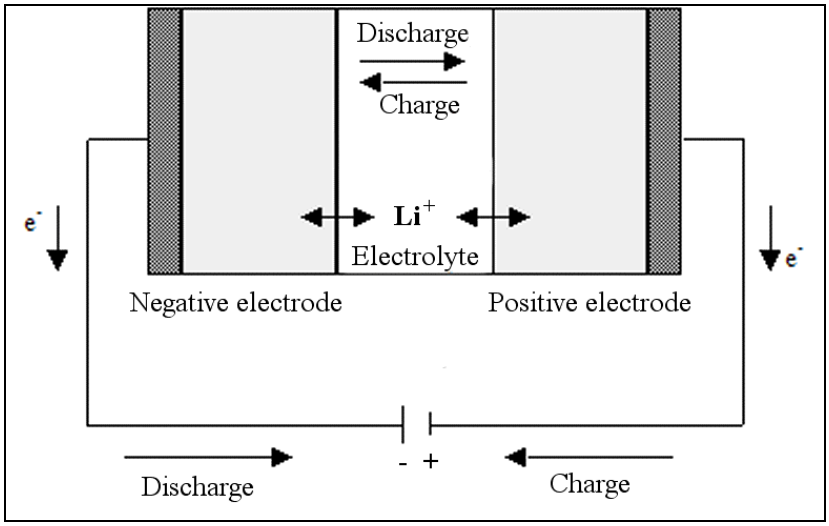

Figure 4: Scheme of the electrochemical process of a Li-ion cell.

5.5 Advantages of Li-ion batteries

Considering the use of conventional batteries as power source for consumer electronics or electric vehicles, the principal problem is their low specific energy compared with other batteries. This low specific energy is mainly due to their low voltage. This relationship is demonstrated in Figure 5. The most important property a battery should have, is a high energy density and this parameter is much more important than voltage or specific charge alone. The second important property to consider is how this energy is supplied; the potentials should be as constant as possible. In operative terms, it is better not having any flex in the curve *"Potential vs. capacity"* (Figure 6). The presence of flexes implicates that the energy is furnished at different potentials. Of course, this potential can be stabilized easily by an appropriate electronic component, but with additive costs. That is why it is preferable having a no-flexes discharge shape (good behaviour). From the users point of view, Li-ion batteries have the following advantages:

- High energy density: approx. double than NiCd batteries;
- High output voltage: 3 time output power than NiCd batteries;
- Low self-discharge rate: around 2% per month at 20°C;
- Long life-cycle: 500 recharging cycles with consistent performance;

- Cost-saving: save money on disposal of waste batteries;
- Environmentally friendly: Li-ion batteries do not contain cadmium, mercury or other toxic heavy metals.
- Wide operation temperature range due to non-aqueous electrolytes.

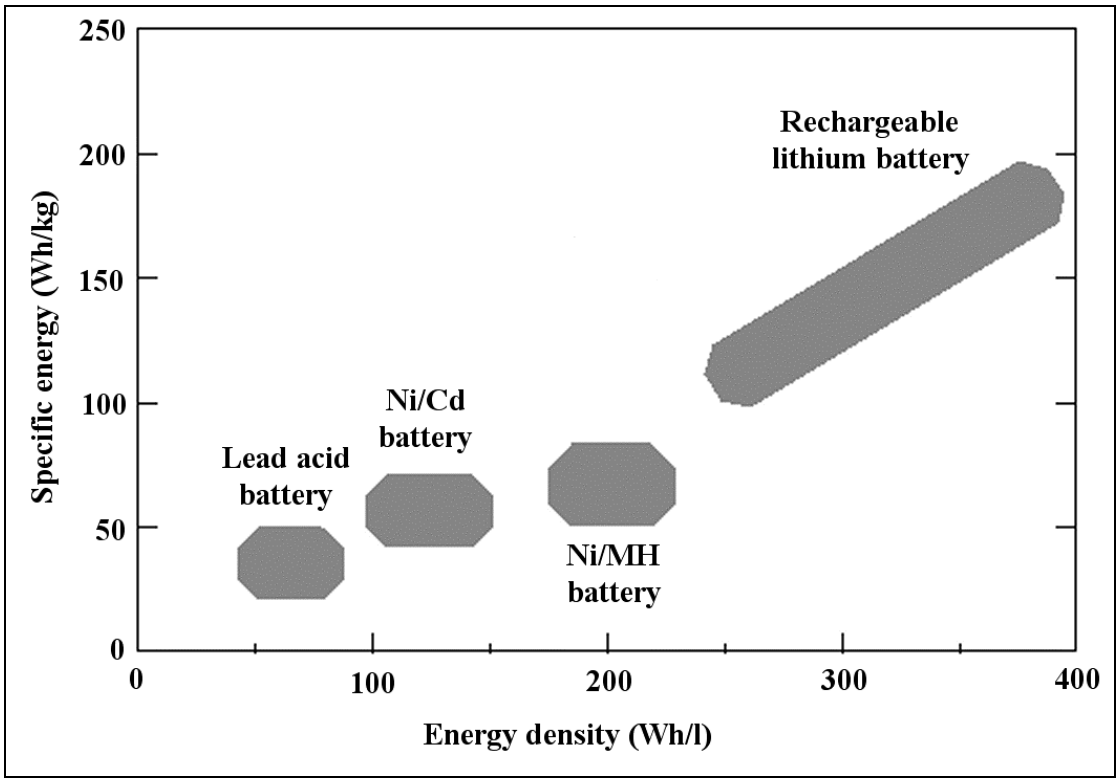

Figure 5: Comparison of the specific energy and energy densities of rechargeable lithium batteries with those of other systems (redrawn from [25]).

For large batteries, for example in electric vehicles, this higher voltage is an additional advantage because it reduces the number of cells required to achieve the necessary voltage. This makes the battery management system less complex [**26**,**27**,**28**]. Moreover, the specific energy of the lithium-ion cells is high (>200Ah/kg) as demonstrates Figure 7.

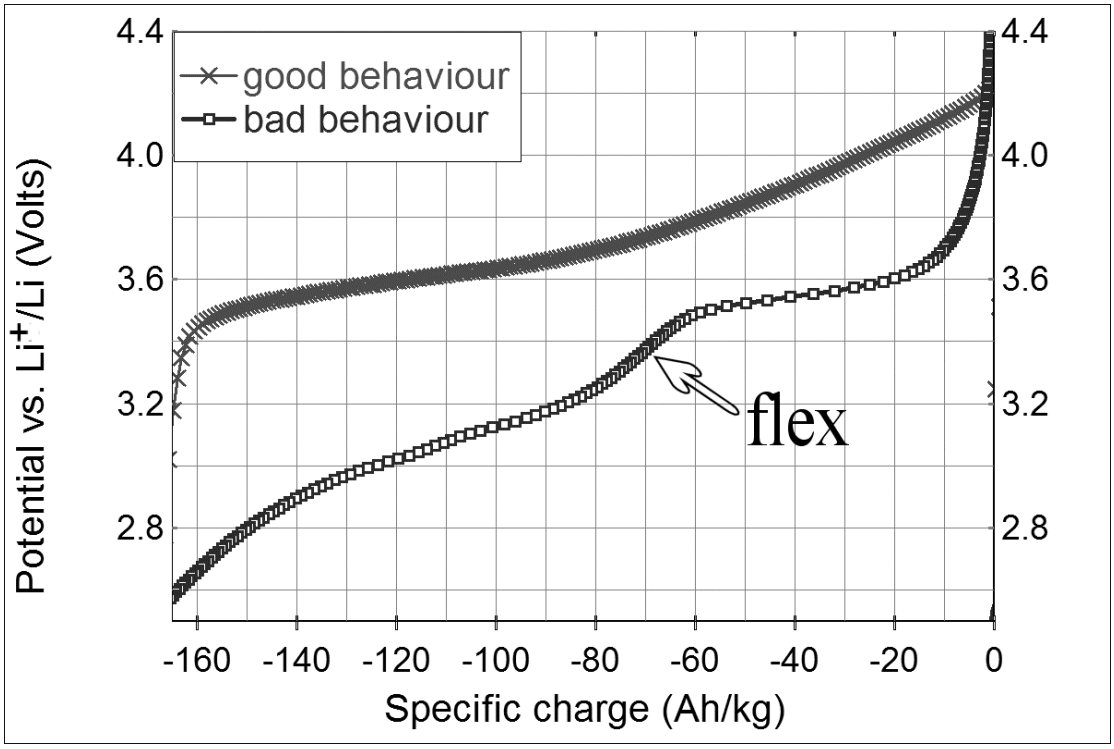

Figure 6: Discharge behaviour of different batteries.

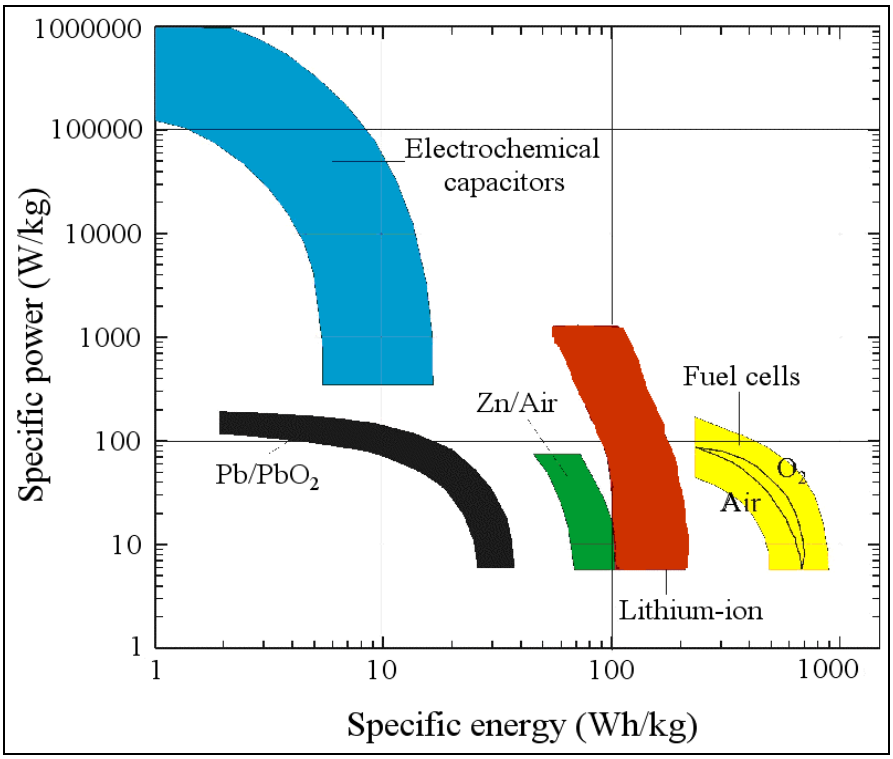

Figure 7: Ragone plot for different battery systems [29].

Chapter 6.

Solid state syntheses and characterization

6.1 Oxide syntheses

The compounds have been synthesized in one of these two ways:

- ***WET SYNTHESIS***: an oxidative co-precipitation of hydroxides is followed by thermal treatment
- ***DRY SYNTHESIS***: oxides or hydroxides are mixed in a ball mill, followed by thermal treatment.

6.1.1 Nomenclature for complex oxide systems

Oxides synthesized during this work have the general formula Li_xMeO_2, in which Me is a combination of nickel, manganese, cobalt and eventually a small amount of aluminum. In order to denote clearly the product composition the following nomenclature was used:

- For ***wet synthesis*** products: LiMnNiAl-xyzBr-T°C.
  eg: LiMnNiAl-451Br-800°C refers to $Li_xMn_{0.4}Ni_{0.5}Al_{0.1}O_2$ synthesized using Br_2 as oxidant agent, and treated at 800°C.
- For ***dry synthesis*** products: LiMnNiCoAl.x.y.z.k-ttt°C where k denotes the Al content.

eg: LiMnNiCoAl.335.495.160.010-950°C refers to
$Li_xMn_{0.335}Ni_{0.495}Co_{0.16}Al_{0.01}O_2$ treated at 950°C.

6.1.2 Wet synthesis procedure

The wet synthesis of $LiMn_{0.5}Ni_{0.4}Al_{0.1}O_2$ is described as an example for all wet syntheses performed in this work. Generally sample syntheses follow this procedure with exception of the relative amount of salts, which are defined product by the composition. The first step involves the preparation of the following three solutions:

Solution A		
$Mn(NO_3)_2 \cdot 4H_2O$	8.66 gr. (34.4 mmoles)	⇦ *Molar ratio* *Mn : Ni : Al = 5 : 4 : 1*
$Ni(NO_3)_2 \cdot 6H_2O$	8 gr. (27.5 mmoles)	
$Al(NO_3)_3 \cdot 9H_2O$	2.588 gr. (6.9 mmoles)	
H_2O	135 gr.	

Solution B		
$LiOH \cdot H_2O$	12.5 gr.	⇦ *Involved reaction*: $Br_2 + 2OH^- \Leftrightarrow Br^- + BrO^- + H_2O$ *disproportion of* Br_2 *and generating the oxidant species* BrO^-. *The* ***solution B*** *was prepared by dropping the* Br_2 *to the LiOH solution at 0 °C.* *Time to add Bromine: about 2 minutes.*
H_2O	200 gr.	
Br_2	11.47 gr. (~4 cc)	

Solution C		
$LiOH \cdot H_2O$	3.46 gr.	⇦ *The amount of lithium is 1.2 times the stoichiometric quantity, the exceeding part will evaporate during thermal treatment.*
H_2O	As less as possible	

Synthesis (oxidative coprecipitation)**:**

Keep the solution B at 0°C[1]. Add "*Solution A"* drop by drop to the "*Solution B"* under vigorous stirring (time required 1.5-2 hours). Once the addition is finished, wait 15-20 minutes keeping the solution under vigorous stirring.

Filtration:

Filtration is carried out, using a glass separative funnel under vacuum. The precipitate has to be washed and re-filtered two more times using 100-150 ml of water. Of course the product must be perfectly dissolved in the water before filtering. After filtration, the product has to be suspended in about 100-150 ml water and "*solution C"* is added followed by strong stirring at 100-110 °C until the water is completely removed. A dry powder is obtained, which is then well homogenized in a mortar. In order to complete the preliminary drying process, the powder has to be kept for 2-3 hours at 180 °C. At the end of this step, a thermal treatment is performed as described in section 6.1.4.

Table 3: Starting material used for the wet synthesis

		Purity	M_r **[g/mol]**
$LiOH•H_2O$	Fluka	≥ 99%	41.96
$Ni(NO_3)_2•6H_2O$	Fluka	≥ 99%	290.81
$Mn(NO_3)_2•4H_2O$	Fluka	≥ 97%	251.01
$Al(NO_3)_3•9H_2O$	Fluka	≥ 99%	375.13
Br_2	Fluka	≥ 99.5%	159.81
LiClO	Riedel de Haën	not known	58.40

[1] It is strongly recommended to keep the solution at 0°C, in order to avoid the formation of extremely soluble permanganate ion, easily lost during filtration.

6.1.3 Dry synthesis procedure

Dry synthesis is a much faster way to produce compounds. It simply consists of mixing solid reagents in a ball mill. An example of this route: the synthesis of LiMnNiCoAl.283.566.141.010-950°C is reported in Table 4.

Table 4: Reagents used for LiMnNiCoAl.283.566.141.010-950°C synthesis

Molecular weight	Reagent	molar fraction	Weight (grams)
70.94	MnO	**28.3**	1.606
74.71	NiO	**56.6**	3.383
74.93	CoO	**14.1**	0.845
78.004	$Al(OH)_3$	**1**	0.062
41.99	$LiOH•H_2O$	**120**	4.031
		Tot.	9.928

Like in wet synthesis, a 20% surplus of LiOH compared to the stoichiometric amount has been added, because it is supposed to evaporate the exceeding part during thermal treatment.

The weighted reagents are placed in an agata mill and kept for 20 periods composed for 1 hour and a rotation of 400 r.p.m. + 10 minutes rest for dissipating the heat.

At the end of this step, the thermal treatment has been performed as described in section 6.1.4.

Table 5: Starting materials used for the dry synthesis

		Purity	M_r [g/mol]
$LiOH•H_2O$	Fluka	≥ 99%	41.96
MnO 60+170 mesh	Aldrich	≥ 99%	70.94
NiO black <10μm	Aldrich	≥ 99%	74.71
CoO	ABCR	≥ 99%	74.93

$Al(OH)_3$	Sigma	≥ 99%	78.00
FeO(OH)	Aldrich	≥ 99%	88.85

6.1.4 Thermal treatment

As mentioned before, thermal treatment is analogous for both ways of synthesis. The sample (5 to 8 grams) is transfered into an open corundum (α-Al_2O_3) crucible, which is placed in a quartz tube inside a tube furnace. For the whole period of the thermal synthesis an oxygen flux of about 5cm/min is pertained. A bubble counter was used to control the flux. Oxygen is needed to keep an oxidative atmosphere and to remove volatile exceeding substances like Br_2 (see wet synthesis), H_2O and LiOH. In Figure 8, the thermal treatment for all syntheses at 800°C (see nomenclature) is shown. Syntheses for other temperatures are given in Figure 9.

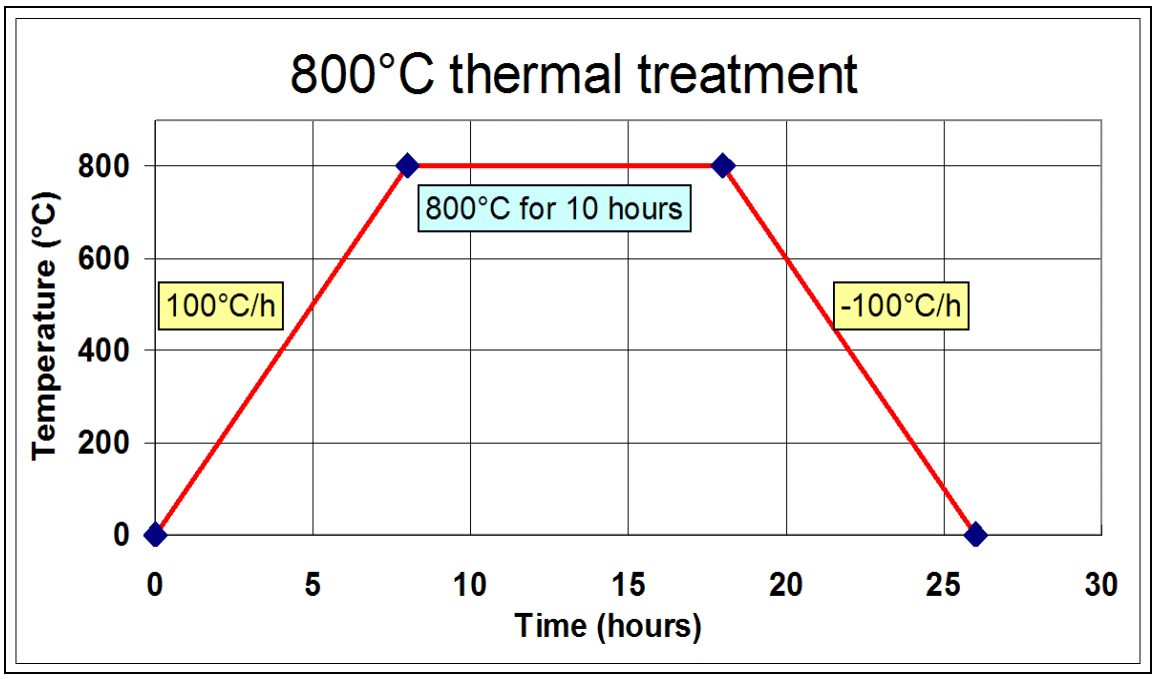

Figure 8: Temperature profile for the thermal treatment at 800°C constant

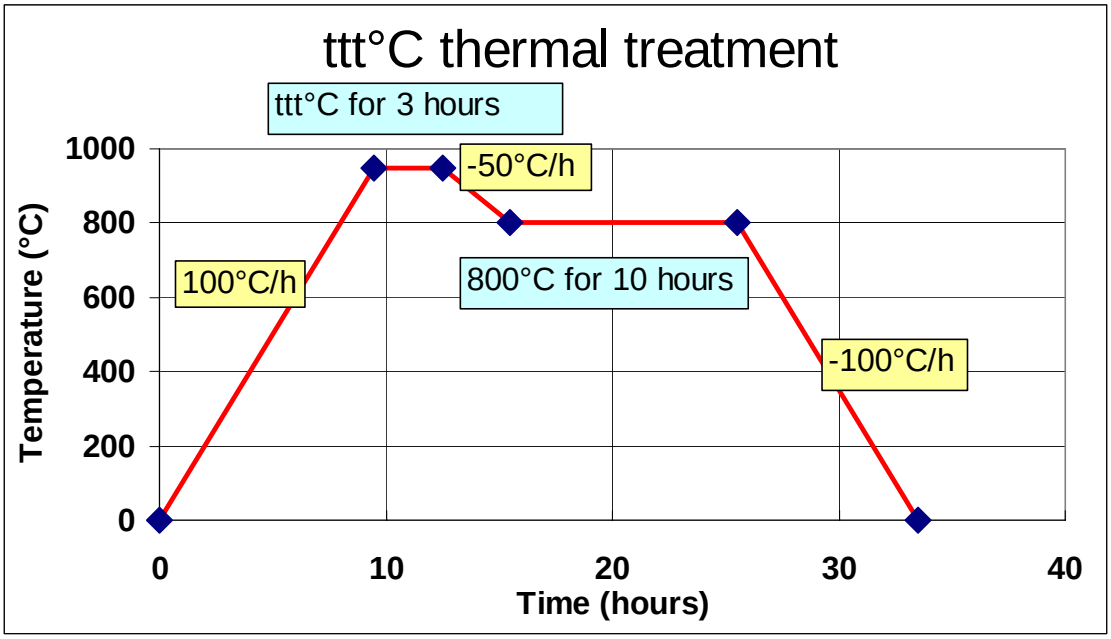

Figure 9: Two step thermal treatment at ttt°C as highest temperature.

6.2 X-ray powder diffraction (XRD) characterization

Due to the strong fluorescence of manganese, an X-ray powder diffractometer Bruker AXS mod. D8Advance with Bragg-Bentano geometry was used, with $\lambda_{CuK\alpha1}$ = 1.54056 Å radiation (40 mA, 40 kV) and a germanium monochromator. The samples were mounted on a rotating flat plate holder. A SiO_2 sample has been used as external standard.

6.2.1 In-situ XRD cell

An diffraction cell for in-situ X-ray measurements was assembled for air-sensitive compounds for cases of more than one X-ray measurement on the same electrochemical cell. The cell is shown in Figure 10. A thin aluminum foil keeps an electric contact with the oxide cathode (placed immediately below it) and separates the oxide itself from air contact. Although aluminum shields part of the incident X-ray and gives rise to some X-ray scattering, these reflections can be easily subtracted from the original pattern. In Figure 11 an example of XRD powder pattern, taken by the in-situ cell, is shown.

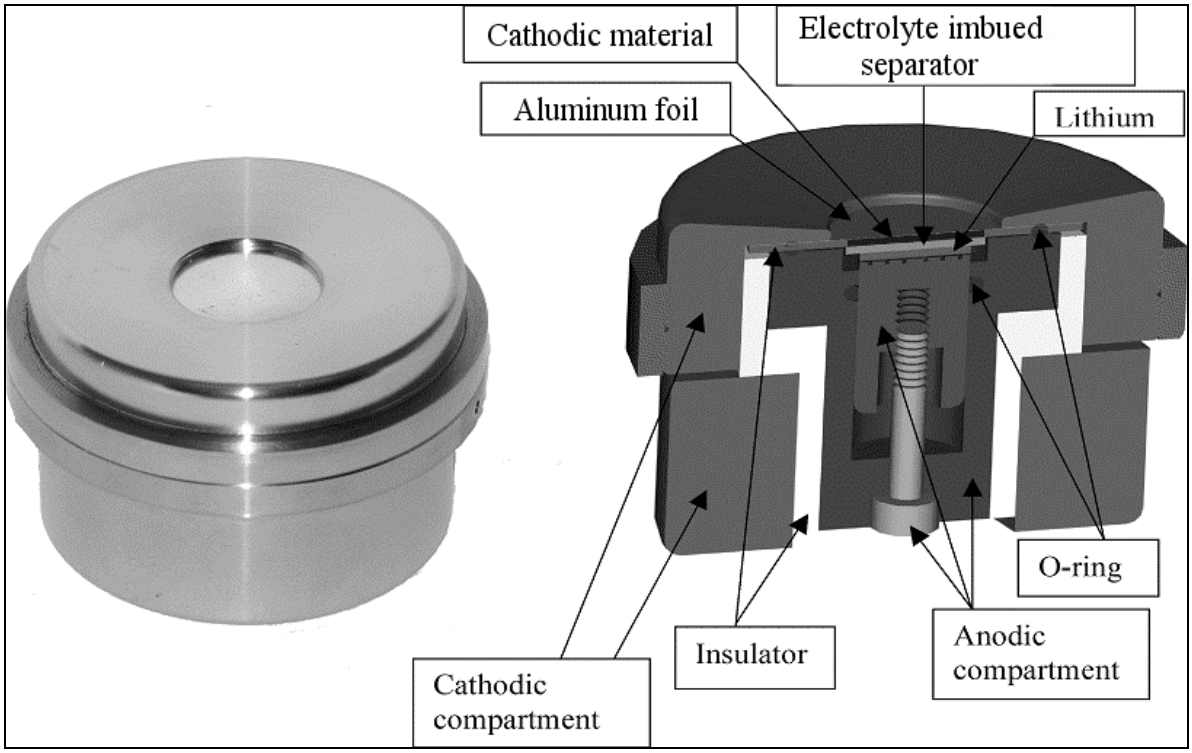

Figure 10: Cell setup for in-situ X-ray pattern acquisition

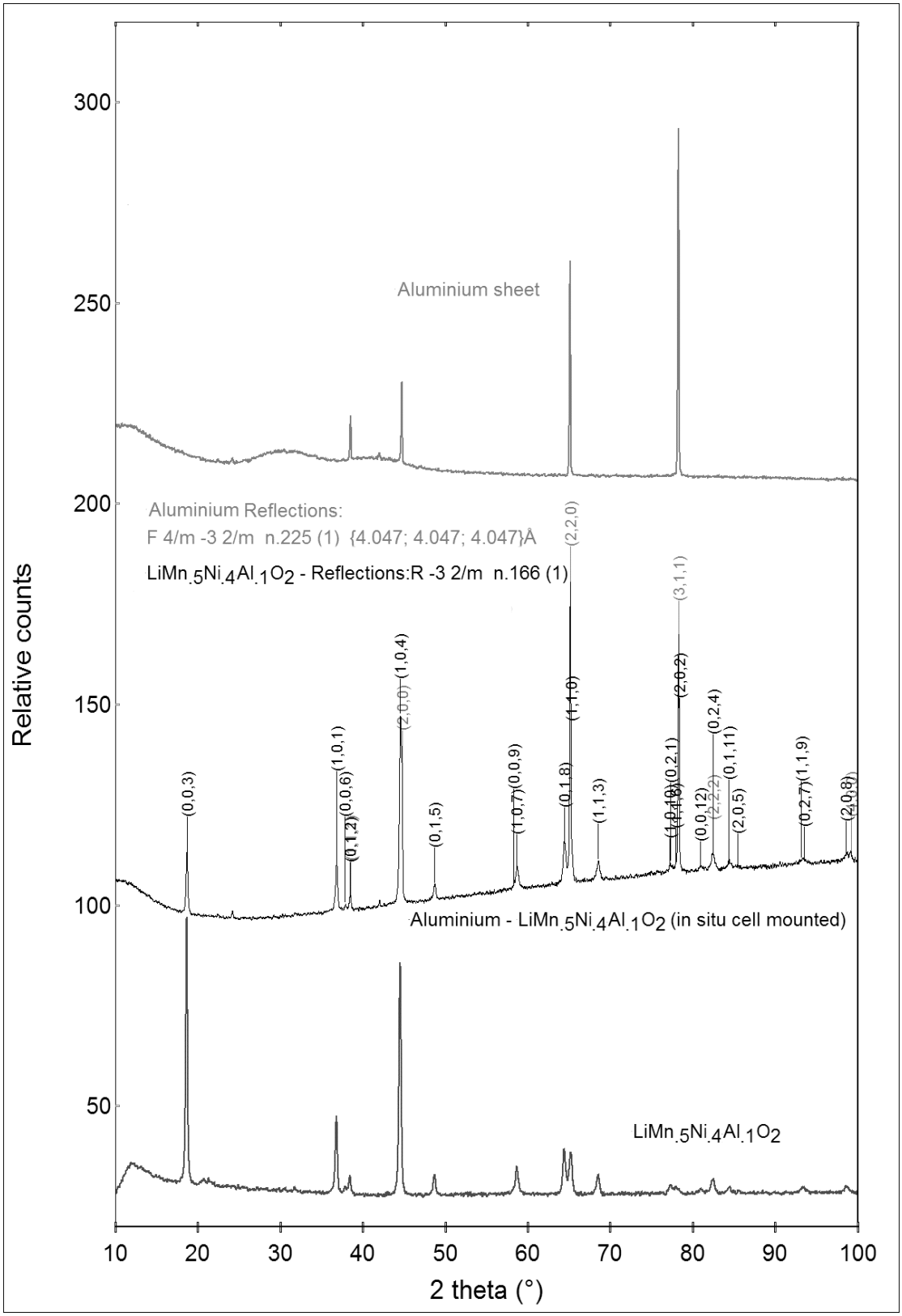

Figure 11: In-situ measurements by the X-ray cell, the upper pattern represents aluminum, the lower pattern represents $LiMn_{0.5}Ni_{0.4}Al_{0.1}O_2$ and the middle pattern represents what has been obtained using the in-situ cell.

Chapter 7.

Electrochemical characterization

7.1 Instrumentation

All electrochemical measurements were performed using a computer-controlled charger system furnished by Astrol Electronic AG, Switzerland, using a two-electrode configuration. In Figure 12, two different schemes are shown. CE is the counter electrode, RE the reference electrode and WE the working electrode. During the measurements, which require the control of the potential (V), a current is forced between working electrode and counter electrode, high enough and in proper polarity to keep the working electrode potential at a constant value with respect to the reference electrode.

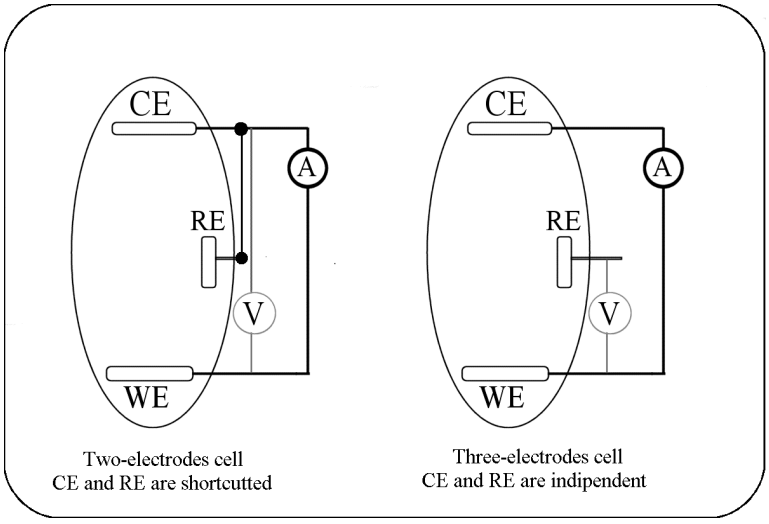

Figure 12: Schematic representation of a two- and a three-electrode setup for electrochemical cells.

7.2 The cell

All electrochemical measurements were performed in a titanium cell as shown in Figure 13. In between the counter and the working electrode, an electrolyte soaked separator is placed. The cell assembling was always done in a dry box under argon atmosphere.

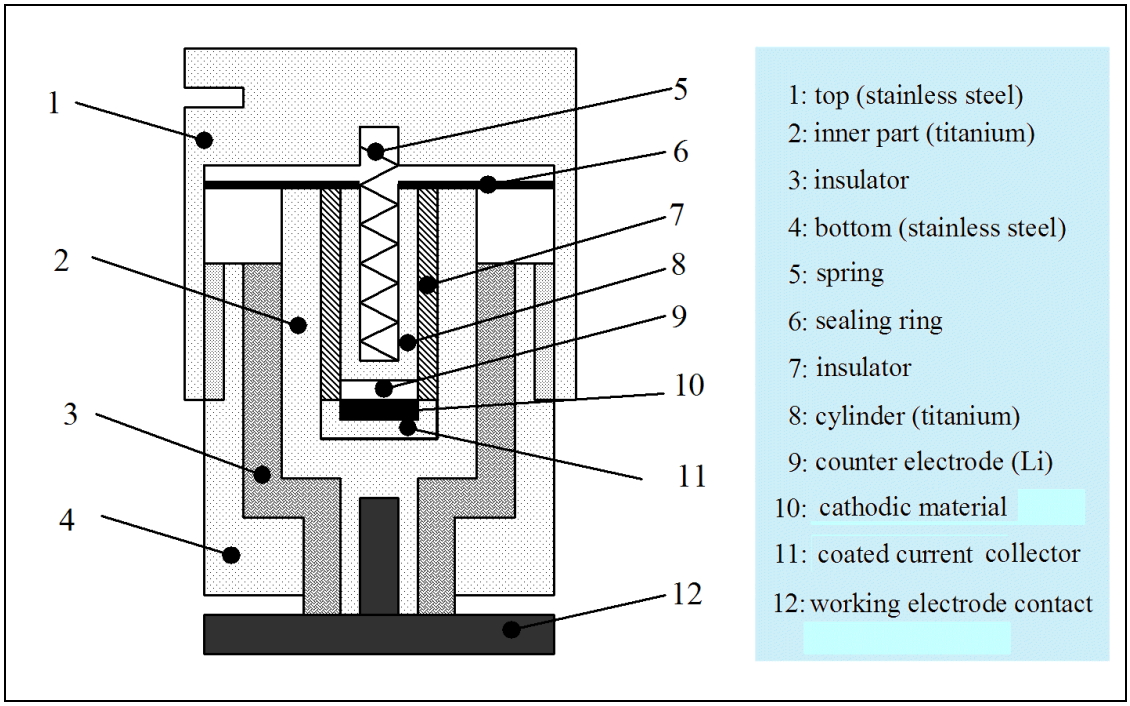

Figure 13 : Two electrodes electrochemical cell.

7.3 Electrode preparation

7.3.1 The working electrode

To study electrochemical reactions at the working electrode that contains the oxide, sample has to be blended by carbon black and graphite as additives, since the electronic conductivity of the oxide is not high enough, and the conductivity of the complete electrode has to be enhanced. In addition a binder was added to keep the active material and the conductivity enhancer together. Additives and binders are shown in Table 6.

Table 6: Additives used for sample preparation.

Additives	**Furnished by**	**Solvent for suspension (Fluka)**
Graphite SFG6	TIMCAL	
Ensaco 250E	M.M.M.	
Carbon Black XC72	Cabot Corporation	
Binders		
Oppanol (polyisobutene)	BASF	n- Hexane
PVDF	Aldrich	THF or Acetone

- ***Working electrode sample's preparation:***

In Figure 14 a cyclic voltammetry of the additives is shown. With exception of the first cycle (in which electrolyte decomposition arises at high potential), the additives do not affect the electrochemical measurements between 1.0 and 5.0 Volts.

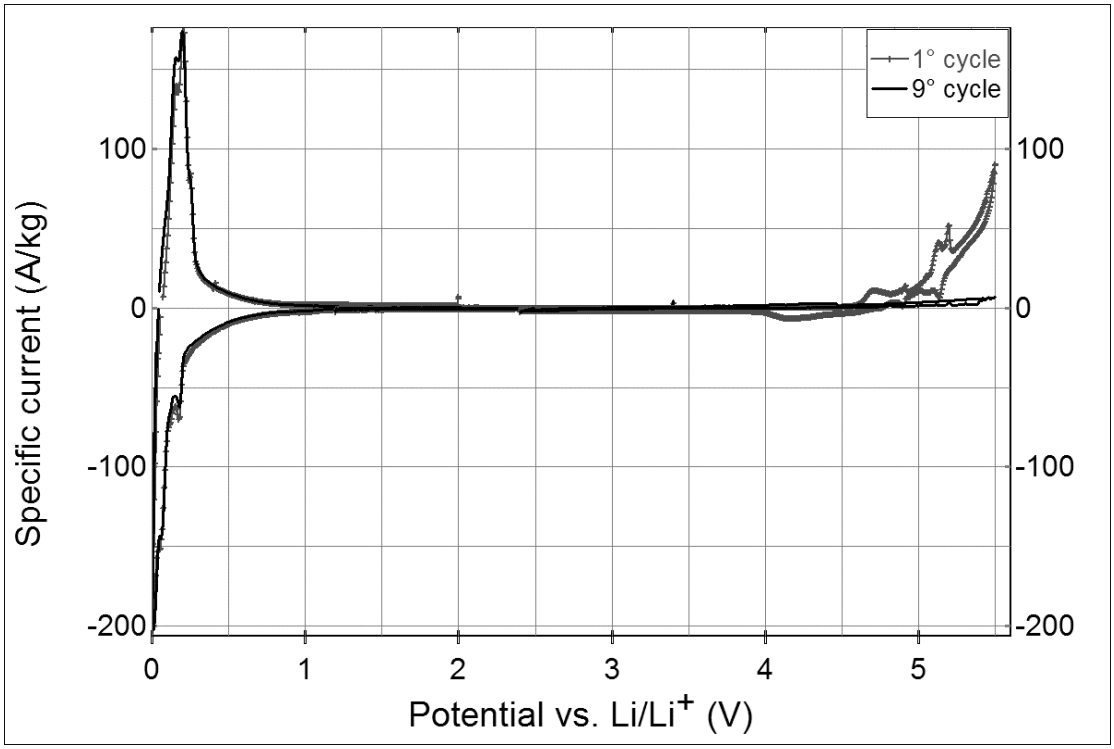

Figure 14: Cyclovoltammetry of a mixture of carbon black XC72 : graphite SFG6 = 3:1. The plot is the sum of three independent cyclovoltammogramms, taken in the ranges (0.0-2.0V), (1.2-3.4V) and (2.4-5.5V).

The active material, the carbons and the binder (Oppanol or PVDF) have the following ponderal ratio:

Oxide : XC72 or Ensaco 250 : Graphite SFG6 : Oppanol = 74 : 18 : 6 : 2

Oxide and additives were mixed and grained together by hand in a mortar until visual mechanical homogenization was reached (3-5 min.). The mortar was warmed up at 90°C and an Oppanol solution at 0.2% in n-Hexane was added to the mixture. The suspension was mixed up until the complete evaporation of n-Hexane.

- ***Pills***

The electrode mass obtained (active material, carbon, and binder) was put on the current collector (see Figure 15).

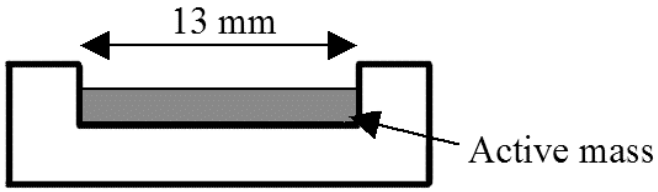

Figure 15: Current collector.

By using a pill-maker, 15 to 30 mg of electrode material were brought onto the current collector. The pressure was generated by hand and was estimated to become about 100 N/cm^2. In order to eliminate any trace of water from the material, the pill was then kept at 120°C for at least 12 hours, followed by a period of at least 12 hours under vacuum at room temperature.

7.3.2 The reference electrode

Usually, a reference electrode is used when measuring the working electrode potential. A reference electrode should have a constant electrochemical potential as long as no current flows through it. It should also be similar enough to the working electrode in order to reduce an ohmic potential drop, due to the solution between it and the working electrode.

We preferred to use a counter electrode as reference for the following reasons:

- At its interface, the counter electrode furnishes a very high exchange current, being composed of lithium in contact with a solution containing Li^+ in high concentration (1M)
- The overpotential is de facto negligible if a high concentration of Li^+ is present in solution (due to its concentration's gradient at the *interface*) .
- The current passing through the electrode during the experiments was small enough not to polarize the electrode itself;
- When the counter electrode surface is very large (the same holds for the working electrode), the current density is kept low;
- The counter electrode should be placed very close to the working electrode.

7.3.3 The counter electrode

A counter electrode is also called auxiliary electrode, and represents a conductor completing the cell circuit. In our case it is also used as a reference electrode and it is made of pure lithium (ribbon 0.75 mm thick, Aldrich). It has the same geometric surface area as the working electrode and is placed in front of it at a distance given by the embedded separator (typically about 1mm).

7.3.4 The electrolyte

In this work, all measurements were performed with a mixture of ethylene carbonate and dimethyl carbonate 1:1 (w/w), with 1 M $LiPF_6$ (MERCK Selectipur, LP30). The water content of the electrolyte was measured, using the Karl Fischer method with a 684 KF Coulometer (Metrohm). It did not exceed 10 ppm.

7.4 Cyclic voltammetry

One of the most important techniques often used for a first characterization of electrochemical processes is the cyclic voltammetry. The cell is cycled in a potential window, the potential applied on the working electrode is then continuously changed in a periodic way (see Figure 16, right down) with a constant rate (eq.18):

$$v = \frac{\Delta E}{\Delta t} \qquad \text{[mV/s]} \qquad \textit{(eq. 19)}$$

ΔE_i: potential at the beginning *v: sweep rate*

t: time

Other important parameters include the maximum and the minimum potential, which define the potential window. The choice of this potential window must take into account the stability of the electrolyte, to avoid its decomposition. Cyclic voltammetry provides information about the chemistry of the redox couple. For example if a redox couple undergoes three sequential electron-transfer reactions, it will show three different peaks in the cyclovoltammogram (see Figure 16).

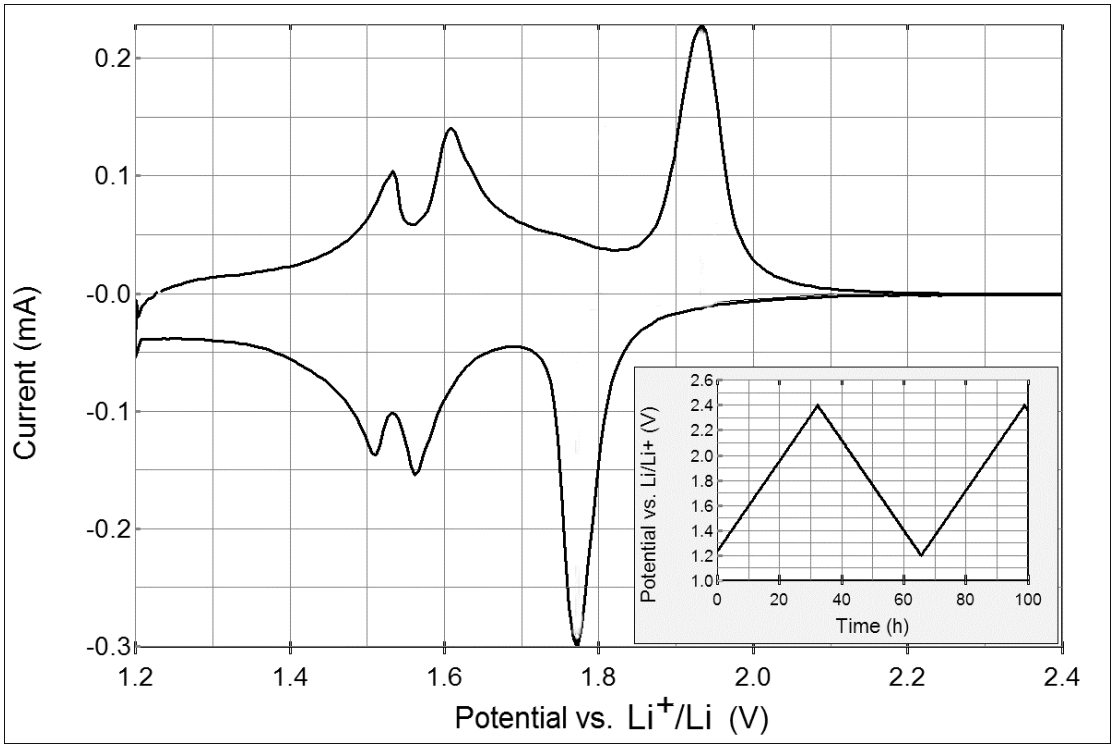

Figure 16: Example of a cyclic voltammetry at 10µV/sec of a TiO_2 Anatase sample.

The current is measured and plotted versus the potential. We observe an increase in the current, corresponding to the potential of an electrochemical reaction. For a positive electrode, the part of the curve under the zero line is the discharge (or cathodic) curve. The one above the zero line is the charge (or anodic) curve. The surface under the curve is proportional to the total amount of the charge flow. Following the "Convention of Stockholm", a positive sweep rate causes the oxidation of the working electrode, and the resulting current has a positive sign [**30**]. With a negative sweep rate we obtain the reduction of the working electrode and a negative current.

This technique has been used to identify the potential of the intercalation/de-intercalation processes, and to verify their stability after a certain number of cycles. In our particular case slow cyclovoltammetry is used (typically about 10 to 100µV/sec), giving a more detailed identification of the charge-discharge potentials close to equilibrium conditions.

7.5 Galvanostatic measurements

Galvanostatic measurements have been used to conduct charge-discharge cycles on our products. Unlike in cyclovoltammetry, the current density is kept constant and the electrode processes are investigated under real working conditions, like in a battery.

In a galvanostatic measurement, a constant current is applied between the working and the counter electrode. This current is applied until the upper or the lower potential limit is reached. In this case, a positive current causes the oxidation of the working electrode, whereas a negative current causes its reduction. The study of the variation of the potential in time (Figure 17 left side) is also called chronopotentiometry.

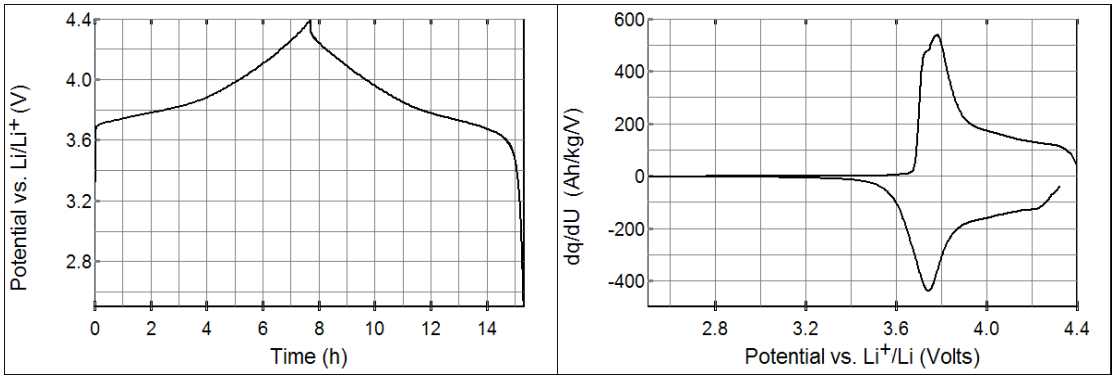

Figure 17: Example of galvanostatic measurements : fourth cycle of an $LiMn_{0.283}Ni_{0.566}Co_{0.141}Al_{0.01}O_2$ cathode taken in the range 2.5-4.4Volts at 20A/$kg_{active\ material}$. Chronopotentiometry plot (left side) and dq/dU vs. U plot (right side).

For an insertion/deinsertion process where '*A*' is the guest species, the amount of guest according to (eq. 20) can be calculated as given by (eq. 21).

(eq. 20) $$A_x \cdot Host + \Delta x \cdot A^+ + \Delta x \cdot e^- \leftrightarrow A_{x+\Delta x} \cdot Host$$

(eq. 21) $$\Delta x = \frac{I \cdot \Delta t \cdot M_r}{z \cdot F \cdot m}$$

- I: current — Δt: time interval
- M_r: Host molecular weight — m: mass of the active component

The curve obtained by plotting the first derivative of the charge over the potential versus the potential (*dq/dU* vs. U) is called *differential specific charge plot*. The curve obtained in this way is usually more structured than a common cyclic voltammogram and will be discussed in the next section.

7.6 Differential specific charge plot

A useful method to characterize electrochemical systems is obtained by plotting curve dq/dU vs. U (first derivative of specific charge vs. potential). These curves (see Figure 17 right side) look like a cyclicvoltammetry curve but show the following characteristics:

1. The curve position is affected, in all its extension, by the same I•R overpotential (because the current is kept constant), unlike the two electrode cyclovoltammetry in which I•R varies because I varies.
2. It is easier to compare the extremes between different dq/dU curves than to compare $U_{1/2}$ between different cyclovoltammetric measurements.
3. Unlike in cyclovoltammetry, it is possible to compare it to each other galvanostatic cycle taken at different currents.
4. Applying this technique at the coulometric titration (see section 7.7), it is easy to calculate $U_{1/2}$ without any affection by overpotentials.

7.7 Coulometric titration

The coulometric titration is a variation of the galvanostatic experiment. The coulometric titration is close to an in-situ investigation and allows to determine phase equilibria. Using this technique, the dependence of the equilibrium cell voltage with respect to the composition of the working electrode (A_xM) is being investigated. A charge transport $\int I \cdot dt$ through the galvanic cell changes the electrode composition according to Faraday's law. This time integral of the current is a very precise measure of the variation of the concentration of the electroactive component. The variation of the stoichiometric number x of the

electroactive component in the electrode is given in (eq. 21). After a required amount of charge has passed through the galvanic cell, the current is interrupted and the equilibrium cell voltage is measured. Recording the time dependence of the cell voltage until it becomes constant can follow the equilibration process. Then, further charge is injected and the equilibrium cell voltage is recorded again. In this way the dependence of the equilibrium cell voltage (or the electrode potential) is measured as a function of the working electrode composition. The observation of this equilibrium cell voltage during titration allows getting information to record the thermodynamics of the system.

Chapter 8.

Experimental data analysis

Experimental data elaboration has always been the foundation of natural sciences. It allows extracting a few pieces of information from a great amount of raw data where each single measurement may be without direct importance. By means of statistical treatment a method to establish the reliability of these "*pieces of information"* is also accessable.

8.1 The program Comparis

During the experimental work, a program has been written ex-novo by the author named *"Comparis"* in C++ by help of the Borland C++ Builder package running under the Windows systems. The aim of the program is to analyse the experimental data, workout their representation and allow for different comparisons. The entire data analyses and the results produced in this work have been performed using *Comparis* as well as the entire plots inherent *XRD pattern*, *cyclovoltammetry studies, specific charge* and differential *capacity plots, respectively.*

A detailed description of the performance of *Comparis* will not be given here, but it is useful to know how some of the calculations have been performed.

8.2 XRD powder pattern data analyses

The elaborative path for XRD powder pattern data treatment is performed in two steps:

1. Fitting the pattern with a simulation curve, constituted by a set of peaks and a background function;
2. Unit cell parameter calculation.

8.2.1 Raw pattern fitting

The XRD raw file from X-ray diffractometer has been decomposed as follows:

$$\textit{(eq. 22)} \quad Count(\theta) = \sum_{i=1}^{n\_of\_peaks} Peak_i(\theta) + Background(\theta)\text{; where}$$

$$Peak_i(\theta) = \begin{cases} (\theta_i - \theta)^2 \le \dfrac{\ln(2)}{b} & = h_i \cdot \exp\left(-b_i \cdot (\theta - \theta_i)^2\right) \\ (\theta_i - \theta)^2 > \dfrac{\ln(2)}{b} & \begin{cases} l = \ln(2) \big/ b_i \\ f = \exp(-w_i \cdot (|\theta - \theta_i| - l) \\ = \dfrac{f \cdot 0.5 \cdot h_i}{1 - \left(1 - \ln(2) + b_i \cdot (\theta - \theta_i)^2\right)} + (1 - f) \cdot h_i \cdot \exp\left(-b_i \cdot (\theta - \theta_i)^2\right) \end{cases} \end{cases}$$

The function $Peak_i(\theta)$ obtained does not yet contain any asymmetry factor. The symmetry Rietveld factor $\left(\dfrac{1 - P_{Rietveld} \cdot (\theta - \theta_i)}{\tan(\theta_i)}\right)$, is being factorized in (eq. 23) and it contains a further parameter $(P_{Rietveld})$.

$$\textit{(eq. 23)} \quad Peak_i(\theta) = Peak_i(\theta) \cdot \frac{1 - P_{Rietveld} \cdot (\theta - \theta_i)}{\tan(\theta_i)}$$

with:

- h_i=height of the peak
- θ_i=peak position
- w_i=weight (if w=∞ the function $Peak_i(\theta)$ is a gaussian)
- Background(θ) = polynom of 10^{th} degree.
- $P_{Rietveld}$= gives the peak asymmetry

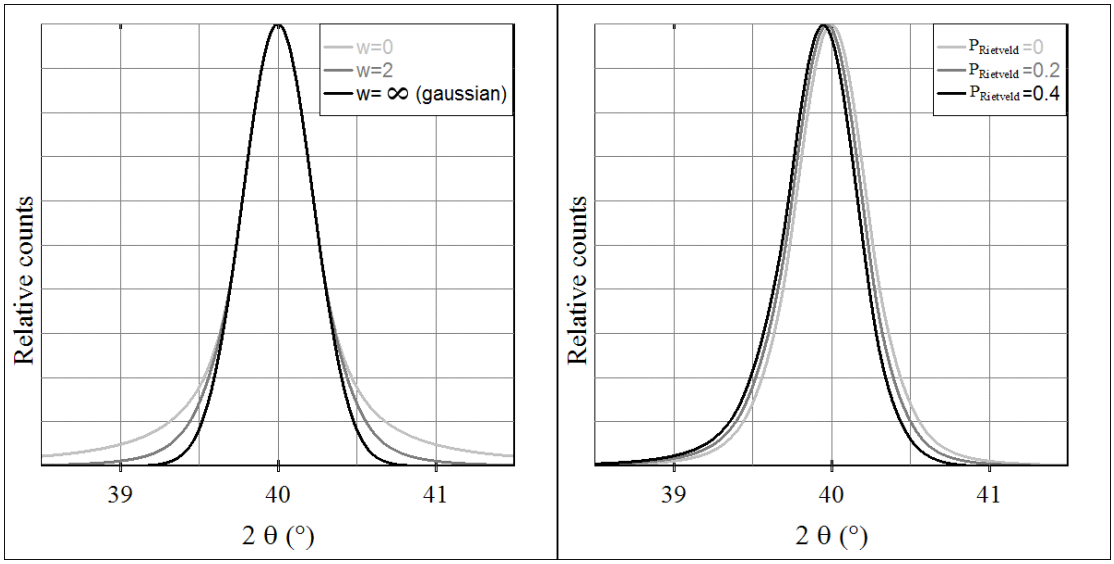

Figure 18: Parameter effect on the peak shape according to eqs. 22 and 23. Left side: effect of *w*. Right side: effect of Rietveld parameter (peak is loosing its symmetry).

The peak fitting is performed, minimizing the function ***S*** defined as follows:

$$(eq.\ 24) \qquad S = \sum_{j=1}^{np} \left| Count_{\exp}(\theta) - Count(\theta) \right|$$

with: *np*=number of points.

The result of this fitting is a parameter set that represents the characteristics of a set of the X-ray peaks.

8.2.2 Cell parameter calculation

For fitting procedure the following is considered:

1. The set of the allowed reflections for a particular space group ($\theta_H(a,b,c,\alpha,\beta,\gamma)$, where H =the set of allowed {h,k,l} in the 2θ range of the pattern);
2. The peak positions previously calculated θ_H^{calc}.

In Figure 19, a visualization of the meaning of the symbols is presented.

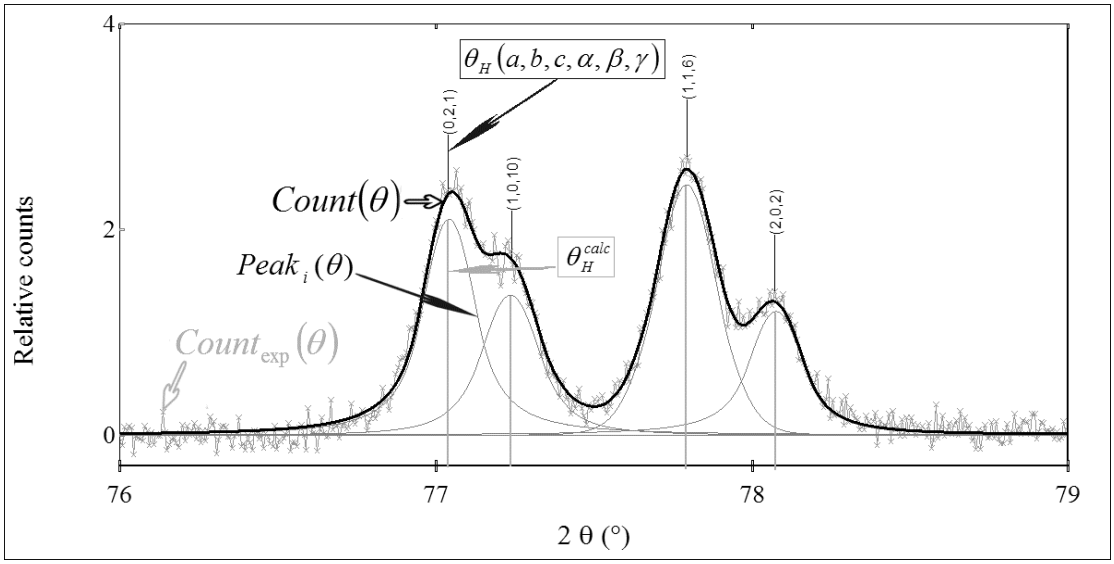

Figure 19: Graphic representation of the symbols used in the fitting procedure.

Seeking the minimum of an ***S*** function defined as follows performs the peak fitting:

$$(eq.\ 25) \qquad S = \sum_{j=1}^{n\_of\_peaks} \left|\theta_H(a,b,c,\alpha,\beta,\gamma) - \theta_H^{calc} - Shift\right| \cdot \theta_H^{calc} \cdot h_H^{calc}$$

or at least, to find a point in the $(a,b,c,\alpha,\beta,\gamma)$ space in which the following conditions are satisfied:

$$(eq.\ 26) \qquad \frac{\partial S}{\partial a}=0,\ \frac{\partial S}{\partial b}=0,\ \frac{\partial S}{\partial c}=0,\ \frac{\partial S}{\partial \alpha}=0,\ \frac{\partial S}{\partial \beta}=0,\ \frac{\partial S}{\partial \gamma}=0.$$

with:

- h_H^{calc} =Peak intensity
- *Shift*=Pattern shift

"At least", means that ***S*** is at least in a local minimum. Respecting the conditions given in (eq. 26) does not mean that ***S*** is necessarily in its absolute minimum. The ability of the algorithm to find the right minimum plays a fundamental role[1].

[1] In Figure 49, an example of a pattern simulation is given. The plot shows, how close pattern and simulation curve are. An enlarged detail of a very critical zone of the pattern is given as well, in which,

In (eq. 25), the weight of a single residual is proportional to the peak's position and its intensity.

8.2.3 Deviation calculations

The last point to treat is how to calculate the parameter deviation. The standard deviation is calculated as follows[1]:

$$\sigma_p = \sqrt{\frac{\sum_{i=1}^{n_p}\left(p_{calc} - p_{peak}\right)^2}{n_p - 1}} \qquad \textit{(eq. 27)}$$

with:

- p = a considered parameter, one of the following: $a, b, c, \alpha, \beta, \gamma$;
- n_p= number of peak positions affected by "p" parameter (not necessarily all the peaks can be affected by p parameter variation);
- p_{calc} = Parameter calculated value, respecting the conditions given in (eq. 25);
- p_{peak} = Parameter value, for which $\theta_H(a,b,c,\alpha,\beta,\gamma) = \theta_H^{calc}$

Two more quantities have yet to be calculated:

- V = cell volume (in case of hexagonal cell $V = \frac{\sqrt{3}}{2} \cdot a^2 \cdot c$);
- c/a = parameter which variation gives the cell anisotropic deformation.

the standard deviation for both quantities have been calculated as follows:

$$\sigma_V = \left(\left|\frac{\partial V}{\partial a}\right| \cdot \sigma_a + \left|\frac{\partial V}{\partial c}\right| \cdot \sigma_c \right) \qquad \textit{(eq. 28)}$$

in case of hexagonal cell is:

---

it is also possible to appreciate the peak constituents (plotted in grey). Finally, the magnitudes of the residuals, comparable with the noise's magnitude, determine the quality of the fitting.

[1] In (eq. 27), the demographic parameter is taken as $n_p - 1$ as results from the Čebyšev theorem, instead of n_p .

$$\text{(eq. 29)} \quad \sigma_V = \left(\left| \sqrt{3} \cdot a \cdot c \right| \cdot \sigma_a + \frac{\sqrt{3}}{2} \cdot a^2 \cdot \sigma_c \right)$$

and for the anisotropic deformation:

$$\text{(eq. 30)} \quad \sigma_{c/a} = \left(\left| \frac{\partial (c/a)}{\partial a} \right| \cdot \sigma_a + \left| \frac{\partial (c/a)}{\partial c} \right| \cdot \sigma_c \right) = \left(\left| -\frac{c}{a^2} \right| \cdot \sigma_a + \left| \frac{1}{a} \right| \cdot \sigma_c \right)$$

8.3 Specific charge vs. cycles: an empirical description

Applying a "specific charge" plot yields a direct view of the cycling behavior of a system. By interpretation of the plot, an estimation of the s*pecific charge* of the sample and its fading during cycling is possible. In literature, expressions like *"The sample shows a specific charge of 120Ah/kg"* or *"The sample undergoes a specific charge fading of 10Ah/kg after 100 cycles"* are quite common. It means that, although a perfect model explaining such behavior does not exist, it is common practice to *assume* a linear decay of s*pecific charge* along with cycle numbers. The absence of such a model generates two problems:

1. It is very difficult to describe a non-perfect linear behavior;
2. This leads to the problem to catalogue the products versus their specific characters (eg: specific charge and fading).

Here, an empirical description will be proposed to introduce a systematic criterion for the product classification. We take the following assumptions:

1. The main component of a product's specific charge is a linear function of the cycle number: $C(z) = C_o + \alpha \cdot z$ *(C=Specific charge, C_o= initial specific charge, α= slope or fading parameter, z=cycle number)* and
2. The linearity deviation is assigned to another component *(F)* in which the fading is proportional to the component itself as follows:

$$\text{(eq. 31)} \quad dF(z) = -a \cdot F(z)$$

(a = constant), integrating this component and substituting for $a = \ln(2)/\tau$ we obtain[1]:

$$(eq.\ 32) \qquad F(z) = F_o \cdot \exp\left(-\frac{\ln(2)\cdot z}{\tau}\right)$$

The global function can be rewritten as a sum of the two components:

$$(eq.\ 33) \qquad C(z) = C_o + \alpha \cdot z + F_o \cdot \exp\left(-\frac{\ln(2)\cdot z}{\tau}\right)$$

Since the function *F* has an exponential behavior, it will be called *"Exponential component"* of the specific charge. Analogously, the function *C* will be called *"Linear component"* of the specific charge.

(eq. 33), will be intensively used in the course of this work. Although it can fit the major part of the specific charge plots satisfactory, it does not take into account the processes while the cell is going to shut down. Generally that happens with a quick fall of the specific charge, which also can be represented by an exponential decay, in which dY[2] is proportional to both *Y* and to *(Yo-Y)* like:

$$(eq.\ 34) \qquad dY(z) = -k \cdot Y(z) \cdot \left(Y_o - Y(z)\right)$$

with *k= constant*. Integrating (eq. 34) we obtain: $Y(z) = \left(\exp(k \cdot z) + 1\right)^{-1}$

This function is centered on 0, for our purposes, must be centered in a point (a cycle, z_f) to be established, then the function can be rewritten:

$Y(z) = \left(\exp\left(k \cdot \left(z - z_f\right)\right) + 1\right)^{-1}$

Substituing for $k=ln(3)/\chi$ we obtain:

$$(eq.\ 35) \qquad Y(z) = \left(\exp\left(\frac{\ln(3)\cdot\left(z - z_f\right)}{\chi}\right) + 1\right)^{-1}$$

[1] τ has a more immediate meaning, because it represents the number of cycles to have F_o reduced to the half.

[2] We are still talking about specific charge, the new variable *Y* is used to avoid confusion.

χ represents the number of cycles apart from z_f, Y function is assumed the values 3/4 and 1/4 respectively. $Y(z_f - \chi)=3/4$ and $Y(z_f + \chi)=1/4$. In this case χ is assumed a clearer physical meaning than k.

In Figure 20, an example of the function Y at different χ values is shown.

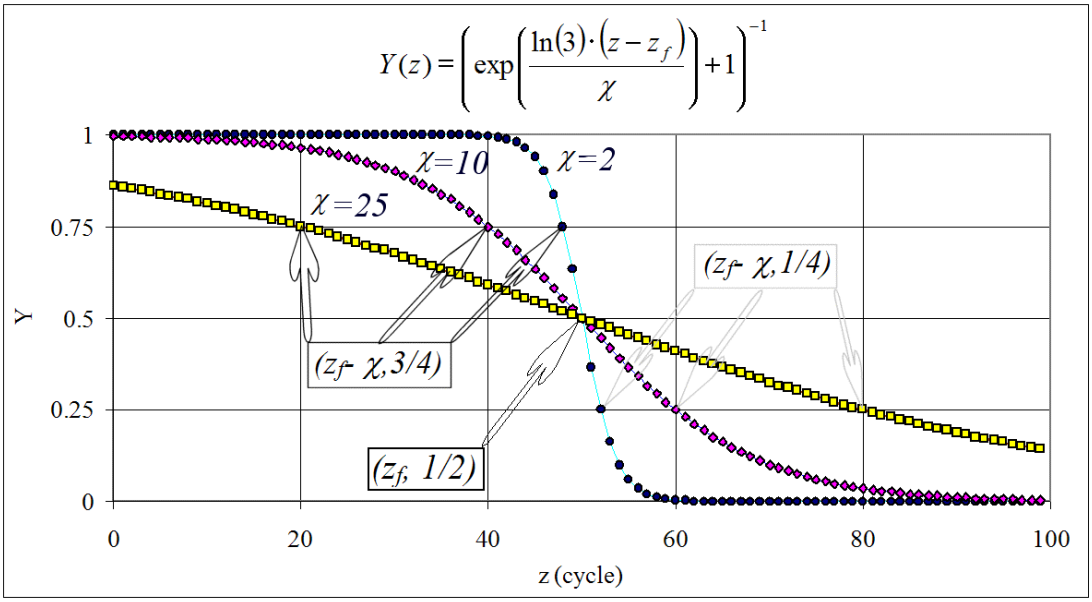

Figure 20: Example of *Y* function at different χ values centred at z_f=50.

Finally, combining (eq. 33) with (eq. 35), and considering that cycles begin with cycle number 1, an extended form is obtained by :

$$C(z) = \frac{C_o + \alpha\cdot(z-1) + F_o\cdot\exp\left(\frac{-\ln(2)\cdot(z-1)}{\tau}\right)}{\exp\left(\frac{\ln(3)\cdot(z - z_f)}{\chi}\right) + 1} \qquad \textit{(eq. 36)}$$

In Figure 21, an example plot of (eq. 36) is given. In particular, the straight line represents the linear component ($C(z) = C_o + \alpha\cdot z$).

For our purposes, the Y component is used to compensate the distortion from the behavior, given by (eq. 33) in the case of an incipient cell shut down (see ellipse in Figure 21. The parameters z_f *and* χ have a precise meaning only in case of an incipient cell shut down. In the case presented we are far from a shut down (far from z_f). Thus, the calculation of z_f cannot be very precise. For this

reason, the four parameters: C_o, α, F_o, τ and the square root of the deviation σ_{Cap} (eq. 37) will be used further.

$$\textit{(eq. 37)} \quad \sigma_{Cap} = \sqrt{\frac{\sum_{i=1}^{n_c} \left(C(z_i) - C_i\right)^2}{n_c - n_p}}$$

with:

- n_c = total number of cycles;
- n_p = number of parameters (C_o, α, F_o, τ, z_f, χ);
- C_i = ith cycle cathodic capacity;
- $C(z_i)$ = Capacity calculated by (eq. 36).
- z_i = ith cycle.

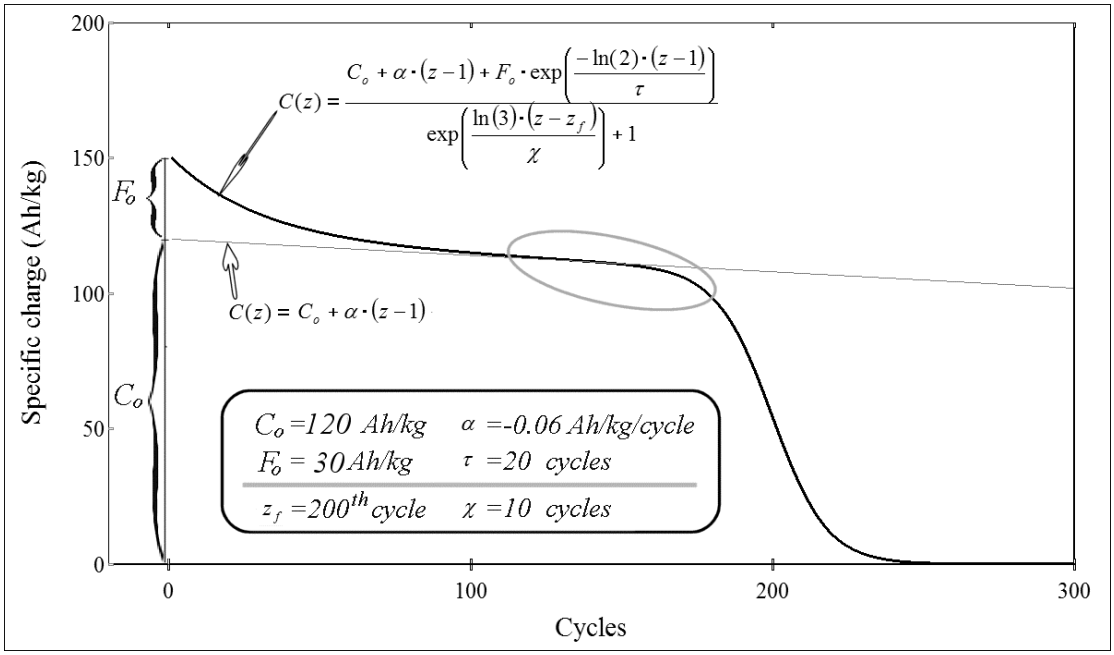

Figure 21: Example of a plot according to (eq. 36) (extended form).

Examples of this empirical description application will be given for some of *wet synthesis* products in Figure 82 and for some of dry synthesis products in Figure 83. A new quantity will be also used to characterize the product:

The average capacity after "*n*" cycles $\overline{C_n^{Calc}} = \frac{1}{n} \cdot \sum_{z=1}^{n} C(z)$.

Chapter 9.

Electroactive Manganese-based materials

Manganese is a transition metal of group VIIB in the 4th period. The metal itself does not occur in elemental form in nature, but its compounds are widely distributed, usually as oxides, silicates, and carbonates, with pyrolusite and psilomelane (grape-like spheres of manganese dioxide) being the most common ones. MnO_2 represents the most important compound of Mn based phases.

9.1 Manganese dioxide

Manganese came into the history of battery for its extensive use in the so called "dry cell". Its use was completely different from today. In fact MnO_2 (pyrolusite) is used as a depolarizer in dry cells for the following reason: A common dry cell battery has a Zn metal anode, a carbon cathode, and contains MnO_2 and NH_4Cl as well. The cathode reaction is:

$$2 \cdot NH_{4\,(aq)}^{+} + 2 \cdot e^{-} \Leftrightarrow 2NH_{3(gas)} + H_{2(gas)} \qquad \textit{(eq. 38)}$$

Because both products are gases the battery would explode if they were not removed. The ammonia is taken up by Zn^{2+} ions (the product of the anode reaction), while H_2 is removed by the reaction:

$$2 \cdot MnO_{2(s)} + H_{2(gas)} \Leftrightarrow Mn_2O_{3(s)} + H_2O \qquad \textit{(eq. 39)}$$

MnO_2 exists in various phase modifications (α-MnO_2, β-MnO_2, γ-MnO_2, λ-MnO_2, ramsdellite-MnO_2) and these well defined samples can be used for many electrochemical applications [**31**,**32**]. It is also available for the insertion of small ions (H^+, Li^+) (see (eq. 40)):

$$(eq.\ 40) \qquad x \cdot Li^+ + MnO_2 + x \cdot e^- \Leftrightarrow Li_xMnO_2$$

Although MnO_2 can exist in several forms, all of the variations are built with different packages of an octahedrical structural unit, in which Mn is in the centre of an octahedra surrounded by 6 O^{2-}. In Figure 22, four different crystal structures of MnO_2 are shown:

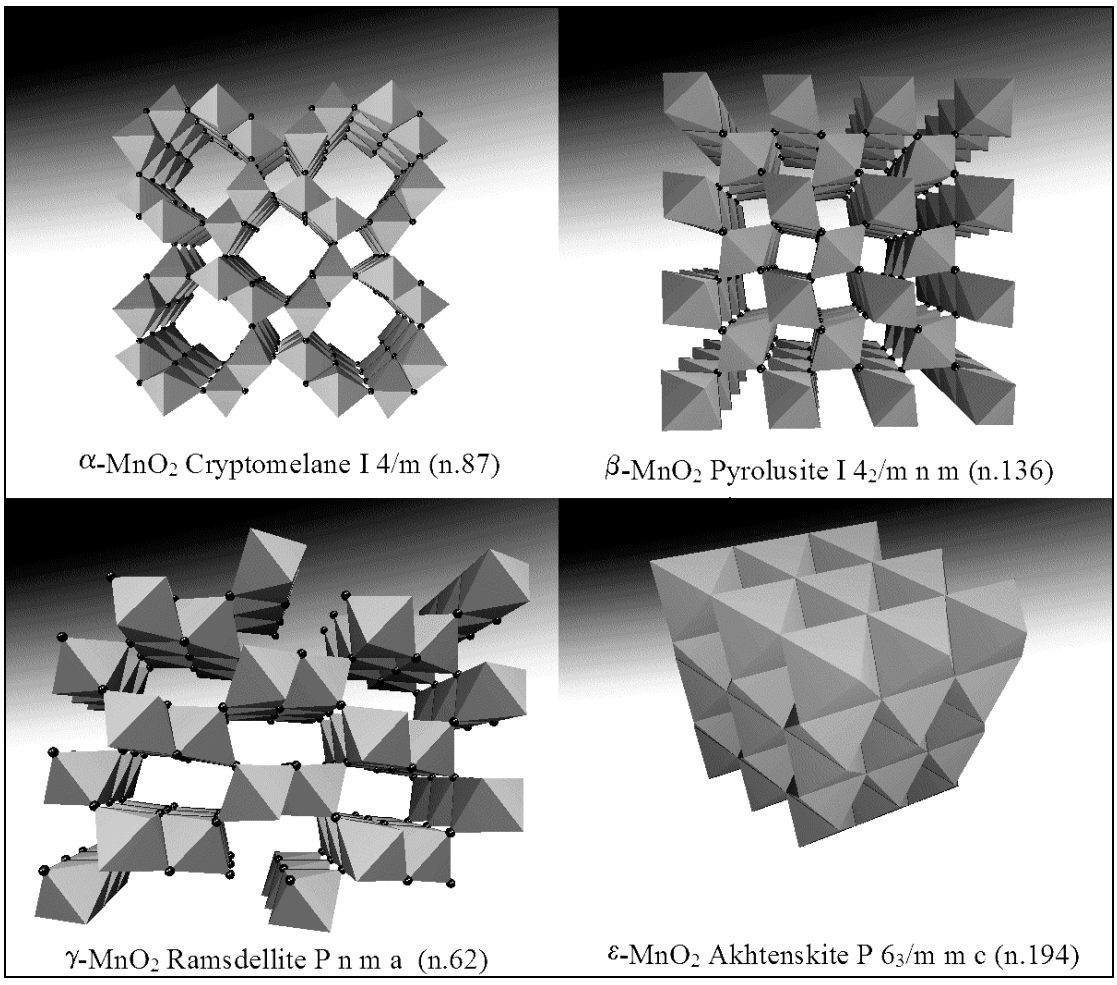

Figure 22: Crystal structures of four modifications of MnO_2

Crystals of α-MnO_2 are based on long chains of MnO_6 octahedra, which are linked to each other by their corners, leaving a cavity of (2x2 octahedra units) that easily enables other species to accommodate. γ-MnO_2 crystals with a (2x1)

cavity, as well as β-MnO_2 where (1x1) cavities occur also allow to accommodate guests ions. In contrary, ε-MnO_2 crystals cannot accommodate inclusions because of lacking cavities.

Although α-MnO_2, β-MnO_2, and γ-MnO_2 show an initial specific charge of >200 Ah/kg in the potential range 2-4 V vs. Li/Li^+, they have a strong tendency to lose specific charge during electrochemical cycling. For this reason they are not considered competitive for the use in Li-ion cells [25].

9.2 $LiMn_2O_4$ spinel

In the past, many efforts were made in order to synthesize a form of MnO_2, which could be suitable for reversible lithium insertion, until Hunter reported lithium extraction from $LiMn_2O_4$ spinel (see Figure 23) by acid treatment at ambient temperature [32]. The resulting material was identified as λ-MnO_2.

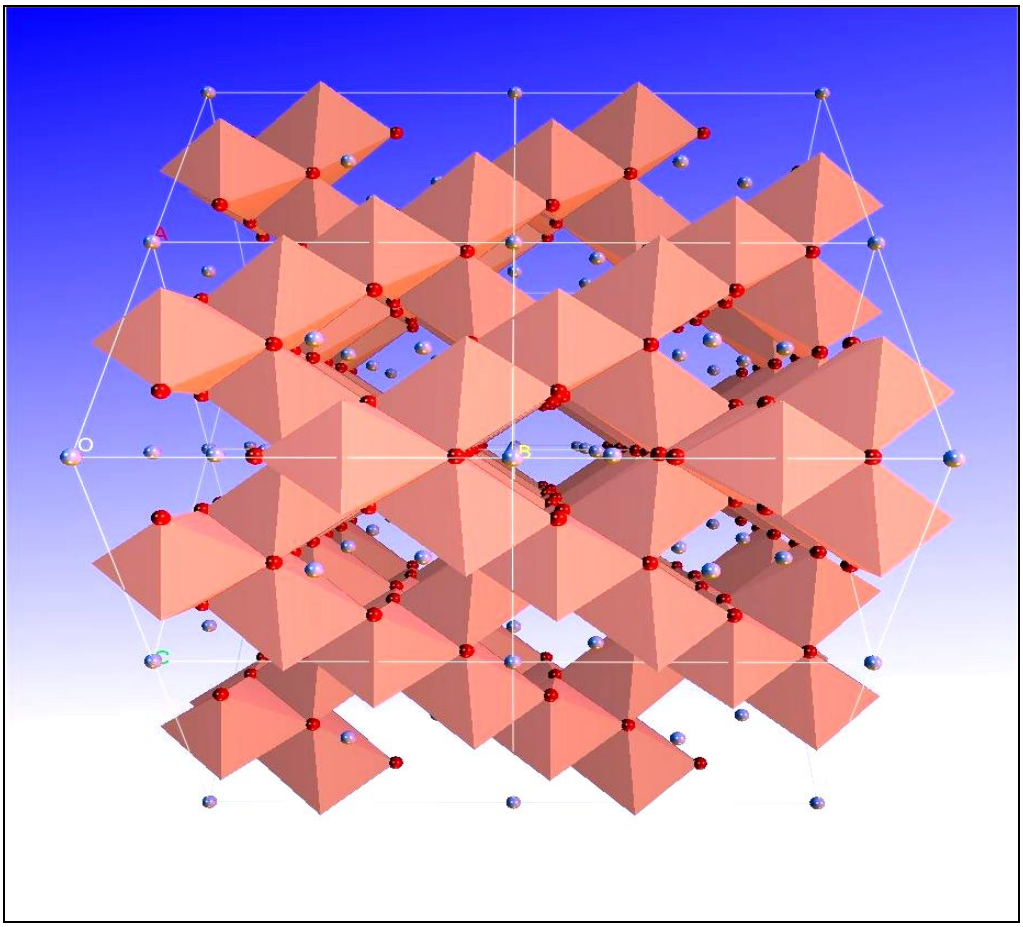

Figure 23: Graphic representation of $LiMn_2O_4$ spinel, space group $Fd\bar{3}m$ *(n.227)*

The $[Mn_2O_4]$ framework is a spinel structure with partial lithium ocupancy on the tetrahedral sites. Lithium spinel $Li[Mn_2]O_4$ is of great interest for Li-ion battery applications, because of its high specific charge. In Figure 24, a typical cyclic voltammogram of $LiMn_2O_4$ is shown. Considering the electrochemical reaction (eq. 41):

$$LiMn_2O_4 \Leftrightarrow Li_{1-x}Mn_2O_4 + x \cdot Li^+ + x \cdot e^- \qquad \textit{(eq. 41)}$$

Peak (2) corresponds to (0.0<x<0.5) and peak (3) to (0.5<x<1.0). The theoretical capacity for the complete reaction (x=1) is 148 Ah/kg, but in the applied potential range it is limited to 110-120 Ah/kg. Further insertion of Li^+ into $LiMn_2O_4$ generates the peak (1), but this addition of Li also results in a great distortion of the crystal structure leading to formation of a tetragonal phase.

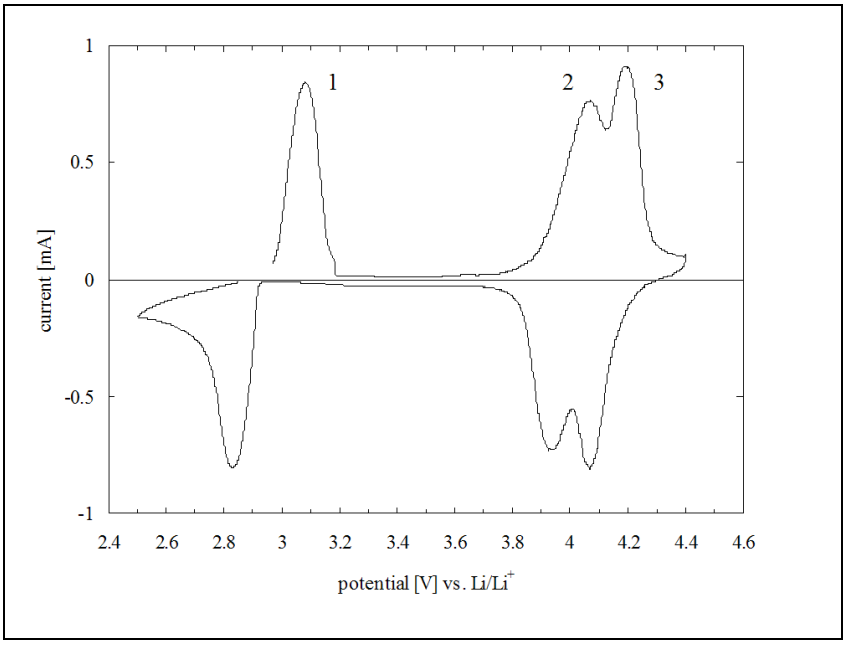

Figure 24: Typical cyclic voltammogram of $LiMn_2O_4$ measured at a sweep rate of 10 µV/s in 1 M $LiPF_6$ EC:DMC 1:1 (w/w). Redrawn from [33]

This large anisotropic expansion of the unit cell (increase in the *c*-parameter) is too severe for cubic and tetragonal phases to remain as an intergrown structure and soon mechanical decomposition occurs. The potential drop at x=1 (average

Mn oxidation state of +3.5) is caused by the Jahn-Teller distortion. It is caused by the presence of Mn^{3+} that has an unevenly occupied e_g set of orbitals by one electron only. This problem makes the spinel to be cycleable only in the 4 Volts range. A further step was to synthesize $LiMnO_2$ in the isostructural form to $LiCoO_2$ (space group $R\bar{3}m$ *n.166)*.

9.3 $LiMnO_2$

This compound was considered to have the same layered structure as $LiCoO_2$ (see Figure 25) and the economical and ecological benefits of manganese.

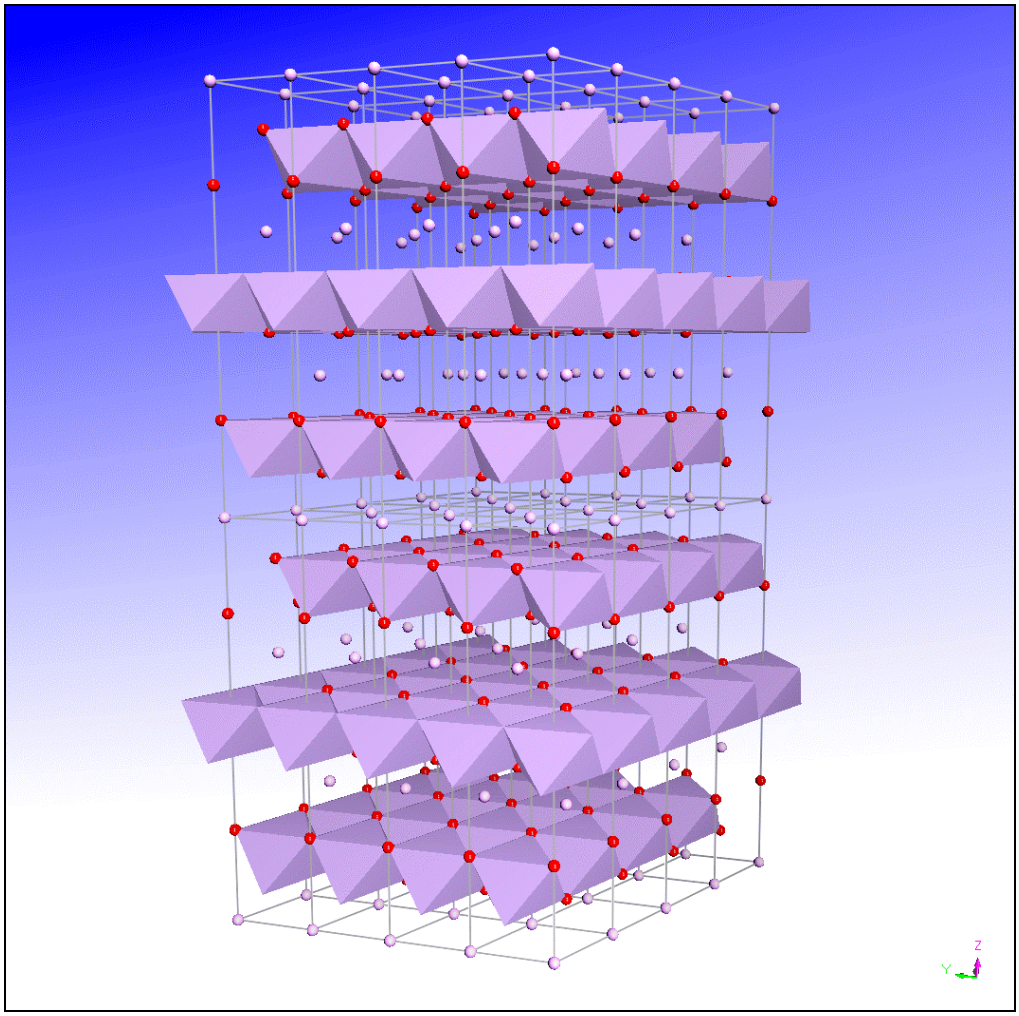

Figure 25: Layered structure of $LiCoO_2$ (α–$NaFeO_2$ structure type, space group $R\bar{3}m$ (*no.166)).*

Unfortunately, solid state synthesis of this phase was unsuccessful, because non-layered or puckered structures (spinel and the orthorhombic phase, respectively) are favored thermodynamically. The first synthesis of layered $LiMnO_2$, obtained by chemical exchange of the sodium from α-$NaMnO_2$ (isostructural with $LiCoO_2$), resulted in a monoclinic phase (space group *C2/m*). In this product, Li^+ ions were disposed in between the MnO_6 layers. Unfortunately, under electrochemical conditions the structure undergoes a breakdown, due to manganese migration into the lithium layer, and its structure is quickly converted into the spinel structure during cycling. The resulting problem was, how to reduce the Jahn-Teller distortion effect and get a thermodynamically stable layered product? It was clear that, if there were a way to stabilize layered $LiMnO_2$ thermodynamically, it would be an interesting candidate for the cathode material in Li-ion cells.

Chapter 10.

Characterization and doping of $LiMn_{0.5}Ni_{0.4}Al_{0.1}O_2$

10.1 Introduction

The previous work of Spahr [**29**] on layered mixed Mn/Ni oxides synthesized on a wet route for the system $LiMn_xNi_{1-x}O_2$, showed, that the layered structure is lost if the amount of manganese was more than or equal to 50% ($x \geq 0.5$). When $x > 0.5$ the compound converted into a spinel type.

It was the aim of that work to keep the maximum amount of Manganese in the structure for environmental reasons. The synthesized $LiMn_{0.5}Ni_{0.5}O_2$ is a layered product, with relatively high specific charge at the first cycle and it showed a fast capacity fading during further cycles. The structure destabilization was due to the Jahn-Teller distortion occurring at the manganese.

A subsequent work of Coluccia [**33**] revealed that by adding 10% of Aluminum (very light and non-electroactive element), the structure could be stabilized for a long number of cycles. This new high performance compound was determined to be $LiMn_{0.5}Ni_{0.4}Al_{0.1}O_2$, and it represents the starting point of the present work.

At a first step, the sample has been synthesized and checked in order to verify our synthesis methodology. The resulting properties are identical to those

shown by Coluccia's product. In Figure 26, four images of the newly synthesized $LiMn_{0.5}Ni_{0.4}Al_{0.1}O_2$, are shown.

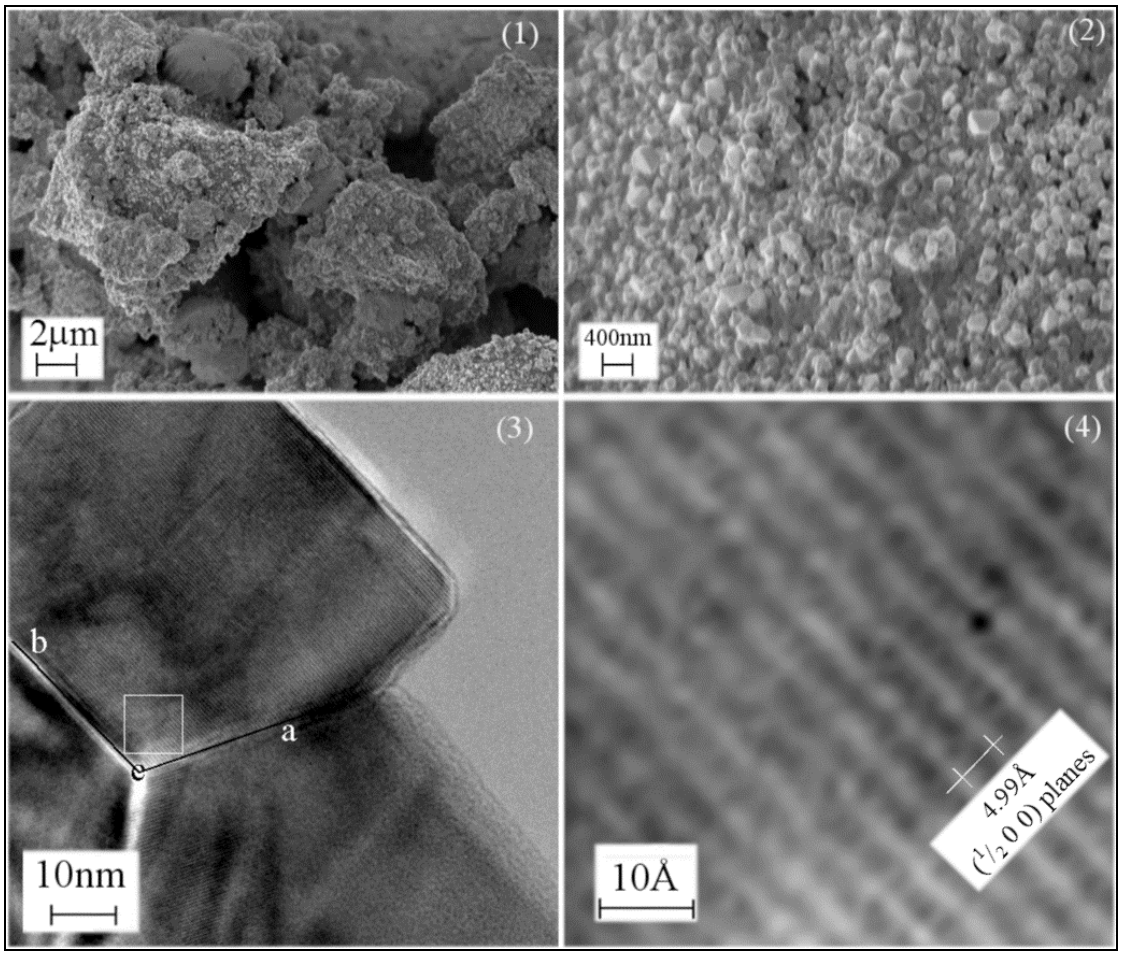

Figure 26: Images taken by S.E.M. and T.E.M. at different magnifications (1,2,3). In (3), crystallographic axes have been drawn, c axis is perpendicular to the sheet. In (4) a suggestive enlarged detail of (3) is shown. It was also possible to measure the distance between two rows representing the perpendicular view of two planes of the ($^1/_2$ 0 0) set.

In (3), crystallographic axes have been drawn; c is perpendicular to the sheet. In (4) a suggestive enlarged detail of (3), gave the opportunity to easily identify the distance between two rows representing the perpendicular view of two planes of the ($^1/_2$ 0 0) set.

10.2 $LiMn_{0.5}Ni_{0.4}Al_{0.1}O_2$ doped with Sodium

In order to increase the diffusivity of lithium through the oxide, an alternative approach has been tried. The idea was, that a small amount of Na^+ in the

structure would induce an expansion of the layer distance of the structure because of its larger ionic radius. Sodium was supposed to occupy prevalently the same lithium tetrahedrical position in the crystal.

Both doped samples have been formulated according to the *wet synthesis* method, sodium has been added as NaOH in the last step together with LiOH and thermal treatment has been performed at 800°C as shown in Figure 8. The content of Na was 0.64% and 1.2%, respectively, of the lithium content. According to Figure 27 no remarkable differences[1] were found for the lattice constants but a small difference is recognized for the intensity ratio $I_{(0,0,3)}/I_{(1,0,4)}$. This shows that in the sodium doped compound Mn, Ni and Al tend to maintain their octahedral site occupancies better than in the non doped

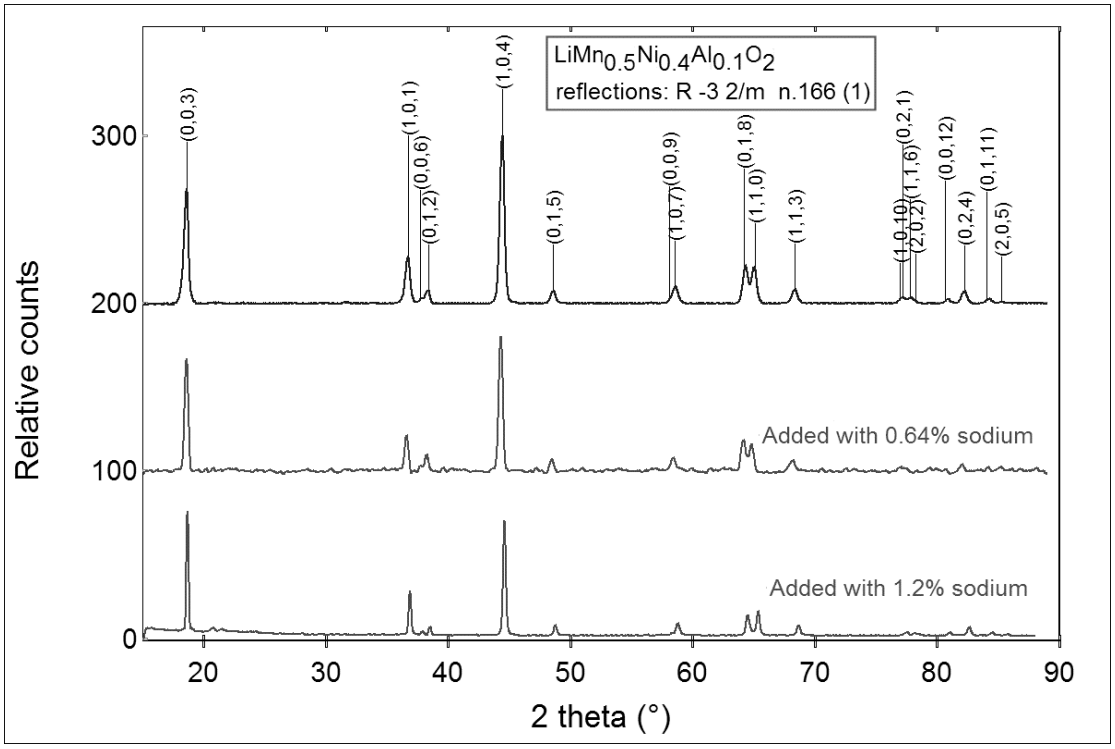

Figure 27: XRD pattern comparison of (top) $LiMn_{0.5}Ni_{0.4}Al_{0.1}O_2$ and its corresponding doped derivates with different amounts of sodium (lower two).

compound because this ratio is very sensitive cation exchange between transition metal and lithium layers.

[1] Differences between the sodium doped products and the $LiMn_{0.5}Ni_{0.4}Al_{0.1}O_2$.

In Figure 28, the electrochemical cycling behavior of the two doped samples is shown.

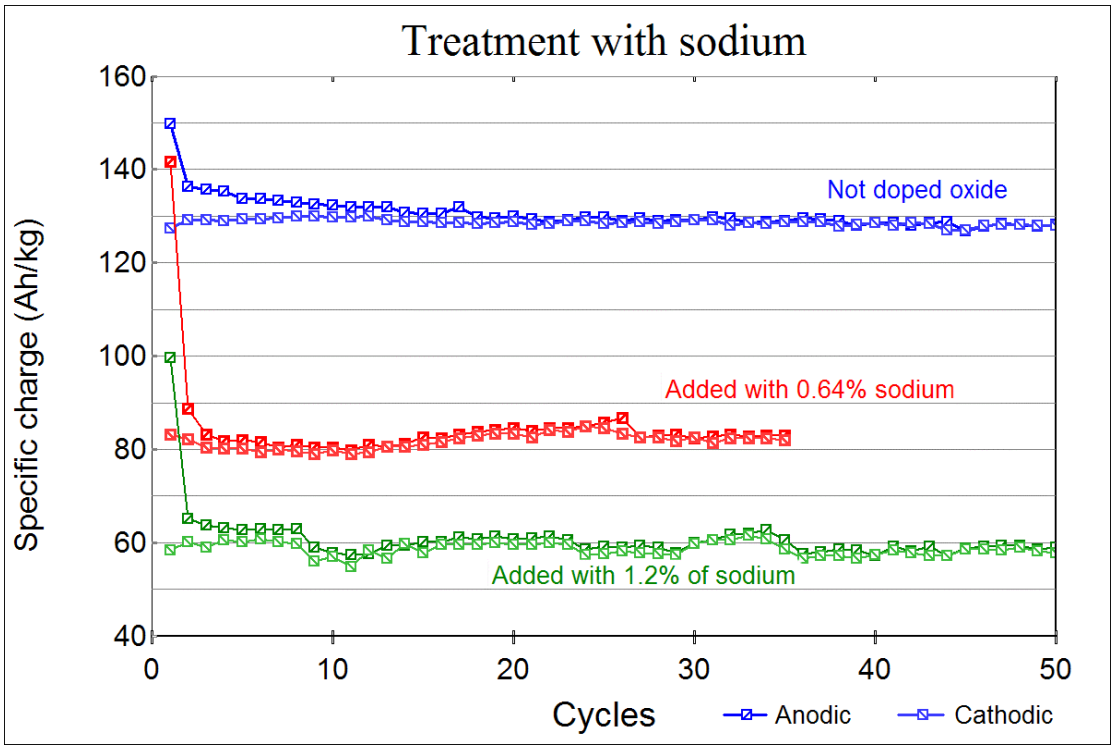

Figure 28: Galvanostatic cycles (2.5 – 4.4 Volts at 10 A/kg) of $LiMn_{0.5}Ni_{0.4}Al_{0.1}O_2$ and its corresponding doped derivates with different amounts of sodium.

It is evident that the doped oxides give a quite constant response in terms of specific charge, even if they perform a very low specific charge.

Details, related to the 4th cycles of the mentioned compound are shown in Figure 29. It can be seen that peaks related to the doped compounds:

- are smaller than the $LiMn_{0.5}Ni_{0.4}Al_{0.1}O_2$ peaks;
- have their related maximum and minimum abscissa position shifted more than for $LiMn_{0.5}Ni_{0.4}Al_{0.1}O_2$.

The result means that the polarization is higher because of lower lithium diffusivity in sodium doped compounds just contrary to expectation.

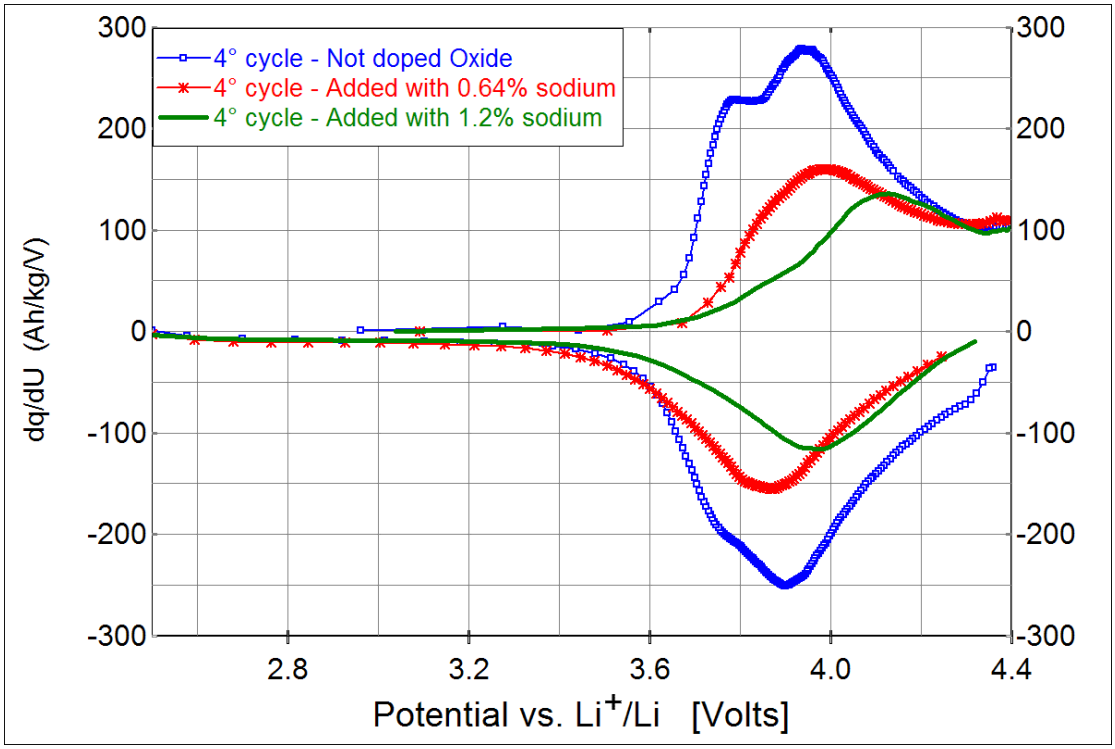

Figure 29: Comparison amongst the 4th cycles of $LiMn_{0.5}Ni_{0.4}Al_{0.1}O_2$ and its corresponding sodium doped derivates (these data are taken from galvanostatic cycles shown in the Figure 28).

10.3 Boron – Aluminum replacement in $LiMn_{0.5}Ni_{0.4}Al_{0.1}O_2$

In the previous section, a sodium doped compound performance is described. Sodium was supposed to occupy prevalently the lithium tetrahedral position in the crystal. In the following, the investigation has been focused on the octahedral sites (prevalently occupied by Mn, Ni and Al). Aluminum replacement with boron is supposed to give more mechanical stability to the structure. In this case a slightly lighter material would result, too. Both kinds of doping have been applied according the *wet synthesis* method. Boron has been added as B_2O_3 in the last step of the synthesis together with LiOH. Thermal treatment has been performed at 800°C as shown in Figure 8. The products have the nominal compositions $LiMn_{0.5}Ni_{0.4}Al_{0.05}B_{0.05}O_2$ and $LiMn_{0.5}Ni_{0.4}B_{0.1}O_2$, respectively. From their XRD patterns (shown in Figure 30), no remarkable differences arise, while both samples show low and quick specific charge fading (Figure 31). Further investigation (Figure 32) of

galvanostatic cycles, especially that one coming from $LiMn_{0.5}Ni_{0.4}B_{0.1}O_2$ (B 10%, Al 0%) confirm the presence of a well-defined peak, while the second peak seems totally absent. It seems that the total replacement of aluminum with boron does not allow the lithium to reach the second electrochemical site, in structural terms that could mean that either the octahedral or the tetrahedral positions are prohibited.

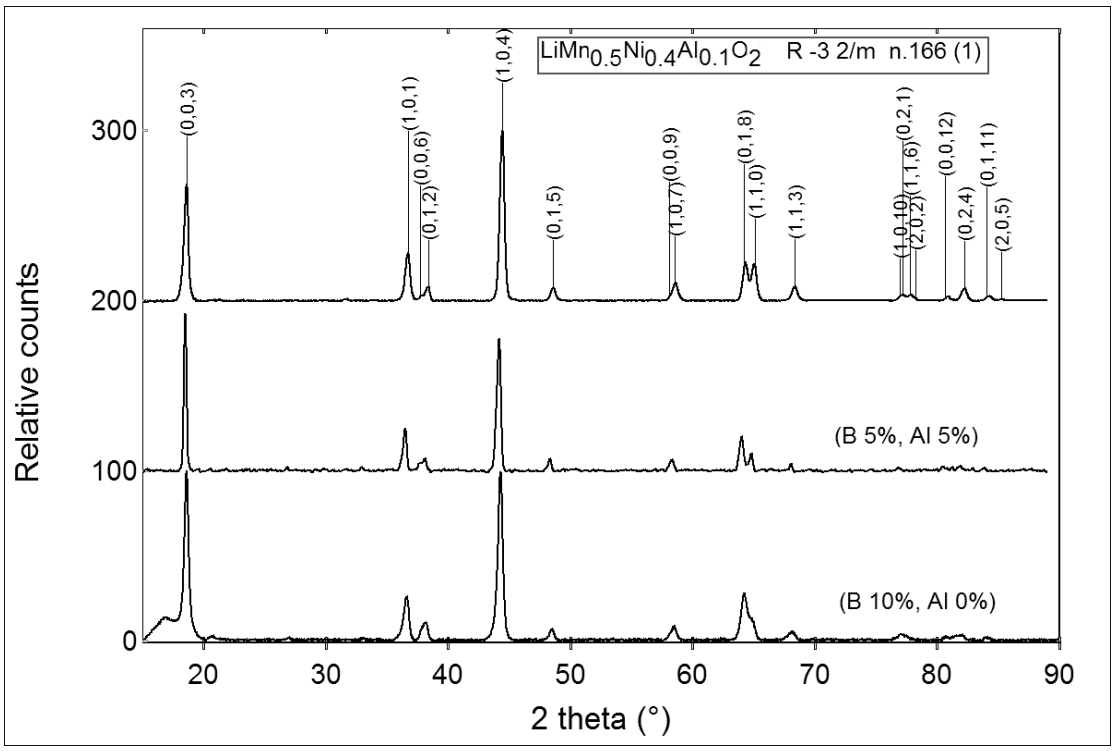

Figure 30: XRD pattern comparison of $LiMn_{0.5}Ni_{0.4}Al_{0.1}O_2$ with partial and whole substitution of B for Al.

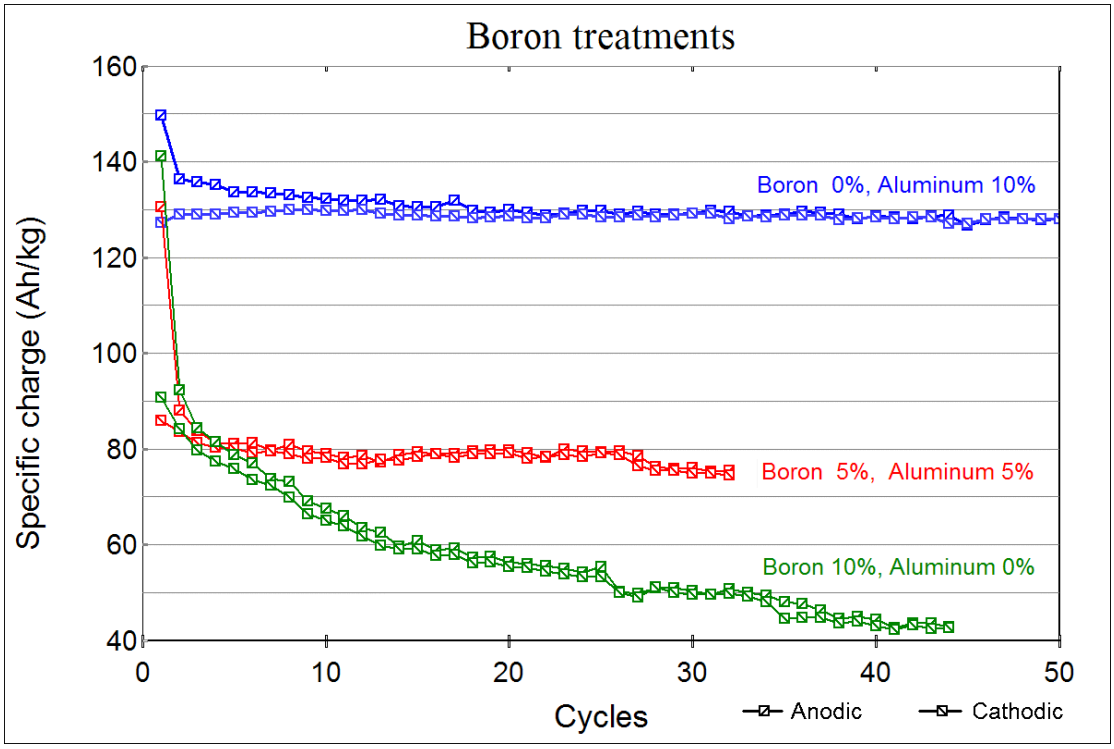

Figure 31: Galvanostatic cycles (2.5 – 4.4 Volts at 10 A/kg) of $LiMn_{0.5}Ni_{0.4}Al_{0.1}O_2$ with partial and whole substitution of B for Al.

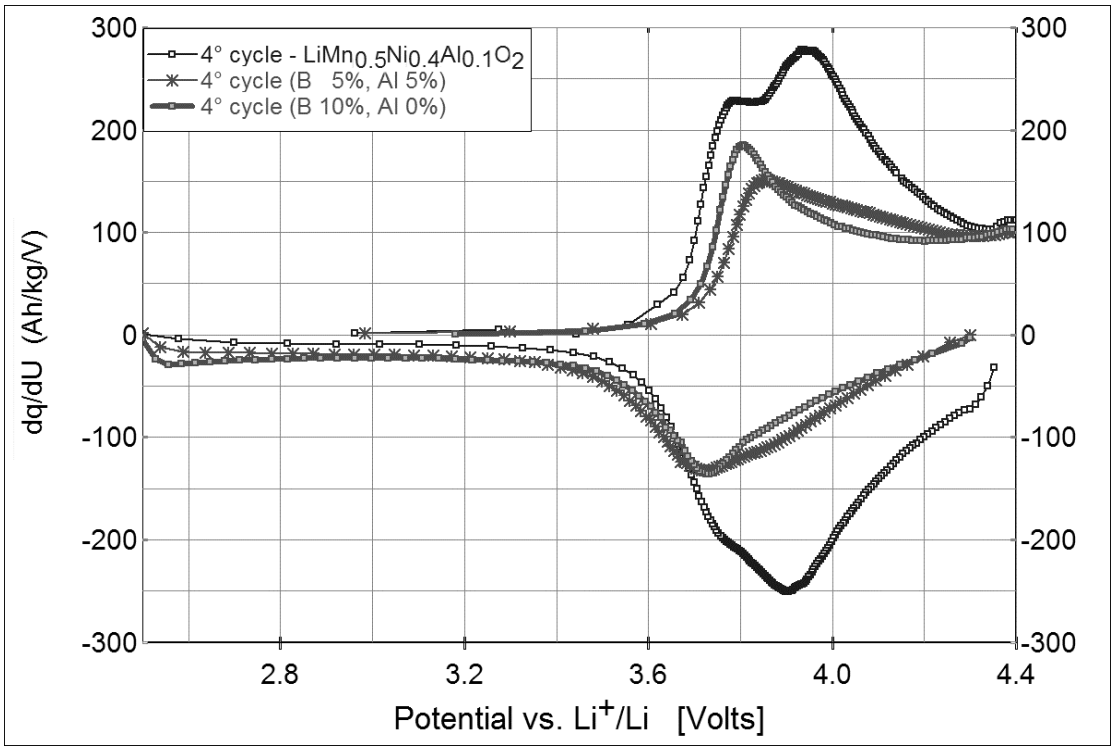

Figure 32: Comparison of the 4th cycles of $LiMn_{0.5}Ni_{0.4}Al_{0.1}O_2$ with partial and whole substitution of B for Al. These data are taken from galvanostatic cycles shown in the Figure 31.

10.4 $LiMn_{0.5}Ni_{0.4}Al_{0.1}O_2$: treatment with graphite oxide

Clearly, increasing the electronic conductivity of the cathode oxides would increase the cycling performances as well. For example, it could allow for using smaller electro-active crystallites and thus a higher active surface, which in turn would raise the power of the batteries. There are two ways to increase the conductivity. One consists in the improvement of the oxide conductivity; the other one tries to improve the effectiveness of the electronic contacts between the oxide particles and the conductor additives (graphite and carbon black). In this section, the attemps for the second approach are being presented.
The contact form between oxide crystallites and graphite grains ist not really known. The components are simply mixed mechanically.
The idea was to substitute the graphite grains by single graphite layers coated onto each crystallite. This could facilitate the electron transfer between graphite bulk and oxide bulk and vice versa. For this purpose graphite oxide (GO) was chosen which easily disperses in alkaline solutions fornishing yellow colloids. As GO contains large numbers of OH, epoxy and COOH groups on each six-ring layer can easily attach oxide surfaces. In a tempering step GO is then backtransformed into graphite layers.

10.4.1 Synthesis procedure

The synthesis was carried out as follows:

Solution A:

{ 5 mgr graphite oxide in 10 ml LiOH 0.01M}

In order to prepare a colloid. The solution has been sonicated for 15 sec at 50% power (1500W max power),

Solution B:

{ Solution A + 500mgr oxide }

was sonicated for 15 sec. at 50% power (1500W max power).

The precipitate obtained by filtration of *Solution B* was treated for 10 hours at 180°C to decompose the graphite oxide and then placed in an exsiccator.

Samples with 1%, 4% and 9%, respectively, of graphite (arising from the graphite oxide decomposition) have been synthesized.

10.4.2 Electrochemical characterization

The synthesized samples have been tested, using the pure product as well as adding additives. Negligible performances in terms of specific charge where shown by 9% treated samples and will not be discussed further. All other samples are represented in Figure 33. In treated products performances are poorer than in the untreated samples. Furthermore Figure 34 reveals, it is evident that the curve related to 1% graphite in the sample is rather similar to the untreated sample. While sample with 4% graphite shows a separation between the maximum (of anodic curve) and the minimum (of cathodic curve) of about 560mV, which is incomparably larger than those shown by other two compounds. That could mean that the resistivity of the sample is strongly increased. This could also be a result of the coating graphite film surrounding the oxide grains by obstacling the lithium ion migration.

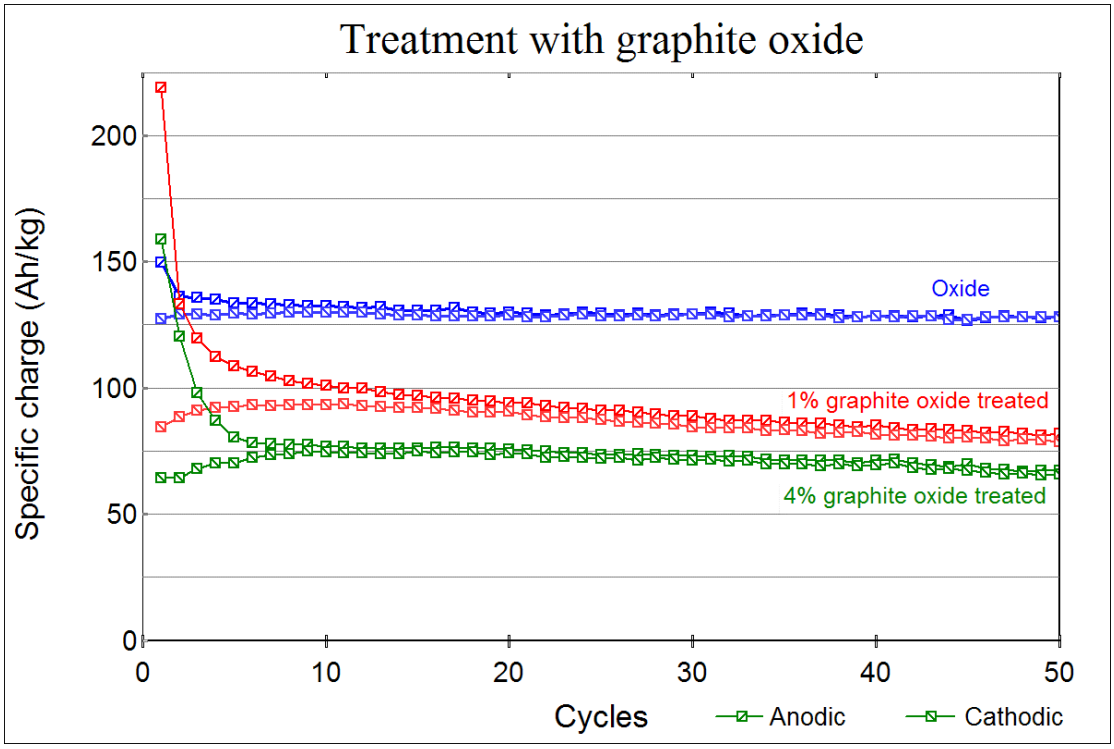

Figure 33: Galvanostatic cycles (2.5 – 4.4 Volts at 10 A/kg) of $LiMn_{0.5}Ni_{0.4}Al_{0.1}O_2$ and its corresponding derivatives treated with 1% and 4% of graphite oxide.

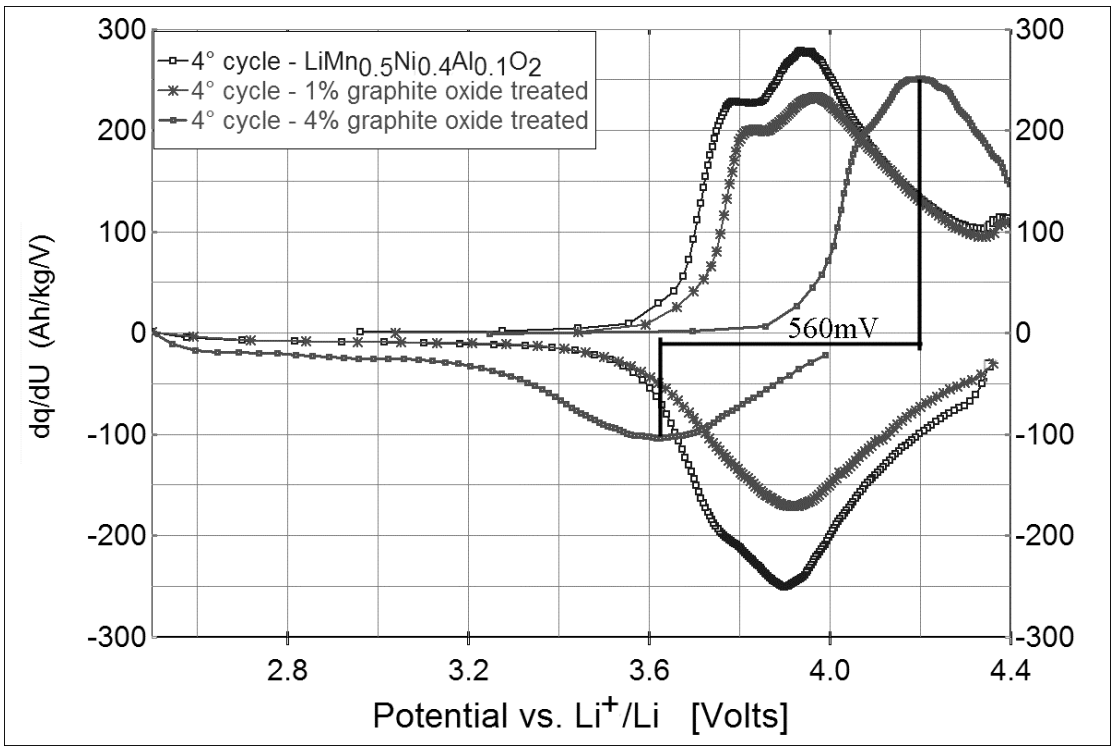

Figure 34: Comparison amongst the 4th cycles of $LiMn_{0.5}Ni_{0.4}Al_{0.1}O_2$ and its corresponding derivatives treated with graphite oxide (these cycles come from galvanostatic cycles shown in the Figure 33).

10.5 Conclusions

To enhance the performances of the $LiMn_{0.5}Ni_{0.4}Al_{0.1}O_2$ cathode material, three different methods have been tested:

1. **Doping with sodium**. Sodium was supposed to occupy the same Li tetrahedral position in the layout;
2. **Boron-Aluminum replacement**. Boron was supposed to occupy the same octahedral position;
3. **Graphite oxide treatment**. This should increase the electronic contacts of the electrode sample by partial surface coating.

Unfortunately, all treatments led to lower performing products.

Chapter 11.

Investigation on $LiMn_aNi_bAl_cO_2$ compounds

This chapter is dedicated to further investigations of oxides of the same $LiMn_{0.5}Ni_{0.4}Al_{0.1}O_2$ family, corresponding to the formula $LiMn_aNi_bAl_cO_2$, (a+b+c =1).

11.1 $LiMn_{0.5}Ni_{0.4}Al_{0.1}O_2$ crystal superstructure

As mentioned before, $LiMn_{0.5}Ni_{0.4}Al_{0.1}lO_2$ crystallizes in space group $R\bar{3}m$ (no.166). However additional few small intensity peaks in the 2θ range between 20° and 30° are revealed. They can be correlated to a superstructure. In the meantime, several other groups also reported on indications of other superstructures for $Li_xMn_{0.5}Ni_{0.5}O_2$ as well [**34**,**35**,**36**,**37**,**38**]. The major evidence for superstructure formation comes from electron diffraction T.E.M.. In Figure 35, the measured pattern is shown and the small intensity reflections in between the typical reflections of $R\bar{3}m$ space group are indicators of the superstructure.

11.1.1 Superstructure models

The diffraction pattern suggests the presence of a three layers c-stacking, different to each other, but very close in terms of composition. According to the overall stoichiometry of the compound, two possibilities are being proposed:

Layer **<A>** = $Li_6Mn_3Ni_2AlO_{12}$ and

layer **<B>** = $Li_6Mn_3Ni_3O_{12}$

with these two layers, two different three-dimensional models can be developed:

- 1st model: **<A><B><A>** with formula: $Li_{18}Mn_9Ni_7Al_2O_{36}$

and

- 2nd model: **<B><A><B>** with formula: $Li_{18}Mn_9Ni_8Al_1O_{36}$

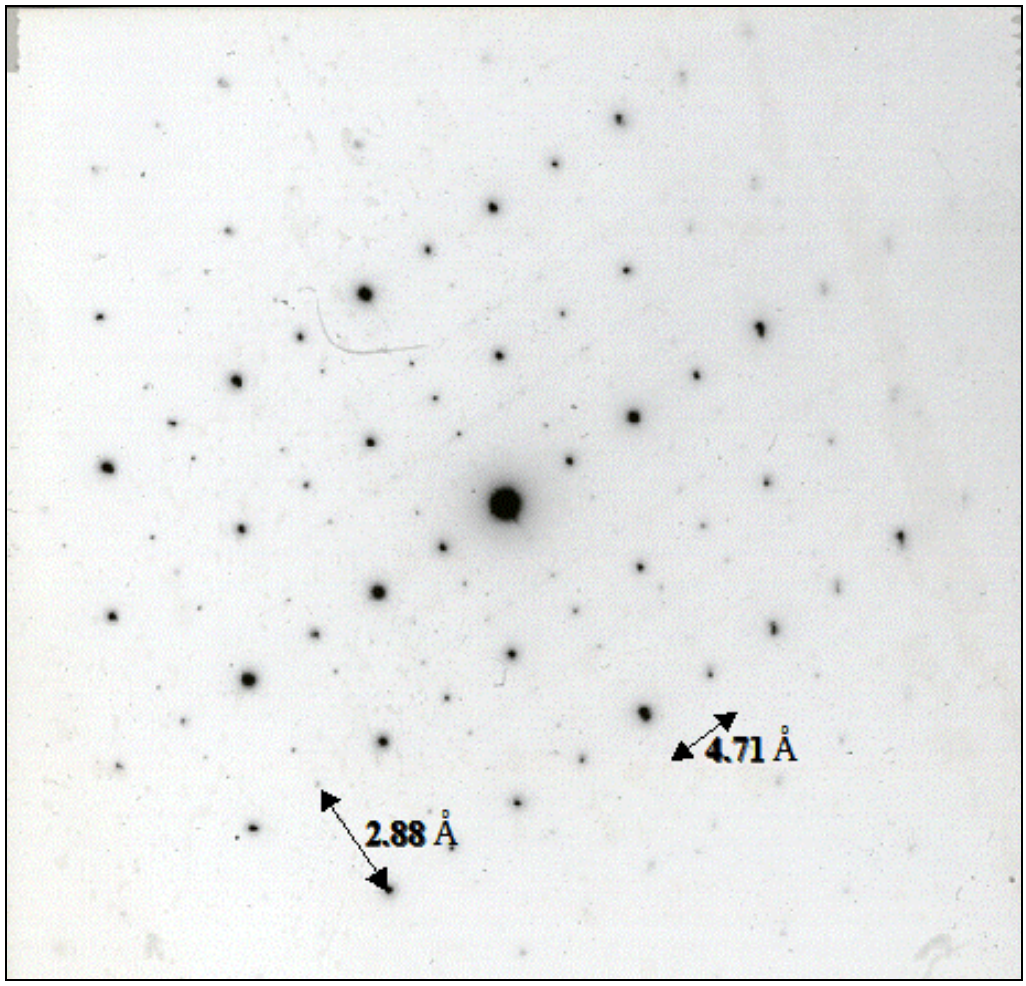

Figure 35: Electron diffraction pattern of $LiMn_{0.5}Ni_{0.4}Al_{0.1}lO_2$ obtained by T.E.M..

Exchanging Mn by Ni, we obtain two more models:

- 3rd model: $Li_{18}Mn_7Ni_9Al_2O_{36}$
- 4th model: $Li_{18}Mn_8Ni_9Al_1O_{36}$

This may be done because of the similar scattering power of the two different cations.

11.2 $LiMn_{0.5}Ni_{0.4}Al_{0.1}O_2$: changing composition to fit superstructure requirements

Previous work by M. Spahr [29] and M. Coluccia [33] showed that a very small change in product composition affects electrochemical performances dramatically. We therefore have a new criterion to adapt the product composition according to the compositions suggested by the different model superstructures. It is noticeable that the first two model compositions are only slightly different with respect to $LiMn_{0.5}Ni_{0.4}Al_{0.1}O_2$. The next step included the syntheses of four new products with compositions according to these layouts, followed by their characterization.

11.3 Syntheses

The syntheses have been performed according to the *wet synthesis* method described in section 6.1.2, new samples have been labeled according to the nomenclature described in section 6.1.1. In Table 7 the correspondence between the products and their aliases is documented:

Table 7: Samples targetting the ABA and BAB models.

$LiMn_{9/18}Ni_{8/18}Al_{1/18}O_2$	LiMnNiAl-981Br
$LiMn_{9/18}Ni_{7/18}Al_{2/18}O_2$	LiMnNiAl-972Br
$LiMn_{8/18}Ni_{9/18}Al_{1/18}O_2$	LiMnNiAl-891Br
$LiMn_{7/18}Ni_{9/18}Al_{2/18}O_2$	LiMnNiAl-792Br

Together with this set of products, which should better enforce the superstructure hypothesis, other samples have been synthesized:

$LiMn_{0.5}Ni_{0.4}Al_{0.1}O_2$	LiMnNiAl-541Br
$LiMn_{0.4}Ni_{0.5}Al_{0.1}O_2$	LiMnNiAl-451Br
$LiMn_{0.3}Ni_{0.6}Al_{0.1}O_2$	LiMnNiAl-361Br

These products have also been generated by the wet route via two different thermal treatments. The first thermal treatment was at 800°C (see thermal profile in Figure 8) in order to compare the results with the product tested by M. Spahr [29] and M. Coluccia [33]. The second thermal treatment has been chosen according to the thermogravimetry plot of two of our precursors (Figure 36) where a last plateau is at 950°C. Figure 9 shows the thermal profile for the treatment at 950°C (ttt=950°C).

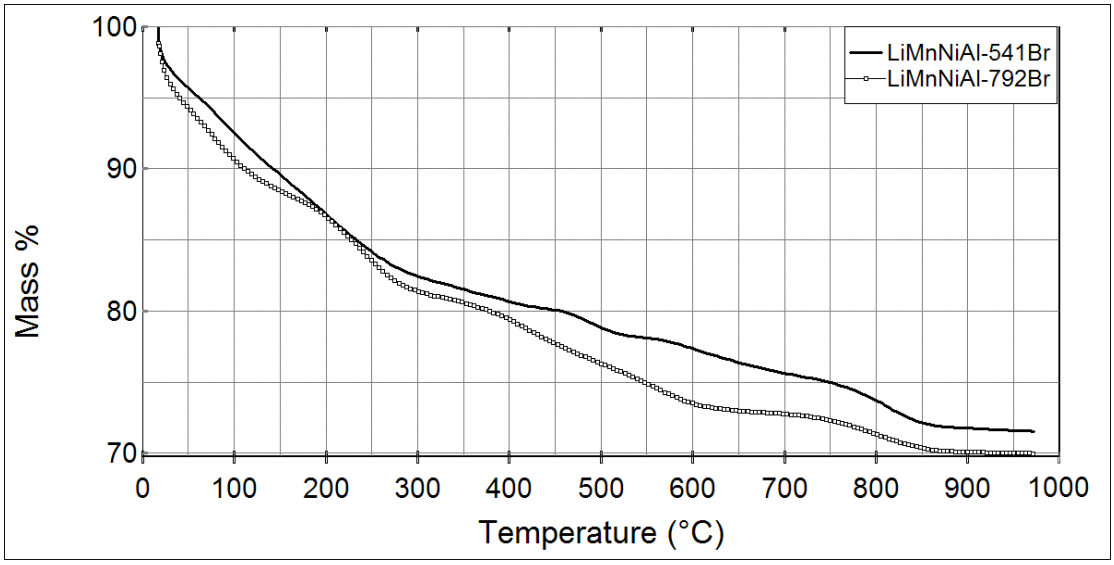

Figure 36: Thermogravimetry plot of two precursors.

11.4 XRD characterization

All products have been characterized by XRD (see section 6.2). In Figure 37 and Figure 39, corresponding XRD powder patterns are presented. All products only exhibit reflections belonging to the desired α–$NaFeO_2$ structure type (space group $R\bar{3}m$, no.166). Reflection indexes are denoted only at the uppermost pattern, but corresponding indices are found for the other patterns as well.

We found that:

1. All peaks in the patterns, resulting from the products synthesized at higher temperature, are better defined in terms of crystallinity with sharper reflections than those synthesized at lower temperature. This is an evidence of the larger crystallite sizes;
2. Products synthesized at higher temperature show higher $I_{(0,0,3)}/I_{(1,0,4)}$ ratio than their homologous synthesized at lower temperature. This is due to the higher fraction of Mn, Ni, Al ions in the octahedral sites (LiMnNiAl-891Br is the only exception);
3. The series of very small intensity peaks present in all compounds, between 20° and 32° in 2θ space (Figure 38) are probably a consequence of the superstructure.
4. Increasing manganese percentages in the product tends to reduce both *a* and *c* cell parameters (see Table 8 and Figure 40).

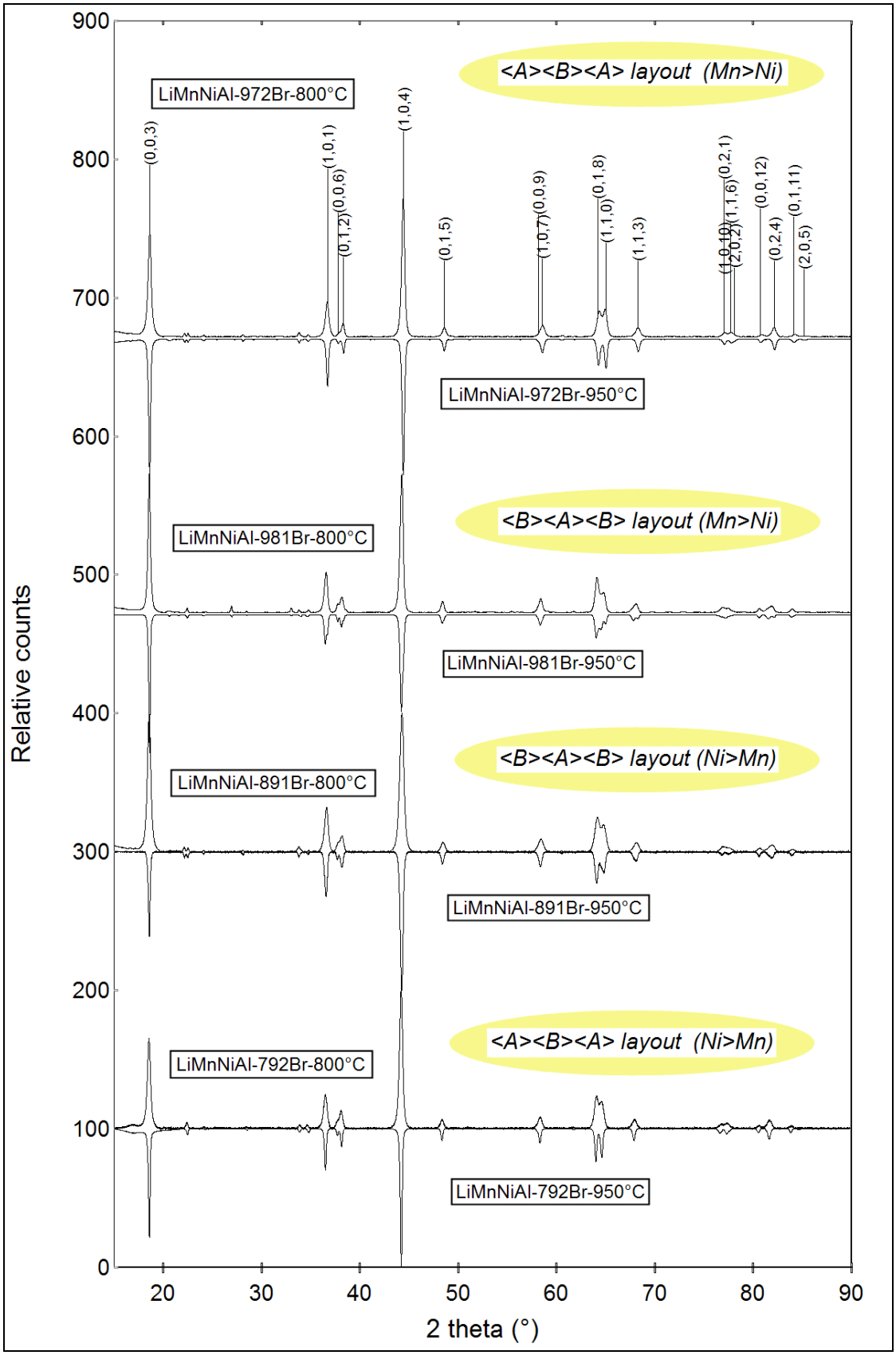

Figure 37: XRD of powder samples all of them being isotypic (space group R$\bar{3}$m, no.166). Patterns are ordered with decreasing Mn:Ni ratio.

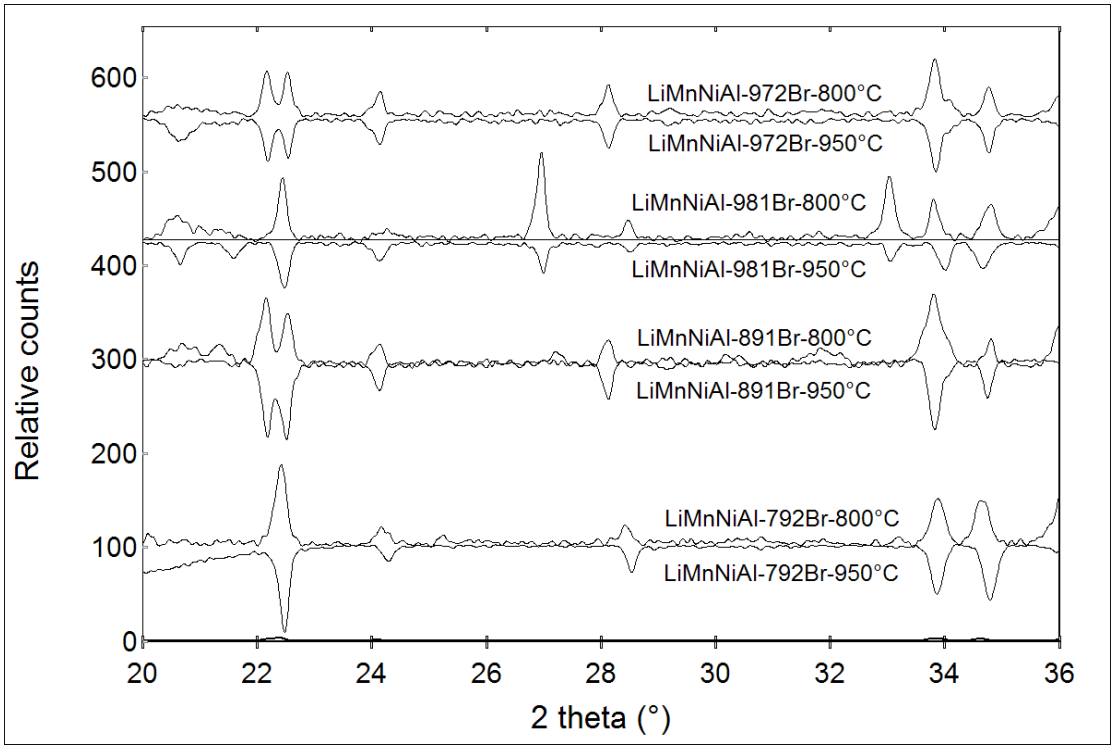

Figure 38: Detail of plot in Figure 37. Some of the peaks in this 2θ range cannot be indexed in the small unit cell but very probably are due to superstructure formation.

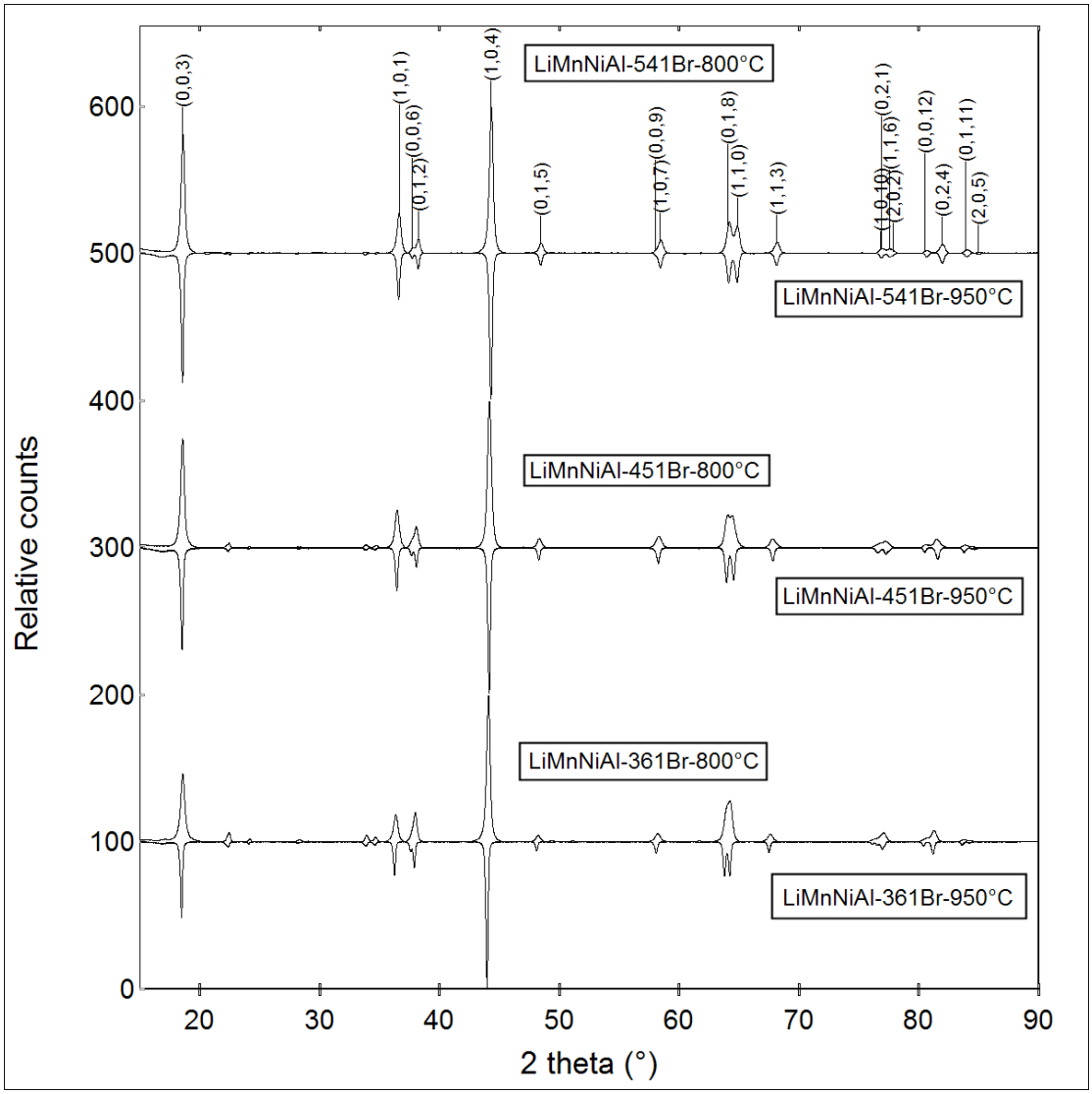

Figure 39: XRD of different powder samples as given in the plots; all samples are single phases crystallizing with the α–$NaFeO_2$ type. Patterns are ordered with decreasing Mn:Ni ratio.

Table 8: Cell parameters vs. product composition for products from wet synthesis, treated at 800°C and 950°C. In brackets standard deviations are given.

Product	%Mn	%Ni	%Al	Thermal treatment at 800°C			
				a(Å)	*c(Å)*	*c/a*	*V(Å³)*
LiMnNiAl-981Br	50.0%	44.4%	5.6%	2.874(1)	14.276(3)	4.967(3)	102.1(1)
LiMnNiAl-541Br	50.0%	40.0%	10.0%	2.870(1)	14.268(5)	4.971(3)	101.8(1)
LiMnNiAl-972Br	50.0%	38.9%	11.1%	2.868(4)	14.243(5)	4.97(1)	101.5(2)
LiMnNiAl-891Br	44.4%	50.0%	5.6%	2.872(3)	14.266(4)	4.97(1)	101.9(2)
LiMnNiAl-451Br	40.0%	50.0%	10.0%	2.887(2)	14.290(4)	4.950(5)	103.1(1)
LiMnNiAl-792Br	38.9%	50.0%	11.1%	2.880(2)	14.284(3)	4.960(4)	102.6(1)
LiMnNiAl-361Br	30.0%	60.0%	10.0%	2.893(2)	14.290(1)	4.940(4)	103.6(1)
Product	%Mn	%Ni	%Al	Thermal treatment at 950°C			
				a(Å)	*c(Å)*	*c/a*	*V(Å³)*
LiMnNiAl-981Br	50.0%	44.4%	5.6%	2.882(3)	14.28(1)	4.96(1)	102.7(2)
LiMnNiAl-541Br	50.0%	40.0%	10.0%	2.8705(6)	14.267(4)	4.970(3)	101.81(5)
LiMnNiAl-972Br	50.0%	38.9%	11.1%	2.8653(5)	14.261(3)	4.977(2)	101.40(4)
LiMnNiAl-891Br	44.4%	50.0%	5.6%	2.876(2)	14.292(6)	4.969(5)	102.4(1)
LiMnNiAl-451Br	40.0%	50.0%	10.0%	2.883(1)	14.297(2)	4.959(3)	102.91(6)
LiMnNiAl-792Br	38.9%	50.0%	11.1%	2.8826(3)	14.300(1)	4.961(1)	102.91(2)
LiMnNiAl-361Br	30.0%	60.0%	10.0%	2.894(1)	14.306(2)	4.943(2)	103.76(6)

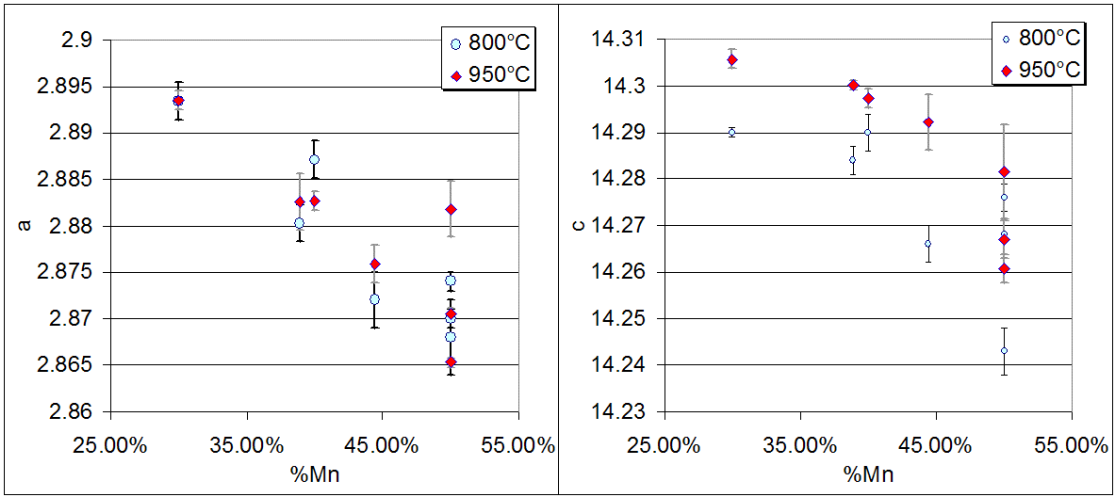

Figure 40: Cell parameter vs. %Mn of the products from wet synthesis, treated at 800°C and 950°C. Bars above and below each point represent sigma values.

11.5 Electrochemical characterization

All products have been tested electrochemically. In Figure 41 galvanostatic cycling performances are shown. In both series synthesized at 800°C and 950°C, every product maintains its rank in terms of performances. LiMnNiAl-541Br is the better in both series; LiMnNiAl-972Br is ranked as second in both series and so on. Every product synthesized at 800°C gives better performances in respect to its analogue synthesized at 950°C. The only exception is LiMnNiAl-541Br-950°C which performs better than LiMnNiAl-541Br-800°C, and it is also the best performing product in electrochemical terms.

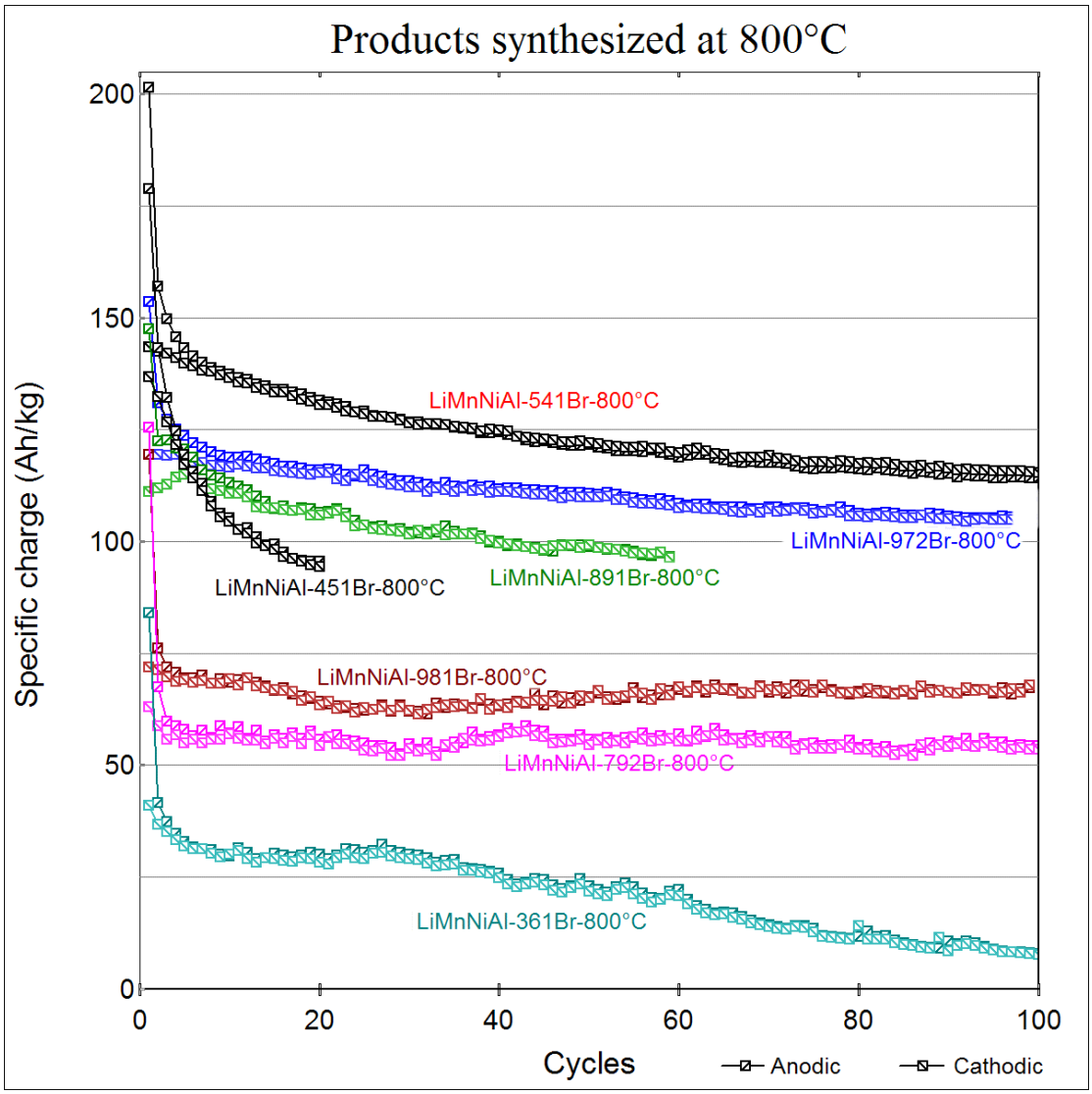

Figure 41: Galvanostatic cycles at 10A/kg (2.5-4.4Volts) of products synthesized at 800°C.

The specific charge plot of these products have been fitted by (eq. 33) as described in sect. 8.3. Fitting examples performed on some of these products are shown in Figure 82. The function fits very well all the plots given and for all of them a very small deviation σ_{Cap} (eq. 37) results.

Without any exception, all product reveal an anomalous high anodic capacity at the first cycle, most probably due to:

1. the deintercalation of partial Li^+ that in normal cycling conditions could not be reinserted anymore[1].
2. the electrolyte decomposition and formation of *SEI* (solid electrolyte interface) on the oxide surface. This reaction also needs an activation energy clearly appreciable from the differential capacity plot;

In Figure 42, an example of this phenomenon is shown and it can be clearly seen that the anodic part of the first cycle is shifted to the right in respect to the other cycles.

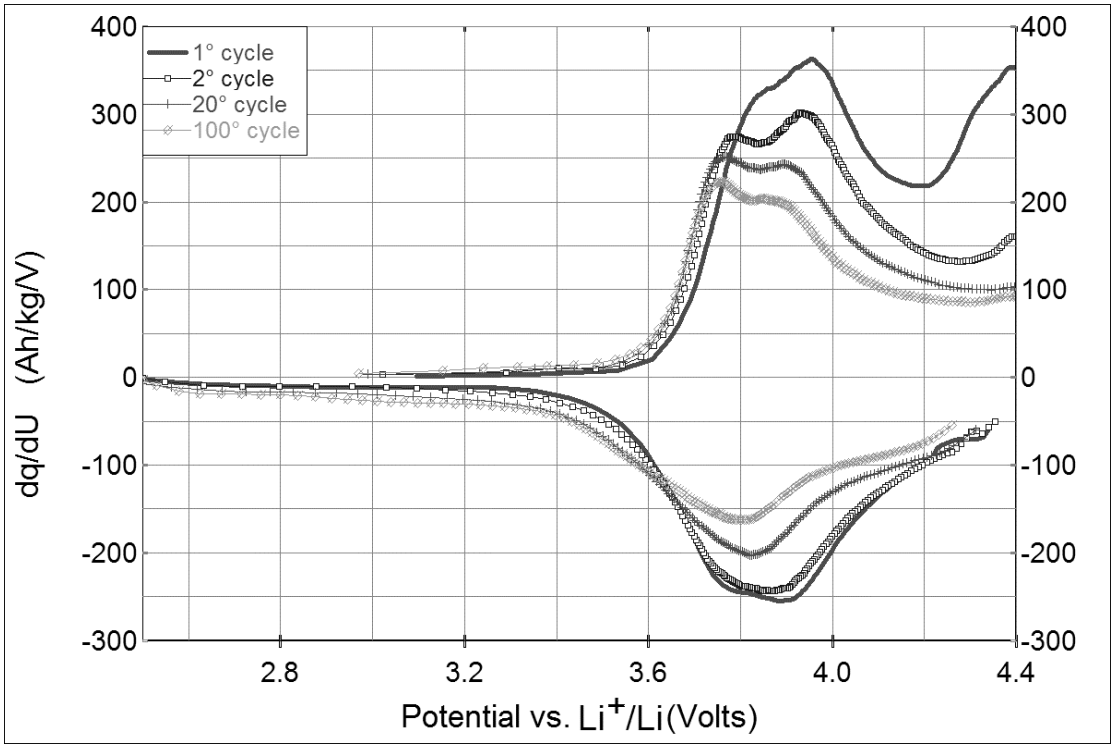

Figure 42: Differential capacity plots from galvanostatic cycles of LiMnNiAl-541Br-800°C. Taken at 10A/kg (2.5-4.4Volts).

[1] See section 13.3

Moreover, it can be found that the first cycle has one additional peak at about 4.4 Volts. In the second cycle, it can still be observed but strongly reduced. This phenomenon takes the major responsibility for the so-called "irreversible capacity" during first cycles. After *SEI* formation, the electrolyte becomes kinetically stable towards the oxide and no further electrolyte oxidation takes place. Other cycles do not seem to be affected. It is also remarkable that for all others cycles (following the second) the anodic processes start at the same potential and two anodic Li^+ de-insertion processes can be observed. The first anodic process identifies the first de-insertion site and is represented by the peak with its maximum at about 3.76V and the second at about 3.88V. During cycling, the magnitude of the second de-intercalation process tends to be smaller than the first one. The reduction of the magnitude of these peaks could indicate a gradual structural change of the oxide to a less ordered state, mainly due to a Jahn-Teller distortion of the manganese octahedra. While peak intensities ratio changing could be an effect of an incipient cationic disorder, due to the migration of ions (Mn and/or Ni and/or Al) towards the lithium site. In the latter case both effects are present.

In Figure 43, differential capacity plots of the 8^{ths} cycles of the galvanostatic measurements of the product synthesized at 800°C are shown.

We can better describe this plot dividing the products in two groups:

- **1th group**: LiMnNiAl541Br-800°C, LiMnNiAl972Br-800°C and LiMnNiAl891Br-800°C. A two step de-intercalation process characterizes these products, and they have a peculiar small potential difference between the maximum and the related minimum (ΔU_{an-cat}).
- **2nd group:** LiMnNiAl451Br-800°C, LiMnNiAl981Br-800°C, LiMnNiAl792Br-800°C and LiMnNiAl361Br-800°C; they show only one de-intercalation process peaks and reveal the peculiarity of having a larger ΔU_{an-cat} between the maximum and the related minimum.

ΔU_{an-cat} values are listed in Table 9.

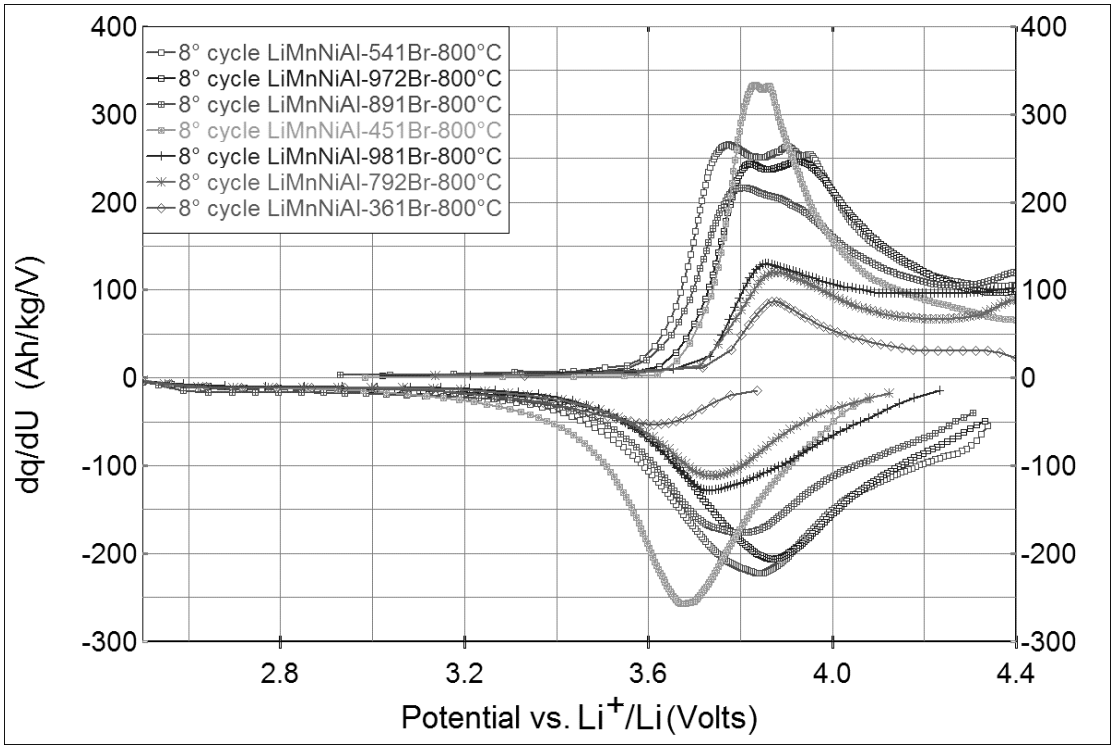

Figure 43: Differential capacity plots of the 8^{ths} cycles of the galvanostatic measurements at 10A/kg (2.5-4.4Volts) charge-discharge plots as shown in Figure 41.

Table 9: ΔU_{an-cat} related to the 8^{ths} galvanostatic cycles of the products synthesized at 800°C[1] (see Figure 43).

Product:	ΔU_{an-cat} (mV)
LiMnNiAl-541Br-800°C	5
LiMnNiAl-972Br-800°C	6
LiMnNiAl-891Br-800°C	57
LiMnNiAl-451Br-800°C	168
LiMnNiAl-981Br-800°C	124
LiMnNiAl-792Br-800°C	140
LiMnNiAl-361Br-800°C	270

[1] ΔU_{an-cat} values have been estimated from graphics, using the first derivative of the plotted curves. In case of multiple peaks, the average of the extremes was taken. The estimated error is about 10% of the measured value.

It is found that electrochemical performances and ΔU_{an-cat} are correlated. In particular, better cycling performance corresponds to lower ΔU_{an-cat}.

In Figure 44 the electrochemical performances of the products synthesized via wet synthesis with thermal treatment at 950°C is presented. $LiMn_{0.5}Ni_{0.4}Al_{0.1}O_2$ is also the best performer of this series. Unlike the series treated at 800°C, the difference between this and the other products is even more accentuated in terms of specific charge (see Figure 41). In Figure 45, a detail of the 8^{ths} cycles of the products is shown. Once again the 8^{ths} cycles were chosen to avoid the effect of electrolyte decomposition.

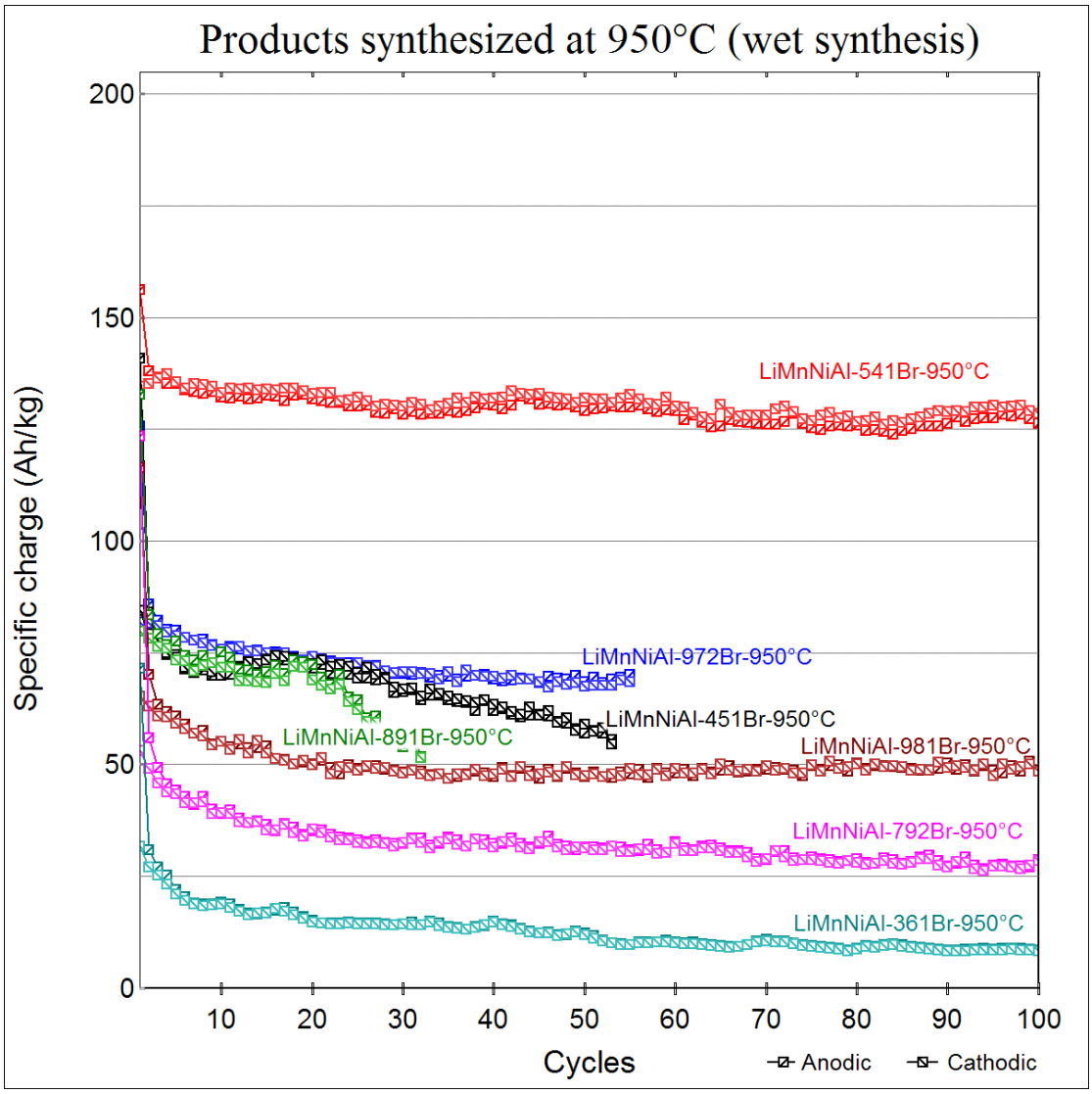

Figure 44: Galvanostatic cycles at 10A/kg (2.5-4.4Volts) of the products synthesized at 950°C (cf. Table 10).

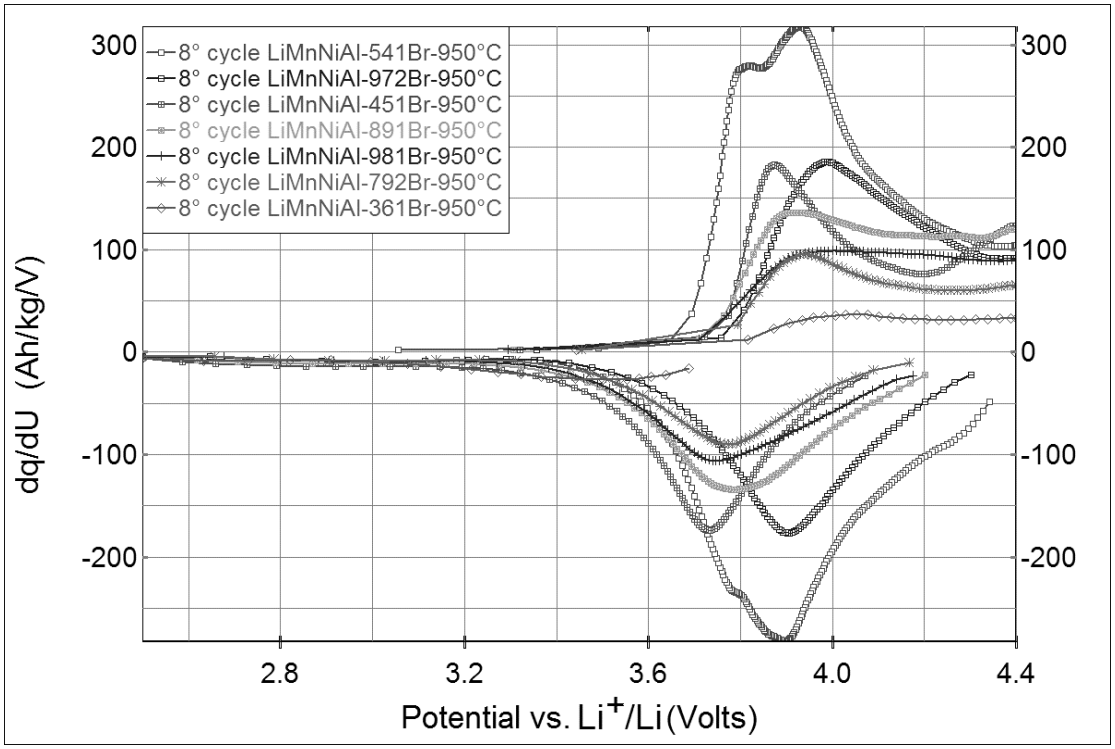

Figure 45: Differential capacity plots of the 8th cycles of the galvanostatic measurements at 10A/kg (2.5 - 4.4 Volts) charge-discharge plots shown in Figure 44.

In this product family, only LiMnNiAl-541Br-950°C is characterized by a two-step de-intercalation process, while the whole set of the remaining products shows only a one-step de-intercalation process.

Once more, the correspondence between good performance behavior and low ΔU_{an-cat} values of the products synthesized at 950°C is noticeable and summarized in Table 10:

Table 10: ΔU_{an-cat} related to the 8^{ths} galvanostatic cycles of the products synthesized at 950°C (Figure 45).

Product:	ΔU_{an-cat} (mV)
LiMnNiAl-541Br-950°C	30
LiMnNiAl-972Br-950°C	80
LiMnNiAl-451Br-950°C	143
LiMnNiAl-891Br-950°C	132
LiMnNiAl-981Br-950°C	150
LiMnNiAl-792Br-950°C	169
LiMnNiAl-361Br-950°C	579

In Figure 46, the cycling behavior of the best product is shown.

It is very interesting to compare this plot with the plot given in Figure 42, related to its same composition but treated at 800°C.

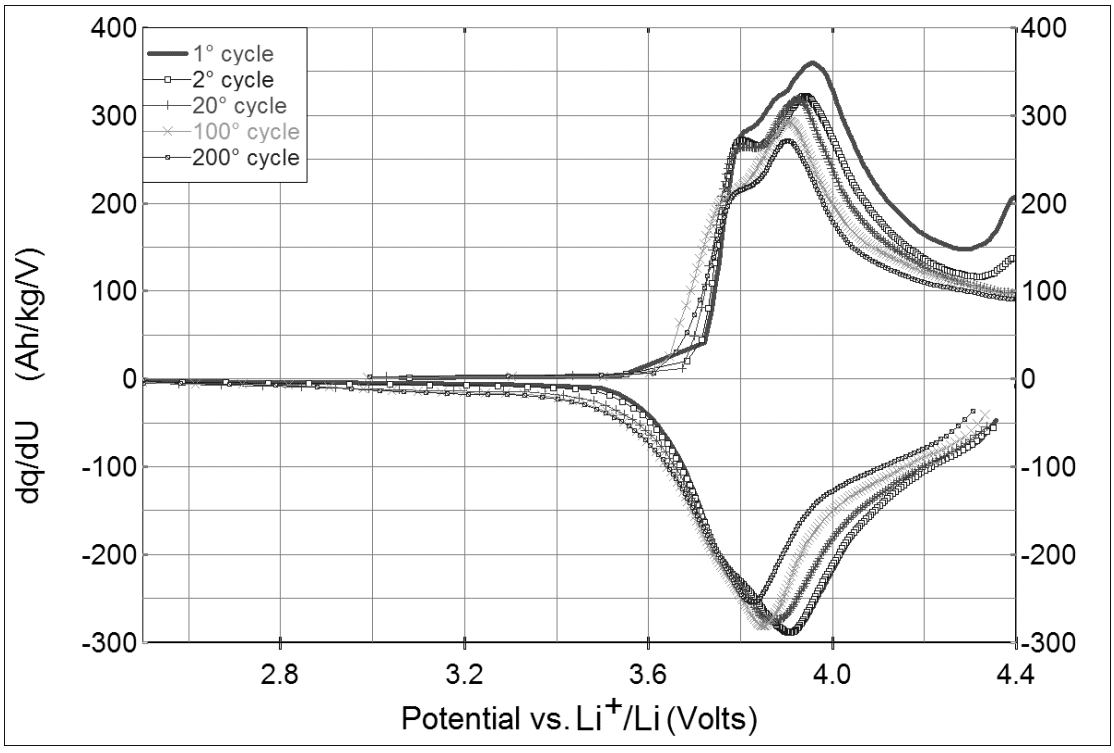

Figure 46: Differential capacity plots from galvanostatic cycles of LiMnNiAl-541Br-950°C, taken at 10A/kg (2.5 - 4.4 Volts).

From the comparison it is easy to observe that:

- In LiMnNiAl-541Br-950°C, peaks related to the two-step-de-intercalation process are better defined (sharper) and more shifted on the right in respect to LiMnNiAl-541Br-800°C.
- In LiMnNiAl-541Br-950°C, the second peak is higher than the first one also after 200 cycles (for LiMnNiAl-541Br-800°C, the second peak becomes smaller than the first one after only 20 cycles). That could mean that intercalation-deintercalation processes do not affect this structure seriously.

During cycling, the magnitude of both peaks tends to be smaller, but at least their magnitude ratio appears quite constant. This may be interpreted so that no cation disorder occurs here but that probably Jahn-Teller transitions destabilize the structure. Nevertheless the capacity fading is very small.

11.6 Conclusions

Several compounds have been synthesized with four of them fitting the superstructure hypothesis requirements. Thermal treatments have been carried out at 800°C (Figure 8) and 950°C (Figure 9 with ttt=950°C) .

The best two compounds have the composition $LiMn_{0.5}Ni_{0.4}Al_{0.1}O_2$. The one synthesized at 950°C gave better performances and maintains the ratio between peaks related to the two de-intercalation processes (shown in Figure 46).

In this product, the cation disorder is less accentuated; and although a charge fading probably due to the Jahn–Teller effect is still present, it is very small.

Chapter 12.

Investigations on $LiMn_aCo_bNi_cAl_dO_2$ compounds

In the previous chapters, several oxides containing manganese, nickel and aluminum were described with the aim to optimize the synthesis and to find the optimal composition for the use in Li-ion batteries.

This chapter is dedicated to a wider range of investigations of oxides containing additional cobalt and iron. It was the main target to increase the capacity and the cycling performances. Oxides treated in this chapter correspond to the formula $LiMn_aCo_bNi_cAl_dO_2$, (a+b+c+d =1).

12.1 Synthesis

In order to enhance the syntheses making them faster, they were carried out according to the *"dry synthesis"* method described in section 6.1.3. Since this kind of synthesis is intrinsically more delicate than the wet one (because homogeneity of the reagents more difficult to be obtained), several pre-investigations were necessary, in order to find the best procedure. In Figure 47, a check path for LiMnNiCoAl.335.495.160.010-950°C has been reported to verify the perfect success of the reactions.

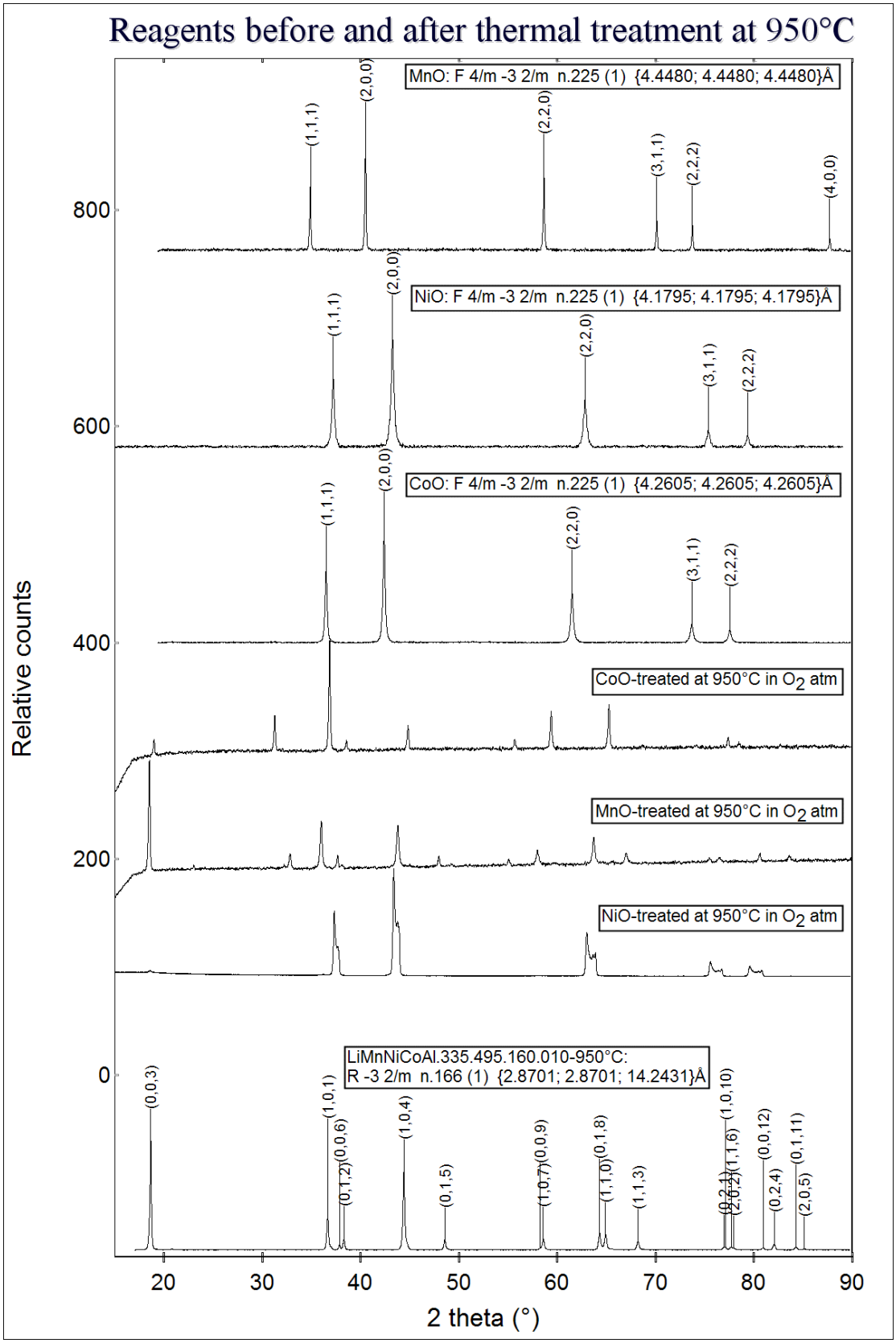

Figure 47: XRD powder patterns of "dry syntheses" products, before and after thermal treatment at 950°C compared with XRD powder pattern of LiMnNiCoAl.335.495.160.010-950°C.

The upper three patterns are related to the reagent used for the synthesis. The 4th, 5th and 6th pattern are related to the same reagents, after thermal treatment at 950°C. The last pattern represents the product. In the latter, no traces of reagents are present, confirming the proper procedure of the synthesis.

Thermal treatments for this series of compounds have been exclusively performed at 950°C (see section 6.1.4 and Figure 9 with ttt=950°C). New samples have been labeled according to the nomenclature described in section 6.1.1. Table 11 lists the products and their aliases:

Table 11: Products synthesized with the *"dry synthesis"* method.

Product	**Alias**	**M_r**[1]
$LiMn_{0.283}Ni_{0.566}Co_{0.141}Al_{0.01}O_2$	LiMnNiCoAl.283.566.141.010	96.29
$LiMn_{0.335}Ni_{0.495}Co_{0.160}Al_{0.01}O_2$	LiMnNiCoAl.335.495.160.010	96.10
$LiMn_{0.415}Ni_{0.160}Co_{0.415}Al_{0.01}O_2$	LiMnNiCoAl.415.160.415.010	95.86
$LiMn_{0.415}Ni_{0.415}Co_{0.160}Al_{0.01}O_2$	LiMnNiCoAl.415.415.160.010	95.80
$LiMn_{0.5}Ni_{0.4}Al_{0.1}O_2$	LiMnNiCoAl.500.400.100[2]	92.59
$LiFe_{0.415}Ni_{0.415}Co_{0.160}Al_{0.01}O_2$	LiFeNiCoAl.415.415.160.010	96.17

12.2 XRD characterization

As mentioned before, all products have been characterized by XRD (see section 6.2), which are shown in Figure 48. All patterns correspond to the desired layer structure (space group $R\bar{3}m$, no. 166). The reflection indexes denoted for the first pattern hold also to the patterns below, which are ordered by their decreasing specific charge. Wherever possible, an accurate fitting of the pattern to calculate cell parameter (see Table 12) was carried out.

[1] Molecular weights have been calculated with x=1 in Li_xMeO_2

[2] An analogous product has been described in a previous chapter, and was labelled as LiMnNi541-Br-950°C, but the synthesis procedure was different

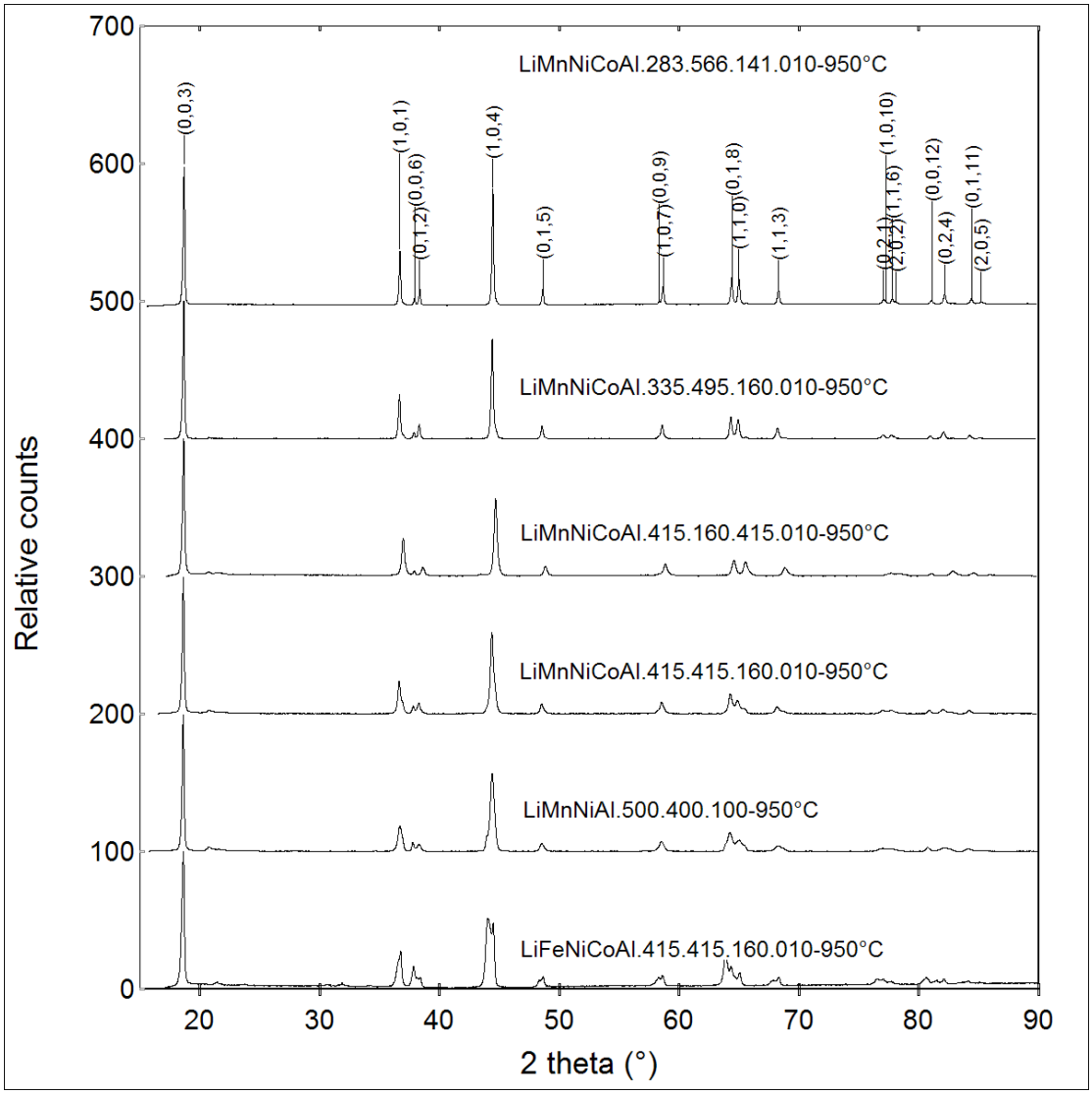

Figure 48: XRD on powders, all samples reveal the layered structure (space group R$\bar{3}$m, no.166). Patterns are ordered with decreasing specific charge (see Figure 51).

Table 12: Cell parameter vs. product composition.

Product	**%Mn**	**%Ni**	**%Co**	**%Al**	**Thermal treatment at 950°C**			
					a(Å)	***c(Å)***	***c/a***	***V(Å^3)***
LiMnNiCoAl.283.566.141.010	28.3%	56.6%	14.1%	1.0%	2.8673(3)	14.223(2)	4.960(1)	101.27(2)
LiMnNiCoAl.335.495.160.010	33.5%	49.5%	16.0%	1.0%	2.870(1)	14.240(1)	4.962(2)	101.58(5)
LiMnNiCoAl.415.160.415.010	41.5%	16.0%	41.5%	1.0%	2.847(1)	14.220(3)	4.995(3)	99.8(1)
LiMnNiCoAl.415.415.160.010	41.5%	41.5%	16.0%	1.0%	--	--	--	--
LiMnNiAl.500.400.100	50.0%	40.0%	0.0%	10.0%	2.866(4)	14.275(4)	4.98(1)	101.5(2)
Product	**%Fe**	**%Ni**	**%Co**	**%Al**	**Thermal treatment at 950°C**			
					a(Å)	***c(Å)***	***c/a***	***V(Å^3)***
LiFeNiCoAl.415.415.160.010	41.5%	41.5%	16.0%	1.0%	--	--	--	--

In Figure 49 the simulation pattern for a cell parameter calculation of LiMnNiCoAl.283.566.141.010-950°C is given. The plot reveals that the simulation curve fits the pattern closely. It includes a very critical zone in which it is also possible to appreciate the pattern's peaks constituent (plotted in gray). Finally, the magnitude of residuals, comparable with that of the noise magnitude, confirms the good fitting.

With the exception of LiMnNiCoAl.415.415.160.010-950°C and LiFeNiCoAl.415.415.160.010-950°C, which both are probably constituted of more than one phase, all other products show very pure one phase patterns. Their peaks are identified precisely and unambiguisly indexed. Thus we can deduce, that they are constituted of single phase materials. Unlike the products presented in the previous chapters, the patterns of this family show a higher $I_{(003)}/I_{(104)}$ ratio which indicates a strong cation order in the structure; the transition metals are preferably in the octahedral position and lithium in between those layers.

A remark is necessary about $LiMn_{0.5}Ni_{0.4}Al_{0.1}O_2$, which is synthesized via the *wet* and the *dry* routes (labeled LiMnNiAl-541Br-950°C and LiMnNiCoAl.500.400.100-950°C respectively). These compounds have the same composition, but exhibit a different XRD powder pattern (see Figure 50). Although both products have the same cell parameter, the main difference is their $I_{(0,0,3)}/I_{(1,0,4)}$ ratio. Thus, the product from the *dry* route shows a more ordered structure in terms of heavy cations placed prevalently in octahedral positions. Another difference arises from the presence of a small shoulder to the left of (1,0,4) peak and a small blow of the (1,1,0) peak in LiMnNiAl.500.400.100-950°C. It suggests the presence of another phase and/or an incomplete reaction. This could be due to imperfect reagent homogenization before thermal treatment.

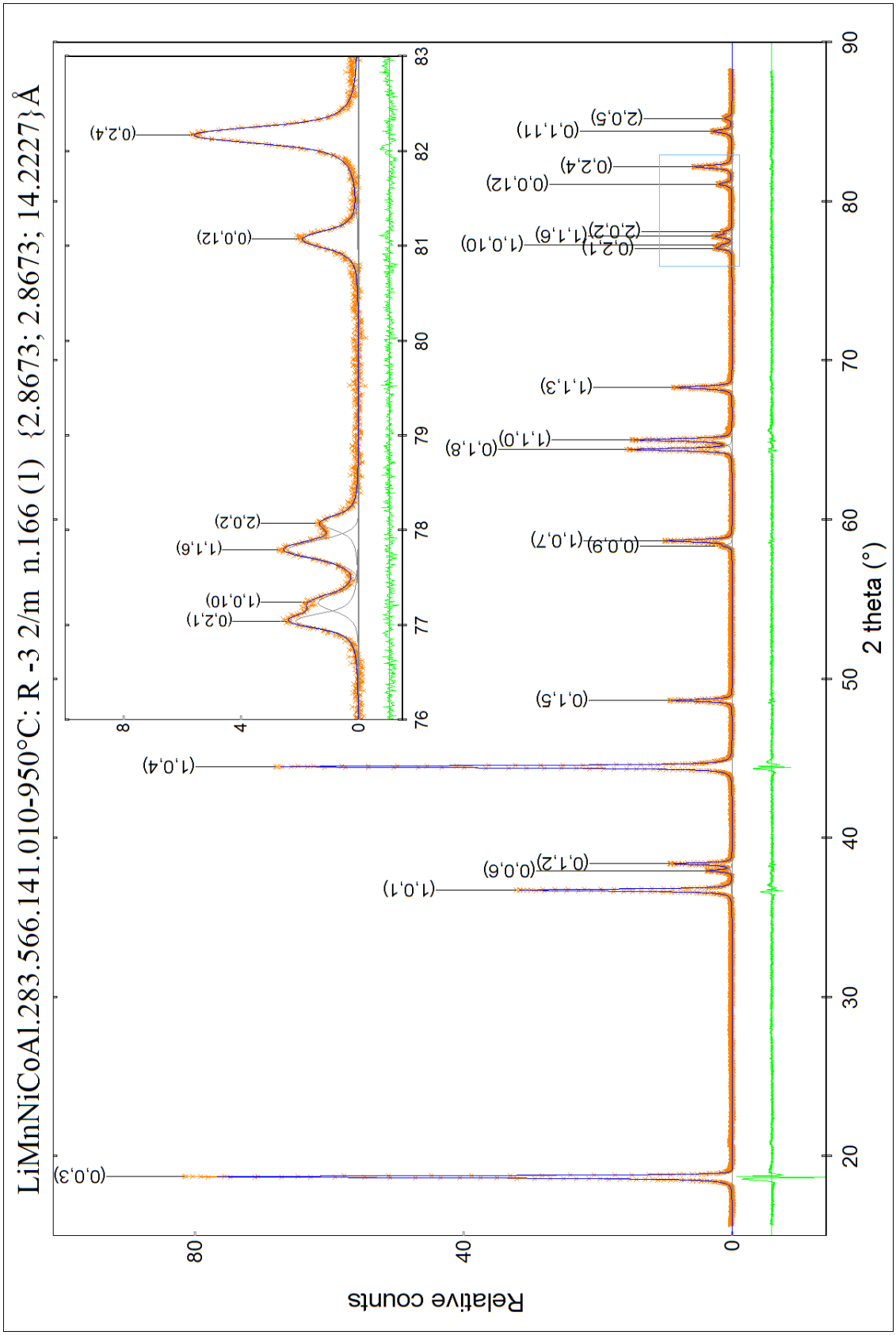

Figure 49: XRD pattern simulation for cell parameter calculation of LiMnNiCoAl.283.566.141.010-950°C. Inlay: enlarged detail from 76°<2θ<83°.

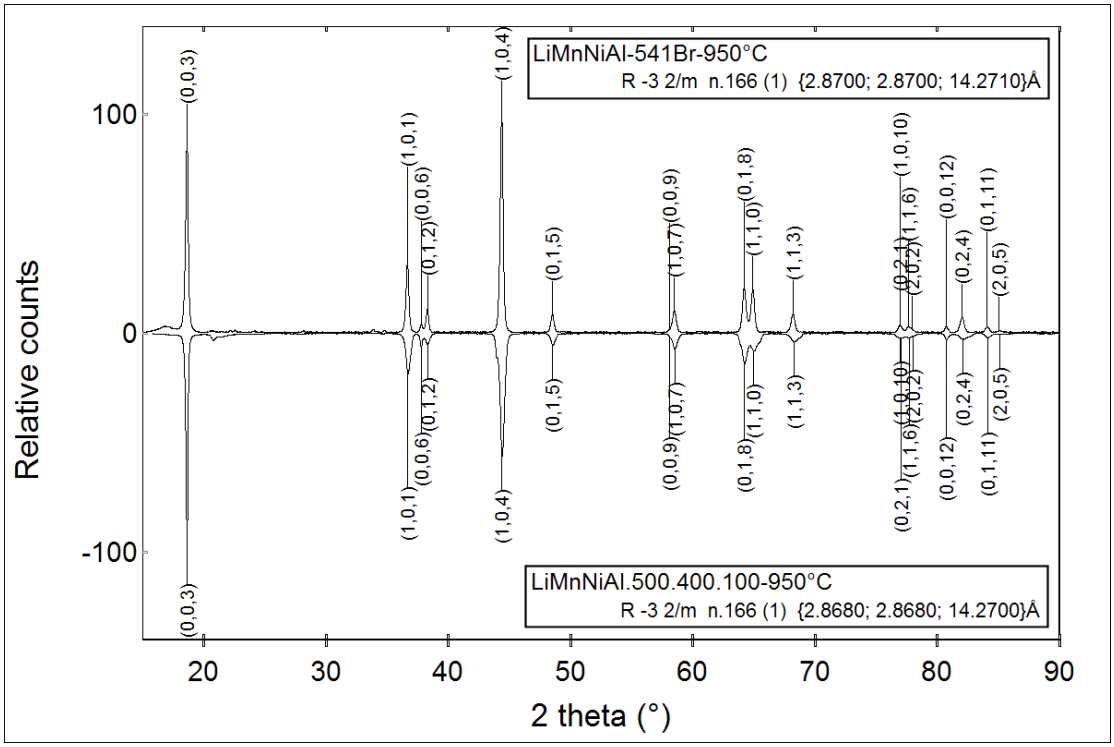

Figure 50: XRD powder patterns; comparison of two different synthesis products of $LiMn_{0.5}Ni_{0.4}Al_{0.1}O_2$.

12.3 Electrochemical characterization

Syntheses were performed in the following order:

1. **LiMnNiAl.500.400.100-950°C**: because it has the same composition as $LiMn_{0.5}Ni_{0.4}Al_{0.1}O_2$ presented in the previous chapter. It gave the best electrochemical performances and thus a different, eventually cheaper way of synthesis was targeted.
2. **LiMnNiCoAl.335.495.160.010-950°C, LiMnNiCoAl.415.160.415.010-950°C, LiMnNiCoAl.415.415.160.010-950°C**: starting with a composition close to our best material and addition of cobalt, because it is known that this enhances the electrochemical performance. Furthermore, to track the influences of the individual redox centers the molar ratios between heavy cations were to be exchanged.

After obtaining first results of the cycling performances (see Figure 51), a new composition has been calculated empirically keeping count of:

- the partial variation: $\frac{\partial q}{\partial [Mn]}$, $\frac{\partial q}{\partial [Ni]}$ and $\frac{\partial q}{\partial [Co]}$;
- the constraint should have a small integer ratio between cations.

The thus optimized result is the composition **LiMnNiCoAl.283.566.141.010-950°C**, with a ratio of cations Mn:Ni:Co = 2 : 4 : 1 (small integers). Aluminum has been kept as a minor dopand, because it is still supposed to stabilize the structure.

In Figure 51 the plot "specific charge vs. cycles" is shown. Two products: **LiMnNiCoAl.283.566.141.010-950°C** and **LiMnNiCoAl.335.495.160.010-950°C** gave surprisingly good performances, with excellent charge retain during cycles. **LiMnNiCoAl.415.160.415.010-950°C** delivered a discrete specific charge with virtually no fading during cycling. **LiMnNiAl500.400.100-950°C** gave 30% less capacity than its isostoichiometric analogous synthesized via the *wet* route (see section 12.2 for more detail).

The iron-based compound shown in Table 13 was the best electrochemical performer of a large series of iron-doped materials but nevertheless so poor that no further investigations on iron-doped compounds were carried out.

The specific charge plot of these products have been fitted by (eq. 33) presented in sect. 8.3. Good examples of some of these products are shown in Figure 83. The function fits are very good and in all plots only very small deviations σ_{Cap} (eq. 37) occur.

Once more it becomes evident that the high irreversible capacity affects the first cycle evaluable from the difference between charge and discharge values. In Figure 52, the charge-discharge series of LiMnNiCoAl.283.566.141.010-950°C is shown. The first cycle's anodic curve (charge) gives a specific charge slightly below 190 Ah/kg (marked with $\dot{1}$), which is much larger than the second cycle capacity (slightly below 170 Ah/kg), while the 1st and 2nd cycle cathodic curves are de facto identical (marked with 2).

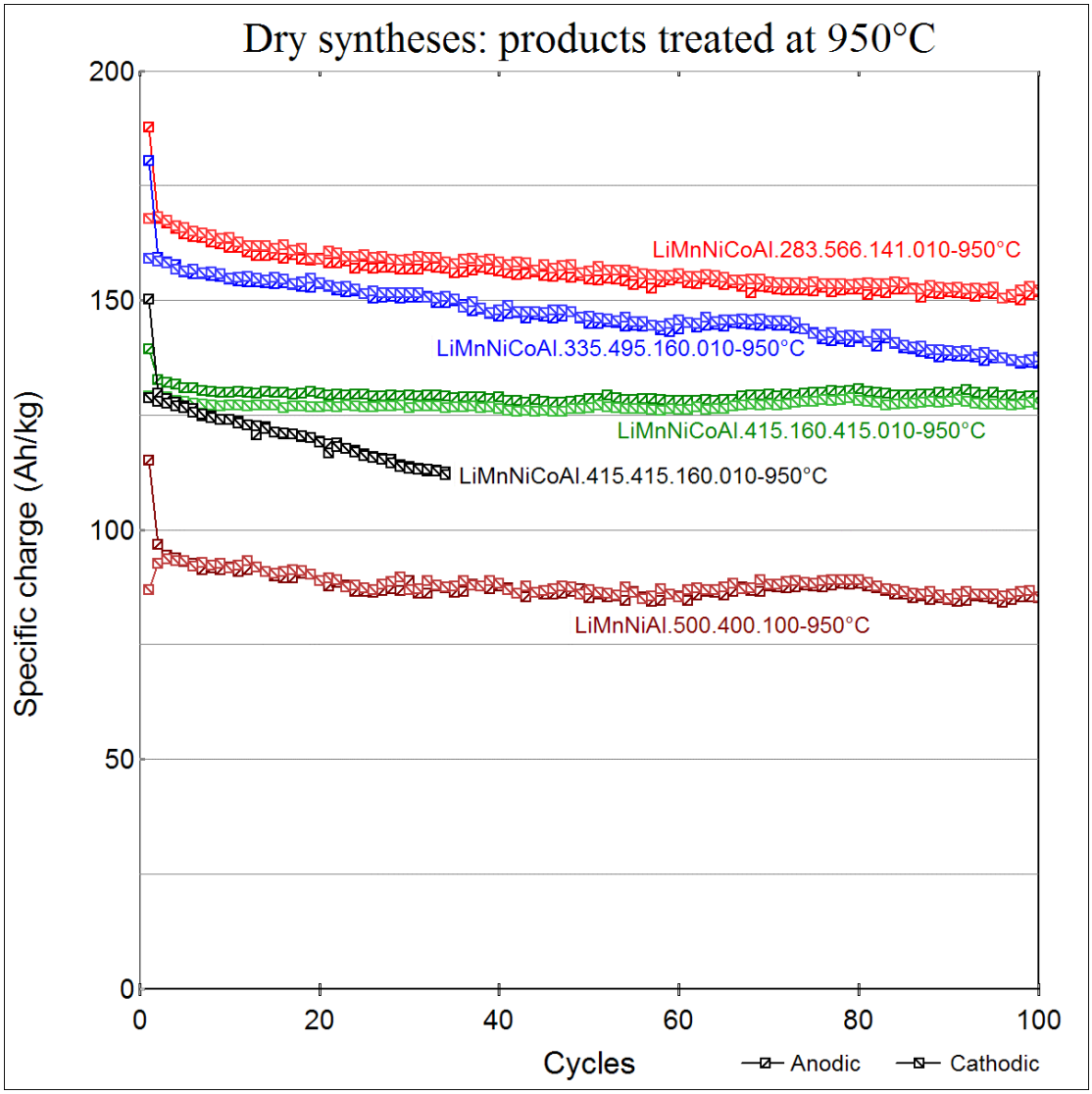

Figure 51: Specific charge plot from galvanostatic cycling at 10A/kg, taken in the range 2.5-4.4 Volts.

In Figure 52 a detail of the first cycles is marked 3. This peculiar gibbosity is common to all our oxides; a higher current density accentuates the gibbosity. This phenomenon could be attributed to the formation of the first Li-permeable electrolyte decomposition layer. Its formation requires an initial overvoltage, which is needed at the first cycle only. From Figure 52 we see that all further cycles have the same initial profile (region close the '3' mark). This phenomenon is very evident suggesting that, after incipient layer formation the voltage undergoes a small diminution even if lithium is forced to deintercalate the oxide. At the end, even after 128 cycles the specific charge is still over 150Ah/kg.

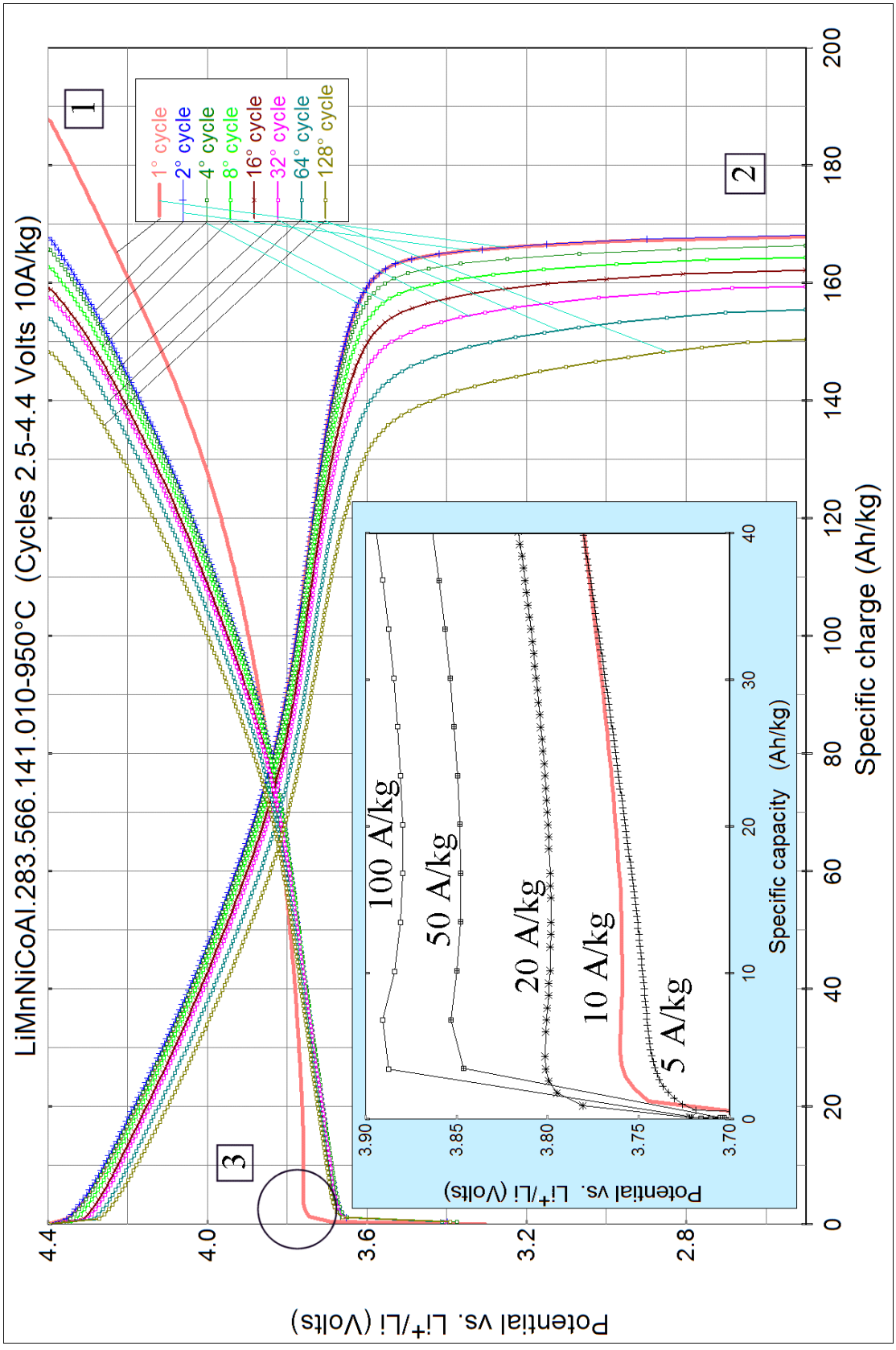

Figure 52: Galvanostatic cyclic performances of LiMnNiCoAl.283.566.141.010-950°C at 10A/kg (2.5 - 4.4 Volts). Insert: Detail of the first cycles at different specific currents.

In Figure 53, a differential capacity plot of the 8^{ths} cycles of the galvanostatic charge-discharge measurements as given in Figure 51 is shown. The 8th cycle was chosen because it is far enough from the first cycle and may still not be influenced by electrolyte decomposition.

The best two products of this series are LiMnNiCoAl.283.566.141.010-950°C and LiMnNiCoAl.335.495.160.010-950°C which show a well-defined two-step de-intercalation process, evidenced by two sharp peaks. Although the other products of this series still exhibit a two-step deintercalation process, their peaks are smaller, broader and shifted to high voltages of about 200mV. Peaks arising from these products are sharper and higher than those coming from wet synthesis (see Figure 45). This suggests a faster diffusion in a more ordered and mechanical stable structure. In Table 13 ΔU_{an-cat} of the new products are listed: correspondences of the increasing character of the specific charge ΔU_{an-cat} can be noted.

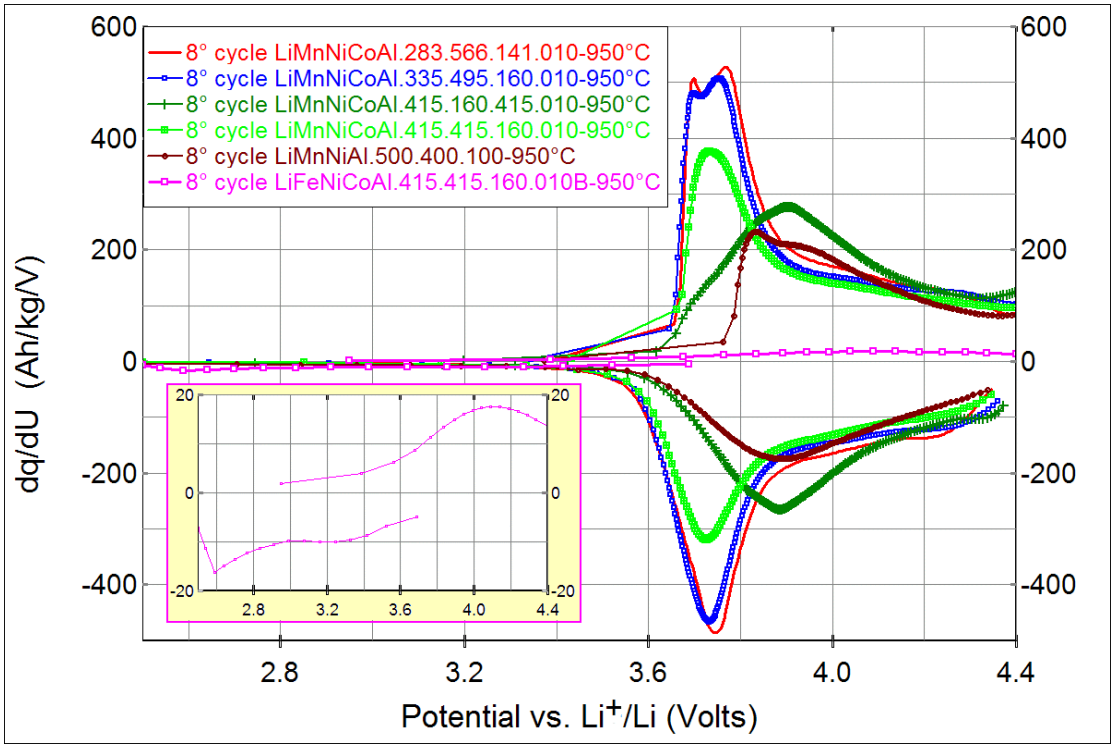

Figure 53: Differential capacity plots of the 8^{ths} cycles of the galvanostatic charge-discharge plot shown in Figure 51. Inside: enlarged detail of Fe-based compound.

Table 13: ΔU_{an-cat} related to the differential plot of 8^{ths} galvanostatic cycles (10A/kg 2.5 - 4.4 Volts) of the products displayed in Figure 53 synthesized at 950°C (*dry synthesis*).

Product:	ΔU_{an-cat} (mV)
LiMnNiCoAl.283.566.141.010-950°C	13
LiMnNiCoAl.335.495.160.010-950°C	7
LiMnNiCoAl.415.160.415.010-950°C	21
LiMnNiCoAl.415.415.160.010-950°C	25
LiMnNiAl.500.400.100-950°C	25
LiFeNiCoAl.415.415.160.010B-950°C	905

12.3.1 LiMnNiCoAl.283.566.141.010-950°C

With an initially available cathodic specific charge of about **170Ah/kg**, LiMnNiCoAl.283.566.141.010-950°C is our best performing product. In Figure 54 differential capacity plots of several galvanostatic cycles of the compound are given. These curves are the first derivatives of those plotted in Figure 52.

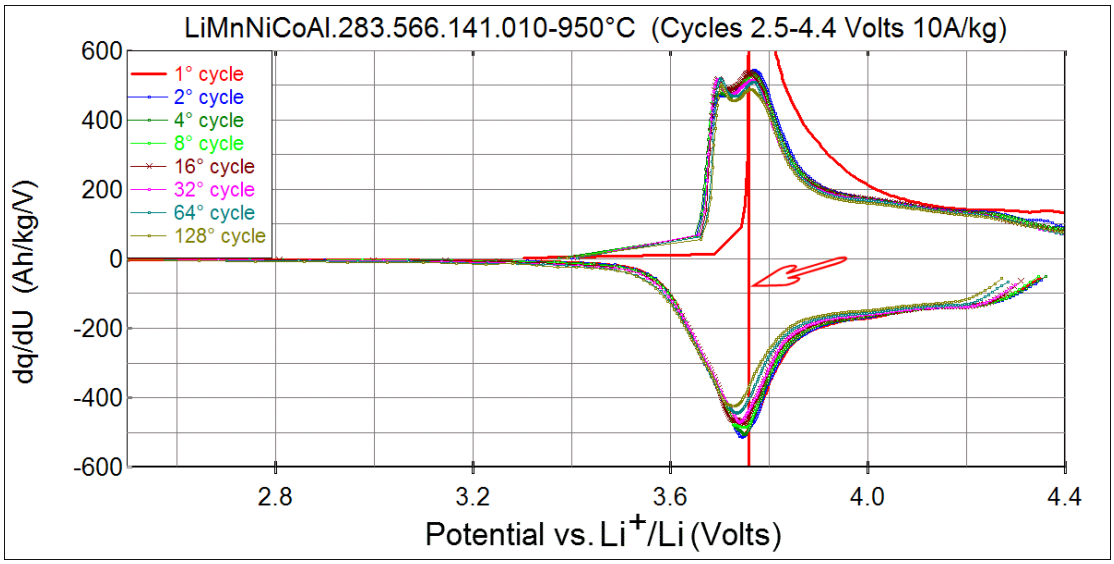

Figure 54: Differential capacity plots of the galvanostatic cycles 10A/kg (2.4 - 4.4 Volts) of LiMnNiCoAl.283.566.141.010-950°C.

The negative spike at the first cycle (arrow) derives from a circled gibbosity (3) of Figure 52.

In Figure 55, a selected voltage range between 3.6V and 3.9V is displayed because the electroactive potential range (3.65-3.85 V) is much better visible here in the context of the total scan. In this small range of

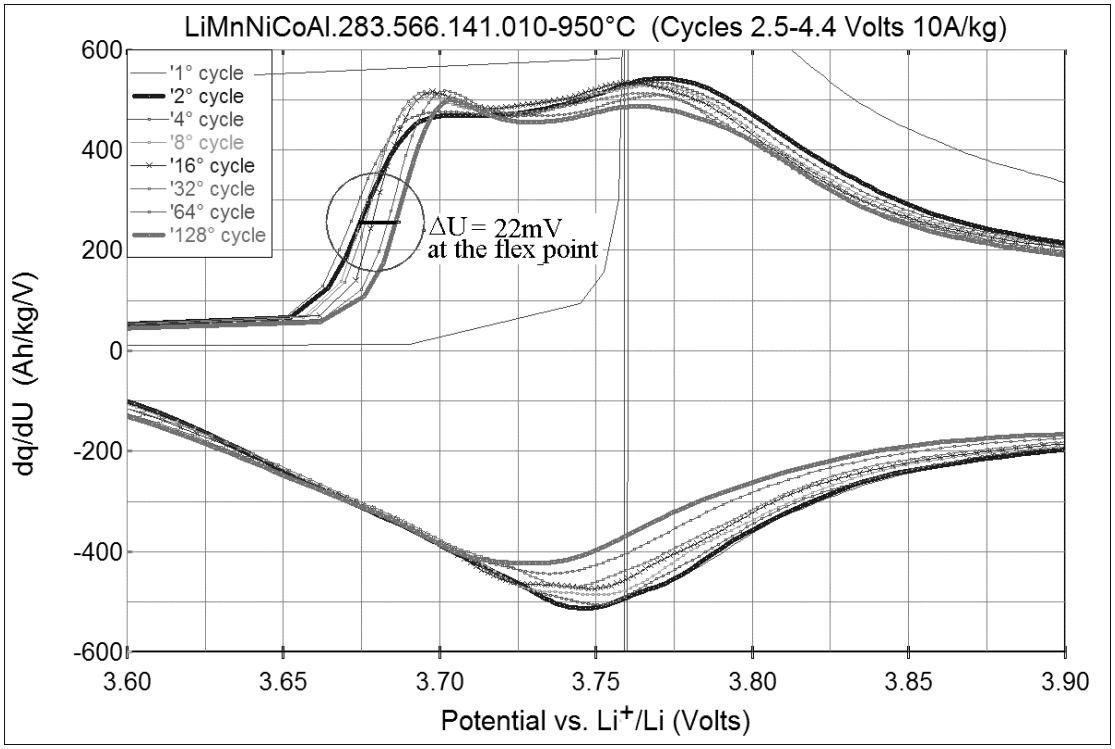

Figure 55: Enlarged region of Figure 54.

potential, the major part of charge is exchanged. The difference between the areas below the curves is small, passing from 170Ah/kg at the 2nd cycle to 150Ah/kg at the 128th cycle.

As already mentioned before, there are two different electroactive regions placed at 3.69 and 3.78 V (vs. $U_{Li^+/Li}$) respectively. The peak intensities of these two processes vary during cycling in a different way. The peak centered at 3.78V tends to become smaller and fading faster than the other one. Moreover, cycling moves the anodic peak position towards a higher potential (see circled detail in Figure 55) of about 22mV from the 2nd to the 128th cycle (measured at the flex point). Cathodic peaks are shifted towards a lower potential. This could be due to a progressive structure degradation, which

opposes a greater resistance to the lithium flux, thus translating it in an observable overpotential.

In Figure 52, overpotential shift at the first cycle at various specific currents has been shown. In Figure 56, differential capacity plots of such cycles are presented.

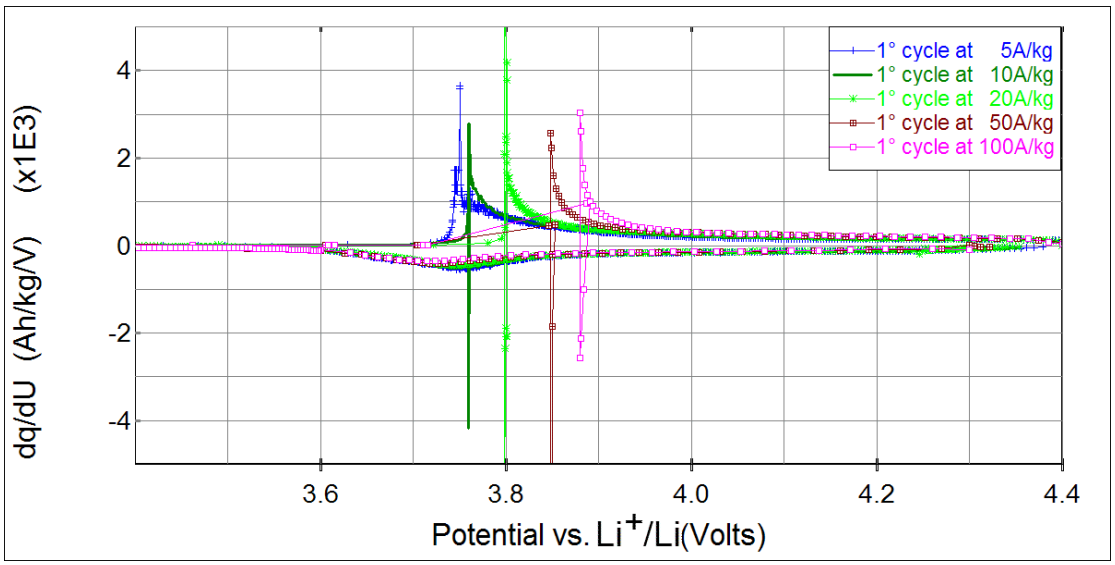

Figure 56: Differential capacity plot of the firsts cycles at various specific current of LiMnNiCoAl.283.566.141.010-950°C.

12.3.2 LiMnNiCoAl.335.495.160.010-950°C

With an initial available discharge capacity of about **160Ah/kg**, this is the second best performing compound of the investigated set. Most considerations made for LiMnNiCoAl.283.566.141.010-950°C are valid also here, therefore only the differences between these two compounds are discussed. In Figure 57, a differential capacity plot of galvanostatic cycling at 10A/kg (2.4-4.4Volts) of LiMnNiCoAl. 335.495.160.010-950°C is shown.

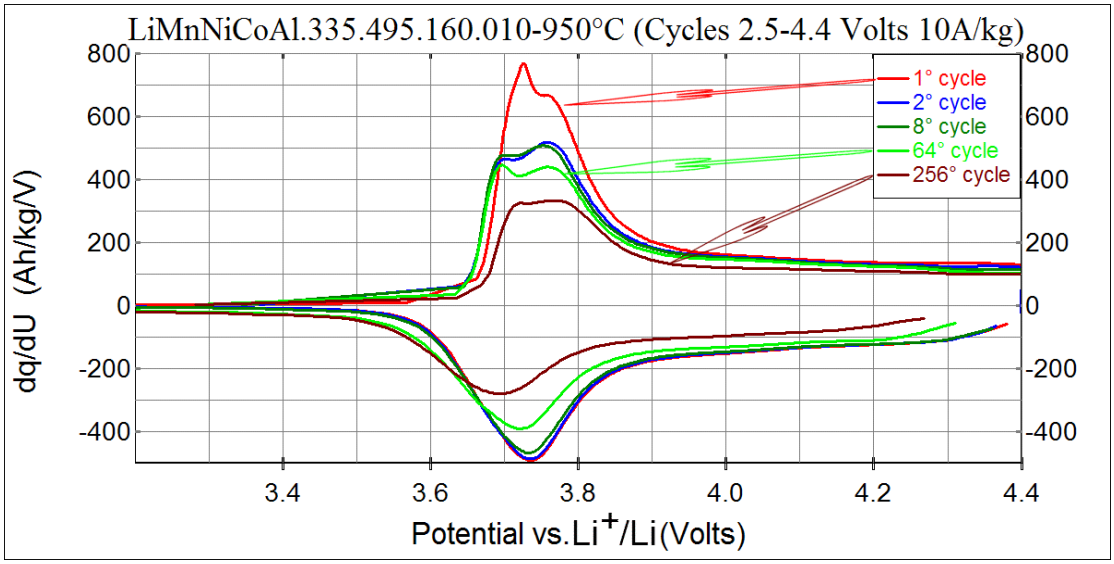

Figure 57: Differential capacity plots of galvanostatic cycling at 10A/kg (2.4-4.4Volts) of LiMnNiCoAl. 335.495.160.010-950°C.

The peak in the first cycle is clearly higher and more shifted to the right than the others, although less shifted than for the first cycle peak of LiMnNiCoAl.283.566.141.010-950°C. This could mean that the lithium permeable electrolyte decomposition layer formation requires less energy for LiMnNiCoAl.335.495.160.010-950°C. In Figure 58, two couples of cycles, at 2nd and at 128th, are compared. One observes a faster capacity fading for LiMnNiCoAl.335.495.160.010-950°C.

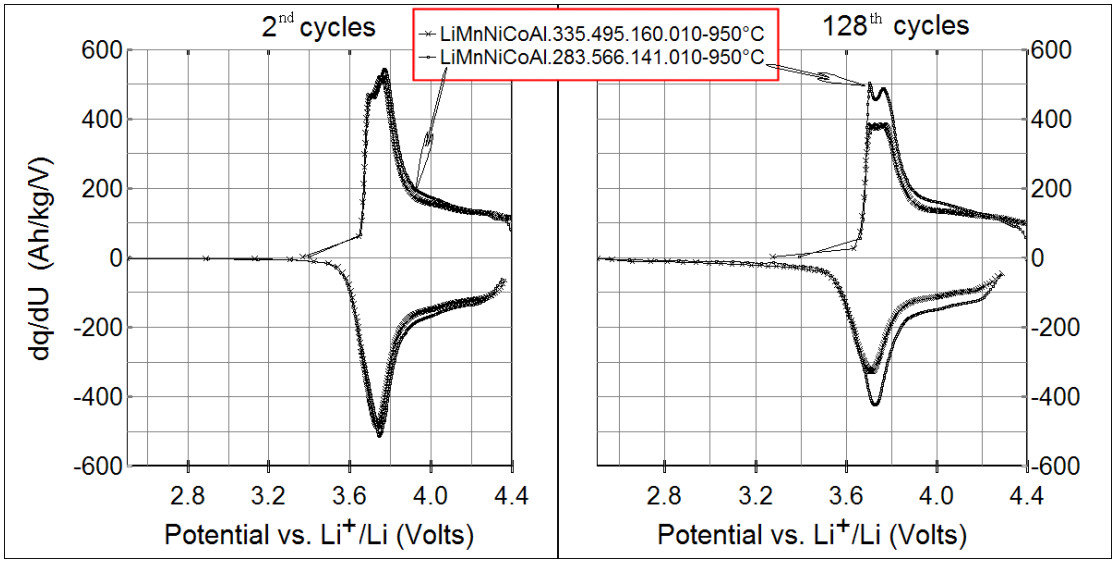

Figure 58: Differential capacity plots: comparison of galvanostatic cycling (10A/kg 2.5-4.4 Volts) between couples of cycles at 2nd and at 128th .

12.3.3 LiMnNiAl.500.400.100-950°C

A special note is given to this compound, because it was our older reference product, and has been synthesized via an alternative way. It would have been interesting to observe differences in performances which could have been traced back only to the way of synthesis. Thus, it will not be compared with the best products from *dry synthesis*, but with LiMnNiAl-541Br-950°C produced by *wet synthesis*. In Figure 59 the morphological differences between the two products taken by S.E.M. are shown. It can be noted that both samples exhibit the same morphological characteristics, but the crystallite size of LiMnNiAl.500.400.100-950°C appears 3-4 times larger (linearly). A comparison between Figure 44 and Figure 51 displays a direct view of the cycling behavior, while from Figure 60, a more detailed description of their cycling behavior can be taken. In particular, one sees that, although the products display clearly two anodic peaks, the main difference is the relative intensity they show.

It seems that in the dry synthesis product, although two electrochemical intercalation processes are still present, their associated sites are less available or alternatively, lithium diffusivity is decreased due to the presence of several phases.

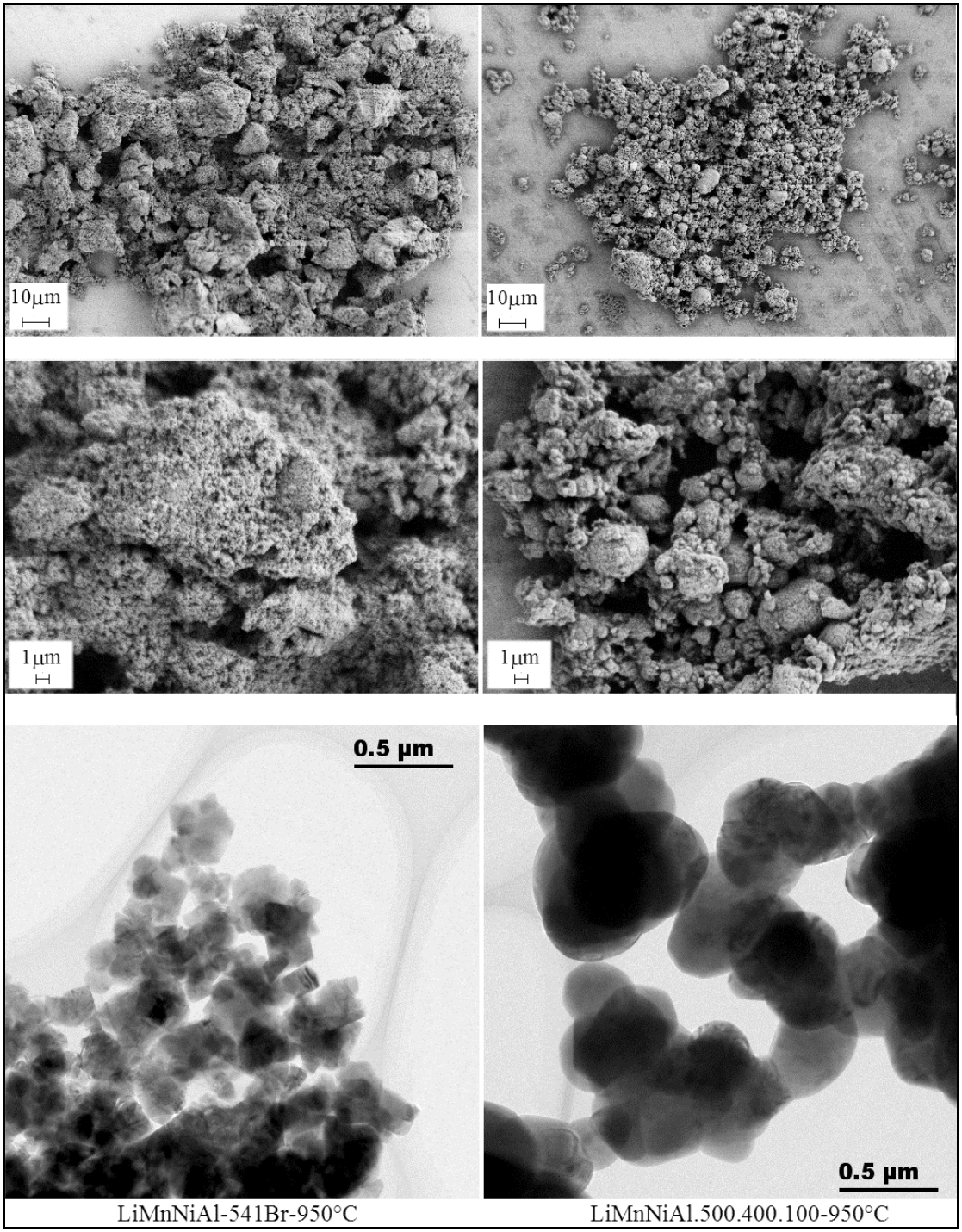

Figure 59: SEM and TEM images comparison between LiMnNiAl-541Br-950°C (on the left) and LiMnNiAl.500.400.100-950°C (on the right). The products have the same composition, but have been synthesized in different ways.

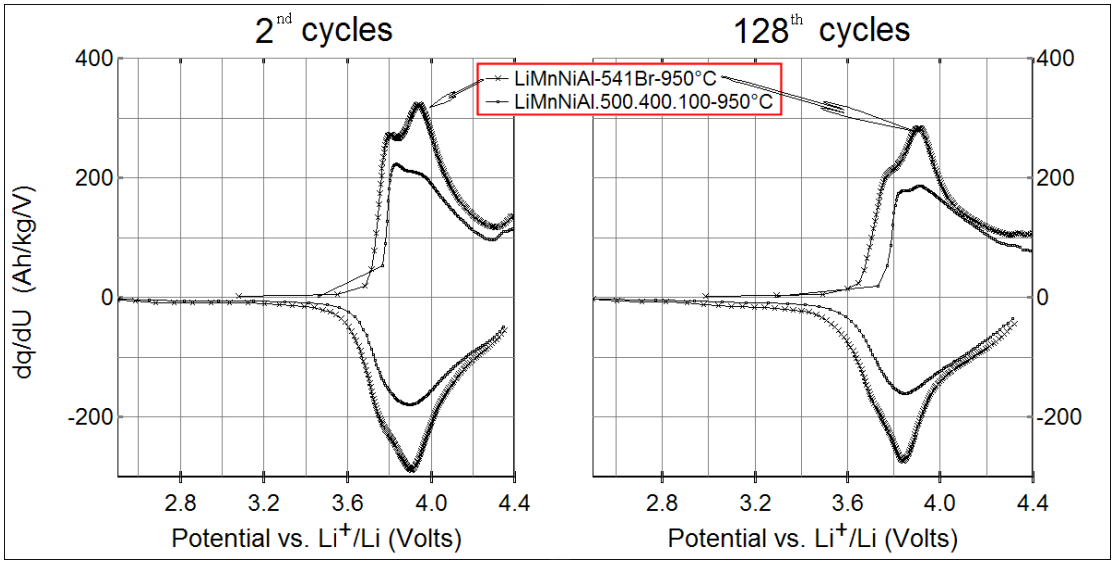

Figure 60: Differential capacity plots: comparison of galvanostatic cycleing (10A/kg 2.5-4.4 Volts) between couples of cycles at 2nd and at 128th .

The XRD powder patterns of the two products are compared in Figure 50. The XRD powder pattern of LiMnNiAl.500.400.100-950°C indicates that there is not pure phase.

12.4 Conclusions

Two new excellent compounds in terms of electrochemical performance have been obtained by optimizing the synthesis routes, i.e. making it faster and cheaper. The compounds in question are the optimized multicomponent single phase materials $\mathbf{LiMn_{0.283}Ni_{0.566}Co_{0.141}Al_{0.01}O_2}$ and $\mathbf{LiMn_{0.335}Ni_{0.495}Co_{0.160}Al_{0.01}O_2}$, both of which have the layered crystal structures of the α–$NaFeO_2$ type (space group $R\bar{3}m$ (no.166)). They show well-defined two-step intercalation and de-intercalation processes, respectively.

The products revealed at the first discharge **170** (0.6F/mole) and **160** Ah/kg respectively, with a capacity retention after 100 cycles of 91% and 86% respectively.

Chapter 13.

Further investigations on $LiMn_{0.283}Ni_{0.566}Co_{0.141}Al_{0.01}O_2$ and $LiMn_{0.335}Ni_{0.495}Co_{0.160}Al_{0.01}O_2$.

Since $LiMn_{0.283}Ni_{0.566}Co_{0.141}Al_{0.01}O_2$ and $LiMn_{0.335}Ni_{0.495}Co_{0.160}Al_{0.01}O_2$ turned out to be the best performing materials, further investigations were carried out in order to enhance their electrochemical properties. Most of the characterizations have been done simultaneously on both compounds, and thus will be discussed together.

13.1 Cycling in different galvanostatic conditions.

These tests have been carried out only on LiMnNiCoAl.283.566.141.010-950°C. To get better idea of the lithium exchanging capacity of our oxide, the data in **Figure 61** plotted against F/mole. It is noticeable that the stochiometry value reaches about 0.6 lithium equivalent exchanged pro mole of the oxide. The high specific charge of the product at 100A/kg (C/1.7) is remarkable, although its fading is rather high at this current.

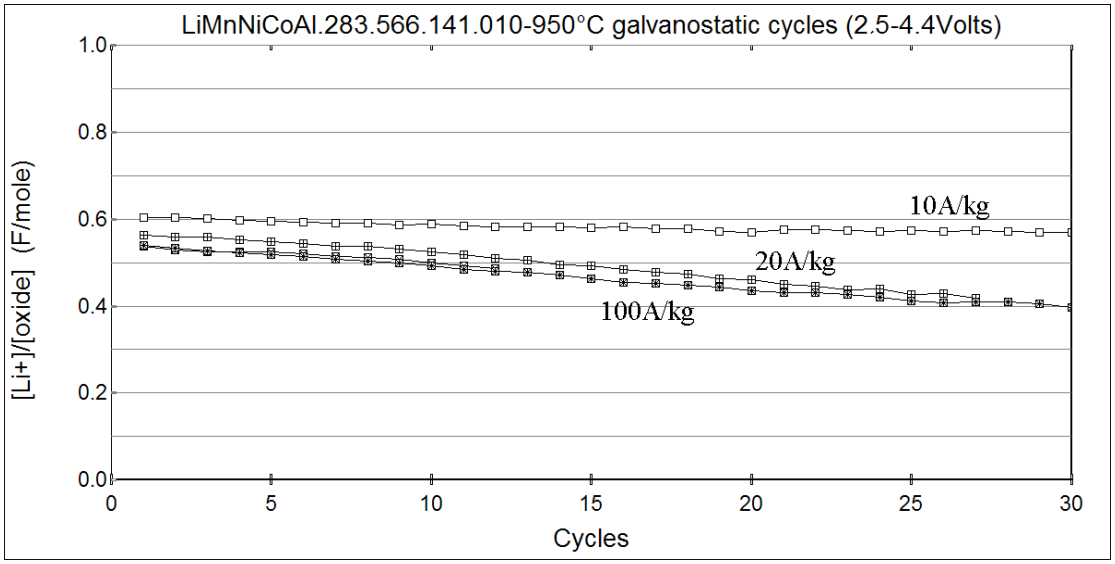

Figure 61: Discharge behaviour of LiMnNiCoAl.283.566.141.010-950°C from galvanostatic cycling carried at different current rates.

While the capacity fading (the slope of the curve) dramatically changes passing from 10A/kg to 20A/kg, it

remains rather unchanged in the range from 20A/kg to 100A/kg. Probably this is at higher current rates due to the intercalation process which then may be controlled mainly by lithium diffusion in the structure.

In other words: a higher current corresponds to a higher a_{Li^+} at the crystal surface, representing an obstacle for the incoming lithium to move from the crystal/solution *interface* towards the oxide bulk (intercalation process). Vice versa, when Li^+ is de-intercalated from the structure at higher currents than the diffusivity flux, the external oxide surface is completely depleted from lithium after a short time. At this point every current increase results in overpotential.

The experimental evidence for this is given in a differential capacity plot (Figure 62). Two de-intercalation processes give rise to defined peaks at low current rates (10A/kg), while at 20A/kg the peaks are hardly distinguishable, and at 100A/kg virtually only one peak is present. The overpotential effect is evident by this peak shifting.

Working with high current rates therefore means that the structure undergoes a regime of maximum lithium concentration gradient which may induce a rather strong stress for the crystal structure. An evidence for this conjecture is clearly

given by the anodic peak shift (Figure 62), passing from the 2nd over the 8th to the 27th cycle. While the peaks at 10A/kg are unchanged at different cycles, the ones related to higher current rates undergo dramatic changes.

This process, which shifts the anodic curve towards the right, makes part of the cycleable lithium de-facto not available, because it is partially out of the potential range we are working with. Capacity fading is then strictly correlated with lithium diffusivity. Increasing diffusivity corresponds to a reduction of charge fading. That is a reason why at higher temperatures the products exhibits a higher specific charge.

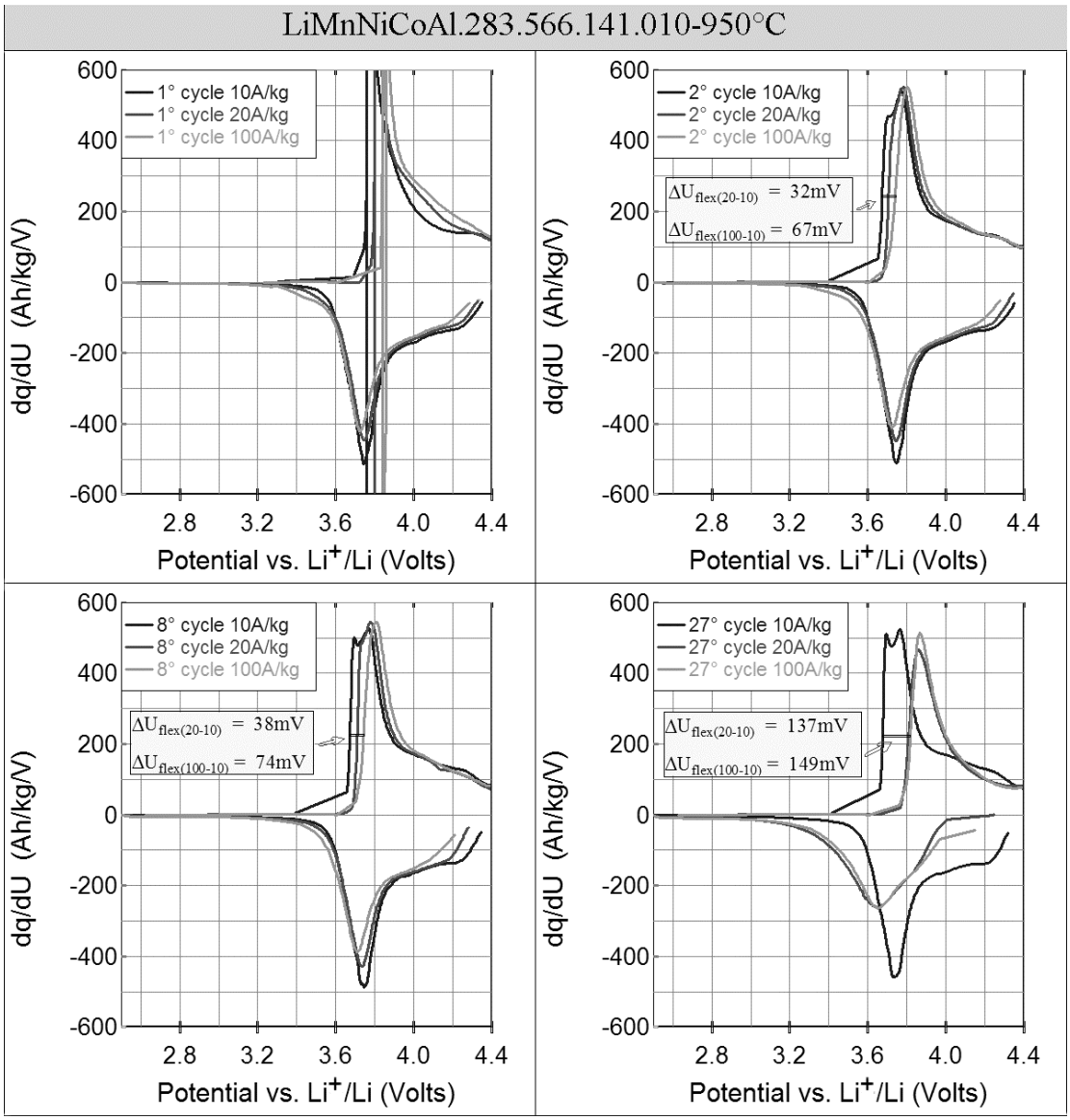

Figure 62: Differential capacity plots: comparison of several galvanostatic cycles taken at different current intensities.

13.2 Syntheses at different temperatures

In a further step of optimization, four new syntheses at 900°C and 1000°C of these very promising products have been performed. Syntheses have been carried out following the procedure given in section 6.1.3. Thermal treatment has been carried out following the path given in Figure 9 with ttt=900°C and 1000°. For the electrochemical performance tests, the samples have been prepared following the procedure described in section 7.3. In Table 14 products and their aliases are listed.

Table 14: Products and their aliases

Product formula	alias
$LiMn_{0.283}Ni_{0.566}Co_{0.141}Al_{0.01}O_2$	LiMnNiCoAl.283.566.141.010-900°C
	LiMnNiCoAl.283.566.141.010-1000°C
$LiMn_{0.335}Ni_{0.495}Co_{0.160}Al_{0.01}O_2$	LiMnNiCoAl.335.495.160.010-900°C
	LiMnNiCoAl.335.495.160.010-1000°C

In Figure 63, a comparison of the XRD powder patterns of $LiMn_{0.283}Ni_{0.566}Co_{0.141}Al_{0.01}O_2$ synthesized at different temperatures is given. The patterns of the products synthesized at 950°C and 1000°C are very similar, both in terms of cell parameter and in terms of peak ratio, while the one at 900°C seems to denounce an incomplete synthesis, evidenced by little shoulders at the right of (1,1,0) and (1,1,3) peaks (enlarged detail marked by arrows). Figure 64 shows the comparison of the XRD powder patterns of $LiMn_{0.335}Ni_{0.495}Co_{0.160}Al_{0.01}O_2$ synthesized at different temperatures. The two sets of compounds behave in the same way, but also in this case, for compounds synthesized at 900°C little shoulders at the right sides of the reflections (1,1,0) and (1,1,3) appear (enlarged detail marked by arrows).
Cell parameters of the new products are listed in Table 15. The parameters are so close to each other that not further interpretation is given.

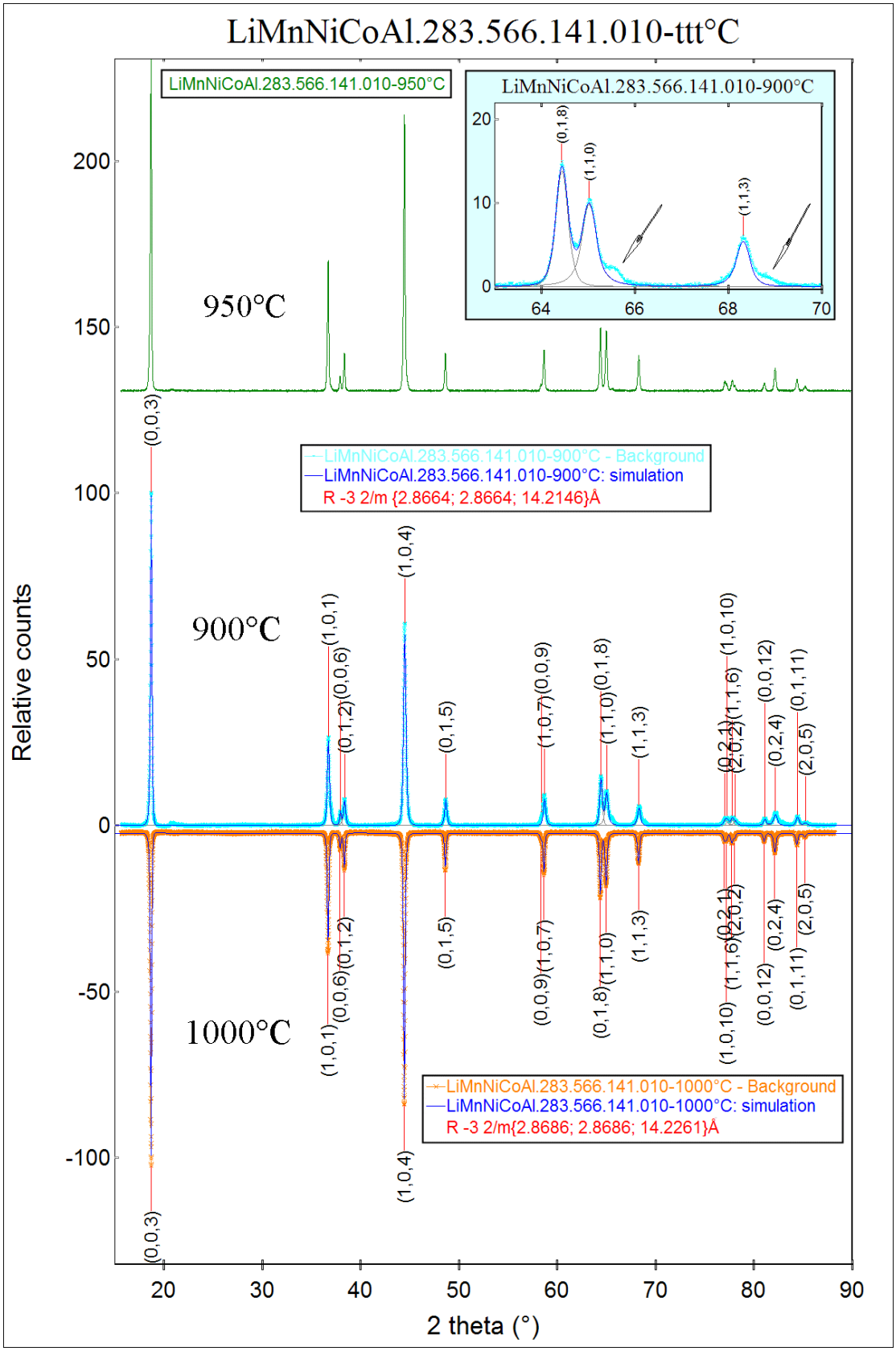

Figure 63: XRD powder pattern comparison of $LiMn_{0.283}Ni_{0.566}Co_{0.141}Al_{0.01}O_2$ synthesized at different temperatures. Inside: enhanced detail of the region between 63° and 70° of LiMnNiCoAl.283.566.141.010-900°C.

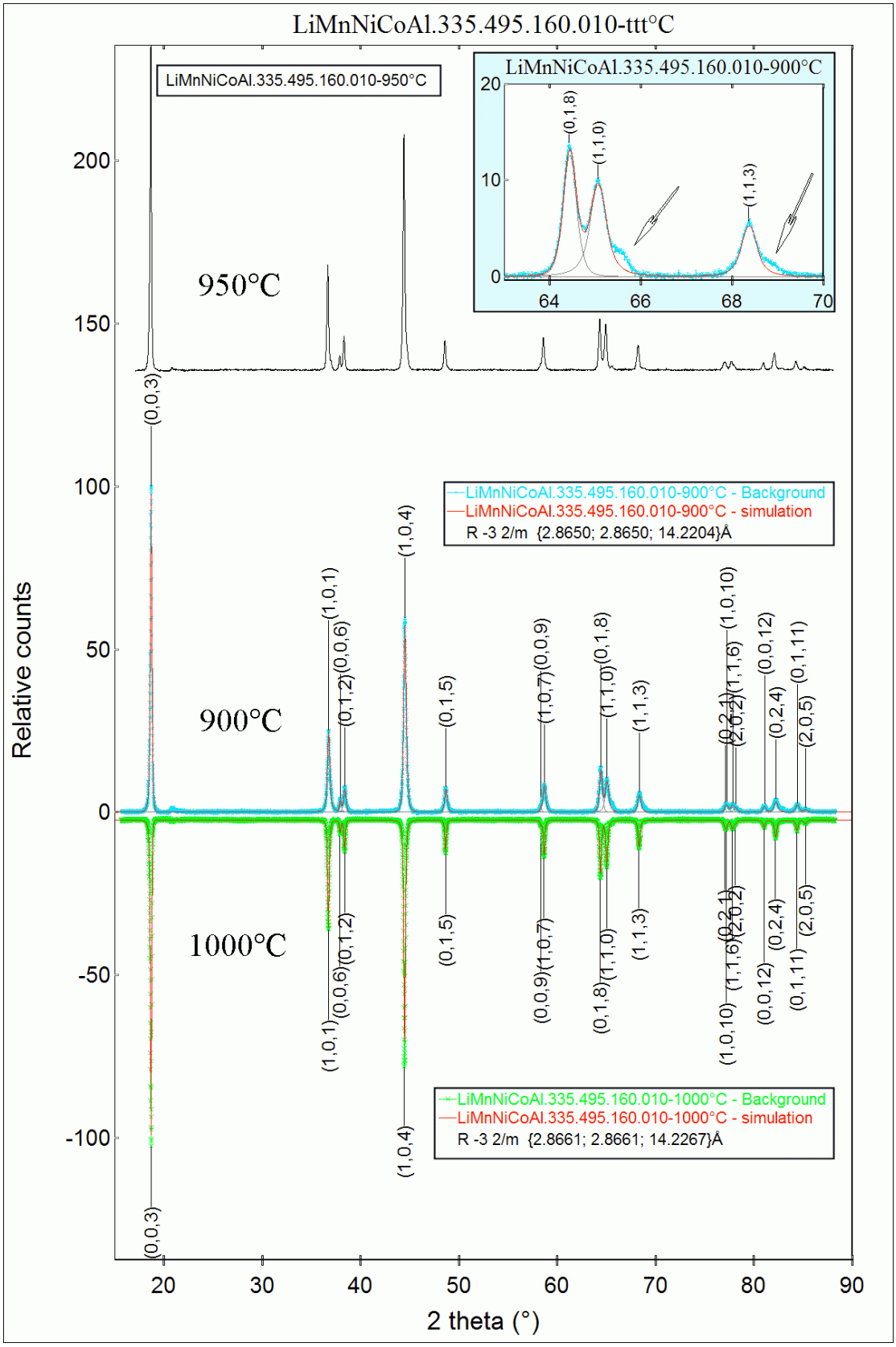

Figure 64: XRD powder patterns comparison of $LiMn_{0.335}Ni_{0.495}Co_{0.160}Al_{0.01}O_2$ synthesized at different temperatures. Inside: enhanced detail of the region between 63° and 70° of LiMnNiCoAl.335.495.160.010-900°C.

Table 15: Cell parameters of the new products *(reference products are evidenced)*.

Product	*a(Å)*	*c(Å)*	*c/a*	*V(Å^3)*
LiMnNiCoAl.283.566.141.010-900°C	2.8664(5)	14.215(2)	4.959(1)	101.15(3)
LiMnNiCoAl.283.566.141.010-950°C	2.8673(3)	14.223(2)	4.960(1)	101.27(2)
LiMnNiCoAl.283.566.141.010-1000°C	2.8686(3)	14.226(2)	4.959(1)	101.38(2)
LiMnNiCoAl.335.495.160.010-900°C	2.8650(5)	14.220(1)	4.963(1)	101.08(3)
LiMnNiCoAl.335.495.160.010-950°C	2.870(1)	14.240(1)	4.962(2)	101.58(5)
LiMnNiCoAl.335.495.160.010-1000°C	2.8660(2)	14.2267(6)	4.9640(5)	101.20(1)

Figure 65 and Figure 66 show the specific charge plots of galvanostatic cycles of the products synthesized at different temperatures. For both compositions the better performer is the one synthesized at 950°C. Figure 67 reveals details of the crystallite morphology of $LiMn_{0.283}Ni_{0.566}Co_{0.141}Al_{0.01}O_2$ and $LiMn_{0.335}Ni_{0.495}Co_{0.160}Al_{0.01}O_2$ synthesized at the two temperatures. As expected a higher temperature corresponds to larger crystallites. Crystallite dimensions in our experiments vary between 0.5 and 2µm.

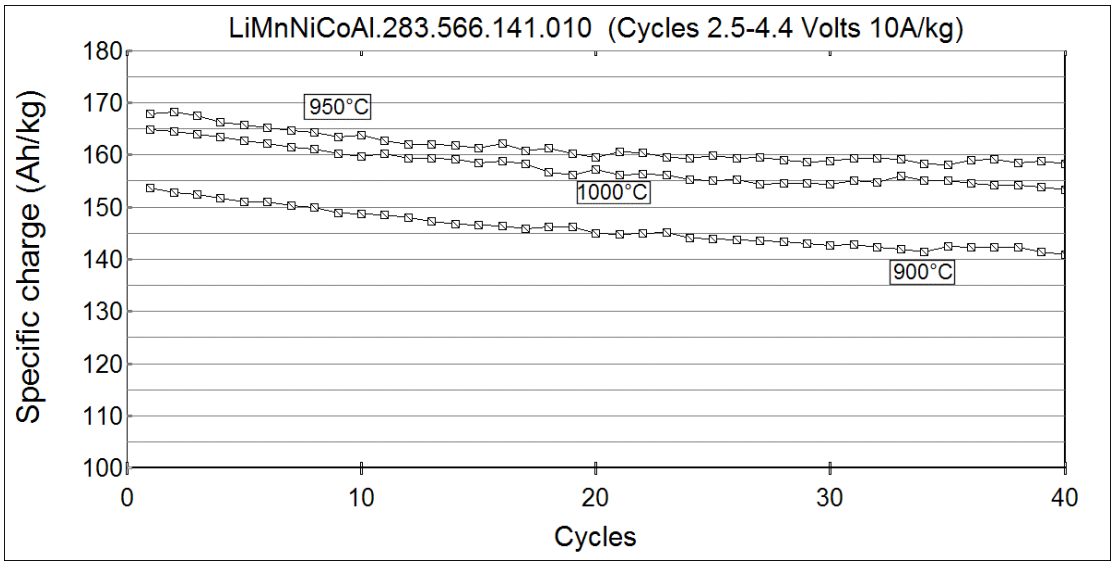

Figure 65: Specific charge plot from galvanostatic cycling experiments at 10A/kg (2.5-4.4Volts) of $LiMn_{0.283}Ni_{0.566}Co_{0.141}Al_{0.01}O_2$ synthesized at 900, 950, and 1000°C.

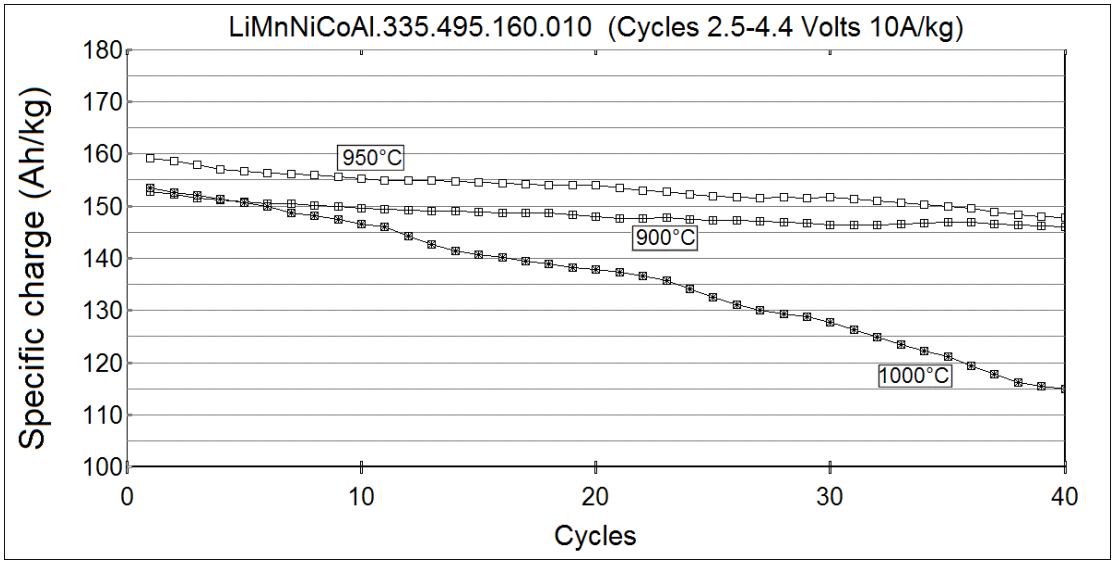

Figure 66: Specific charge plot from galvanostatic cycling of $LiMn_{0.335}Ni_{0.495}Co_{0.160}Al_{0.01}O_2$ synthesized at 900, 950, and 1000°C.

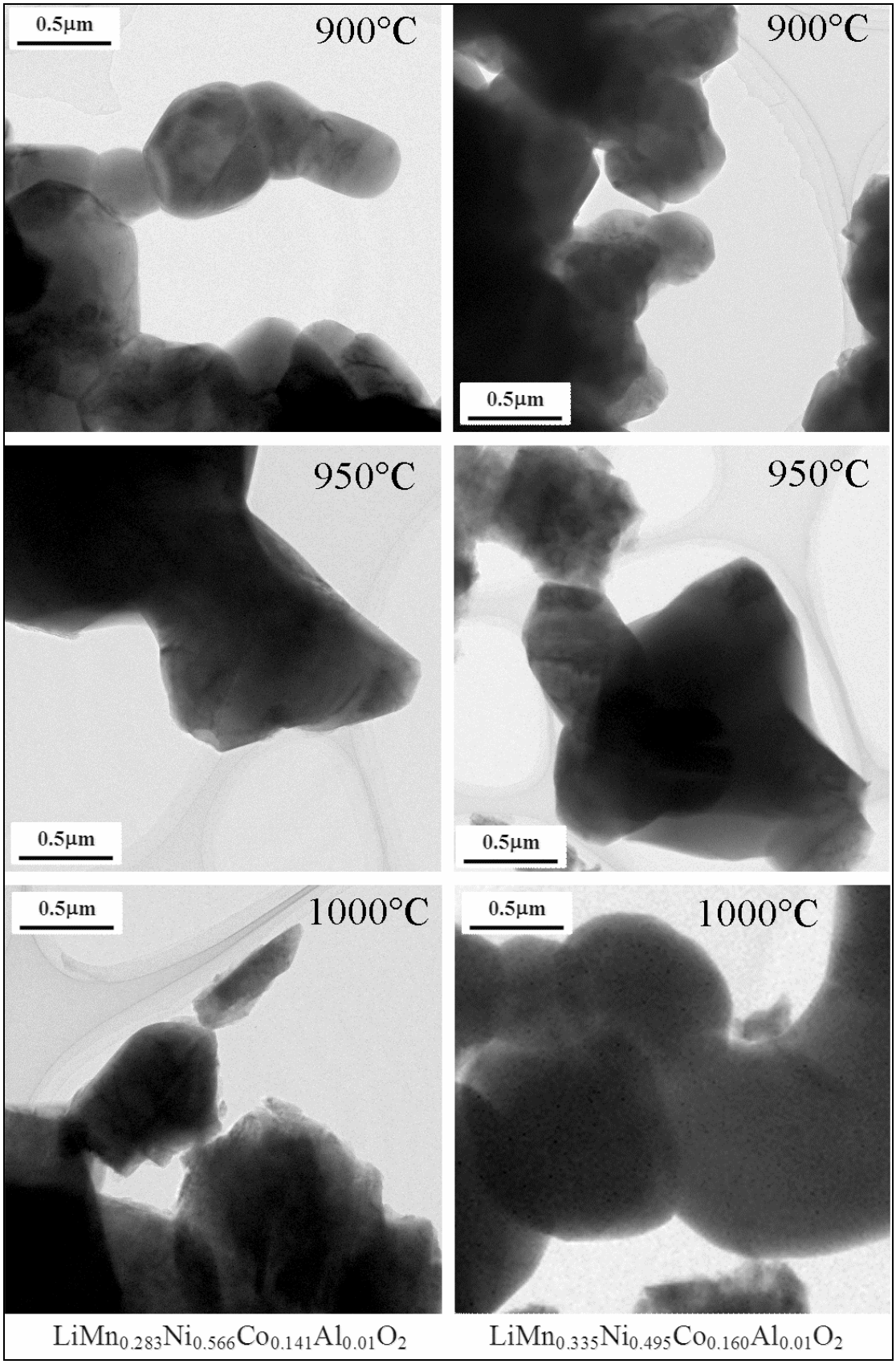

Figure 67: Details of the crystallite morphology of the compounds $LiMn_{0.283}Ni_{0.566}Co_{0.141}Al_{0.01}O_2$ and $LiMn_{0.335}Ni_{0.495}Co_{0.160}Al_{0.01}O_2$ synthesized at 900, 950, and 1000°C. Taken by TEM.

13.3 Irreversible capacity at the first cycle

So far, every product shows a high irreversible capacity at the first cycle. This exceeding charge furnished to the system during the anodic charge is expected to be mainly due to two processes:

- SEI formation.
- de-intercalation of parts of lithium, which cannot be reintercalated under the actual cycling conditions.

13.3.1 Experimental

An LiMnNiCoAl.283.566.141.010-950°C sample[1] has been treated for 173 cycles[2]. Then after a total discharge down to reach the equilibrium at O.C.V.=3.57 Volts, the sample has been cycled again under the same conditions.

In Figure 68 a specific charge plot of this sample can be seen. The first part (I part) shows the process during the first 173 cycles, and the second part (II part) demonstrates the behavior after the reintercalation process. The second part seems to be the exact continuation of the first, with the exception of the first anodic cycle part (see arrow) in which it is evident that a loss of 13Ah/kg of lithium[3] occurs. Circles mark the exceeding anodic capacity at the first cycles in Figure 68.

While, The "*second cycling"* differential capacity plot of the firsts cycles (II part) are compared with the "*first cycling"* differential capacity plot (I part) in Figure 69. On the right side, the right shift of the peak potential is not present anymore because the SEI has already been formed (zone inside the circle).

The area representing the non-reintercalable lithium portion of 13.4Ah/kg, is still present and visible in the difference between the first and second peak anodic hemicycles (see arrow). It can be concluded that also in the first cycle

[1] Sample has been assembled following the procedure described in section 7.3.

[2] Galvanostatic cycles at 10A/kg (2.5-4.4Volts).

[3] Given by the difference between anodic and cathodic specific charge.

(on the left side) the area represents not only SEI formation, but also the non-reintercalable portion of the lithium.

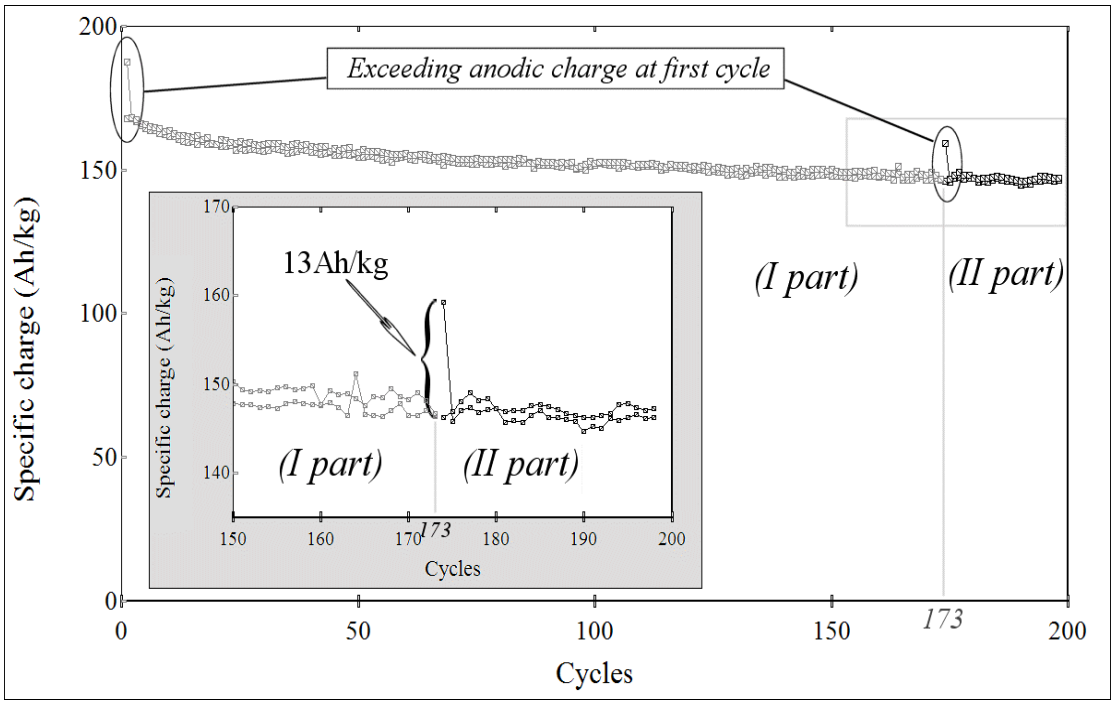

Figure 68: LiMnNiCoAl.283.566.141.010-950°C specific charge plots. (I part): the first 173 cycles. (II part): further cycles after Li^+ reintercalation down to 3.57Volts.

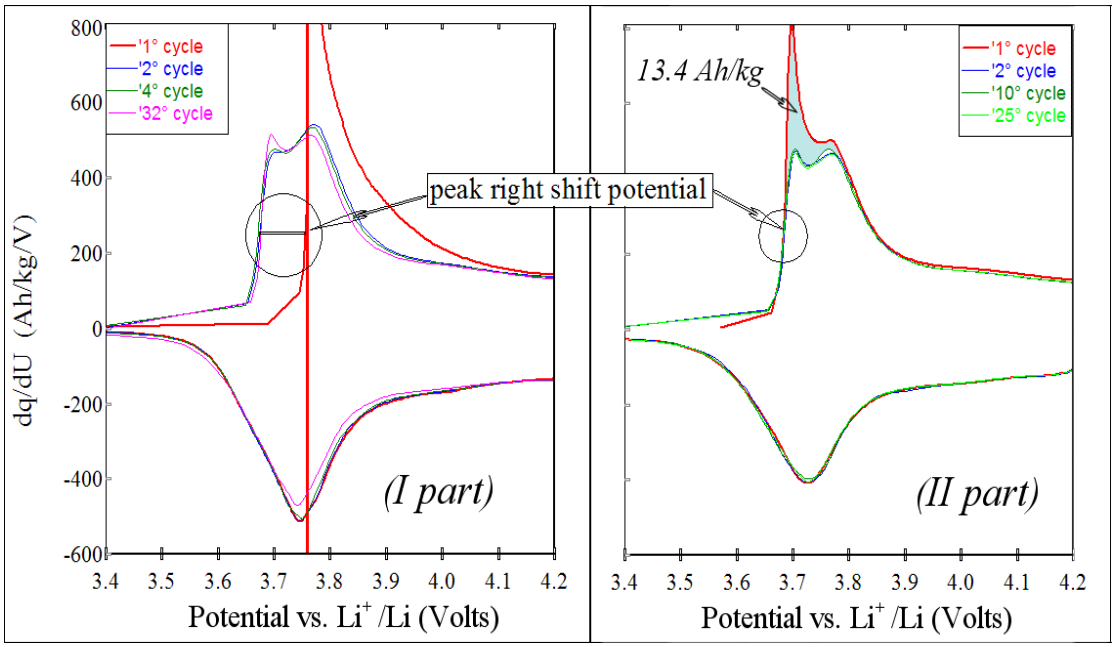

Figure 69: LiMnNiCoAl.283.566.141.010-950°C differential capacity plots. Left side: measurements during the first 173 cycles. Right side: data for further cycles after Li^+ reintercalation down to 3.57 Volts.

A possible explanation is that close to the point where the structure is intercalated completely, lithium diffusivity drops down to a level, which does not allow for further uptake, before the electronic system reverses the current. This could be due to a complete blocking of all the peripheral sites by Li^+ but not of the innermost ones.

13.3.2 Conclusions

The great part of the so-called "irreversible capacity" is explained by the prevention of reintercalation of parts of the lithium during cycling. However, it has been demonstrated that it is possible to reintercalate also this part of lithium by suitable modification of cycling conditions. Therefore this Li-loss should not be termed *"irreversible capacity"* but a kind of *"not usable capacity"*, depending on the experimental conditions[1].

[1] In slower cycling (<10A/kg) or deeper cycling (<2.5Volts) or higher temperature cycling (>R.T., in which the lithium diffusion is faster) conditions, the *"not usable capacity"* can be reduced.

13.4 Coulometric titration of LiMnNiCoAl.283.566.141.010-950°C

In Figure 70, a coulometric titration on LiMnNiCoAl.283.566.141.010-950°C sample is shown.

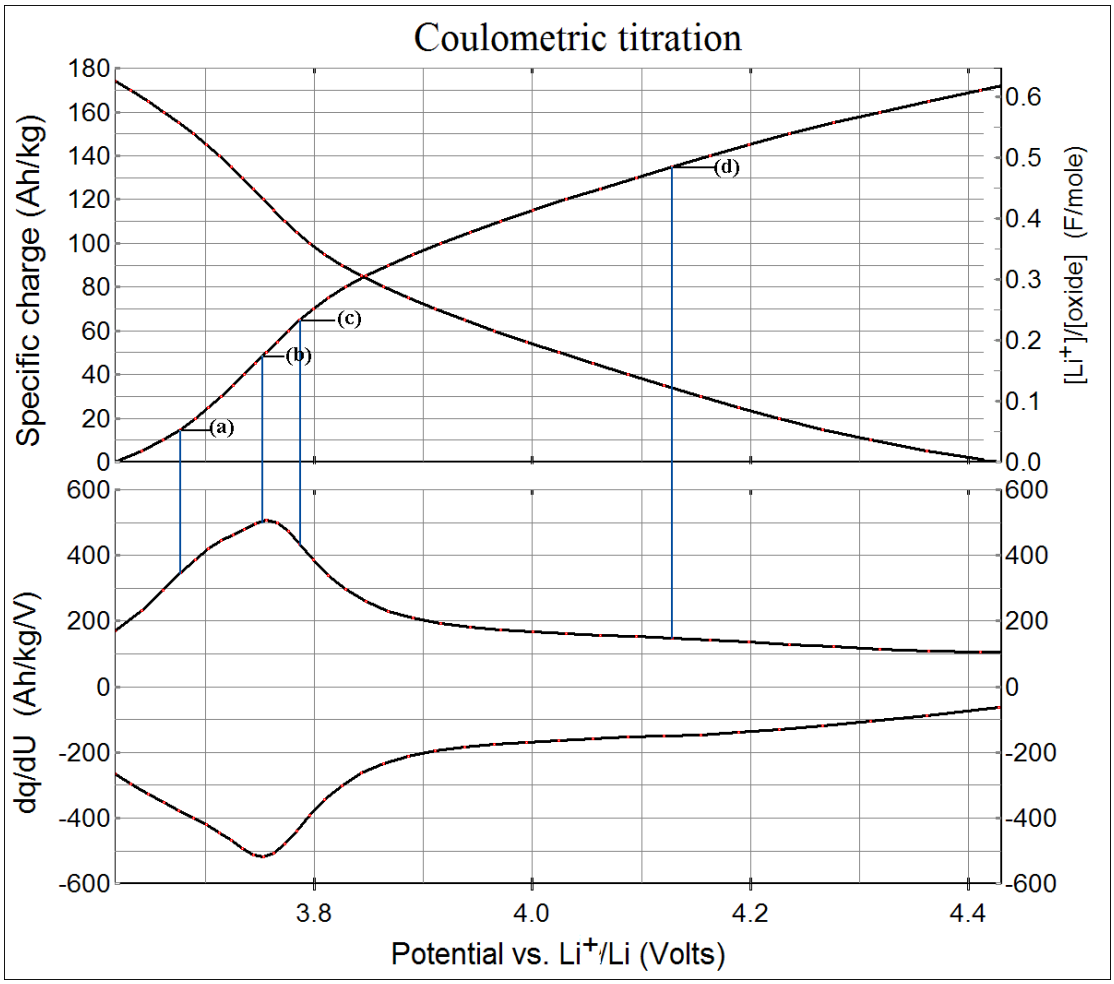

Figure 70: Coulometric titration of LiMnNiCoAl.283.566.141.010-950°C taken after 3 galvanostatic cycles (10A/kg 2.5-4.4Volts).

The sample underwent three galvanostatic cycles (to avoid problems due to SEI formation and not usable capacity) then the coulometric titration was performed. In this galvanostatic experiment, constant current pulses of 10A/kg pass through the cell for 5 minutes. After each pulse the current was switched off until the cell reaches voltage equilibrium conditions again. The equilibrium condition is defined as $\frac{dU}{dt} \leq 1\frac{mV}{h}$. It can be seen that the major part of the

lithium is exchanged in the range 3.6- 4.0 V with two main processes centered at 3.68 and 3.76 V, respectively.

13.5 How lithium intercalation affects the structure

In order to achieve a deeper understanding of the intercalation phenomenon, an important piece of information is gained from studying the cell parameters and their changes by lithium intercalation.

LiMnNiCoAl.283.566.141.010-950°C samples[1] have been previously treated galvanostatically at 10A/kg in the potential range (2.5-4.4V) for three cycles[2]. Subsequent charging by partial Li^+ removing was followed by a waiting time until the potential was stabilized[3]. Then the cells were disassembled and XRD powder pattern measurements performed. Marks (a), (b), (c) and (d) in Figure 71 are referring to those denoted in Figure 70 and refer to different states of intercalation. All patterns have been indexed to facilitate identification of Bragg peaks; most of them have changed their positional orders because of anisotropic cell deformation (i.e. products change c/a ratios). It is evident from Table 16 that Li^+ extraction strongly contributes to a reduction of the *volume* and of the *a* axis of the unit cell, while the *c* axis is expanded.

Table 16: Cell parameters of LiMnNiCoAl.283.566.141.010-950°C samples at different intercalation states.

Product	Ah/kg	O.C.V.	Cell parameter			
			a(Å)	*c(Å)*	*c/a*	*V(Å³)*
Untreated product	-----		2.8673(3)	14.223(2)	4.960(1)	101.27(2)
(a)	14.1	3.664	2.8600(4)	14.2754(6)	4.991(1)	101.12(2)
(b)	48.7	3.754	2.845(1)	14.360(2)	5.048(2)	100.66(6)
(c)	64.8	3.786	2.8390(3)	14.408(1)	5.075(1)	100.57(2)
(d)	134.4	4.124	2.820(1)	14.501(2)	5.142(2)	99.87(6)

[1] Samples have been assembled following the procedure described in section 7.3.

[2] Three cycles do allow the cell to work at regime and to allow the complete formation of *SEI*

[3] Equilibrium potential was taken to be reached for dU/dt<1mV/h or after 1 day.

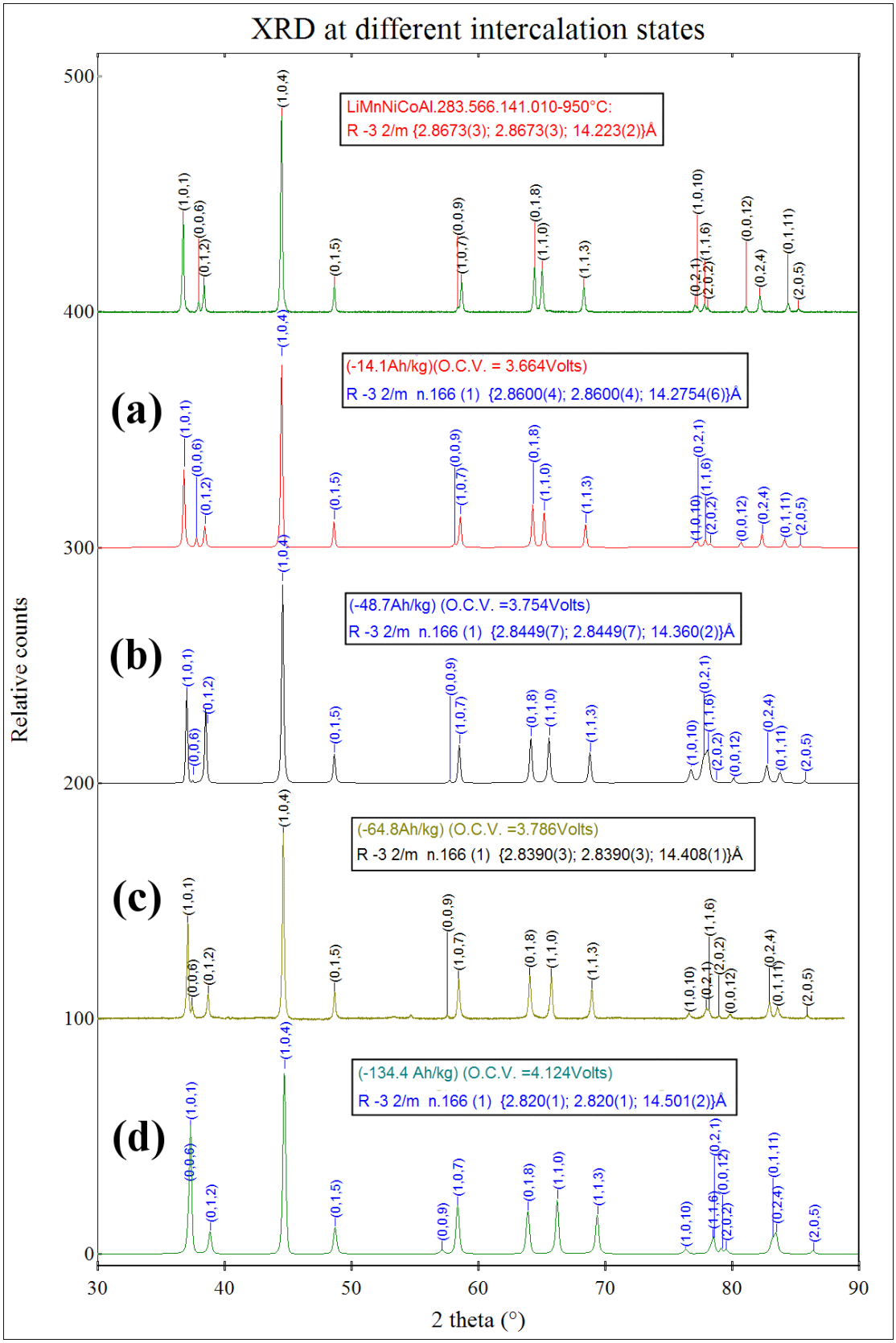

Figure 71: XRD powder patterns taken on LiMnNiCoAl.283.566.141.010-950°C samples after 3 galvanostatic cycles (10Ah/kg 2.5-4.4Volts) at different intercalation states.

This anisotropic deformation might be explained by considering the electrostatic contribution of Li^+. Lithium ions attract the MeO_6 layers so that they get closer to each other (MeO_6 layers are perpendicular to *c* axis).

In Figure 72, plots of lattice parameters *a* and *c* as well as *c/a ratio* and *unit cell volume* vs. *specific charge* are shown.

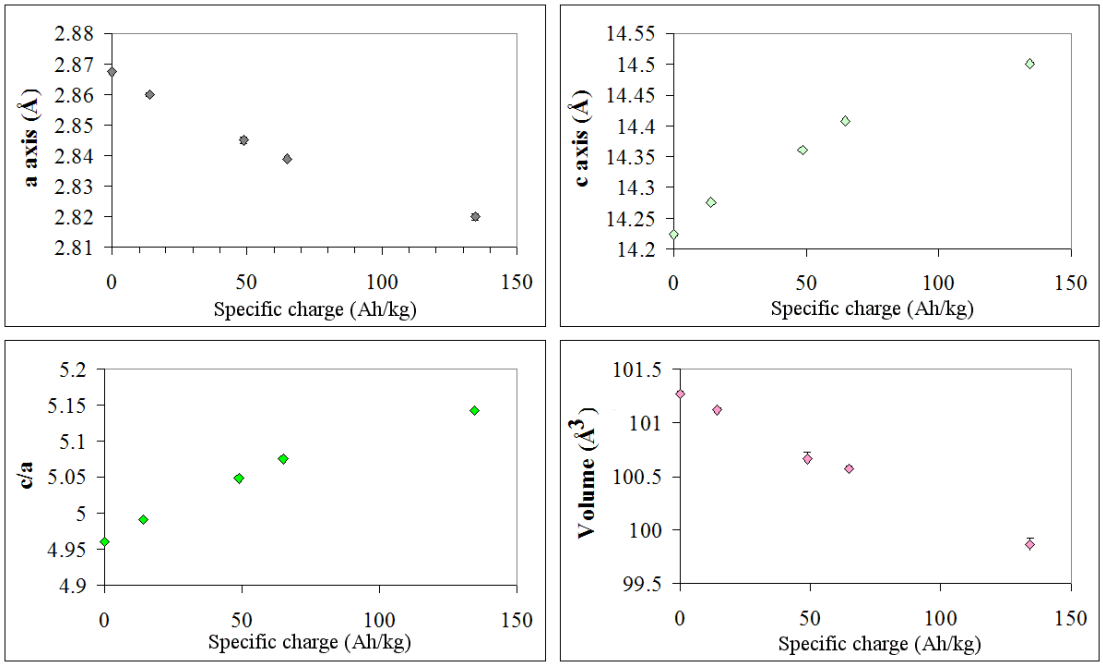

Figure 72: Lattice parameters *a and c as well as c/a ratio and unit cell volume* vs. *specific charge* for LiMnNiCoAl.283.566.141.010-950°C samples at different intercalation states. Error bars are so small that they are mostly covered by the symbol.

A change in cell volume of non-intercalated compounds and fully intercalated compounds is about 1.5%, which is very small compared to the cell volume variation of $LiNi_{0.8}Co_{0.2}O_2$ of about 4.5% [**39**].

13.5.1 Discussion of the results

In the XRD powder patterns, the peak positions are exclusively depending on the cell parameters, in this case *a* and *c*. Relative peak intensities are depending on the atom distribution inside the unit cells [1].

[1] Rigorously, peak intensities depend on the electronic density distribution inside the unit cell.

In Figure 73 it is possible to compare peak intensities[1] reflections 018, 110 and 113 reflections very well. Their differences of intensities can be explained by:

- The presence or absence of Li^+ in the intercalation layers during cycling;
- The partial migration of some of Me[2] into the intercalation layers.

Me migration can be considered negligible during one cycle because:

- The comparison of XRD powder pattern of LiMnNiCoAl.283.566.141.010-950°C with the one of a fully lithiated state of the same sample (see sect. 13.6) after 257 cycles shows no significant differences. Therefore if such variations are due to Me migration after 257 cycles (see Figure 74), it is reasonable to assume that during one cycle only migration must necessarily be much smaller.

This consideration completely excludes Me migration as a partial source for changing peak intensities during one single cycle.
Therefore, the variations exhibited from Figure 72 must be attributed to the Li^+ intercalation and de-intercalation only. The variation has two contributions:

1. power scattering of Li^+ (very small);
2. structural changes induced by Li^+.

[1] Differences between peak intensities of charged samples (nominally a, b, c, d) vs. peak intensities of the untreated sample LiMnNiCoAl.283.566.141.010-950°C.

[2] Me = Mn, Ni, Co, Al or whichever combination of them.

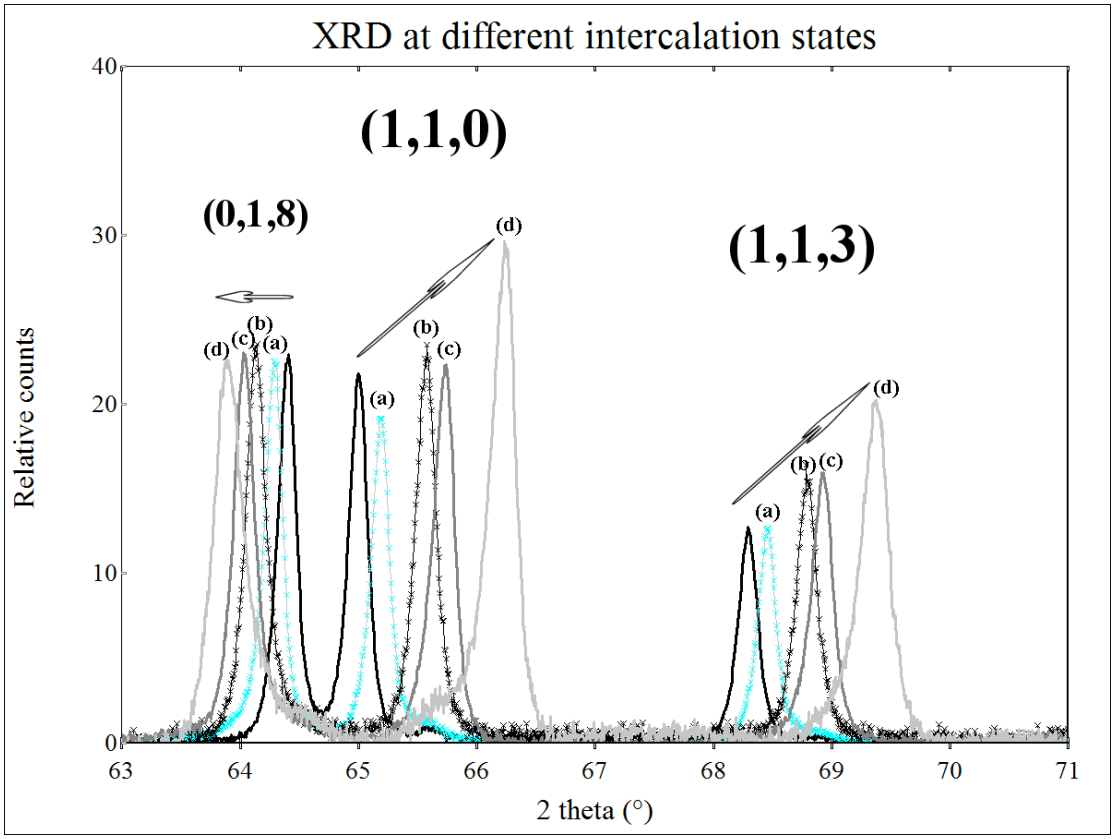

Figure 73: XRD powder patterns taken on LiMnNiCoAl.283.566.141.010-950°C samples after 3 galvanostatic cycles (10Ah/kg 2.5-4.4Volts) at different intercalation states. Detail of the region between 63° < 2θ < 71°. Arrows indicate the progression along a, b, c, d. The unsigned peaks are from the untreated sample. Peaks are normalized to (1,0,4) peaks intensities =100 for each pattern.

13.6 How cycling affects the structure

In this section, it will be investigated how cycling affects the crystal structure of LiMnNiCoAl.283.566.141.010-950°C samples have been cycled by two different ways:

1. at 10A/kg in the potential range of 3.0-4.2 Volts for 257 cycles, then complete lithiation down to 3 Volts, and
2. at 20A/kg in the potential range 2.5-4.4 Volts for 149 cycles, then fully lithiated down to 3 Volts.

The samples have then been disassembled and XRD powder patterns were taken as described above. In Figure 74 and Figure 75 these XRD patterns are shown in comparison with the one of LiMnNiCoAl.283.566.141.010-950°C.

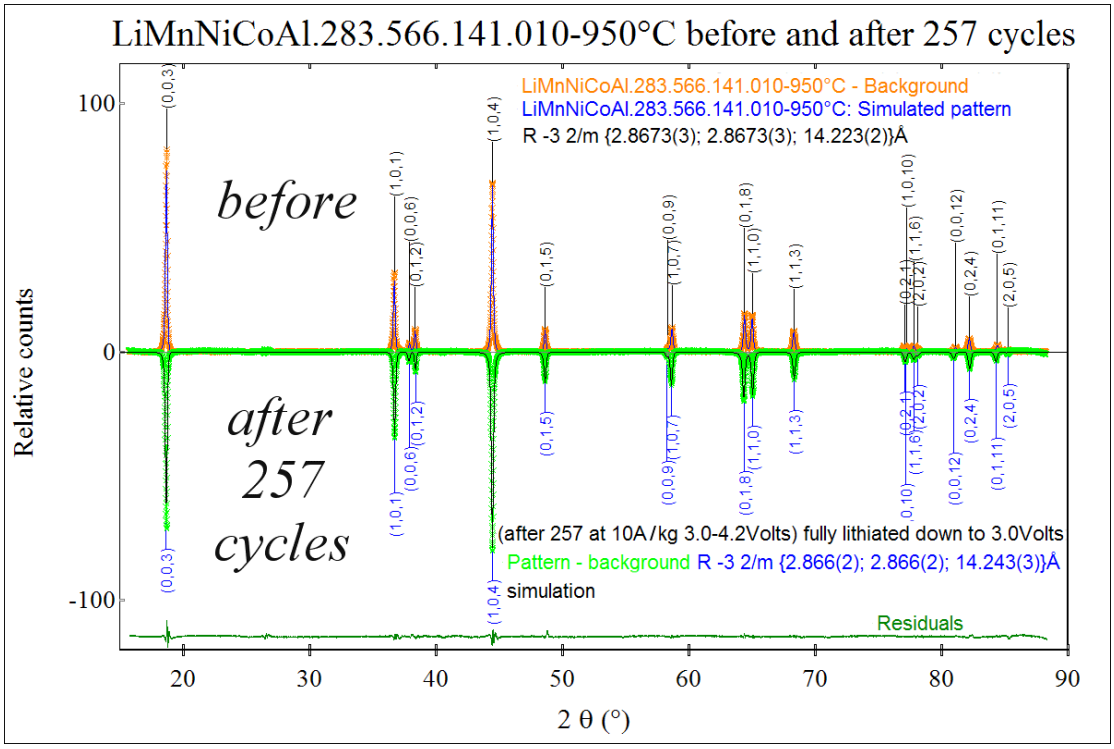

Figure 74: XRD powder patterns of LiMnNiCoAl.283.566.141.010-950°C taken before and after 257 cycles at 10A/kg (3.0-4.2Volts) with complete lithiation (discharging down to 3.0 Volts).

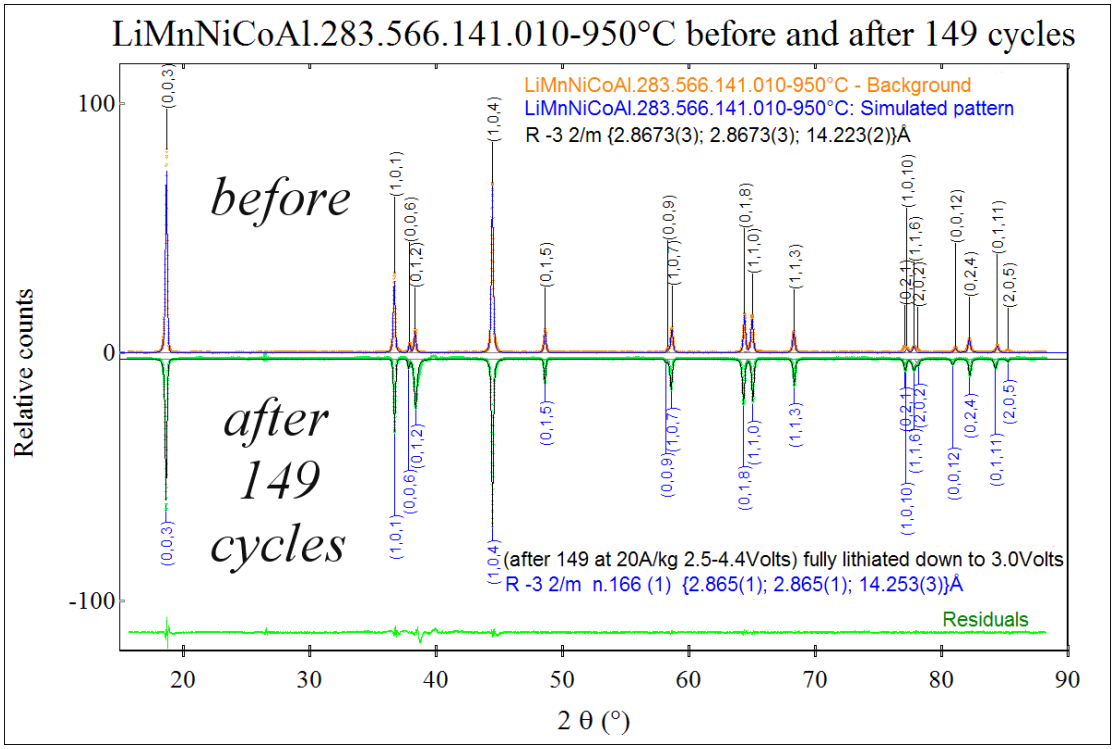

Figure 75: XRD powder patterns of LiMnNiCoAl.283.566.141.010-950°C taken before and after 149 cycles at 20A/kg (2.5-4.4Volts) with complete lithiation (discharging down to 3.0 Volts).

In both experiments, the cell parameters remain almost unchanged (Table 17). Small differences arise in the $I_{(0,0,3)}/I_{(1,0,4)}$ ratio and can be attributed to Me[1] migration towards the tetrahedral lithium site and/or even their exit from the structure.

Table 17: Cell parameters of LiMnNiCoAl.283.566.141.010-950°C samples after cycling.

Product	Cell parameter			
	a(Å)	*c(Å)*	*c/a*	*V(Å^3)*
LiMnNiCoAl.283.566.141.010-950°C	2.8673(3)	14.223(2)	4.960(1)	101.27(2)
After 257 cycles 20A/kg (2.5-4.4Volts)	2.866(2)	14.243(3)	4.970(5)	101.3(1)
After 149 cycles 10A/kg (3.0-4.2Volts)	2.865(1)	14.253(3)	4.975(3)	101.32(6)

13.7 Syntheses of non-Al doped compounds

Coluccia [33] showed that aluminum stabilizes the layer structure of the cathode compounds investigated here. Therefore we wanted to measure the necessary quantity of this doping-effect. Two compounds without aluminum have been synthesized: LiMnNiCo.283.566.141-950°C and LiMnNiCo.335.495.160-950°C. In Figure 76 and Figure 77, their XRD powder patterns are shown. In these samples the numbers 283, 566, 141 and so on, are not anymore related to mil fractions of the metals, because aluminum is missing and these fractions are 1% higher. Nevertheless, we maintain the same number for faster products identification. The ratio Mn:Ni:Co is still maintained.

[1] Me = Mn, Ni, Co, Al or whichever combination of them.

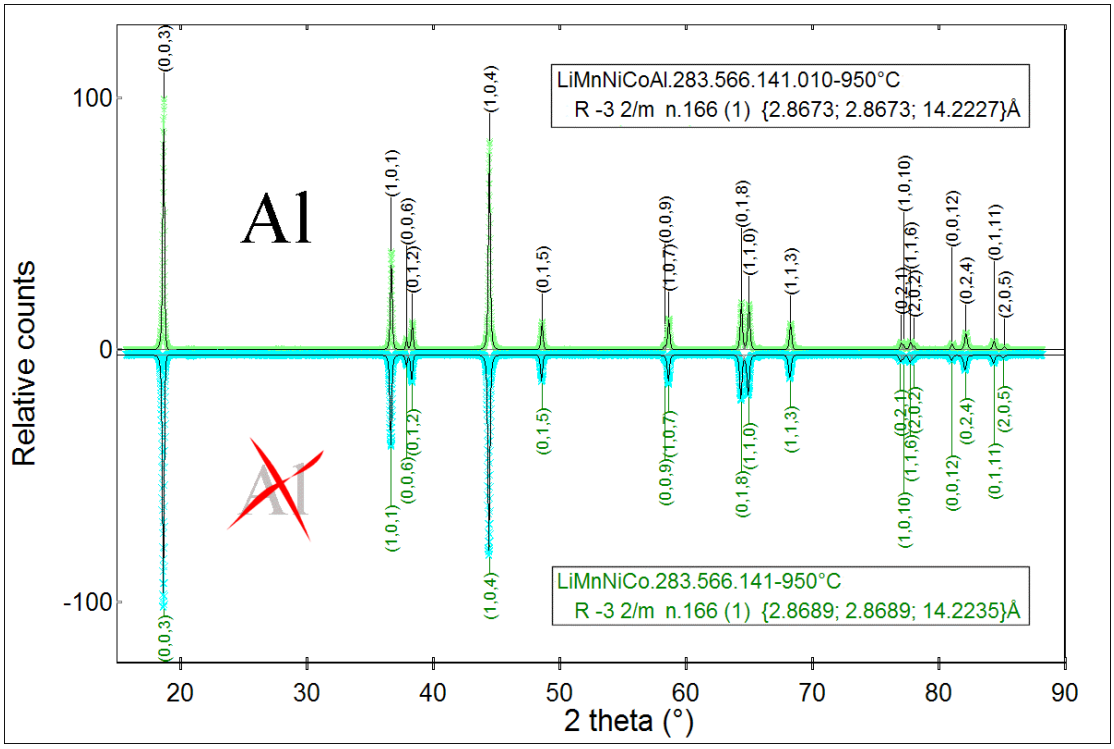

Figure 76: XRD powder patterns: comparison between LiMnNiCoAl.283.566.141.010-950°C and LiMnNiCo.283.566.141-950°C.

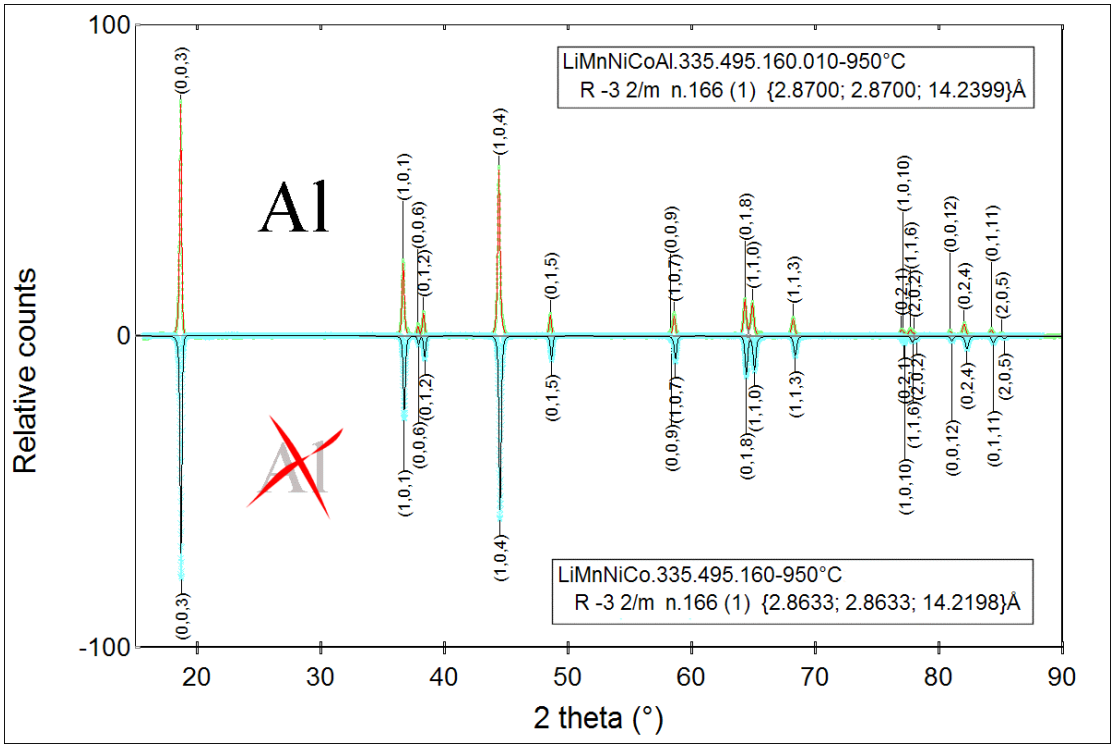

Figure 77: XRD powder pattern: comparison between LiMnNiCoAl.335.495.160.010-950°C and LiMnNiCo.335.495.160-950°C.

The cell parameters and comparison with aluminated isostoichiometric derivatives are listed in Table 18. As it was assumed, difference between the patterns arose neither in terms of cell parameters nor in terms of $I_{(0,0,3)}/I_{(1,0,4)}$ ratios. Although aluminum can stabilize the structure, it is not electroactive, and thus does not introduce any distortions during cycling. The aluminum centers also have some effect on the insertion potential of lithium in oxides. In earlier studies it was calculated that $LiAlO_2$ has an insertion potential of about 5V vs. Li^+/Li, and therefore it was suggested that the solid solution of $LiAlO_2$ with another oxide might increase the insertion potential of lithium ions. This effect was verified for $LiCo_{1-x}Al_xO_2$[**40**] and $LiNi_{1-x}Al_xO_2$[**41**].

Table 18: Cell parameters of the new materials synthesized without Al – doping *(reference products are evidenced*)

Products with and without Al	***a(Å)***	***c(Å)***	***c/a***	***V(Å^3)***
LiMnNiCoAl.283.566.141.010-950°C	2.8673(3)	14.223(2)	4.960(1)	101.27(2)
LiMnNiCo.283.566.141-950°C	2.8689(3)	14.224(1)	4.958(1)	101.39(2)
LiMnNiCoAl.335.495.160.010-950°C	2.870(1)	14.240(1)	4.962(2)	101.58(5)
LiMnNiCo.335.495.160-950°C	2.8633(4)	14.220(1)	4.966(1)	100.96(2)

To evidence the exchanged Li^+ fraction, specific charge plots of the products are shown in Figure 78 and in Figure 79. [1] From these we observe that for LiMnNiCoAl.335.495.160.010-950°C and LiMnNiCo.335.495.160-950°C there is in fact difference neither in terms of capacity nor in terms of capacity fading. Nevertheless, comparing the cycling performances of LiMnNiCoAl.283.566.141.010-950°C with LiMnNiCo.283.566.141-950°C, it is found that after a first start with equal s*pecific charge*, the undoped compound undergoes faster capacity fading.

[1] Unlike the specific charge plot, the value depends also on molecular weights which are slightly different for the two products. The molecular weights have been calculated assuming x=1 in Li_xMeO_2. The difference is about 0.3%.

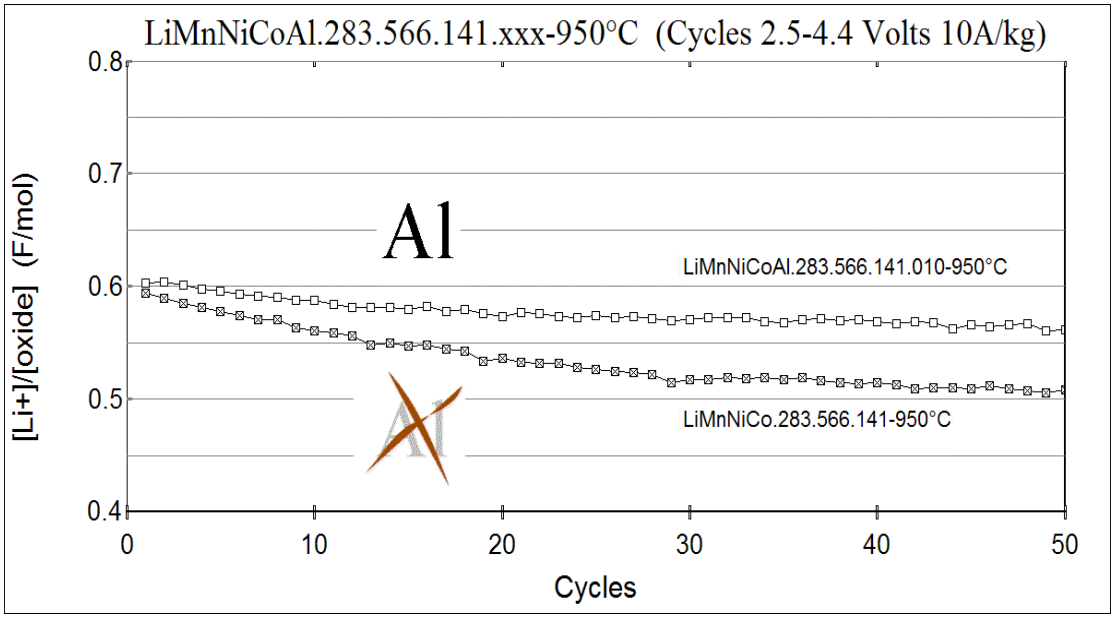

Figure 78: Discharge behaviour of LiMnNiCoAl.283.566.141.010-950°C and LiMnNiCo.283.566.141-950°C from galvanostatic cycling 10/A/kg (2.5-4.4Volts).

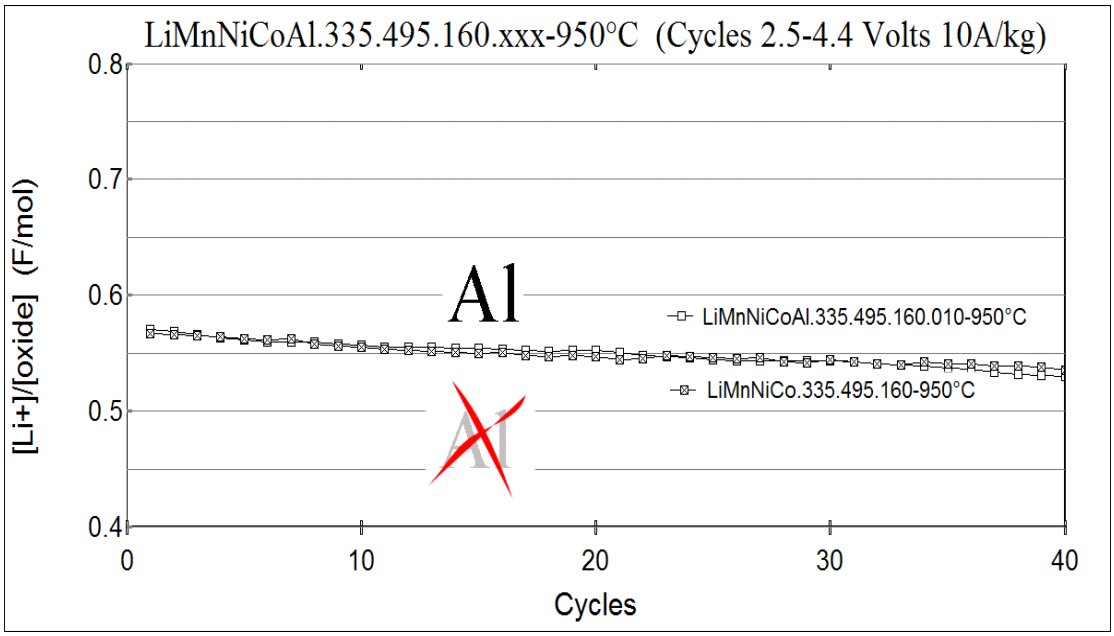

Figure 79: Discharge behaviour of LiMnNiCoAl.335.495.160.010-950°C and LiMnNiCo335.495.160-950°C from galvanostatic cycling 10/A/kg (2.5-4.4Volts).

In Figure 80, capacity fading is demonstrated during cycling (see circles).

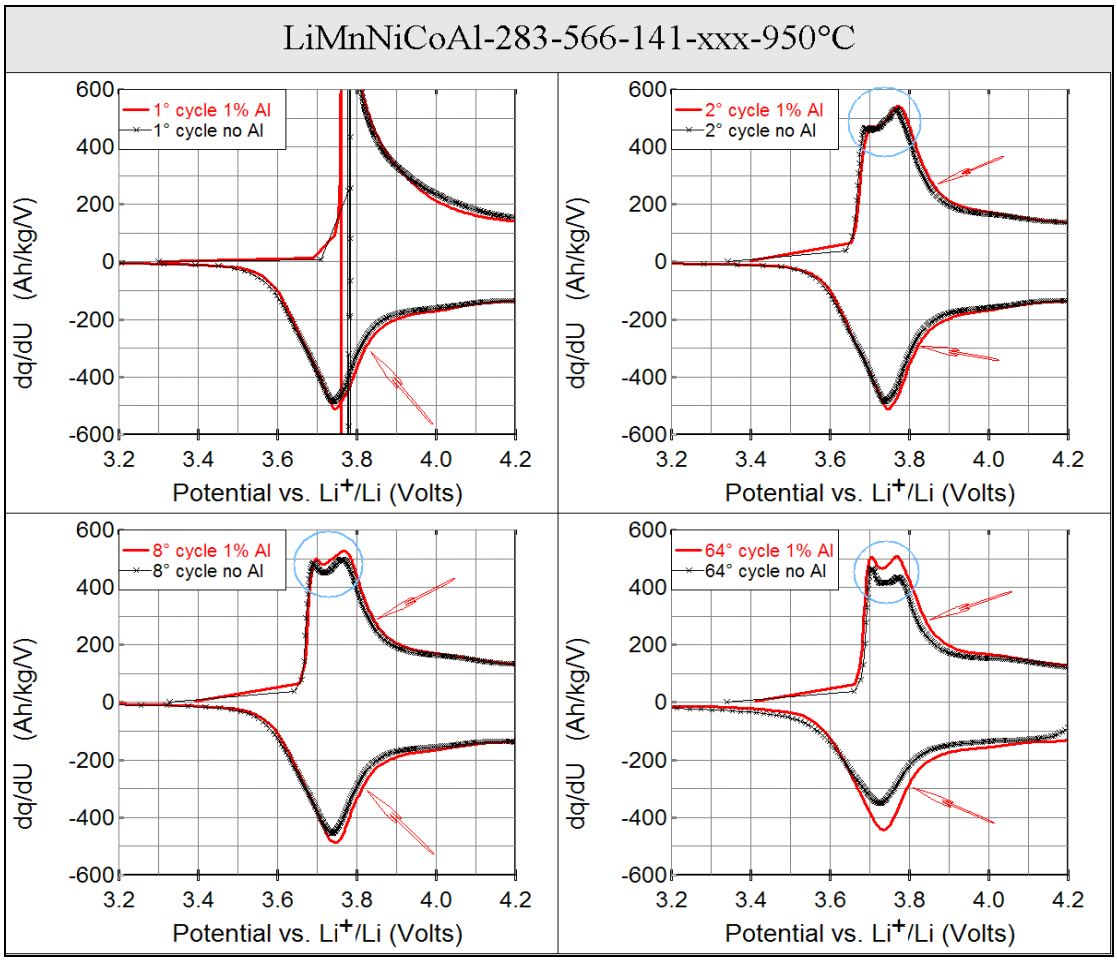

Figure 80: Differential capacity plots of LiMnNiCoAl.283.566.141.010-950°C and LiMnNiCo.283.566.141-950°C extracted from the cycles shown in Figure 78.

The expected upper voltage shifting due to aluminum is observed in LiMnNiCoAl.283.566.141.010-950°C and especially evident at higher potentials (arrows in Figure 80). The differential capacity plot from galvanostatic cycles of LiMnNiCoAl.335.495.160.010-950°C are presented (Figure 81).

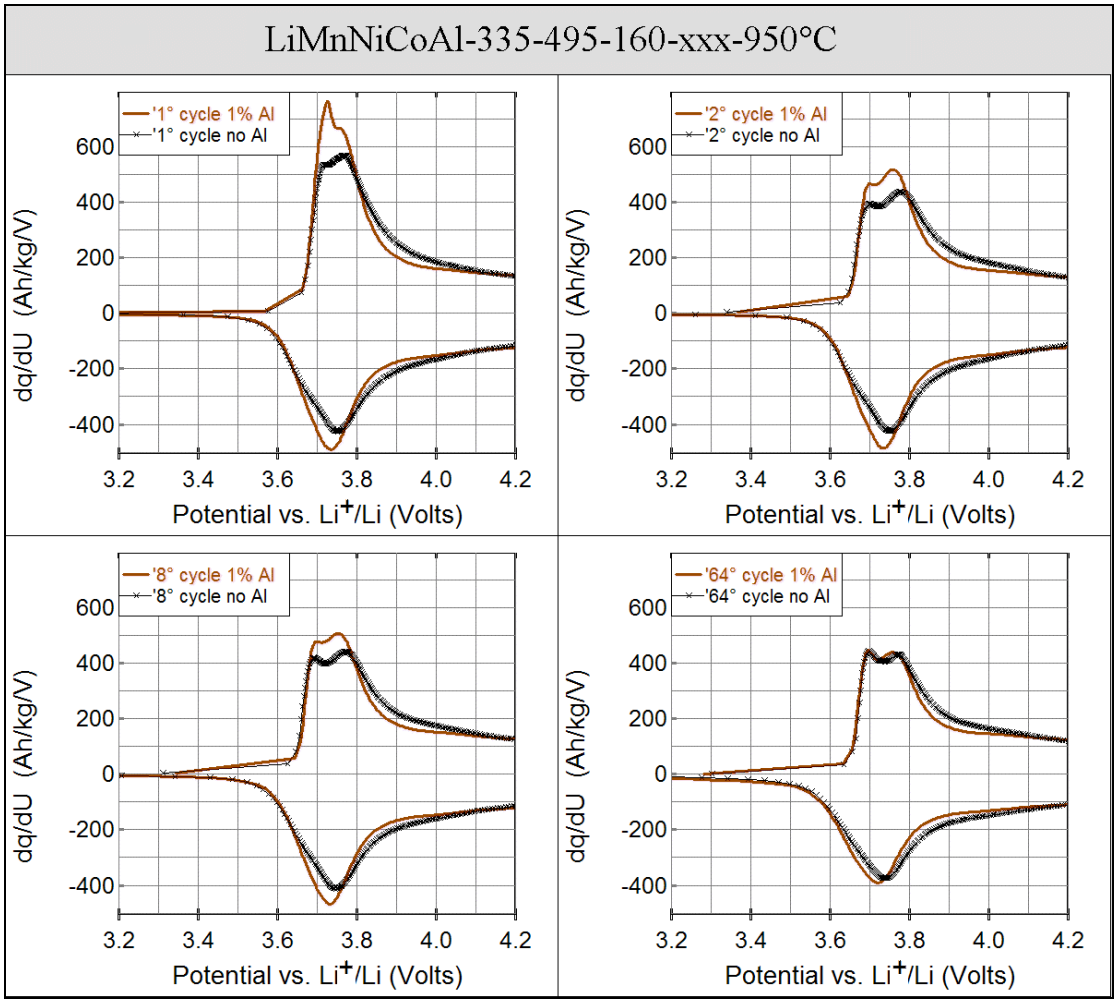

Figure 81: Differential capacity plots of LiMnNiCoAl.335.495.160.010-950°C and LiMnNiCo.335.495.160-950°C extracted from the cycles in Figure 79.

13.8 Conclusions

- Lithium diffusion inside the structure of LiMnNiCoAl.283.566.141.010-950°C is a limiting factor for the use of this material at high C rates (>C/10).
- Syntheses carried out at different temperatures did not lead to better results in terms of electrochemical performances. This should mean that an ideal temperature for the treatment is quite close to 950°C. The gross optimal temperature range for syntheses is between 900°C-1000°C.
- The lithium intercalation de-intercalation process changes the cell constants anisotropically and reversibly.

- Part of the deintercalated Li^+ during the first charge cannot be reinserted during normal cycling conditions but may become reversible again by forcing Li^+ to reintercalate into the structure. Such loss of lithium is the main reason for the high irreversible capacity loss at the first cycle. The second reason is the irreversible SEI formation.
- The experiments confirm the structure stability due to the aluminum content of the compounds.

Chapter 14.

Specific charge vs. cell parameter

One of the main targets of this research was to find a correlation, if any, between electrochemical performances and crystal structures. First of all it has been necessary to find some criteria for the electrochemical performances calculation. These criteria have been described in sect. 8.3 and this empirical description is capable to summarize the specific charge behavior in overall cycles extension by mean of four parameters only.

14.1 Experimental

Since all our products crystallize in the same space group ($R\bar{3}m$) even with different compositions, a correlation between cell parameter and specific charge can be made.
All products presented in this section have undergone the same electrochemical galvanostatic treatment at 10A/kg between 2.5-4.4 Volts.
With the empirical description presented in section 8.3 the following parameters have been calculated: C_o, α, F_o, *and* τ. These parameters are shown in Table 19[1] with the cell parameter. The columns containing values for the *c* axis and the calculated specific charge

[1] In Table 19, only the products for which it was possible calculate both *"specific capacity"* and *"cell parameters"* are shown.

average during the first 100 cycles ($\overline{C_{100}^{Calc}}$) are grey-underlayed because they represent the strongest correlated quantities.

14.2 Results

The results are emphasized by Figure 82 and Figure 83. Very small σ_{Cap} values proof the good fitting. It can be seen that the exponential capacity component *'F'* plays a fundamental role in describing the non-linear specific charge behavior. In Figure 84 plots *"c axis vs.* $\overline{C_{100}^{Calc}}$ *"* and *"a axis vs.* $\overline{C_{100}^{Calc}}$ *"* are shown. In both cases a correlation between the quantities is clear and a small cell parameter corresponds to high $\overline{C_{100}^{Calc}}$. The correlation "*c axis vs.* $\overline{C_{100}^{Calc}}$ *"* is particularly good.

Although the least square straight lines are drawn within the plots, they do not represent any linear dependence between the two quantities. They have been calculated to obtain a correlation index which is in this case the linear regression index *"r"* and drawn to make the tendencies more visible.

14.3 Conclusions

- The empirical description proposed for the specific charge discharge plots seems to fit the experimental data very well.
- A good correlation between the c axis length and the $\overline{C_{100}^{Calc}}$ was found, in particular smaller *c axis* favour electrochemical performances.

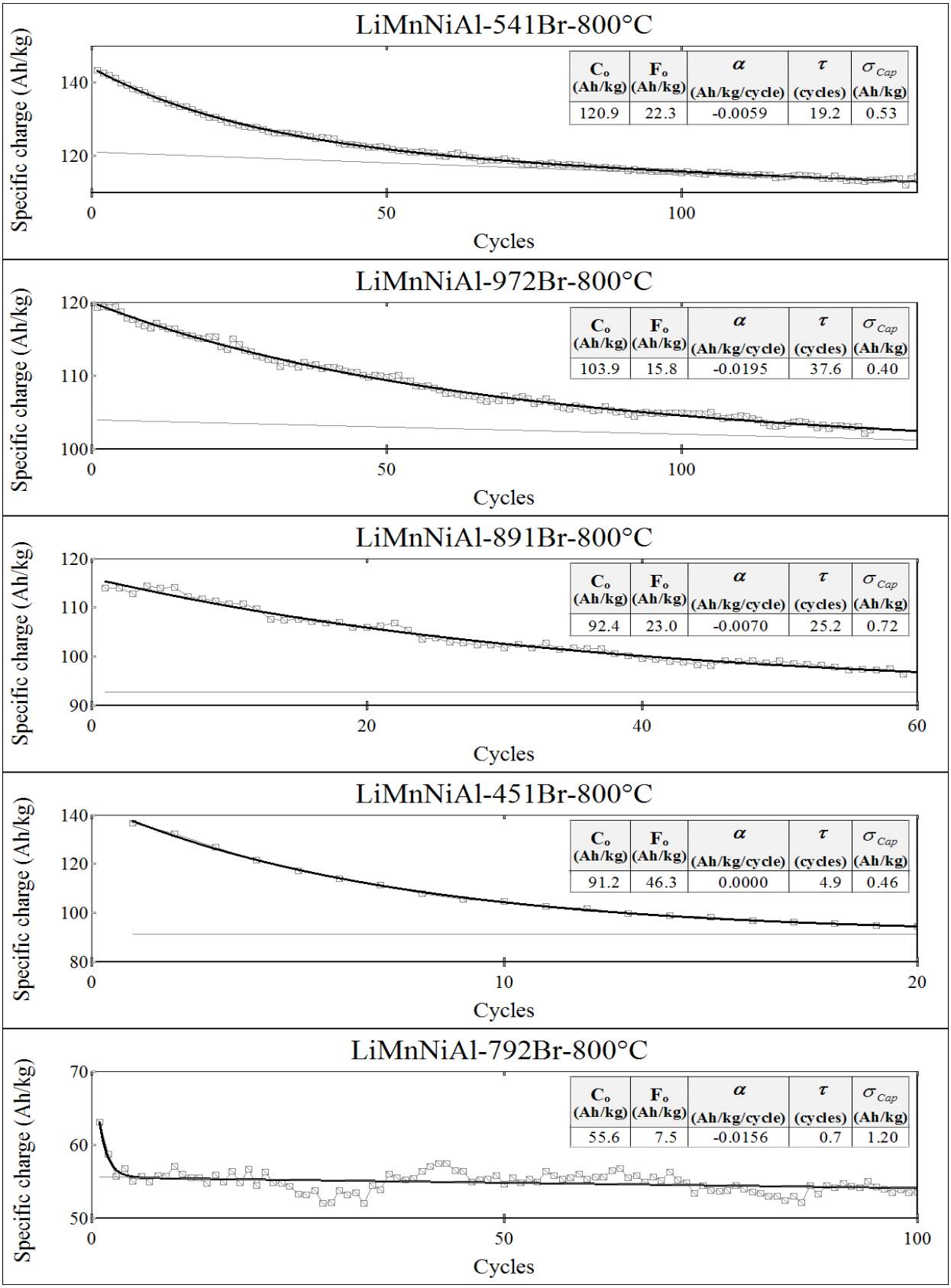

Figure 82: Specific discharge capacity plots from galvanostatic cycling taken at 10A/kg (2.5-4.4Volts) of the products from "wet synthesis". All plots are fitted according to the empirical description given in (eq. 33) of section 8.3.

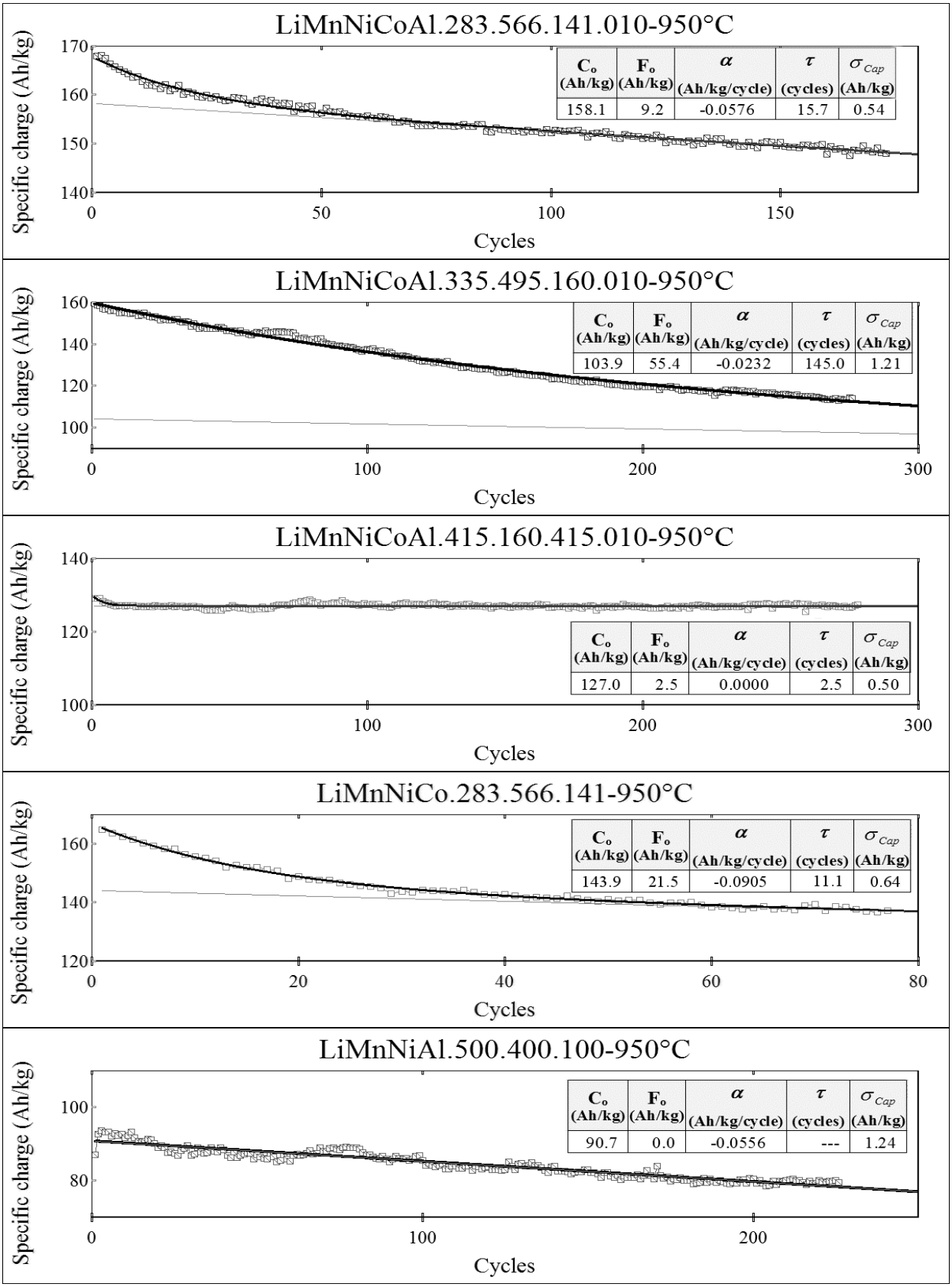

Figure 83: Specific charge plot from galvanostatic cycling taken at 10A/kg (2.5-4.4Volts) of the products via "dry synthesis". All plots are fitted according to the empirical description given in (eq. 33) of section 8.3.

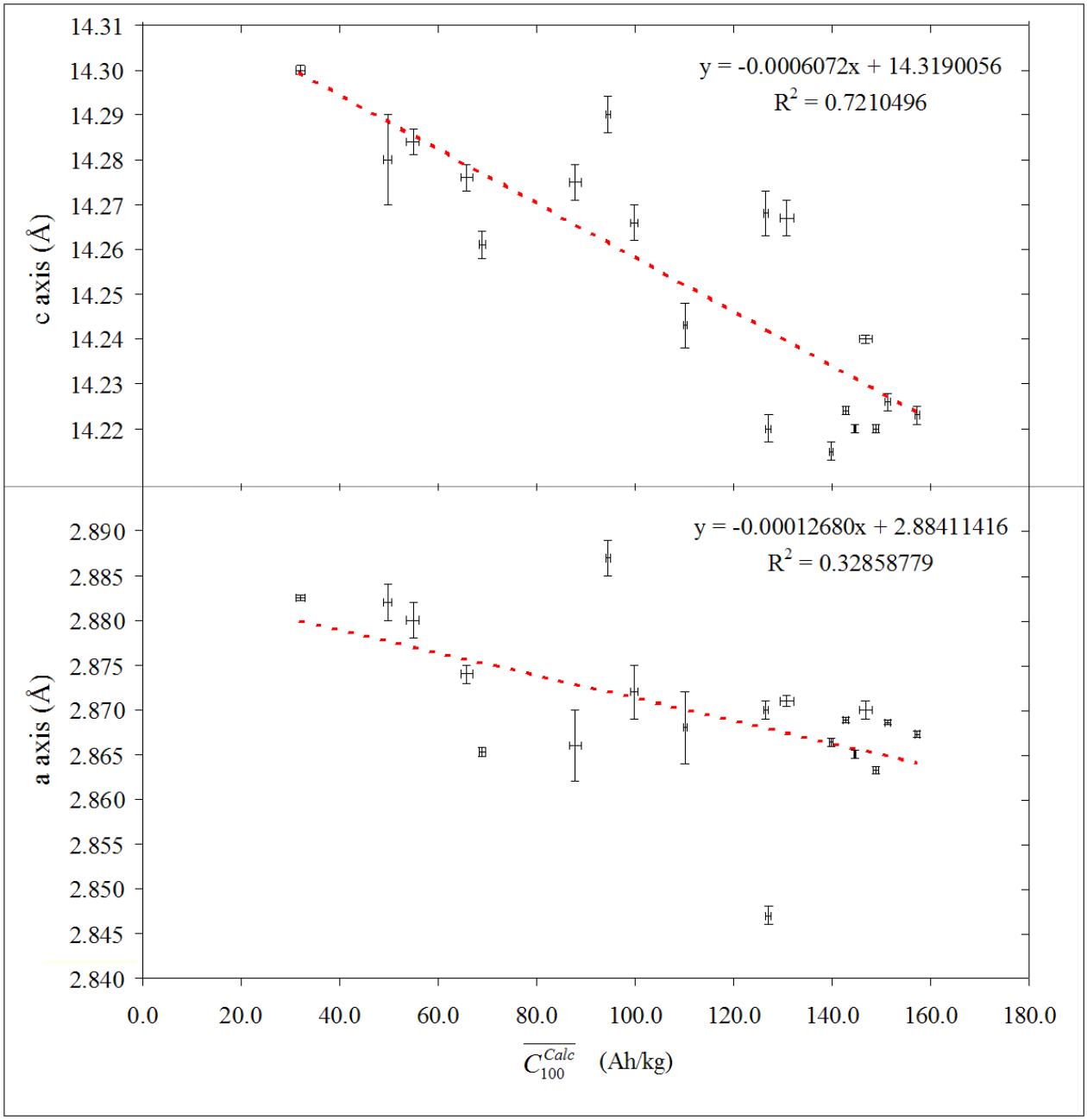

Figure 84: Correlation plots of *"a and c axes"* vs. *"calculated specific charge average during the first 100 cycles* $\overline{C_{100}^{Calc}}$ *"*. Plotted values were taken from Table 19. Straight lines demonstrate the tendencies; they do not represent a linear relationship between the quantities.

Table 19: S*pecific charge* and cell parameter of some products. Values are Tabled with descending $\overline{C_{100}^{Calc}}$ according with (eq. 33) sect.8.3. S*pecific charge* parameters have been calculated by galvanostatic cycles at 10A/kg in the range (2.5-4.4Volts).

Product	Electrochemical performances							Cell parameters			
	C_o (Ah/kg)	F_o (Ah/kg)	C_o+F_o (Ah/kg)	$\overline{C_{100}^{Calc}}$ (Ah/kg)	α (Ah/kg/cycle)	τ (cycles)	σ_{Cap} (Ah/kg)	a (Å)	c (Å)	c/a	Volume (Å^3)
LiMnNiCoAl.283.566.141.010-950°C	158.1	9.2	167.3	157.3	-0.0576	15.7	0.54	2.8673(3)	14.223(2)	4.960(1)	101.27(2)
LiMnNiCoAl.283.566.141.010-1000°C	160.5	5.0	165.5	151.2	-0.1925	4.7	0.65	2.8686(3)	14.226(2)	4.959(1)	101.38(2)
LiMnNiCo.335.495.160-950°C	155.0	3.4	158.4	148.8	-0.1270	3.4	0.57	2.8633(4)	14.220(1)	4.966(1)	100.96(2)
LiMnNiCoAl.335.495.160.010-950°C	103.9	55.4	159.3	146.8	-0.0232	145.0	1.21	2.870(1)	14.240(1)	4.962(2)	101.58(5)
LiMnNiCoAl.335.495.160.010-900°C	150.0	2.6	152.6	144.7	-0.1089	4.1	0.24	2.8650(5)	14.220(1)	4.963(1)	101.08(3)
LiMnNiCo.283.566.141-950°C	143.9	21.5	165.4	142.8	-0.0905	11.1	0.64	2.8689(3)	14.224(1)	4.958(1)	101.39(2)
LiMnNiCoAl.283.566.141.010-900°C	147.0	6.7	153.7	139.9	-0.1577	7.7	0.35	2.8664(5)	14.215(2)	4.959(1)	101.15(3)
LiMnNiAl-541Br-950°C	135.6	0.0	135.6	130.7	-0.0977	---	1.40	2.8705(6)	14.267(4)	4.970(3)	101.81(5)
LiMnNiCoAl.415.160.415.010-950°C	127.0	2.5	129.5	127.1	0.0000	2.5	0.50	2.847(1)	14.220(3)	4.995(3)	99.80(1)
LiMnNiAl-541Br-800°C	120.9	22.3	143.2	126.6	-0.0059	19.2	0.53	2.870(1)	14.268(5)	4.971(3)	101.8(1)
LiMnNiAl-972Br-800°C	103.9	15.8	119.7	110.1	-0.0195	37.6	0.40	2.868(4)	14.243(5)	4.97(1)	101.5(2)
LiMnNiAl-891Br-800°C	92.4	23.0	115.4	99.9	-0.0070	25.2	0.72	2.872(3)	14.266(4)	4.97(1)	101.9(2)
LiMnNiAl-451Br-800°C	91.2	46.3	137.5	94.5	0.0000	4.9	0.46	2.887(2)	14.290(4)	4.950(5)	103.1(1)
LiMnNiAl.500.400.100-950°C	90.7	0.0	90.7	87.9	-0.0556	---	1.24	2.866(4)	14.275(4)	4.98(1)	101.5(2)
LiMnNiAl-972Br-950°C	72.6	9.2	81.8	69.1	-0.0973	10.0	0.58	2.8653(5)	14.261(3)	4.977(2)	101.40(4)
LiMnNiAl-981Br-800°C	60.9	11.6	72.5	65.8	0.0713	8.2	1.20	2.874(1)	14.276(3)	4.967(3)	102.1(1)
LiMnNiAl-792Br-800°C	55.6	7.5	63.1	54.9	-0.0156	0.7	1.20	2.880(2)	14.284(3)	4.960(4)	102.6(1)
LiMnNiAl-981Br-950°C	47.5	17.5	65.0	49.9	0.0133	6.8	0.82	2.882(2)	14.28(1)	4.96(1)	102.7(2)
LiMnNiAl-792Br-950°C	33.3	17.6	50.9	32.2	-0.0519	5.8	1.00	2.8826(3)	14.300(1)	4.961(1)	102.91(2)

Chapter 15.

Characterization of other oxides

Several other oxides have been characterized electrochemically as eligible Li^+ host materials for reversible batteries during the period of this thesis but only the most representative ones will be discussed in this chapter.

15.1 $H_2V_3O_8$ nano fibers

One of the most remarkable products in terms of specific energy was $H_2V_3O_8$ nano fibers[1] (Figure 85). Unlike manganese-based oxides, this compound was not prepared in lithiated form. If it is used in a battery as cathodic material, the system becomes a primary source of energy. The first hemicycle is cathodic and thereafter the system is completely lithiated and can be recharged. Its cyclovoltammogram (Figure 86) at 20μV/sec has been started after the first hemicycle. It contains a multitude of electrochemical processes along the investigated potential range. The entire electrochemical sites available for the Li^+ insertion are below 4 Volts. lowering the specific energy with respect to 4V typical materials, but electrolyte decomposition is also very much reduced. From the cyclovoltammogram it is evident that after just a few cycles a remarkable change in positions and peak sizes arises. This indicates that the structure undergoes important reconstructions.

[1] Synthesized by Michael Stalder (2003) at ETH Zürich.

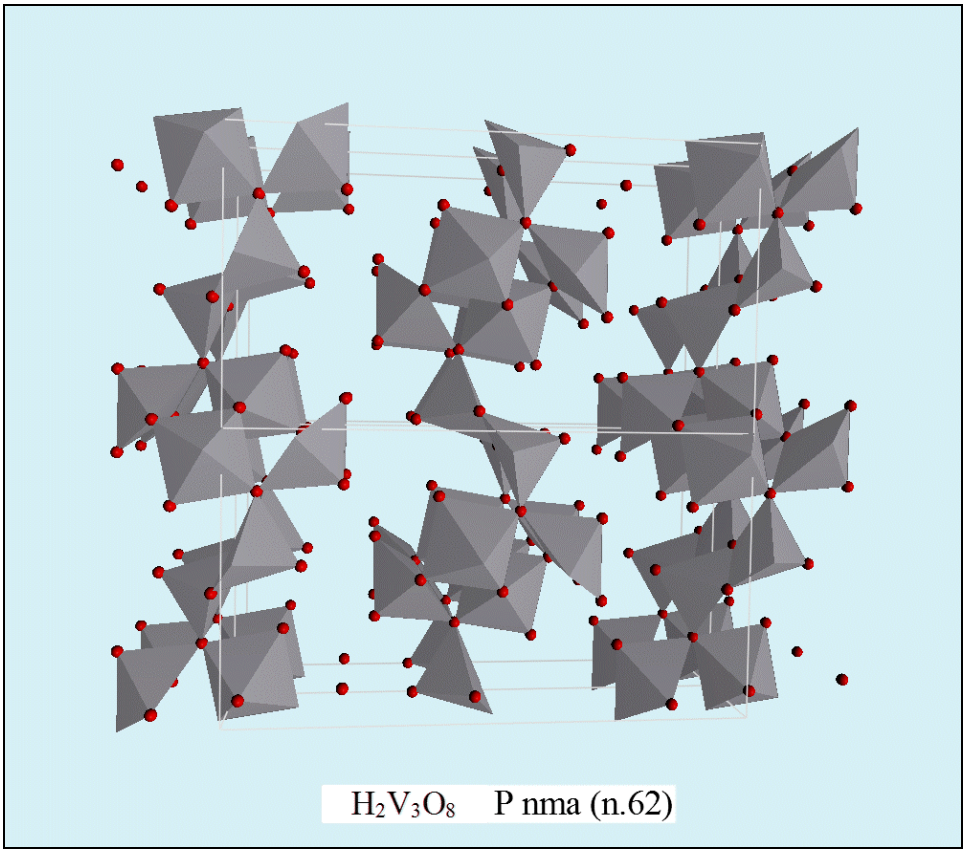

Figure 85: Crystal structure of $H_2V_3O_8$ Pnma (n.62)

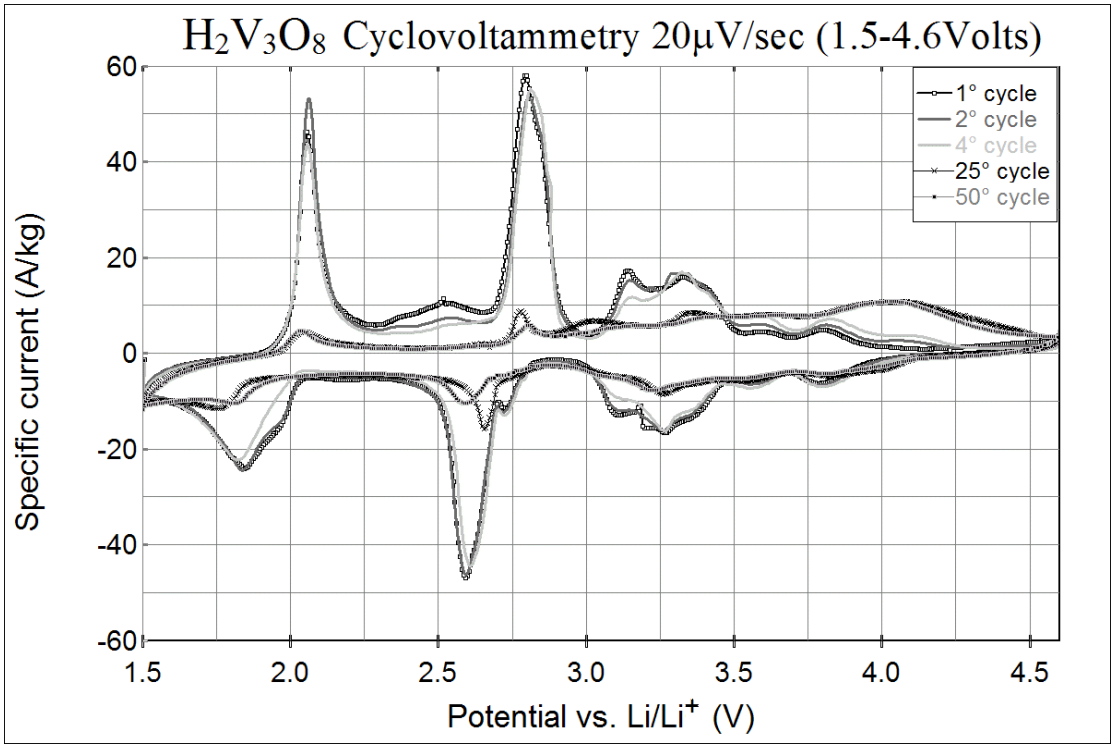

Figure 86: Cyclovoltammetry on $H_2V_3O_8$ nanofibers at 20μV/sec in the range (1.5-4.6Volts).

After cycles 25 and 50 a great part of the structure has obviously been modified while the major part of the charge capacity is being shifted towards higher potentials during cycling, thus keeping the high specific energy. In Figure 87 a the specific discharge capacity vs. cycle plot shown which reveals that at the maximal capacity the compound is able to locate in its structure four moles of lithium pro formula unit or 1.33 Li per one vanadium center.

Since electrochemical processes take place at different potentials it is not possible to compare this product directly to our manganese-based oxides in terms of specific charge. A more rigorous analysis could be done by comparing the specific energies exchanged by the systems versus a same reference system (here Li^+/Li system). Figure 88 displays a specific energy plot of $H_2V_3O_8$ nano fibers at different current densities and as a comparison LiMnNiCoAl.283.566.141.010-950°C ($LiMn_{0.283}Ni_{0.566}Co_{0.141}Al_{0.01}O_2$). It is evident that for the first 40-60 cycles, $H_2V_3O_8$ nano fibers perform better than $LiMn_{0.283}Ni_{0.566}Co_{0.141}Al_{0.01}O_2$ even at higher current densities (in this case 200A/kg = C/1.2) compared to $LiMn_{0.283}Ni_{0.566}Co_{0.141}Al_{0.01}O_2$ (with 10A/kg = C/16). In other words, at 200A/kg the $H_2V_3O_8$ system could undergo a charge and discharge at the same specific energy as $LiMn_{0.283}Ni_{0.566}Co_{0.141}Al_{0.01}O_2$ but 13 times faster. Unfortunately, these amazing performances are kept only for 40-60 cycles and afterwards the system is not competitive anymore with the more stable manganese based oxides.

Figure 87 also reveals two peculiar characteristics of the $H_2V_3O_8$ system:

1. At the beginning of cycling the samples cycled at lower current densities show better charge exchanging performances, while after 40-60 cycles samples cycled at higher current densities show better charge exchanging performances.
2. For each current density a first period (18-22 cycles) is remarkable in which the performances are increasing. After they reached the maximum the specific charge undergoes an inexorable fading.

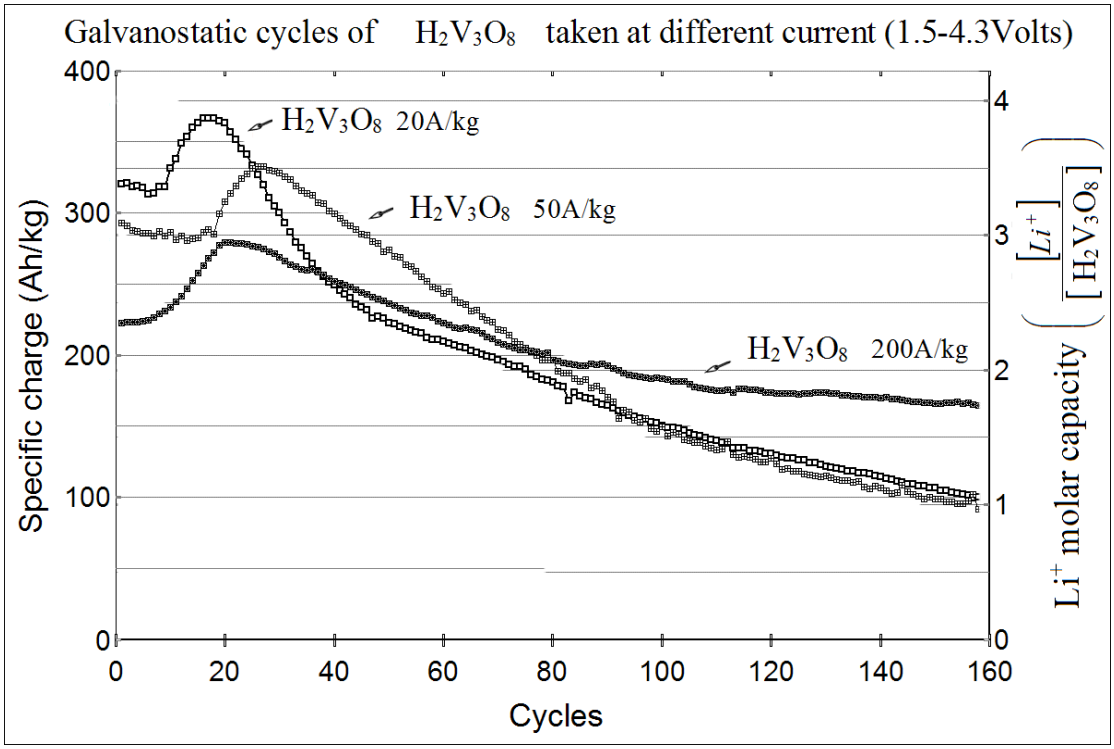

Figure 87: Specific discharge capacity vs. cycle of $H_2V_3O_8$ nanofibers taken at different current densities. Li^+ molar capacity on right axis.

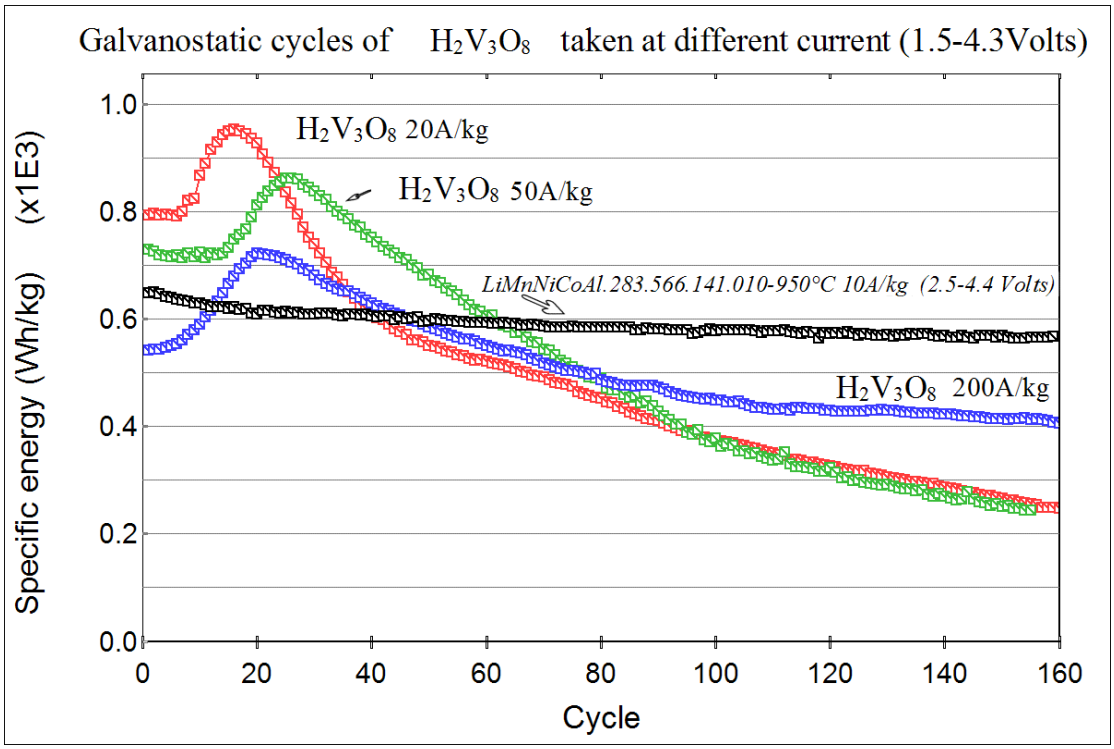

Figure 88: Specific discharge energy vs. Cycle of $H_2V_3O_8$ nanofibers taken at different current densities. The specific energy of active material has been calculated versus the Li^+/Li electrode.

In Figure 89 several images of the sample taken with different magnifications by S.E.M. are presented showing the nanofiber morphology very clearly .

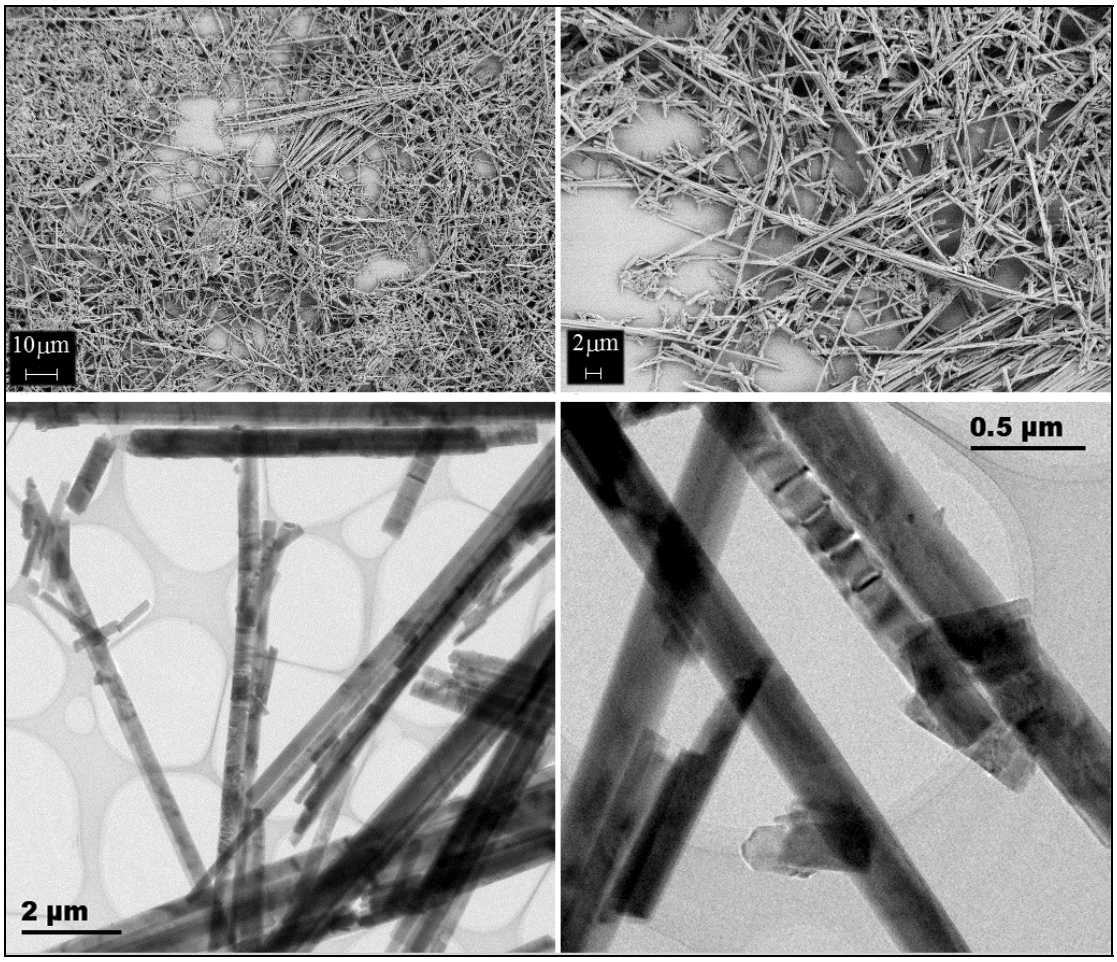

Figure 89: $H_2V_3O_8$ nanofibers. Images taken by S.E.M. and T.E.M. at different magnifications.

15.1.1 Conclusions

$H_2V_3O_8$ nano fibers show very interesting electrochemical performances, being able to host up to four Li^+ equivalents per formula unit. Considering the first 60 cycles, the product is very competitive with present market products both in terms of specific energy and specific power (very high discharge current up to C/1.7). But due to hitherto unknown effects, it undergoes constant energy fading. Another problem is the multizone discharge potential which may be more difficult to be stabilized by electronic equipment (see 5.5).

15.2 Titanium dioxide

Titanium dioxide has several practical advantages: it is readily available, chemically stable, semiconducting, inexpensive and non-toxic [**42**]. The most common forms of TiO_2 are rutile and anatase. Lithium intercalation in both forms have been studied extensively. From Li_xTiO_2 maximum electrochemical insertion is reported:

- Rutile: x= (from 0.1 up to 1.0) [**43**, **44**];
- Anatase: x= (from 0.5 up to 1.0) [**45**, **46**];

Both forms, *anatase* (see Figure 90) and rutile (see Figure 100) crystallize in tetragonal structures. *Anatase* consists of edge sharing TiO_6 octahedra, while in *rutile* the octahedra share the edge in *c* direction with corner sharing in *ab* plane. In between the octahedra sites two potential lithium intercalation sites exist having either an octahedral or a tetrahedral oxygen coordination.

15.2.1 TiO_2 anatase

In this section a family of TiO_2 anatase nanofibers [1] will be presented.
Unlike the manganese-based oxides and just as the vanadic acid, this compound is not lithiated in advance. Thus, if it is used in a battery as anodic material with a lithiated cathode material, a primary battery derives. If it is used as cathodic material, the battery will be a secondary one. Several investigations have been performed in the past on Li^+ insertion in TiO_2 anatase [**47**, **48**], in which titanium is supposed to undergo reduction from Ti^{+4} to Ti^{+3} during the cathodic process, with a specific charge of about 325Ah/kg. In Figure 90, a stereoscopic view of TiO_2 anatase crystal structure is shown.
A preliminary cyclovoltammogram has been taken for each product, in order to establish the opportune potential range for each of the different samples, followed by a series of suitable cyclovoltammetric measurements.

[1] All products have been kindly furnished by Dr. V. Lorenzen (SusTech GmbH). The products are labelled as they were delivered. Their names are given in every plot shown in this section.

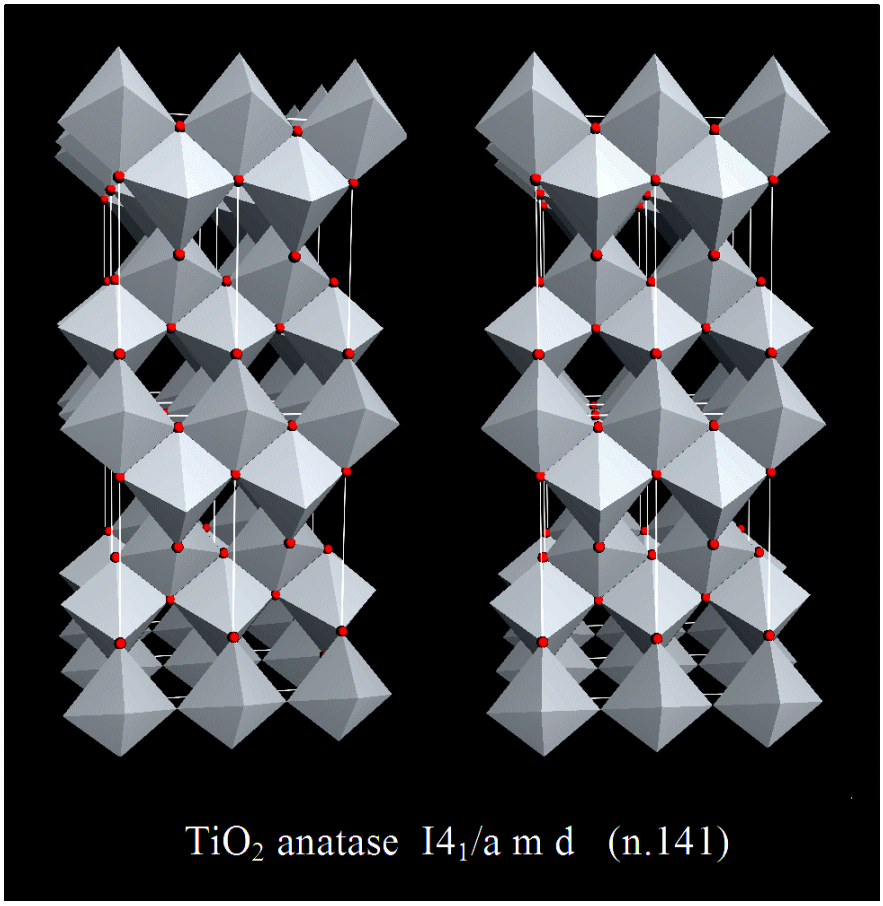

Figure 90: Stereoscopic view of the anatase crystal structure of TiO_2.

Figure 91 shows a specific discharge plot of the first set of samples. Unlike the manganese-based compounds previously described, a faster capacity fading during cycling is being observed (compare Figure 41, Figure 44 and Figure 51). Nevertheless, the major part of the samples exhibits a specific charge even higher than $\mathbf{LiMn_{0.283}Ni_{0.566}Co_{0.141}Al_{0.01}O_2}$. Certainly, this is not the only criterion for the use in lithium batteries and one also has to evaluate at which potential the insertion-deinsertion process takes place. Cyclovoltammetric investigations allow studying in detail at which potentials the reactions take place.

In Figure 92, Figure 93 and Figure 94 cyclovoltammetric curves taken at 10µV/sec are shown with S.E.M. pictures of the corresponding materials; the graphs are ordered with decrescent specific charge performances (better on top) Each cycle starts with the cathodic hemicycle. It can be seen that all samples

show two anodic regions (de-intercalation regions) in which the process take place:

- 1st region (1.45-1.7 V) and
- 2nd region (1.85-2.0 V); with a competition of a higher shifting with its corresponding cathodic peak.

The differences occur for the relative intensities of the peaks and for their broadnesses. "Better" samples (in terms of cycling performances) show well defined peaks in the 1st region (see sample *'141A'*, *'066C'* and *'142B'*). It seems that there is a correlation between the fiber form and so-called well-defined behaviour in the 1st region. Samples which are loosing their fiber shape tend to have broader peaks in the 1st region until they show a fish shaped morphology (samples *142A, 42F,141i* and *142K*). Samples *146B (big fibers), 174a (nanotubes)* and *147A (platelets)* have almost completely lost their nanofiber shape and do show the lowest cycling capabilities.

As discussed before, TiO_2 undergoes intercalation and de-intercalation processes in the range of 1.45 to 2.0 Volts. That means that the discharge potentials are too low for being good cathodic materials, but also too high for good anodic materials.

To quantify these arguments specific discharge energy plots for all samples are shown in Figure 95. The plots are taken from the cyclovoltammetric studies already discussed above. The specific energies are related to the Li^+/Li potential (without considering the mass of the lithium counter electrode) and it is obvious that they cannot be competitive to the one furnished by $LiMn_{0.283}Ni_{0.566}Co_{0.141}Al_{0.01}O_2$ (about 600 Wh/kg, see Figure 88).

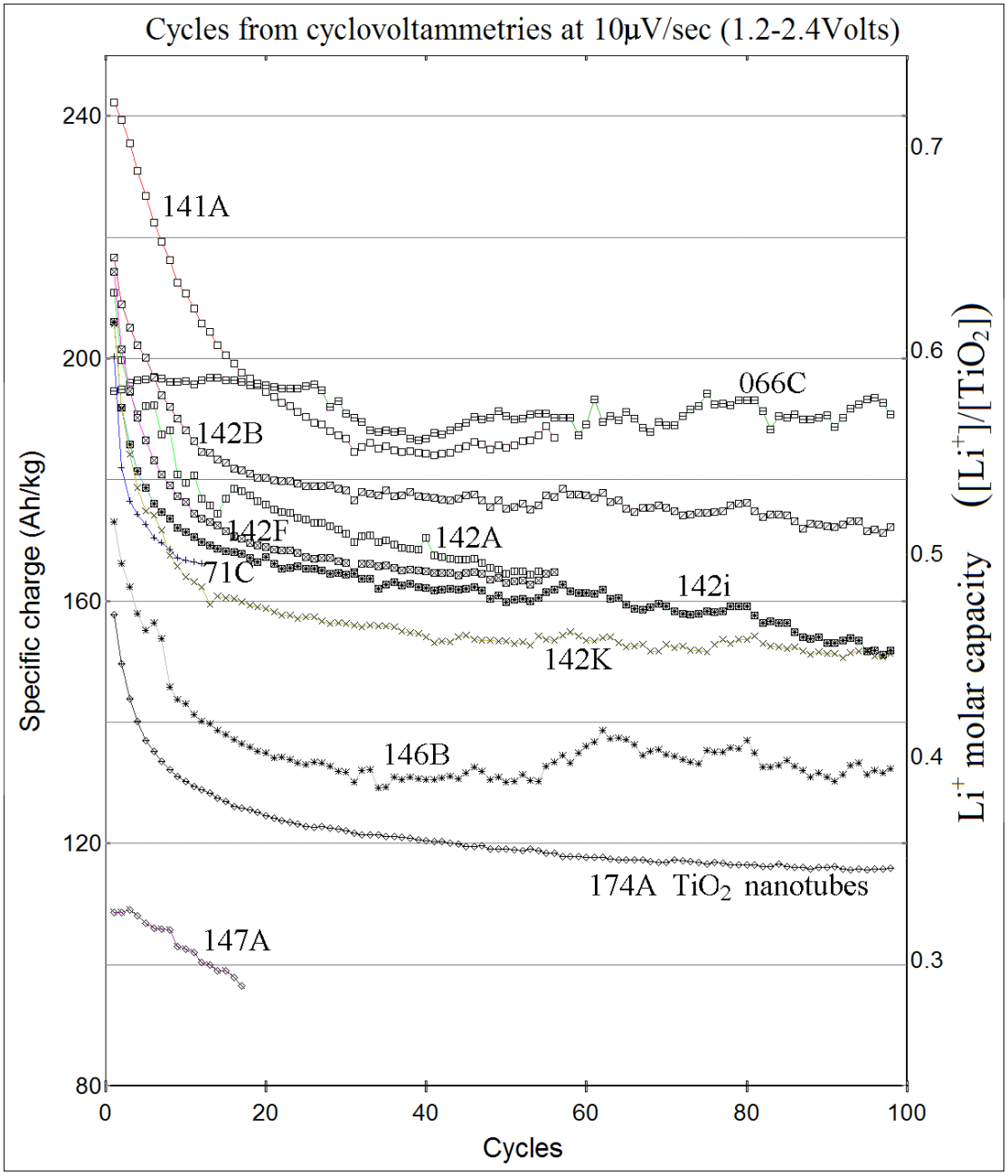

Figure 91: Specific discharge capacity plots of anatase nano fiber samples, taken from cyclovoltammetric studies at 10µV/sec in the range (1.2-2.4 Volts).

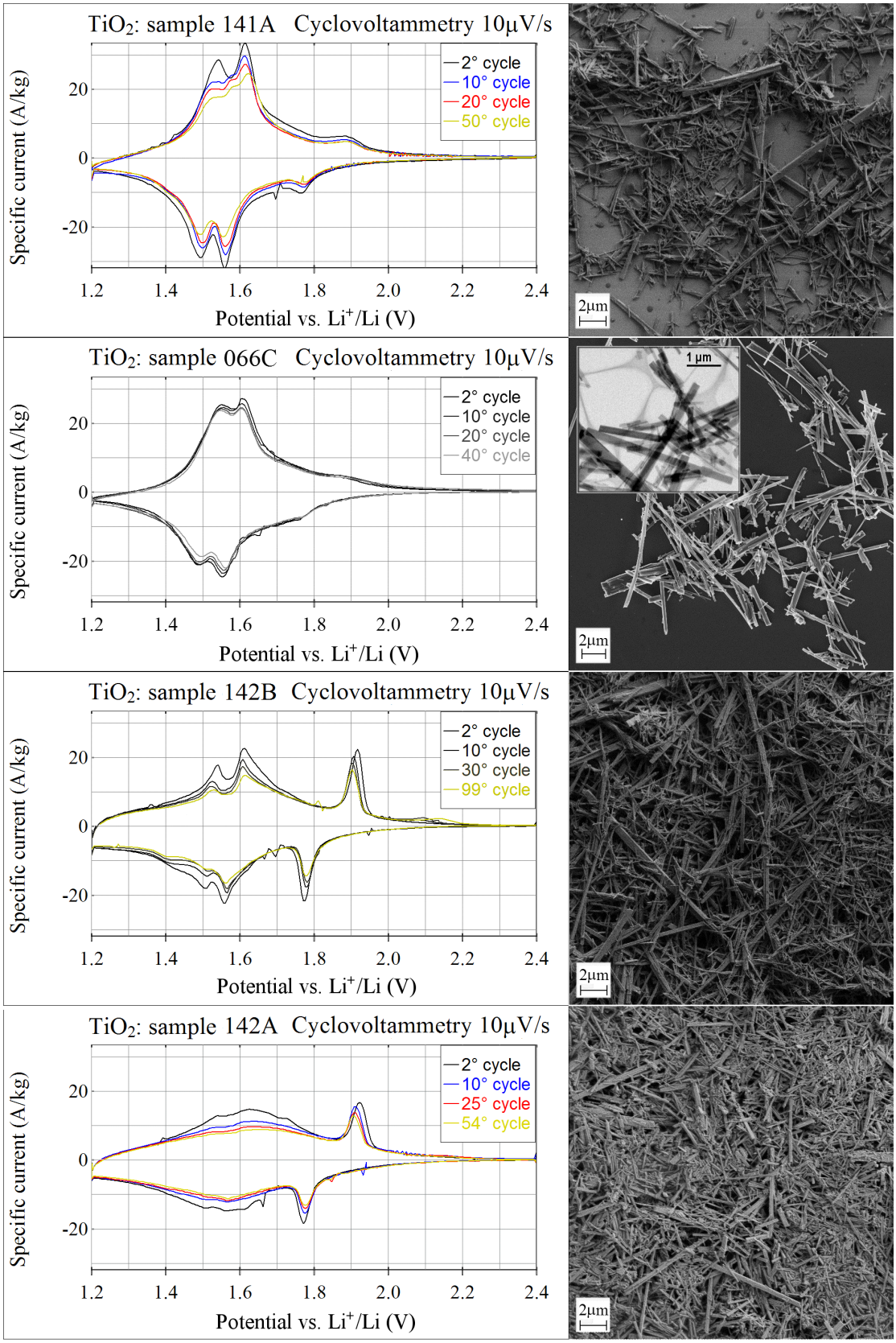

Figure 92: Cyclovoltammetric plots (10µV/s 1.2-2.4 Volts) of anatase nano fiber samples ordered for decreasing capacity (samples from 1 to 4 of Figure 91). Right: S.E.M. images.

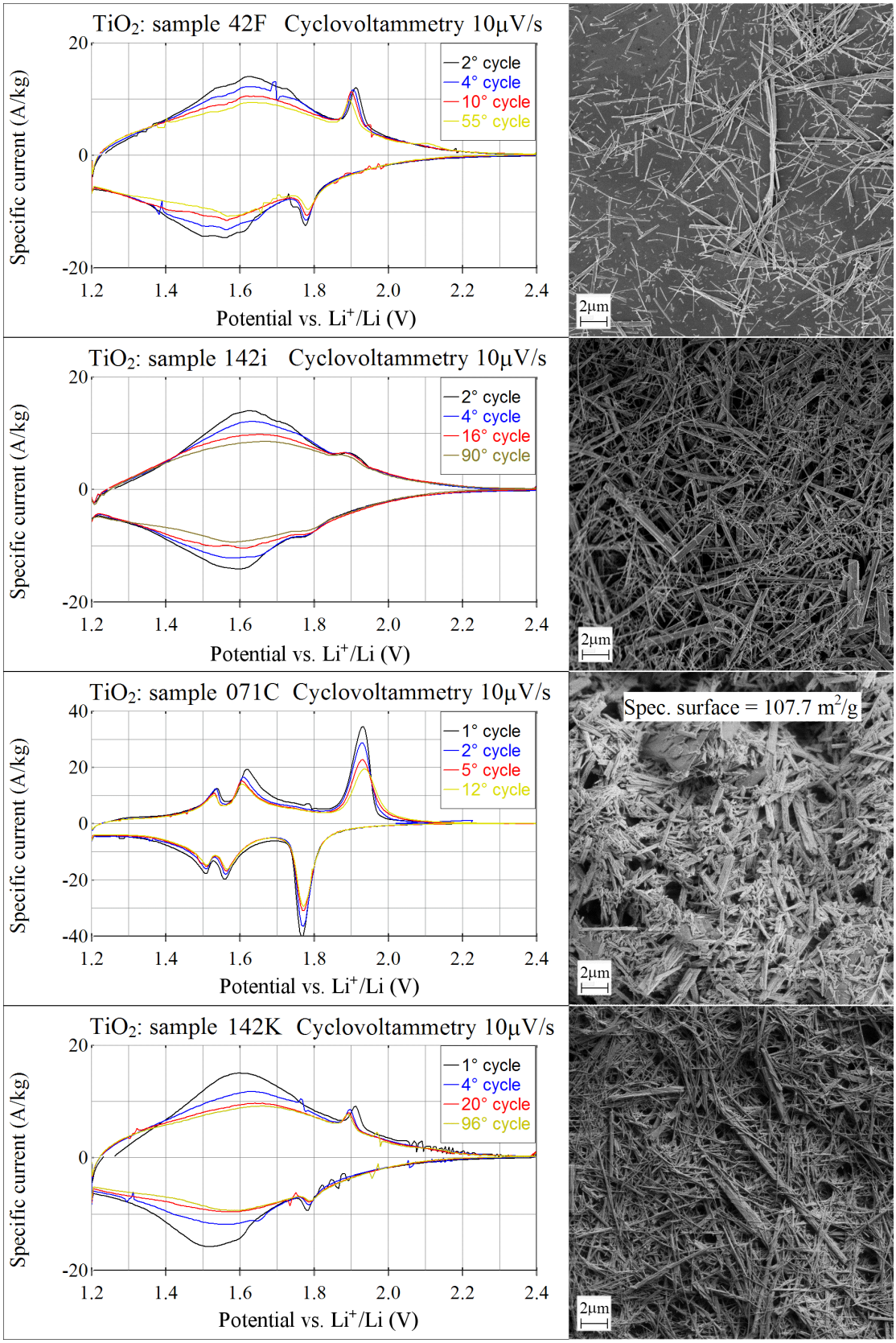

Figure 93: Cyclovoltammetric studies (10µV/s 1.2-2.4 Volts) of anatase nano fiber samples ordered for decreasing capacity (samples from 5 to 8 of Figure 91). Right: S.E.M. images.

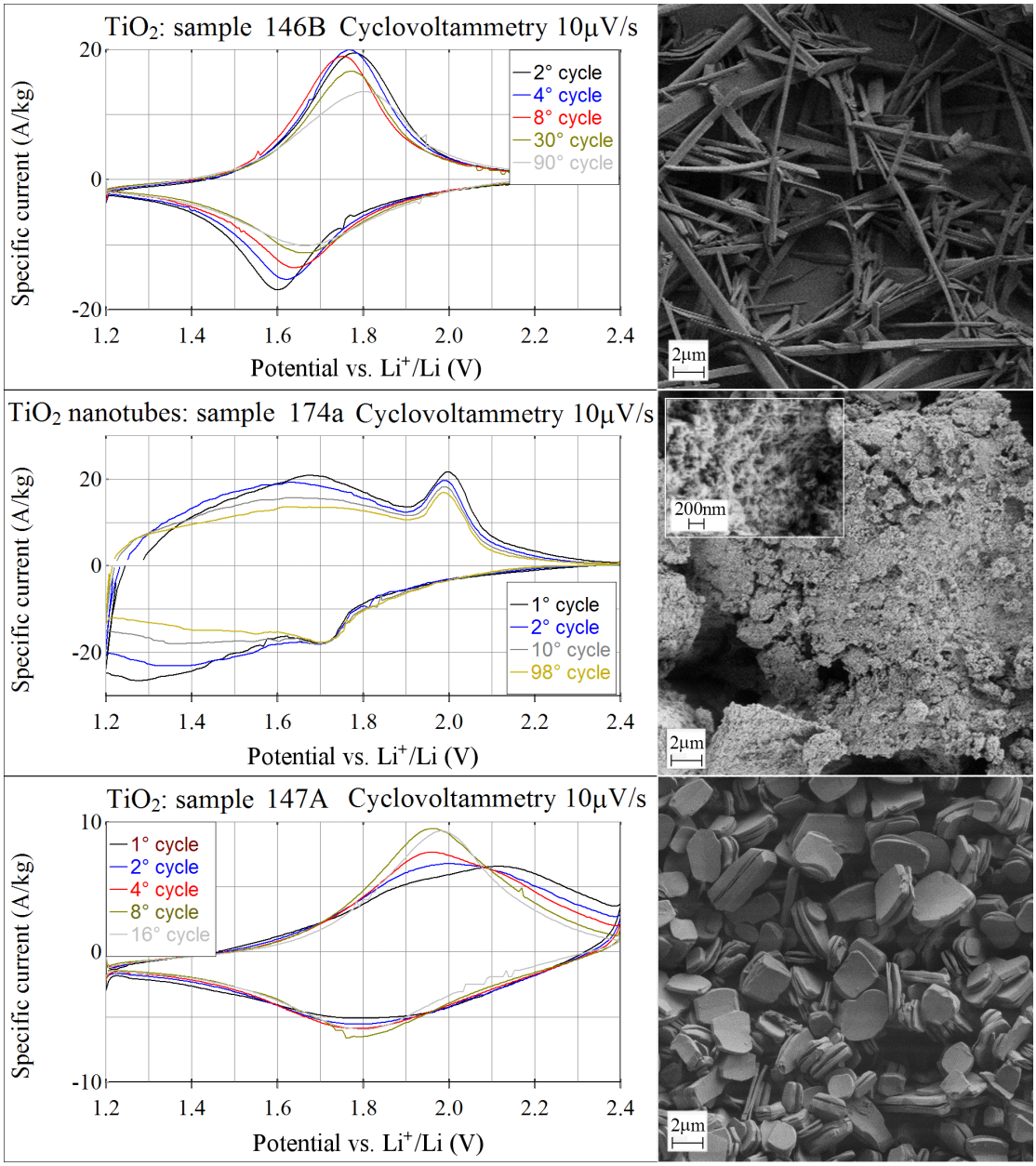

Figure 94: Cyclovoltammetric studies (10µV/s 1.2-2.4 Volts) of anatase nano fiber samples ordered for decrescent capacity (samples 9 and 11 of Figure 91). Right: S.E.M. images.

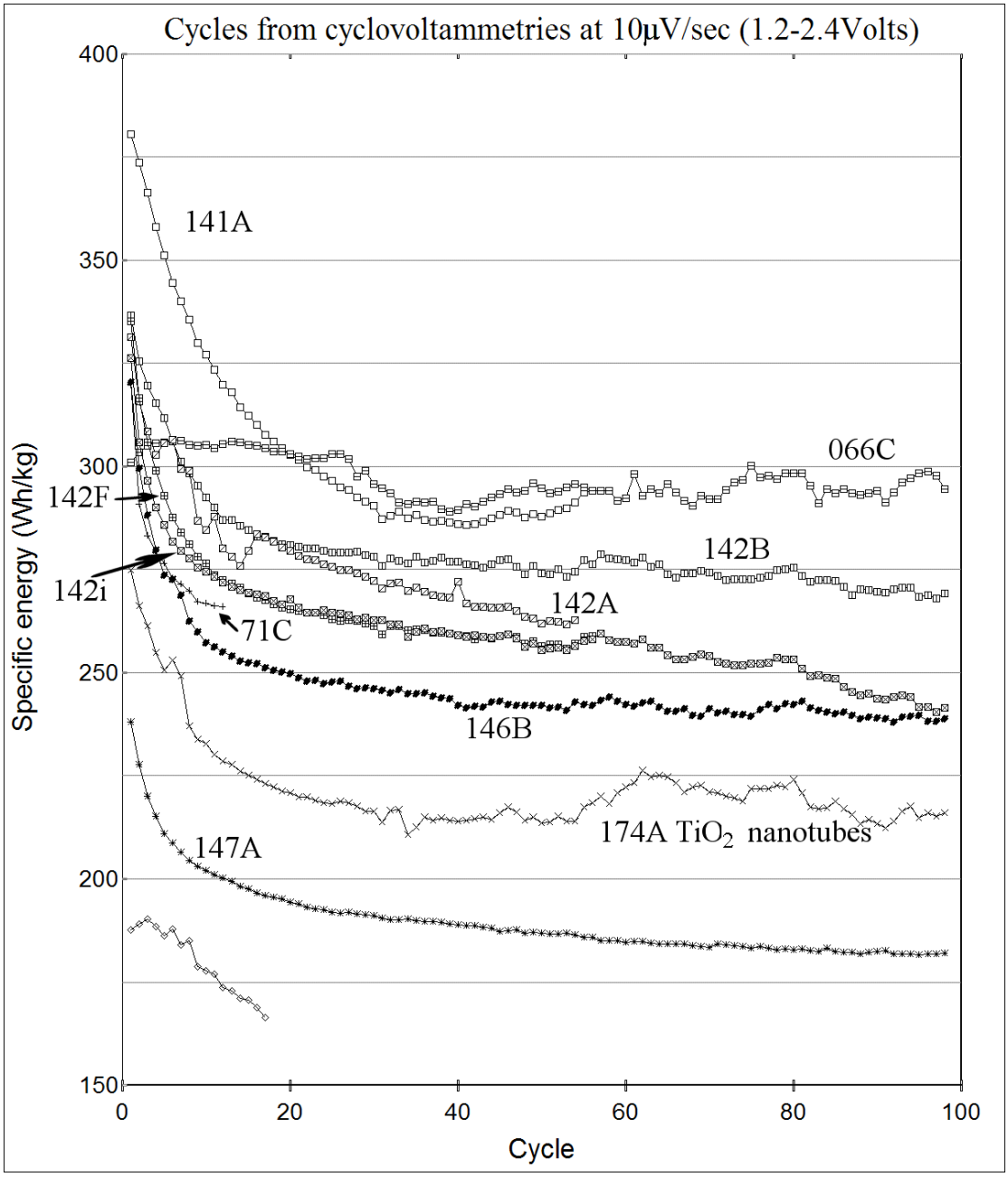

Figure 95: Specific discharge energy plots of anatase nano fiber samples, taken from cyclovoltammetric measurements at 10µV/sec in the range (1.2-2.4 Volts).

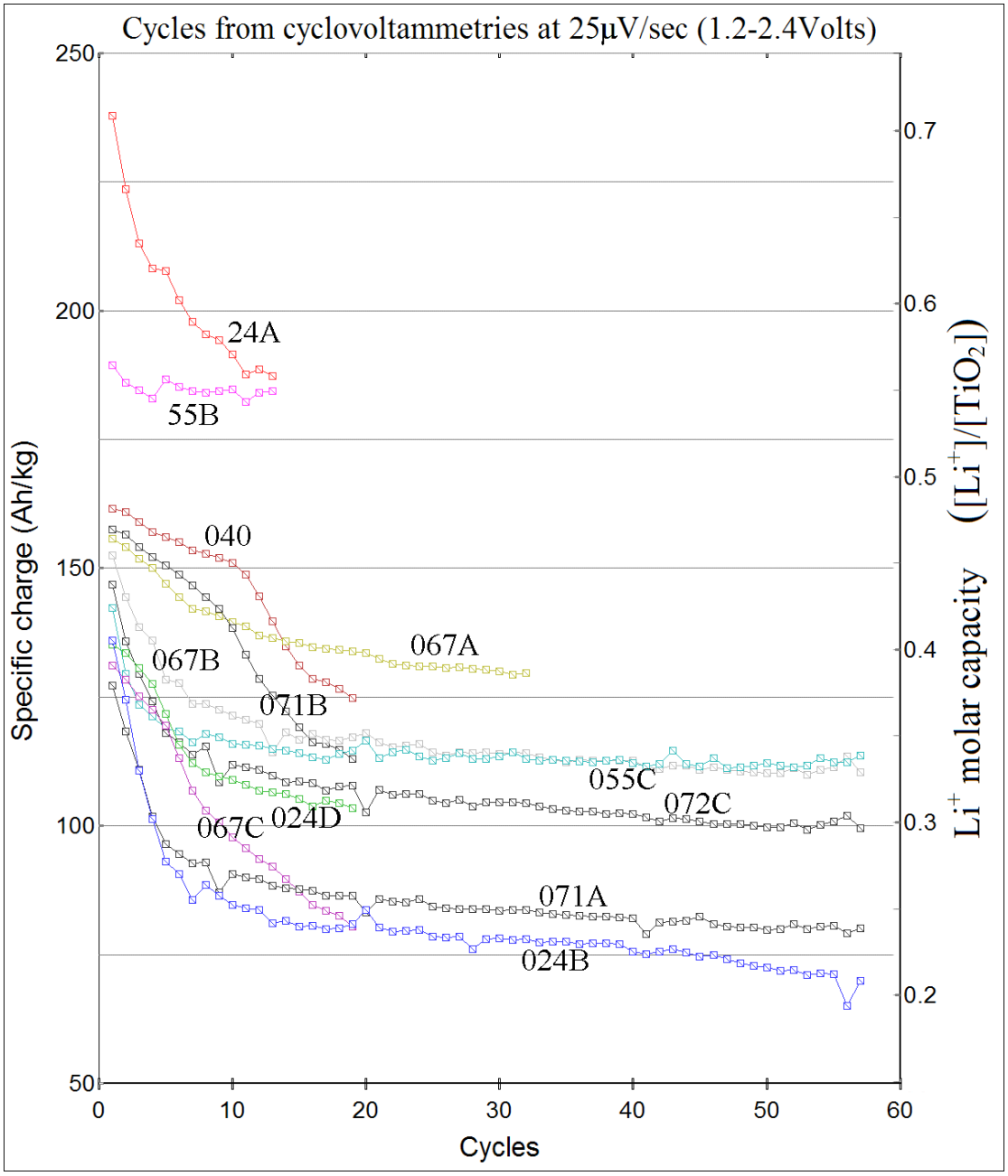

Figure 96: Specific charge plots of anatase nano fiber samples, taken from cyclovoltammetric measurements at 25µV/sec in the range (1.2-2.4 Volts).

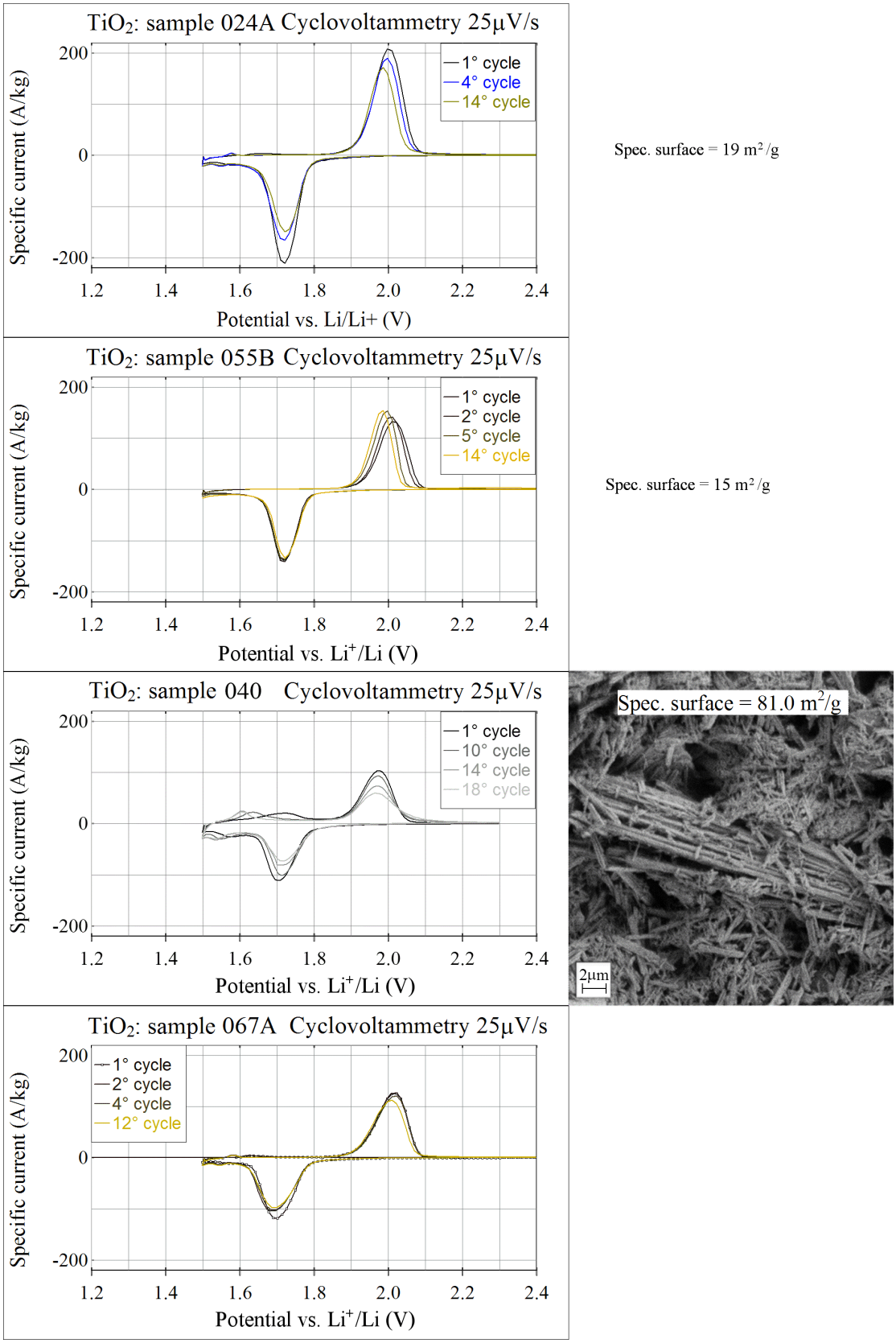

Figure 97: Cyclovoltammetric studies (25µV/s 1.5-2.3 Volts) of anatase nano fiber samples ordered for decreasing capacity (samples from 1 to 4 of Figure 96). Right: S.E.M. images.

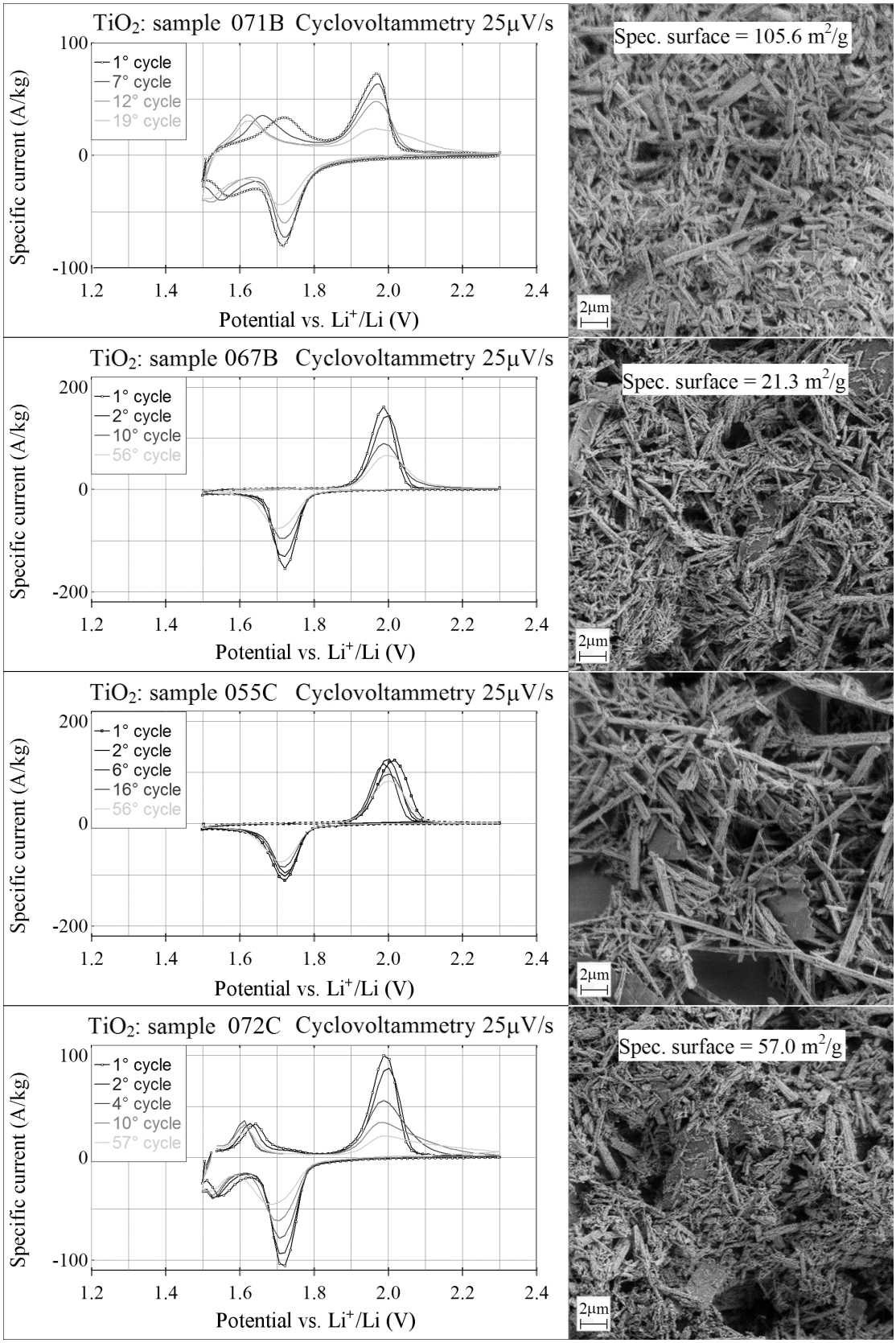

Figure 98: Cyclovoltammetric studies (25µV/s 1.5-2.3 Volts) of anatase nano fiber samples ordered for decreasing capacity (samples from 5 to 8 of Figure 96). Right: S.E.M. images.

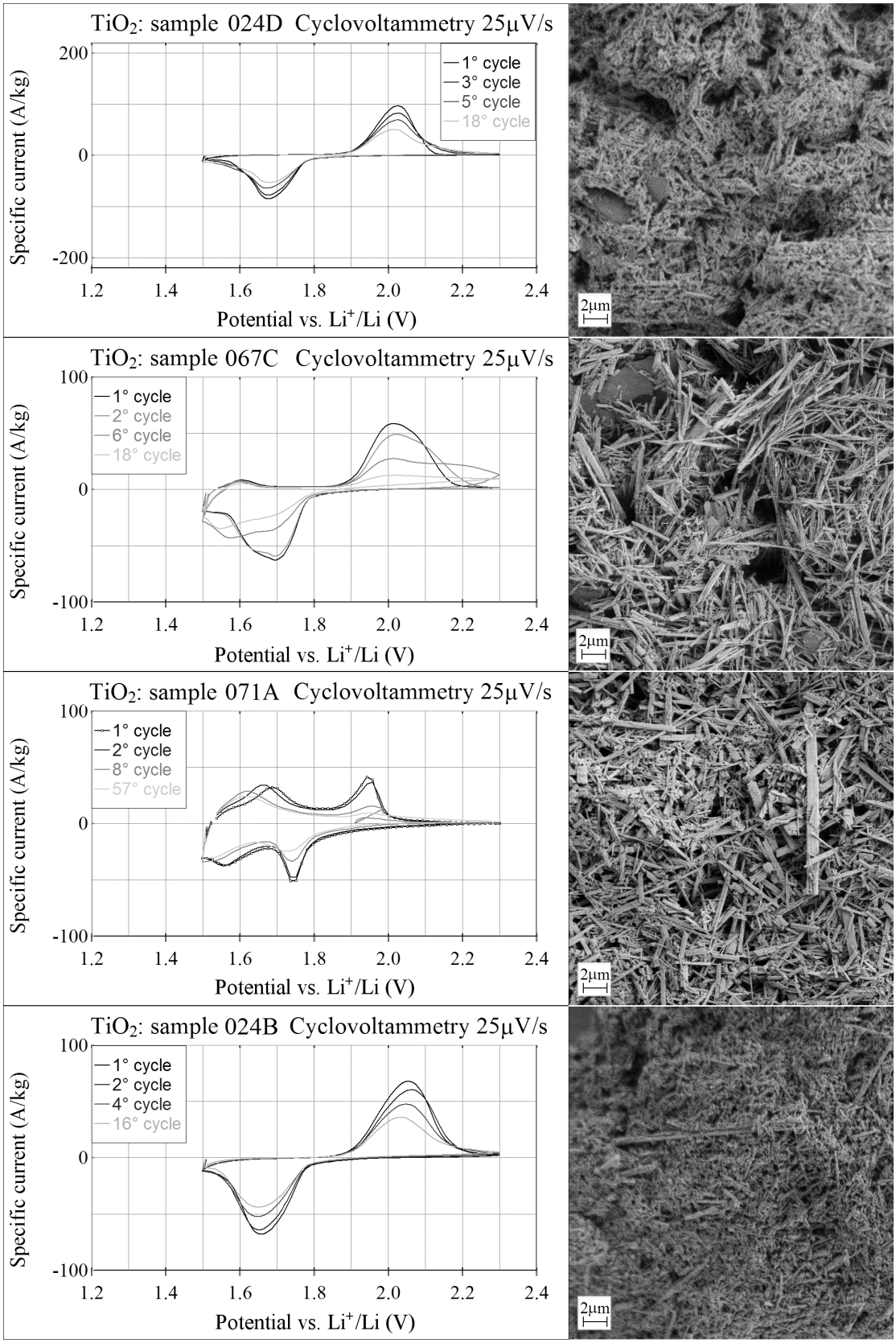

Figure 99: Cyclovoltammetries (25µV/s 1.5-2.3 Volts) of anatase nano fiber samples ordered for decreasing capacity (samples from 9 to 11 of Figure 96). Right: S.E.M. images.

15.2.2 Zirconia coated Titanium dioxide

The main problem affecting the electrode material is their capacity fading. Many efforts have been made by several researcher groups [**49**] in order to solve, or at least to reduce this important problem. Generally, capacity fading is a consequence of the disordering or destruction of the host crystal structure. One method was applied to prevent crystal destruction, coating or doping with another Li^+ permeable compound, whose structure remains unaffected by cycling (it does not matter whether this coating compound is electroactive versus Li^+).

Samples tested in this section are ZrO_2-coated TiO_2 in which TiO_2 is present as anatase and rutile. Zirconium is supposed to stabilize these structures by a stronger interaction with oxygen through dπ–pπ backbonding. In Figure 100, a stereoscopic view of the rutile crystal structure is shown. A stereoscopic view of TiO_2 anatase has been shown in Figure 90.

The samples are:

- Sample 132D: anatase : rutile = 96 : 4
- Sample 132A: anatase : rutile = 70 : 30

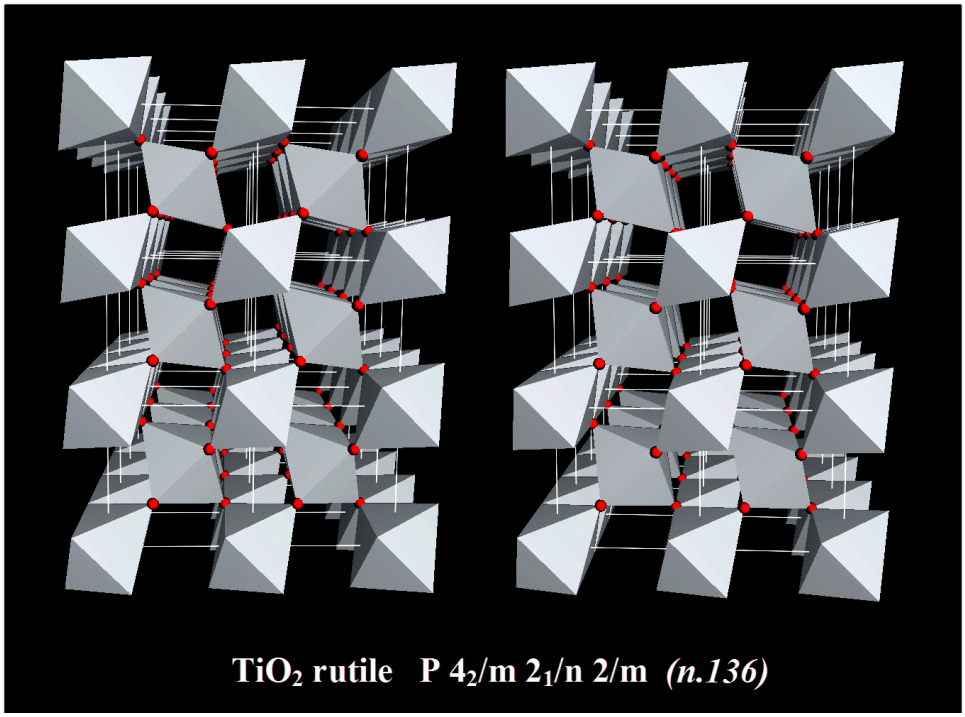

Figure 100: Stereoscopic view of TiO_2 rutile crystal structure.

In Figure 101, cyclovoltammetries of the two products are shown. They reveal the same peak position; with the same big potential gaps between the anodic peak at 1.94Volts and its related cathodic peak like those found in the cyclovoltammetry of the other TiO_2 based products. But unlike the other products, negligible fading is seen in the specific charge plots (Figure 102). Sample *132A* (anatase : rutile = 70 : 30) exhibits de-fact no fading at all. This is good evidence for the success of the stabilization of the method.

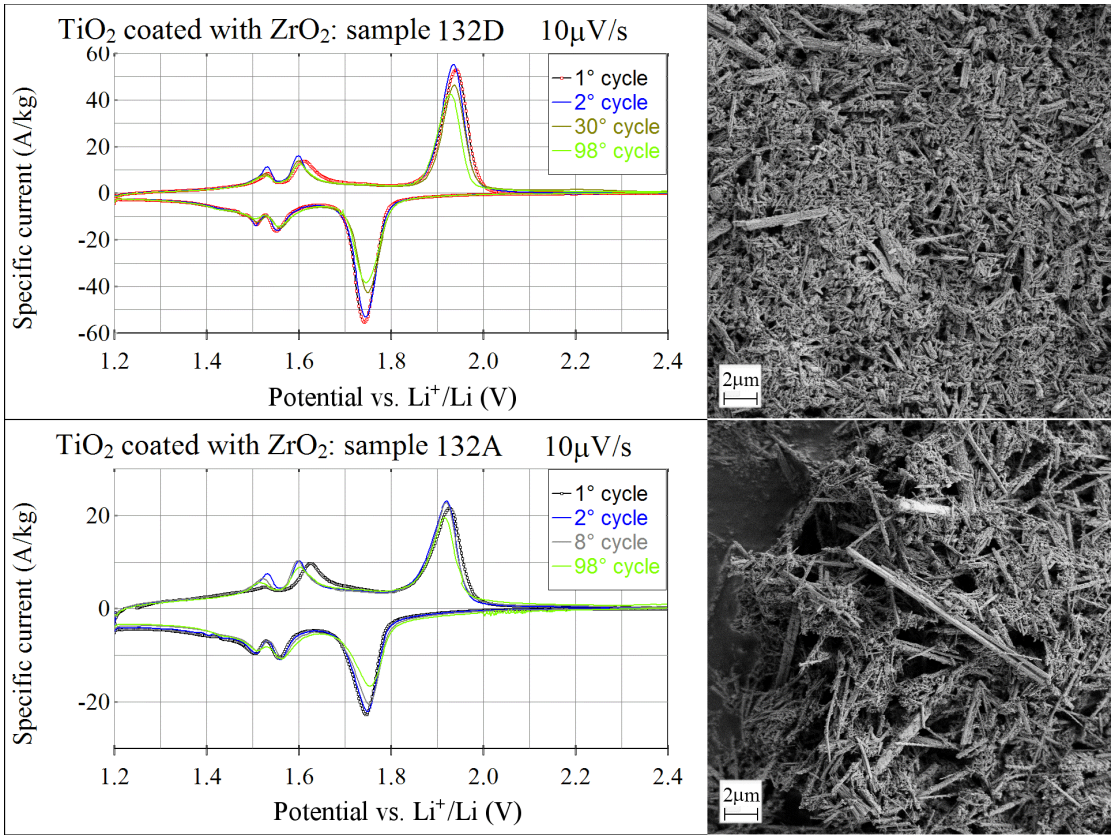

Figure 101: Cyclovoltammetric studies (10µV/s 1.2-2.4 Volts) of the Zirconia stabilized anatase nano fiber samples ordered for decreasing capacity. Right: S.E.M. images.

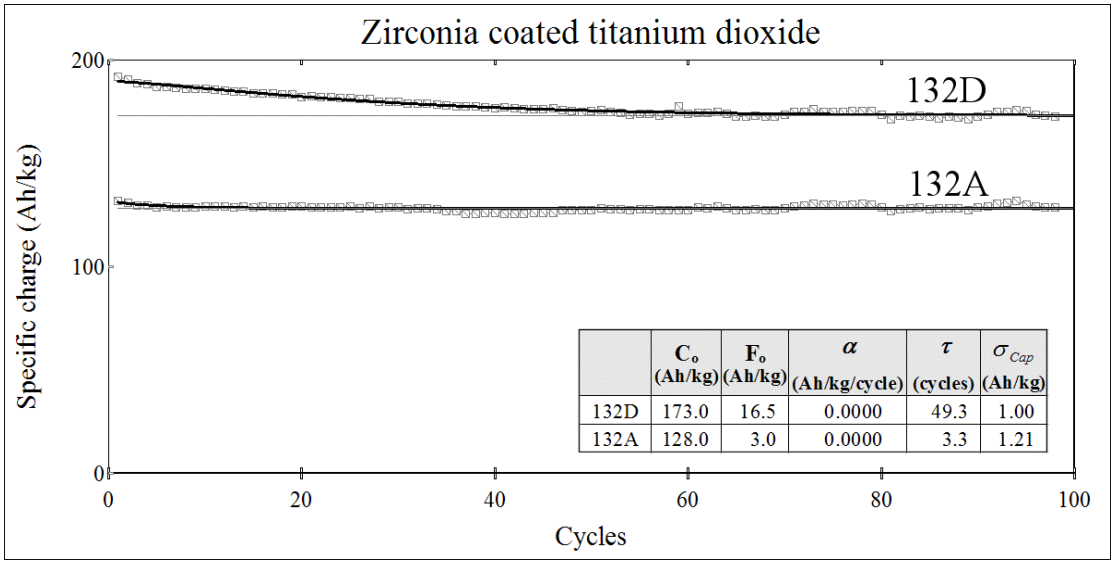

	C_o (Ah/kg)	F_o (Ah/kg)	α (Ah/kg/cycle)	τ (cycles)	σ_{Cap} (Ah/kg)
132D	173.0	16.5	0.0000	49.3	1.00
132A	128.0	3.0	0.0000	3.3	1.21

Figure 102: Specific discharge capacity of Zirconia stabilized anatase nano fiber samples.

Chapter 16.

Conclusions

Selected oxide-based materials have been synthezised, optimized and investigated with respect to applications in Li-high energy battery applications. Three groups of materials are discriminated : 1. Mn-based compounds related to the commercial $LiCoO_2$ material. 2. Nano fibers of vanadic acid $H_2V_3O_8$ and 3. nano fibers of TiO_2.

To enhance the performance of $LiMn_{0.5}Ni_{0.4}Al_{0.1}O_2$, three methods were applied:

1. Doping by sodium (sodium was supposed to occupy the Li tetrahedrical position in the layout);
2. Aluminum replacement by boron (boron was supposed to occupy the octahedral position);
3. Graphite oxide treatment (this was supposed to increase the electronic conductivity of the sample by partial surface coating).

The results showed that all these treatments led to low performance products.
Various compounds have then been synthesized, with four of them fitting the superstructure hypothesis requirements. Products were made via the *wet synthesis* method and via thermal treatment were carried out at 800°C, 950°C, and 1000°C.
The two best compounds have the same composition $LiMn_{0.5}Ni_{0.4}Al_{0.1}O_2$, but the one synthesized at 950°C gave the better performance and maintains the ratio between peaks related to two de-intercalation processes.

Investigations of $LiMn_aNi_bCo_cAl_dO_2$ resulted in the syntheses of two new high performances products; both were produced in a pure phase, with the desired layered α–$NaFeO_2$ structure (space group $R\bar{3}m$, no.166), and show as well defined two-step de-intercalation processes.

They are labeled $\mathbf{LiMn_{0.283}Ni_{0.566}Co_{0.141}Al_{0.01}O_2}$ and $\mathbf{LiMn_{0.335}Ni_{0.495}Co_{0.160}Al_{0.01}O_2}$. The products gave at the first discharge **170** (0.6F/mole) and **160 Ah/kg** respectively. Further investigations of $\mathbf{LiMn_{0.283}Ni_{0.566}Co_{0.141}Al_{0.01}O_2}$ led to the following results:

- Lithium diffusion inside the LiMnNiCoAl.283.566.141.010-950°C structure is a limiting factor for use at high C rates (>C/10).
- Syntheses carried out at different temperatures did not lead to better results in terms of electrochemical performance. Therefore, if an optimal synthesis temperature exists, it should be quite close to 950°C. The gross optimal temperature range is from 900°C to 1000°C.
- The lithium intercalation/de-intercalation processes vary anisotropically the unit cell constants. These changes are reversible.
- During the first charge, a part of deintercalated lithium cannot be reinserted in the normal cycling condition. This process is nevertheless reversible and the lithium can be “forced” to reintercalate the structure. This loss of lithium is the major factor causing the high irreversible capacity loss at the first cycle; the other cause is the irreversible SEI formation.
- The experiments confirm the structure stabilizing properties of incorporated aluminum.

An empirical description has been proposed in section 8.3 with the aim to introduce a systematic criterion for the product classification. The empirical description proposed for specific charge discharge plots seems to fit the experimental data quite well:

A good correlation between the c axis length and $\overline{C_{100}^{Calc}}$ has been found, in particular shorter *c axes* favor good electrochemical performances.

Investigations on the TiO_2 anatase system, as well as ZrO_2 coated TiO_2 (anatase and rutile) resulted in a specific energies of about just half of the best compounds presented in this work. The effectiveness of the ZrO_2 coating was shown resulting in longer life cycles and virtually no fading.

A very remarkable material for electrochemical applications are $H_2V_3O_8$ nano fibers, which are able to host up to four Li^+ equivalents per formula unit. Considering the first 60 cycles, the product is very competitive to the better market products, both in terms of specific energy and specific power (very high discharge current up to C/1.7). At higher cycle numbers it undergoes energy fading. Once its structure would be stabilized in order to prevent fading after 60 cycles, $H_2V_3O_8$ nano fibers would be a very interesting candidate for Li-ion batteries. The multizone discharge potential would have to be counterbalanced by suitable means of electronic equipment.

Main differences were due to the positioning of a transition metal from their octahedrical site towards the lithium site. A shift of the transition metal towards the lithium site during cycling processes was also noticed. Nevertheless, no phase transitions were observed.

Remarkable performances in terms of specific capacity were obtained from two compounds: $LiMn_{0.283}Ni_{0.566}Co_{0.141}Al_{0.01}O_2$ and $LiMn_{0.335}Ni_{0.495}Co_{0.160}Al_{0.01}O_2$; these compounds furnished 156 and 147 Ah/kg respectively after more than 70 cycles.

The synthesized compounds were characterized by X-ray powder diffraction in order to determine their crystallographic parameters. Additionally, special in-situ X-ray cells were developed and tested during this work in order to investigate their structural changes in the electrodes, such as phase transformations or lattice changes as a result of the electrochemical processes. Relevant products were tested in electrochemical cells by cyclovoltammetry and galvanostatic cycles.

References:

1 P.W. Atkins, Chimica fisica (1982) Chap 11 page 275. Translated from English: P.W. Atkins, Physical Chemistry (1978), Oxford University press.

2 P.W. Atkins, Chimica fisica (1982) Chap 12.1 page 305. Translated from English: P.W. Atkins, Physical Chemistry (1978), Oxford University press.

3 C. M. A. Brett, and A. M. O. Brett, *Electrochemistry: Principles, Methods, and Applications*, Oxford University Press, Oxford (1993).

4 G. Gritzner, and G. Kreysa, Pure & Appl. Chem., **65**, 1010 (1993).

5 E. Mengeritsky, P. Dan, J. Weisman, A. Zaban, and D. Aurbach, J. Electrochem. Soc., **143**, 2110 1996).

6 V. S. Bagotzky, and A. M. Skundin, *Russian Journal of Electrochemistry*, **34**, 654 (1998).

7 J. O. Besenhard, J. Gürtler, P. Komenda, and A. Paxinos, *J. Power Sources*, **20**, 253 (1987).

8 S. Hossain, in *Handbook of Batteries* (ed. Linden, D.), Mc Graw-Hill, 36.1, New York (1995).

9 M. Winter, J. O. Besenhard, M. E. Spahr, and P. Novák, *Adv. Mater.*, **10**, 725 (1998).

10 L. A. Dominey, in *Lithium Batteries: New Materials, Developments and Perspectives* (ed. Pistoia, G.), Elsevier, 137, Amsterdam (1994).

11 D. L. Foster, H. C. Kuo, C. R. Schlaijker, and A. N. Dey, *J. Electrochem. Soc.*, **135**, 2682 (1988).

12 F. Croce, S. Panero, S. Passerini, and B. Scrosati, *Electrochim. Acta*, **39**, 255 (1994).

13 I.A.Courtney and J.R. Dahn, *J. Electrochem. Soc.* **144**, 2045, (1997)

14 A.M.Wilson and J.R. Dahn, *J. Electrochem. Soc.*,, **142**, 326, (1995)

15 J.O'M. Bockris, B.E.Conway, E.Yeager and R.E. White, ed., *Comprehensive Treatise of Electrochemistry*, Plenum Publishing Corp., New York, vol. 3, pp. 341-470 (1981).

16 T.R. Jow and C.C. Liang, *J. Electrochem. Soc.*, **129**, 1429 (1982).

17 D. Billaud, E. MacRae, and A. Herold, *Mat. Res. Bull.*, **14**, 857 (1979).

18 Y. Matsuda, M. Morita, T. Hanada, and M. Kawaguchi, *J. Power Sources*, **43**, 75 (1993).

19 M. Morita, T. Hanada, H. Tsutsumi, Y. Matsuda, and M. Kawaguchi, *J.Electrochem. Soc.*, **139**, 1227 (1992).

20 K. Brandt, *Solid State Ionics*, **69**, 173 (1994).

21 L. Xie, W. Ebner, D. Fouchard, and S. Megahed, *The Electrochemical Society Proceedings*, **94-28**, 263 (1994).

22 S. Yamada, M. Fujiwara, and M. Kanda, *J. Power Sources*, **54**, 209 (1995).

23 B. Garcia, P. Barboux, F. Ribot, A. Kahn-Harari, L. Mazerolles, and N. Baffier, *Solid State Ionics*, **80**, 111 (1995).

24 D. Larcher, M. R. Palacín, G. G. Amatucci, and J.-M. Tarascon, *J. Electrochem. Soc.*, **144**, 408 (1997).

25 A. Manthiram, and J. Kim, *Chem. Mater.*, **10**, 2895 (1998).

26 B. Scrosati, *Nature,* **373**, 557 (1995).
27 K. Brandt, *J. Power Sources,* **54**, 151 (1995).
28 L. F. Trueb, and P. Rüetschi, *Batterien und Akkumulatoren,* Springer, Berlin-Heidelberg (1998).
29 M. E. Spahr, *Ph. D. Thesis, ETH Zürich,* **Nr. 12281** (1997).
30 A. d. Bethune, *J. Electrochem. Soc.,* **102**, 288C (1955).
31 D. Rahner, S. Machill, H. Schlörb, K. Siury, M. Kloss, and W. Plieth, *J. Solid State Electrochem.,* **2**, 78 (1998).
32 J. C. Hunter, *J. Solid State Chem.,* **39**, 142 (1981).
33 M. Coluccia, *Ph. D. Thesis, ETH Zürich*, **Nr. 13751** (2000)
34 T. Ohzuku, H. Yoshizawa, M. Nagayama, Patent Appl. WO 02/078105 A1.
35 J.M. Paulsen, R.A. Donaberger, J.R. Dahn, "Layered T2-, O6-, O2-, and P2-type $A_{2/3}M'_{1/3}{}^{2+}M_{2/3}{}^{4+}O_2$ bronzes, A=Li, Na; M'=Ni, Mg; M=Mn, Ti", Chem. Mater. **12**, 2257 (2000).
36 J.C. Paniz, P. Novák, O. Haas, "Raman microscopy Applied to Rechargeble Li-ion Cells – Steps Towards In Situ Raman Imaging with increasing Optical Efficiency", Appl. Spectrosc. **55**, 1131 (2001).
37 Z.Lu., R.A. Donaberger, C.L. Thomas, J.R. Dahn, "T-2 and O2 $Li_{2/3}Co_xNi_{1/3-x/2}Mn_{2/3-x/2}O_2$ electrode materials", J. Electrochem. Soc. **149**, A1083 (2002)
38 Y. Koyama, I. Tanaka, H. Adachi, Y. Makimura, N. Yabutuchi, T. Ohzuku, Book of abstracts, 11th International meeting on lithium batteries, Monterey (2002).
39 F. Ronci, B. Scrosati, V. Rossi Albertini and P. Perfetti, *J.Phys. Chem.* B, **105**, 754-759 (2001).
40 G. Ceder, Y.-M. Chiang, D. R. Sadoway, M. K. Aydinol, Y.-I. Jang, and B. Huang, *Nature,* **392**, 694 (1999).
41 Y.-I. Jang, B. Huang, H. Wang, G. R. Maskaly, G. Ceder, D. R. Sadoway, Y.-M. Chiang, H. Liu, and H. Tamura, *J. Power Sources,* **81-82**, 589 (1999).
42 S. Huang, L. Kavan, A. Kay, and M. Grätzel, *J. Electrochem. Soc*. **141**, 142 (1995).
43 F. Bonino, L. Busani, M. Manstretta, B. Rivolta, and A. B. Scrosati, J. Power Sources **14**, 261 (1985).
44 W. J. Macklin and R. J. Neat, Solid State Ion. **53–56**, 694–700 (1992).
45 B. Zachau-Christiansen, K. West, and S. Atlung, Solid State Ion. **28–30**, 1176–1182 (1988).
46 T. Ohzuku and T. Kodama, J. Power Sources **14**, 153 (1985).
47 Lindstrom, H., S. Sodergren, et al.. "Li^+ ion insertion in TiO_2 (anatase) 2. Voltammetry on nanoporous films." Journal of Physical Chemistry B 101(39): 7717-7722 (1997).
48 Van de Krol, R., A. Goossens, et al.. "Spatial extent of lithium intercalation in anatase TiO_2." *Journal of Physical Chemistry B* **103**(34): 7151-7159 (1999).

49 Kavan, L., A. Attia, et al.. "Lithium insertion into zirconia-stabilized mesoscopic TiO_2 (anatase)." *Journal of the Electrochemical Society* 147(8): 2897-2902 (2000).

Acknowledgements:

I would like to express my sincere gratitude to:

Prof. Dr. Reinhard Nesper, for giving me the opportunity to join his group and for his scientific support. It was a honor to work with him.

PD Dr. Petr Novák, for his helps and support

Prof. Dr. Alexander Wokaun, for taking on the task of co-examiner

Dr. Frank Krumeich, for taking all the SEM and TEM measurements I used in this work

Dr. Michael Wörle, for his fruitful support in XRD measurements

Dr. Barbara Hellermann, for patiently corrected my English

Dr. Marcello Coluccia, for introduce me to the thematic related to this work

Al mio socio, Juan Matias Reinoso

Christian Mensing, for his technical assistance

All the members of the Nesper group at ETH

All the member of the lithium batteries group at PSI

CURRICULUM VITAE

Personal data

Name:	Andrea Piotto Piotto
Place and date of birth:	Monterotondo (Rome), 3rd July 1963
Nationality:	Italian

Education

- **1977-1982 Diploma in Industrial chemistry**. Taken at "I.T.I.S. G.L. Bernini, Rome Italy
- **1982-1988 Doctor in Chemistry cum laudae (110/110 con lode)**. Università di ROMA "La Sapienza" Thesis: Characterisation of $Cr_2Mo_3O_{12}$ oxide as cathodic material in Lithium reversible battery.
- **1999-2004 PhD in Natural sciences ETH Zürich** with a thesis upon lithium-reversible batteries.

Congress and Courses

1. School of N.M.R. (Siena (Italy) 1990)
2. Sensors & their applications V (Edinburgh Sept. 1991)
3. Sixth international forum on electrolysis in chemical industry (Fla Nov. 1992)
4. Introduction to the petroleum refinery processing (Amsterdam May 1993)
5. Membrane separations technology (Amsterdam May 1993)

Publications:

1. Lead-selective FET: complexation selectivity of ionophores embedded in membrane. *Andrea PIOTTO PIOTTO*, E DAVINI, G. MAZZAMURRO. Sensors and actuators Vol. 7 n. 1-3 pp.580-583 1992.
2. CHEMFET Devices for Biomedical and Environmental Applications. *Andrea PIOTTO PIOTTO*. E. DAVINI, C.COLAPICCHIONI, G. MAZZAMURRO, F. PORCELLI, A. BARBARO. ADVANCED MATERIALS.
3. ION SELECTIVE ELECTRODE CHARACTERIZATION: A COMPUTER SOFTWARE FOR THE MATHEMATICAL CALCULATION OF DETECTION LIMIT AND SELECTIVITY

CONSTANTS.
Andrea PIOTTO PIOTTO, E. DAVINI, G. MAZZAMURRO.
ANALYTICA CHIMICA ACTA.

Congress Communications:

1. CHEMFET devices for environmental monitoring. *Andrea PIOTTO PIOTTO*, E. DAVINI, C.COLAPICCHIONI, G. MAZZAMURRO, F. PORCELLI, A. BARBARO. [CISCI 1991]
2. Lead-selective FET: complexation selectivity of ionophores embedded in membrane. *Andrea PIOTTO PIOTTO*. E. DAVINI, G. MAZZAMURRO. [Eurosensors V Conference, Rome 1991]
3. Neutral carrier mediated ion transport through solid membranes. *Andrea PIOTTO PIOTTO*. E. DAVINI, G.MAZZAMURRO. [Sensors & their applications, Edinburgh 1991]
4. CHEMFET in biomedical and environmental applications. *Andrea PIOTTO PIOTTO*. E DAVINI, C.COLAPICCHIONI, S.PASSERINI.[Solid State Chemical Sensors for Environmental Applications (Ferrara, Italy 1991)]

Professional History

1990 - 1993 **Eniricerche S.p.A.** (research division of ENI group)

As research chemist, I was involved in the development of new ISFET (ion sensitive field effect transistor).

1993 - 1995 **Nalco Italiana S.p.A.**

Nalco is an American company for the prevention and technical support of corrosion problems (paper mill, refinery, ecc.).
As senior research chemist I was responsible of microbiology and water analytical treatments laboratories, I was entrusted to coordinate both the laboratory activities, in field survey and to give technical support to the sell & marketing. Further, during these activities, I implemented new products mainly for biocide use.

1996 - 1998 **2M Strumenti**

Sell promoter, my duty was to sell scientific instruments to the industries.

1998-1999 Firotek S.r.l.

Marketing responsible for chemical products and services in water treatment.

1999 – 2004 PhD (ETH Zürich and Paul Scherrer Institut)

Thesis work under the supervision of Prof. Dr. Reinhard Nesper (ETH) for the solid-state syntheses and structural characterizations and the supervision of PD Dr. Petr Novak for the electrochemical characterizations.